Design and Testing of Metal Hydride Reactors for Stationary Hydrogen Storage and Cooling Applications

A thesis submitted in partial fulfilment of the requirements for the degree of

Doctor of Philosophy

by

Sayantan Jana

(Roll No. 186103033)

Department of Mechanical Engineering

Indian Institute of Technology Guwahati

Guwahati – 781039, Assam, India

September 2023

Department of Mechanical Engineering

Indian Institute of Technology Guwahati

Assam – 781039, India

Certificate

It is certified that the work contained in the thesis entitled “**Design and Testing of Metal Hydride Reactors for Stationary Hydrogen Storage and Cooling Applications”** submitted by **Mr. Sayantan Jana** to the Indian Institute of Technology Guwahati for the award of the degree of Doctor of Philosophy has been carried out under my supervision in the Department of Mechanical Engineering, Indian Institute of Technology Guwahati. This work has not been submitted elsewhere for any other degree or diploma award.

Prof. P Muthukumar

Professor

Department of Mechanical Engineering

Indian Institute of Technology Guwahati

Assam – 781039, India

Department of Mechanical Engineering

Indian Institute of Technology Guwahati

Assam – 781039, India

Declaration

I declare that this thesis is composed by me, that the work contained herein is my own unless explicitly stated otherwise in the text, and that this work has not been submitted for any other degree or professional qualification other than those specified.

Significant parts of the work outlined in this thesis have been published in academic journals. Wherever the work described is based on the results of other investigations, appropriate acknowledgment has been made following the standard practice of reporting scientific findings.

Sayantan Jana

Roll No: 186103033

Department of Mechanical Engineering

Indian Institute of Technology Guwahati

Assam – 781039, India

Dedicated to

My Family

Acknowledgements

To begin with, I would like to express my sincerest gratitude to my supervisor Prof. P. Muthukumar for his invaluable guidance, support, and trust in accomplishing the research work undertaken to complete the thesis. Through his immense research experience in the field, knowledge, wisdom, problem-solving abilities and patience, my Ph.D. journey has been exceptionally rewarding throughout.

I am very grateful to my doctoral committee members, Prof. U.K. Saha, Prof. Dipankar Narayan Basu, and Prof. Prabu Vairakannu, for providing me with their crucial commendations and insightful evaluations that have assisted me in shaping the thesis.

I express my wholehearted gratitude to Prof. S. K. Dwivedy (ex. HOD), Prof. S. Senthilvelan (ex. HOD), and Prof. K. S. R. Krishna Murthy (HOD) for providing all the lab amenities and opportunities needed during my research work, and financial support rendered by the Department of Mechanical Engineering, IIT Guwahati.

I take this opportunity to convey my sincere thanks to the Department of Science and Technology, Government of India, for the rendered financial support from the following projects: (Project No. DST/IMRCD/BRICS/PilotCall2/RICS-MH/2018(G) and Project No. DST/TMD/MECSP/ 2k17/14(C).

I would like to convey my appreciation to everyone who has contributed in some way to my Ph.D. journey for their assistance, suggestions, support, humour, persistence, patience, tolerance, and many other virtues.

Special thanks should go to the following individuals:

To my seniors and present group members of the Metal Hydride research team, Dr. R. Nithin Narmada, Dr. J. Sunku Prasad, Dr. Alok Kumar, Mr. Abhishek Parida, Mr. Shubham Parashar, and Ms. Akshini More.

To my fellow lab mates, Mr. G. Sureandhar, Ms. Pratibha Maurya, Mr. Arun Kumar, Mr. Suraj Tat, Mr. C. Aswin Karthik, Ms. Juri Sonowal, Ms. Nayanita Kalita, Mr. Puneet Kumar Nema and Mr. Masresha Adasho Achomo.

To our lab technician Mr. Gobindo Boro for helping to fabricate the experimental setups.

To Mr. A. Prabhakaran and his team at M/s Shakunth Aqua Products, Chennai, for fabrication of the reactors. In particular, thanks go to Mr. Raja Ganesan, Mr. Prakash, Mr. Dass and Mr. Raju.

To Mr. Nandan Kanan Das, Mr. Chandan Banikya, Mr. Dilip Chetri, Mr. Gokul Das, Mr. Dulumoni Das, Mr. Gautam Gogoi, Mr. Santosh Gogoi Mr. Jiten Basumatary, and Mr. Mrinal Sharma at Central Workshop.

To Dr. Rituraj Saikia, Mr. Nip Borah at Thermal Science Lab, and Mr. Saiffuddin Ahmed at Material Science Lab.

To several anonymous reviewers.

To my friends at IIT Guwahati, namely Mr. Rishiraj Purkaystha, Mr. Kunal Singh, Mr. Surjendu Maity, Mr. Trilokpati Tribedi, Mr. Niladri Samanta, Mr. Gaurav Bhattacharjee, Mr. Arup Dutta, Mr. Shantanu Kumar Das, Mr. Rohit Kumar, Mr. Chandan Nashine, Mr. Bikramjyoti Sahariah, Mr. Brijesh Kumar Singh, Mr. Ravi Kumar, Mr. Rishabh Saxena and Mr. Tanuj Srivastava.

Last but not least to my parents, wife, late grandfather, grandmother, elder sister and brother-in-law for their endless love, support, encouragement and patience.

With gratitude,

Sayantan Jana

Abstract

The global temperature rise is inevitable, however, can be slowed down if the consumption of fossil fuels to produce electricity, heat and cooling is reduced. A great alternative to fossil fuels is renewable energy sources (RES); however, irregularity of supply is an inherent limitation of these sources, which calls for an intermediate energy storage platform. Among the available energy storage means, storing electricity in the form of hydrogen and retrieving it to produce heat, electricity or any chemical feedstock or fuels is a viable concept that can transform future energy systems. Metal hydrides (MH) are a class of materials, which by means of chemisorption, can reversibly store a large amount of hydrogen within a wide range of operating temperature and pressure. Among different types of MH, intermetallic compounds are of great interest to the scientific community as they can usually absorb and desorb hydrogen within 0-50 bar at 0-100 °C. High volumetric storage capacity, safety, and ultra-high purity (99.9995%) of desorbed hydrogen make it an excellent candidate as the hydrogen storage medium. Moreover, the reaction heat associated with their formation and decomposition enables to offer various thermal devices, viz., refrigerators, heat pumps, heat transformers, hydrogen compressors, thermal energy storage systems, etc.

In this work, a number of MH rectors (3.5-25 kg capacity) have been designed, fabricated and tested for deployment as ideal stationary hydrogen storage devices to be operated in near ambient conditions. Leveraging the cooling capability of MH materials during desorption, different cooling systems are also developed and tested. Two key reactor design configurations have been considered for study, viz. Tube Bundle Reactor (TBR) and the Embedded Cooling Tube Reactor (ECTR). The design of reactors is supported by model simulation outcomes. The MH alloys used in hydrogen storage experiments are $La_{0.8}Ce_{0.2}Ni_5$, $La_{0.7}Ce_{0.1}Ca_{0.3}Ni_5$, $La_{0.9}Ce_{0.1}Ni_5$, and $MmNi_{4.5}Fe_{0.5}$. For storage tests, the absorption studies were conducted in the temperature and pressure ranges of 5-35 °C, 5-60 bar. Whereas the hydrogen desorption studies were conducted in the temperature range of 40-70 °C. The experimental results for hydrogen storage experiments were analysed in terms of the amount of hydrogen stored, rate of heat input, heat output and energy efficiency. The storage studies confirmed that the designed TBR and ECTR modules could potentially operate 3-4 kW low-temperature fuel cells for 1-1.5 hours.

Two different cooling system concepts were explored in this study, i.e., open and closed cycle cooling. Whereas closed cycle cooling was driven by a mechanical compressor, open cycle cooling studies were performed both with and without the aid of a compressor. The alloys used in cooling studies were $La_{0.8}Ce_{0.2}Ni_5$ and $La_{0.7}Ce_{0.1}Ca_{0.3}Ni_5$. For cooling system tests, two primary performance metrics, i.e., coefficient of performance (COP) and specific cooling power (SCP) were analysed by altering cooling temperature and cycle time. The open-cycle cooling study without a compressor indicated that the optimum temperature ranges for achieving a sustained cooling effect was 15–25 °C. At 25 °C, $La_{0.7}Ce_{0.1}Ca_{0.3}Ni_5$ was able to produce 435.5 kJ cold output within 2048 s. When assisted by a compressor, the open cycle cooling system exhibited 19% ($La_{0.7}Ce_{0.1}Ca_{0.3}Ni_5$) and 51% ($La_{0.8}Ce_{0.2}Ni_5$) improvement in SCP compared to the cooling system without a compressor. For closed-cycle cooling experiments, the maximum cooling power attained at 20 °C refrigeration temperature and 30 °C sink temperature was 1.44 kW generating 537.3 kJ cooling within 600 s.

As far as the numerical study part is concerned, an extended numerical model to mimic the hydrogen absorption and desorption in the designed TBR configuration was developed and simulated in COMSOL Multiphysics 5.5. This numerical model is an extension of the numerical model used to design the reactors. The extended model accounts for the bi-directional coupling of flow and heat transfer influences of the heat transfer fluid. The model predictions accorded with the experimental outcomes reasonably. The model was used to further predict the constant mass flow rate desorption behaviour of the TBR module in the temperature range of 40-70 °C. Additionally, to predict the dynamic performance of the compressor driven closed loop cooling system, a lumped model was developed. The model mimics the compressor effect by invoking appropriate flow and pressure correlations. The model was further utilized to gauge the sensitivity of design and operating parameters on system COP and SCP.

Nomenclature

Alphabets

C	Reaction rate constant [s^{-1}]
c_p	Specific heat capacity [$J.kg^{-1}.K^{-1}$]
E_a	Activation energy of absorption [$J.mol^{-1}H_2$]
E_d	Activation energy of desorption [$J.mol^{-1}H_2$]
E_{in}	Energy input [kJ]
E_{out}	Energy output [kJ]
K	Permeability [m^2]
k	Thermal conductivity [$W.m^{-1}.K^{-1}$]
M	Molecular weight [$g.mol^{-1}$]
m	Mass [kg]
$\dot{m}_f$	Mass flow rate of heat transfer fluid [$g.s^{-1}$]
$\dot{m}_{H2}$	Mass flow rate of hydrogen [$g.min^{-1}$]
N	Number of metal atoms per mole of alloy [mol^{-1}]
P	Pressure [bar]
P_c	Compressor power [W]
P_{pump}	Pump power [W]
Q_c	Cooling power [W]
Q_f	Volume flow rate of heat transfer fluid [$m^3.s^{-1}$]
Q_g	Volumetric heat source term [$W.m^{-3}$]
Q_{gas}	Heat carried to the absorbing reactor from the compressor discharge [J]
Q_t	Cumulative cooling effect [J]
R_{bed}	Radius of cylindrical bed [mm]
r_p	Pressure ratio
R_u	Universal gas constant [$J.mol^{-1}.K^{-1}$]
T	Temperature [°C]
t	time [s]
u	Velocity [$m.s^{-1}$]
U_c	Convective heat transfer coefficient [$W.m^{-2}.K^{-1}$]
U_o	Overall heat transfer coefficient [$W.m^{-2}.K^{-1}$]

X	Hydrogen concentration

Greek symbols

∇	Del, or Nabla
ΔH	Enthalpy of formation [$J.mol^{-1}H_2$]
ΔS	Entropy of formation [$J.mol^{-1}H_2.K^{-1}$]
ΔT	Temperature difference
ε	Porosity
ζ	Rate of change of mass of hydrogen [$kg.m^{-3}.s^{-1}$]
μ	Dynamic viscosity [Pa.s]
ρ	Density [$kg.m^{-3}$]
φ	Hysteresis factor
φ_s	Slope factor
φ_o	Slope constant
φ	Outer diameter [mm]
η	Efficiency
γ	Heat capacity ratio

Subscripts

a	Absorption, Alloy
c	Container, Cooling
$comp$	Compressor
cy	Cycle
d	Desorption
del	delivery
e	Effective
emp	Empty
end	Final
eq	Equilibrium
eqi	Initial equilibrium
f	Heat transfer fluid
g	Gas
h	High

H2	hydrogen
hc	Half-cycle
i	Initial, Interface
in	Inlet, Input
m	Metal, medium
o	Outer
out	Outlet, Output
r	Reactor
ref	Refrigeration
s	Solid phase, Supply
sc	Sensible cooling
sh	Sensible heating
ss	Solid saturated
st	Storage
sink	Sink
t	At any given time
0	Reference state
hyd	Hydride
ut	utilization

Abbreviations

COP	Coefficient of performance
ECT	Embedded cooling tube
HC	Half cycle
HTF	Heat transfer fluid
HTMH	High temperature metal hydride
LPM	Litres per minute
LHV	Lower heating value
LTMH	Low temperature metal hydride
LT-PEMFC	Low temperature polymer electrolyte membrane fuel cell
MFC	Mass flow controller
MH	Metal hydride
MH-CDCS	Metal hydride based compressor driven cooling system

OC-CDMHCS	Open cycle - compressor driven cooling system
OCJ	Outer cooling jacket
PCT	Pressure concentration temperature
SCP	Specific cooling power
TB	Tube bundle
TDMHCS	Thermally driven metal hydride based cooling system

Table of Contents

List of Figures

List of Tables

1. Introduction

1.1. Background

Today, mother earth is the habitat of approximately 8 billion people and it is projected that it will reach 9.7 billion by the mid-21st century. With such a steep rise in population, the demand for heating, cooling and electricity is also bound to increase significantly. A glimpse of the global energy consumption pattern (Fig.1.1) over a span of more than 55 years indicates the dominance of oil, gas and coal over their counterparts. Together the fossil-fuels contribute to more than 80% of the primary source of energy till date. In 2021, 36 billion tonnes of carbon dioxide, almost exclusively from fossil fuels, became part of the world's annual total of around 50 billion tonnes of greenhouse gas emissions (IEA, 2022).

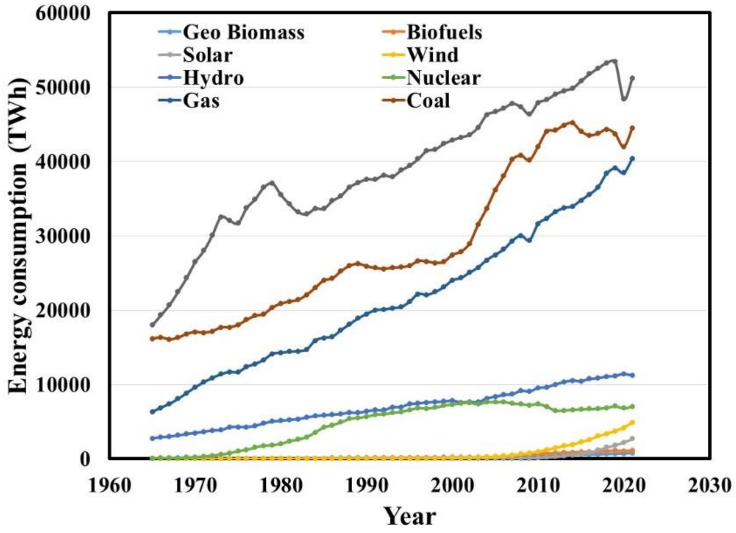

Fig. 1.1: Evolution of global energy consumption from 1965-2021 (Armato, 2013).

A boost in the utilisation of renewable energy is projected as a consequence of the most recent energy policy changes taking place around the world with the purpose of accelerating the deployment of green and clean energy technologies. A few important policy adoptions are USA’s inflation reduction act (The US Press Office, 2022), European Union’s renewable energy policy (Statement, 2003), Japan’s green transformation (GX) basic policy (Implementation Council (The Prime Minister in Action) | Prime Minister’s Office of Japan), China’s Clean Energy policy (Column: China on track to hit new clean & dirty power records in 2022 | Reuters), India’s National Green Hydrogen Mission (Government of India, 2023). Recent data published by the International Energy Agency (IEA, 2022) on worldwide electricity generation and future projections under the Stated Policy Scenario is displayed in Fig.1.2. The share of renewables for electricity generation on 2021 was 7539 TWh (28%) which is predicted to increase to 15073 TWh (43%) in 2030 and by 2050, it is projected to increase to 32452 TWh (65%). Alongside, the share of unabated fossil fuels, i.e., fossil fuels without carbon capture and storage used for electricity generation, is estimated to fall from 17436 TWh (62%) in 2021 to 16324 TWh (47%) in 2030 and to 12862 TWh (26%) by 2050.

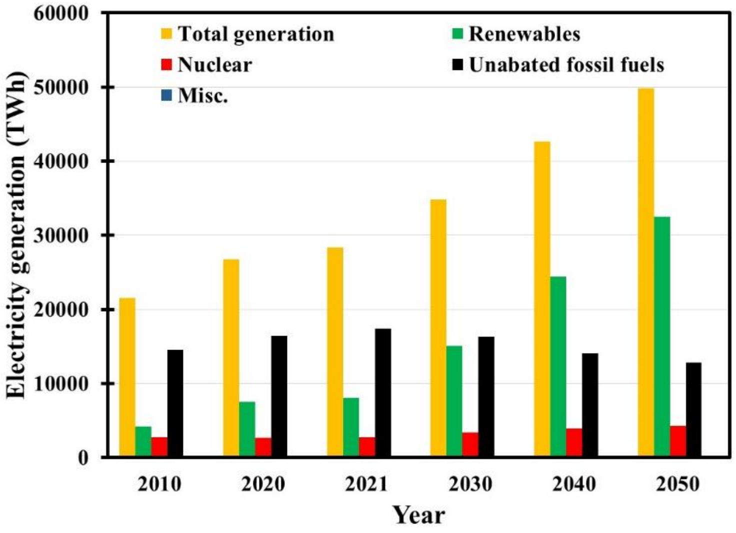

Fig. 1.2: Components of electricity generation (IEA, 2022).

1.2. Need for energy (renewable) storage

As the renewable energy sources are intermittent in nature, the adoption of renewable energy technologies necessitates a storage infrastructure. A very attractive choice of intermediate energy storage is to exercise the Power-to-X concept. The concept relies on the transformation and storage of electrical energy into an energy carrier (gas, fuel or raw material) or a product (basic material, feedstock), etc. The schematic of the utilization of Power-to-X is shown in Fig. 1.3.

The major goal is to store renewable energy for a long time by converting renewable electricity to various forms of energy (e.g., chemical, mechanical etc.) that can be stored easily while also facilitating re-conversion to electricity and thereby reducing strain on electricity grid. With this concept, the excess renewable electricity is converted to hydrogen using electrolysers and the hydrogen is stored or converted to gaseous fuels (e.g., methane, synthetic gas, etc.), or liquid fuels (e.g., methanol), ammonia or electricity (Wulf et al., 2018; Sterner and Specht, 2021). The development of renewable fuels for use in industry, households, transportation, and chemical manufacturing assists in reducing carbon footprint.

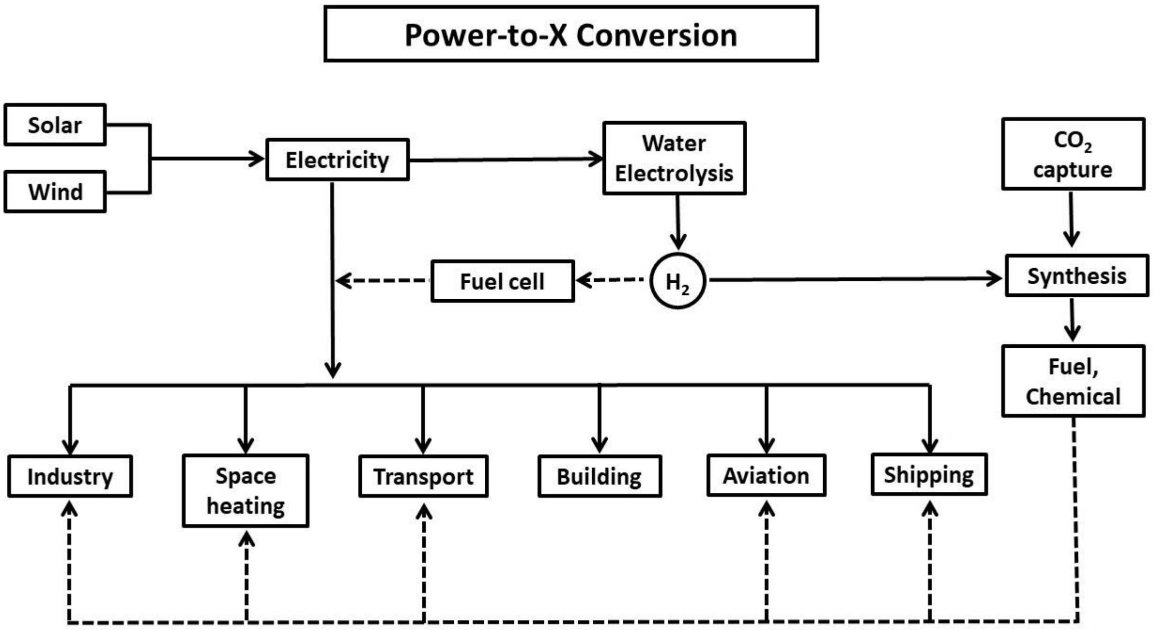

Fig. 1.3: Diagrammatic illustration of Power-to-X conversion concept.

1.3. Role of hydrogen

As the proportion of renewables in the energy mix is expected to increase more than double by 2050 from the 2021 base value (IEA, 2022), hydrogen would play a central role in the successful implementation of the de-carbonized energy infrastructure. Hydrogen as an energy vector offers multiple rewards, e.g., it holds the highest energy content per unit mass (120 $MJ.kg^{-1}$), can be produced from a variety of energy sources (biomass, coal, natural gas, nuclear, water electrolysis, etc.) and also can be utilized to harvest electricity, heat, fuels or chemical feedstock. Worldwide hydrogen demand in 2020 stood at 90 Mt, out of which 40 Mt was consumed in refineries as gas purification and refining agent, more than 45 Mt was spent on chemical industries for ammonia, methanol production, while 5 Mt was used for and steel making. The portion of hydrogen intake in the transportation sector was limited to 20 kt representing only 0.02% of global hydrogen demand. As per records, more than 43000 fuel cell electric vehicles (FCEV) were deployed globally on the road by June 2021 (Glob. Hydrog. Rev. 2022, 2022) which represents a six-fold increment over the 2017 case. The number of FCEVs forecasted to be deployed on the road in the time frame 2025-

2040 sums up to few million as a result of ambitious goals set by countries like China, Japan, Korea, USA and a few EU nations. While on the production side, out of the 90 Mt hydrogen supplied in 2020, 72 Mt was catered by fossil fuels, and the remaining 18 Mt was generated as by-products. Water electrolysis contributed to only 30 kt hydrogen production (~0.03%), whereas, roughly 0.7 Mt (0.7%) was supplied form fossil fuel sources with Carbon Capture, Utilization and Storage (CCUS) technology. Nonetheless, by mid-2021, the global installed electrolyser capacity (300 MW) has doubled over the last five years. By 2030, over 350 projects in various stages of development could increase global electrolyser capacity to 54 GW.

As per a recent review published by the IEA (Glob. Hydrog. Rev. 2022, 2022), to date, 17 nations have declared hydrogen strategies, more than 20 governments have publicly announced that they are working on developing strategies, and numerous enterprises are looking to capitalise on hydrogen economic potential.

1.4. Hydrogen storage

Hydrogen storage methods can be primarily classified into two categories, i.e., physical storage and material based storage (Stetson et al., 2014). The various methods of hydrogen storage are depicted in Fig. 1.4. Physical storage includes compressed, liquid or cryogenic storage, and a combination of cryogenic and compressed storage. The underlying principle of physical storage techniques is to densify hydrogen from ambient conditions (density = 0.089 kg.m^{-3} at STP). Both compressed and liquefied storage are highly energy consuming processes, making it costly. The compression work to attain 800 bar is around 15.5% of its LHV. On the other hand, liquefaction of hydrogen requires approximately 30% of the HHV of hydrogen for large plants (Jensen et al., 2007). Also, liquefied hydrogen at a cryogenic state (20 K) is prone to boil-off losses and incurs high operational costs. Both compressed and liquefied storage are now matured technologies in the market. Cryo-compressed storage (250-350 bar, ~20 K) cartels the advantages of both liquefied and compressed storage (Hwang and Varma, 2014). This method helps to achieve higher volumetric storage density compared to compressed storage or liquefied storage, yet does not require expensive composite fibred cylinders and are safer storage options. Material-based hydrogen storage is a promising alternative to physical storage methods as the volumetric storage density can be improved significantly by virtue of the H-H bond within the host material (Yang et al., 2010). Material-based hydrogen storage is founded on the principle of physisorption or chemisorption (Zhou, 2005; Züttel, 2004). These methods consume less energy compared to the gaseous or liquefied form of storage and are potentially safer storage options (Ren et al., 2017). Whereas physisorption takes place at the surface level sustained by low binding energy (in the order of 4-10 kJ.mol^{-1}), chemisorption occurs in the material bulk region and necessitates much greater binding energy (in the order of 50-100 kJ.mol^{-1}) (Prachi R. et al., 2016). Some of the noteworthy hosts for physisorption-based storage are carbon nanotubes and porous structures, activated carbon, MOF (Langmi et al., 2014), COF (Furukawa and Yaghi, 2009), zeolites (Dong et al., 2007), polymers of intrinsic microporosity (PIM) (Ramimoghadam et al., 2016), etc.

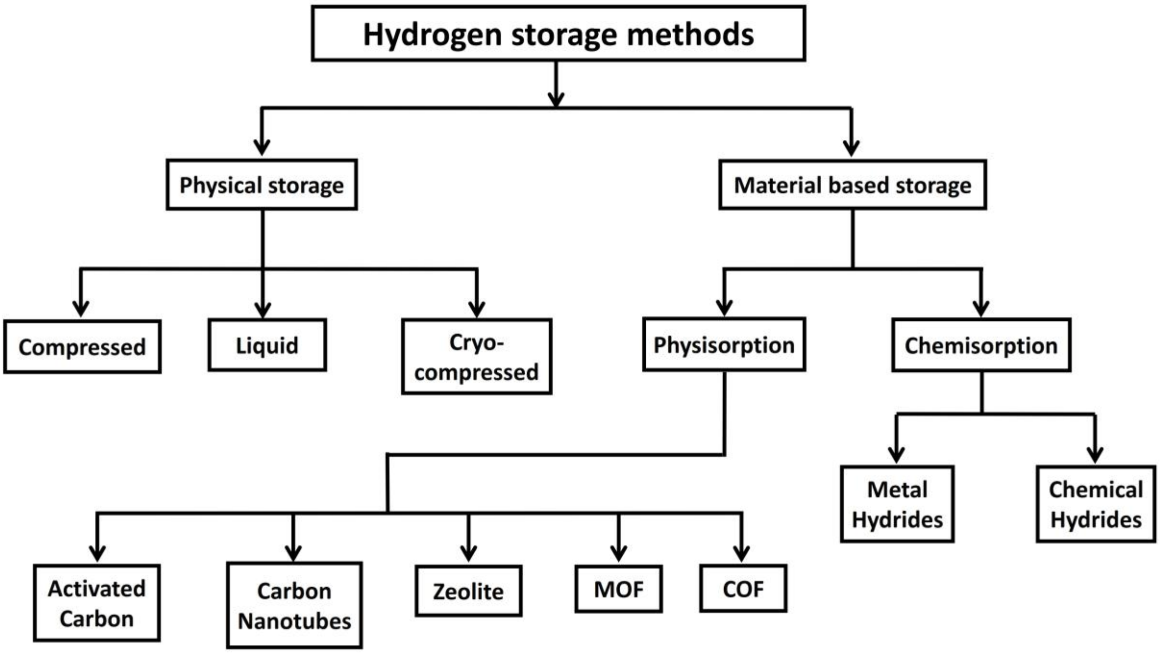

Fig. 1.4: Hydrogen storage methods.

These physisorption-based storage materials are characterized by enormous surface area and pore volume (Chen et al., 2022). Although these physisorbents exhibit excellent hydrogen uptake/release kinetics and substantial reversible storage capacity, the practical application of such materials is narrowed by the need for ultra-low temperature requirement (77 K) at 1 atm pressure (Prachi R. et al., 2016). Metal hydrides are examples of chemisorbents that offer outstanding hydrogen storage characteristics at a broad range of temperatures and pressure (Sakintuna et al., 2007). By virtue of metal hydride formation and dissociation, it offers several practical advantages over compressed and liquefied hydrogen storage, e.g., high volumetric density, safety of operation etc. Intermetallic metal hydrides are excellent choices for near ambient hydrogen storage (1-10 bar, 0-100 °C);

however, their gravimetric storage capacities (wt.% < 2%) are less due to heavy elemental constitution. Among the other hydride materials, a few complex hydrides, chemical hydrides, and elemental hydrides (e.g., MgH_2) possess high storage capacity (7-18 wt.%). Although these hydride materials have drawbacks of sluggish reaction kinetics, high thermal stability and/or irreversibility (Chen et al., 2021). Thermal de-stabilization, nano-confinement and catalyst addition are some of the adopted techniques to mend the suitability of complex hydrides for on-board applications. On the other hand, chemical metal hydrides are completely irreversible. For Mg-based hydrides, surface modification (e.g. ball milling) and catalyst doping are proven technique to positively influence kinetics and lowering the reaction heat (Rusman and Dahari, 2016).

Apart from Metal hydrides, several chemical molecules (Andersson and Grönkvist, 2019), viz. methanol, ammonia, formic acid and liquid organic hydrogen carrier (LOHC) can offer very moderate to high gravimetric storage density. Ammonia has a hydrogen storage density of 17.7 wt.%, and its production, handling and utilization is also very matured; however, dehydrogenation of ammonia calls for high temperature (>200 °C, typically above 650 °C) for complete conversion in the presence of catalysts. Methanol also offers substantial gravimetric capacity (12.5 wt.%); however, renewable synthesis of methanol necessities 10-80 bar pressure at 220-280 °C and going by steam reforming, the produced CO_2 must be separated. Among the chemical molecules mentioned, formic acid (4.4 wt.%) can be decomposed to give off hydrogen even at room temperature. However, the synthesis of formic acid from hydrogen and CO_2 requires a basic medium and phase separation of end products is energy intensive. Also, thermal decomposition of formic acid exhibits a tendency to from CO rather than CO_2, which needs to be controlled via use of catalysts. LOHC materials store and release hydrogen by forming and breaking carbon-carbon bonds. These materials offer decent hydrogen storage capacity (e.g., methylcyclohexane and toluene: 6.1 wt.%, dibenzyl toluene and perhydro-dibenzyl toluene: 6.2 wt.%, etc.); however, both hydrogenation (130-200 °C) and dehydrogenation (200-350 °C) reaction requires high-temperature condition. Nevertheless, a perfect hydrogen storage material which fulfils all-inclusive requirement for on-board storage is yet to be made available (Nagar et al., 2023).

1.4.1. Role of metal hydrides

Metal hydrides are metals and their alloys which reversibly react with hydrogen at certain temperatures and pressure (Srinivasan et al., 2020a). A layman's way of understanding metal hydride behaviour would be to consider it as a hydrogen sponge that take in hydrogen at some exerted pressure and give out hydrogen when it is heated. A typical reversible metal hydride reaction can be presented as:

$$M + \frac{x}{2} H_2 \leftrightarrow MH_x \tag{1.1}$$

Where *'M'* represents the host metal/alloy, and *'MH_x'* represents its hydride. The reaction enthalpy for formation and dissociation are negative and positive, respectively (Fig. 1.5). The thermodynamics and kinetics of metal hydride formation/dissociation are discussed in subsequent sections.

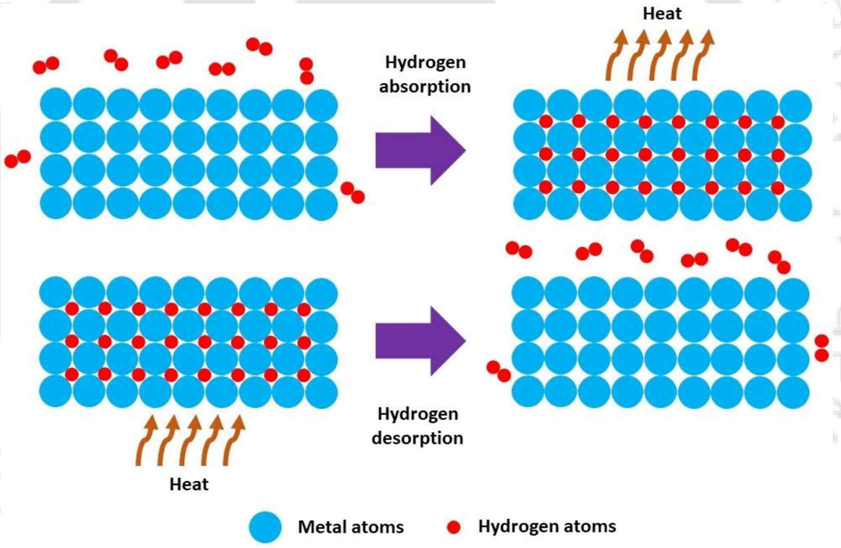

Fig. 1.5: Illustration of hydrogen absorption and desorption in metal hydrides.

Thermodynamics of hydrogen sorption in metal hydride

The thermodynamics of hydrogen sorption in metal hydrides can be understood from its pressure-concentration-temperature diagram as represented in Fig. 1.6. A typical metal hydride–hydrogen formation reaction can be perceived as a sequence of multiple elementary steps (Martin et al., 1996). In step 1, the gaseous hydrogen molecule is physisorbed at the solid-gas interface; in step 2, the molecule is split into hydrogen atoms and chemisorbed at the surface; in step 3, the chemisorbed atoms migrate into the interior of the host; in step 4, the atoms diffuse into the bulk and step 5 marks the beginning of hydride formation. In the reverse reaction, hydride decomposition occurs first, followed by diffusion, surface migration, recombination, and the final step is gas desorption. The elementary steps involved during the formation and decomposition of MH are schematically represented in Fig. 1.7. Just like any other phase transformation diagram, in a metal hydride – hydrogen system, two phases are identified. As hydrogen gas is first supplied to the metal, with an initial low hydrogen concentration (defined as the ratio of the number of hydrogen atoms per unit metal atom), a solid solution starts forming, which is conventionally named as the *'α'* phase.

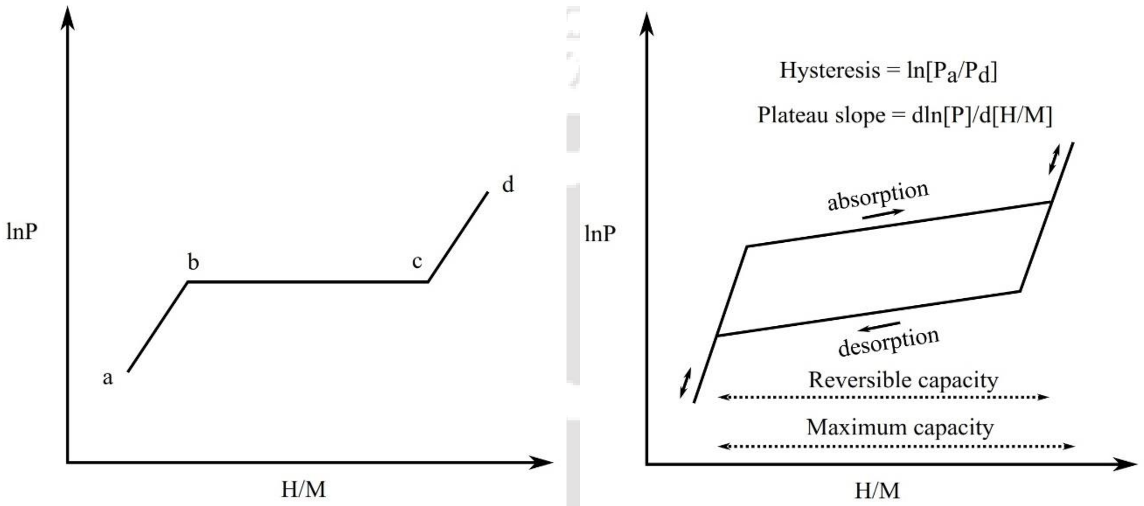

Fig. 1.6: (a) Depiction of an ideal isotherm of MH and (b) depiction of slope and hysteresis.

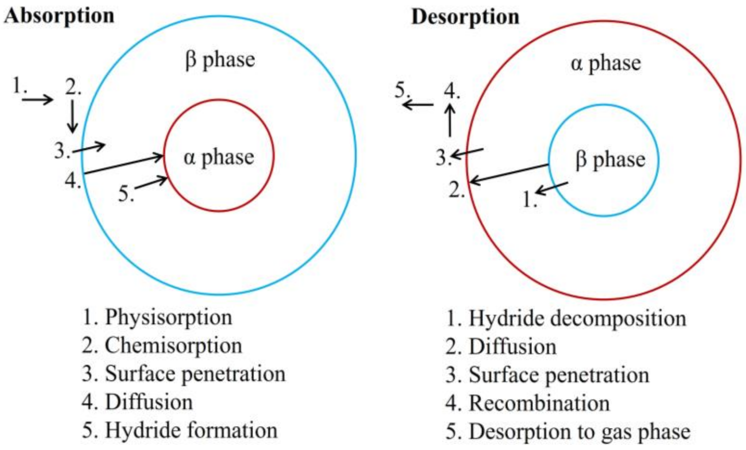

Fig. 1.7: Illustration of elementary steps involved in absorption and desorption of hydrogen in metal hydride (Martin et al., 1996).

The hydrogen atoms diffused in the crystal lattice do not take any ordered position, and hence till saturation of the *'α'* phase, the crystal structure does not deform. The solubility of hydrogen atoms in the *'α'* phase is dictated by the square root of the equilibrium hydrogen pressure (Kirchheim and Pundt, 2014).

$$\frac{H}{M} = k\sqrt{P} \tag{1.2}$$

In Eq. (1.2), *'k'* represents a constant influenced by temperature, and *'H/M'* represents hydrogen concentration. After the α phase is saturated with hydrogen atoms, the hydride phase (also called as the *'β'* phase) starts to form at nearly constant pressure. The *'β'* phase is an ordered phase where the addition of more hydrogen is possible at constant pressure. It is also known as plateau pressure. The right end of the plateau marks the saturation of the *'β'* phase. With further addition in hydrogen, a change in concentration is possible only at raised pressure. The width of the plateau represents reversible hydrogen storage capacity which is one of the most important parameters needed for designing engineering systems. The plateau is often sloped instead of flat; such behaviour can be typically attributed to the continuous dissolution of H atoms into the *'α'* phase in the absence of the formation of a crystallographically distinct hydride phase (Fig. 1.7(a)). The enthalpy of a hydride's formation indicates the strength of the metal-hydrogen bond, whereas the entropy of formation indicates the heat evolution of the reaction. The formation enthalpy is a key decisive parameter of all the thermal engineering applications of metal hydrides. Another deviation in the PCT from ideal behaviour is observed in the form of hysteresis phase (Fig. 1.7(b)), where the absorption pressure is higher than the desorption pressure. The reason for hysteresis can be attributed to strains associated with hydride formation/decomposition and consequent crystal defects (Kirchheim and Pundt, 2014).

The pressure-temperature relation within two phase region is governed by van't Hoff equation, which is given as:

$$ln\left[\frac{P_{eq}}{P_0}\right] = \frac{\Delta H}{RT} - \frac{\Delta S}{R} \tag{1.3}$$

In Eq. (1.3), *'P_{eq}'* signifies the equilibrium pressure of phase conversion corresponding to temperature *'T'*, *'P_0'* is the reference state pressure, *'R'* is the universal gas constant, *'ΔH'* and *'ΔS'* denotes enthalpy and entropy of formation. Two important thermodynamic properties are obtained from van't Hoff equation, viz. enthalpy and entropy (Fig. 1.8). The slope of the straight line obtained using the mid-point plateau pressure of the three isotherms is used to estimate the reaction enthalpy, whereas the reaction entropy is estimated using the intercept of the straight line.

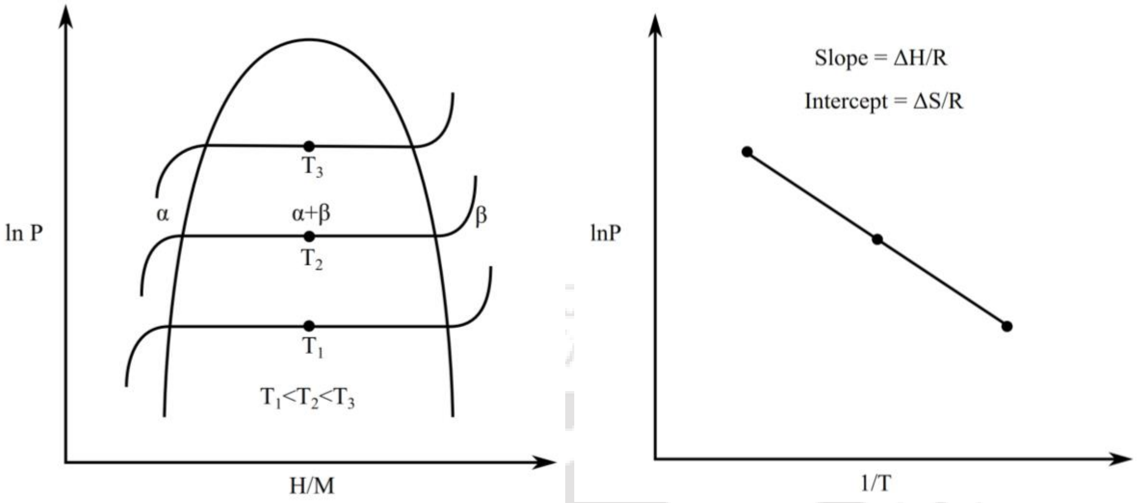

Fig. 1.8: (a) Depiction of PCT diagram and (b) ideal van't Hoff plot.

1.4.2. Classification of metal hydrides

Metal hydrides can be categorized into two major classes based on the type of hydrogen bonding, viz. intermetallic and complex hydrides. In the case of intermetallic hydrides, hydrogen acts as a metal and forms metallic bonds, whereas in the case of complex hydrides, hydrogen is covalently bonded to central atoms in "complex" anions.

Intermetallic hydrides

The intermetallic hydride is composed of two elements of opposite affinity towards hydrogen. The elements of the rare earth or alkaline earth series exhibit stable hydride formation tendency and are referred to as 'A' elements. Whereas the element 'B', which exhibits less hydride formation tendency, often falls into the transition metals group. The elements A and B can be completely or partly substituted by other elements. Depending upon the stoichiometry, the intermetallic hydrides can take the form of AB_5, AB_2, AB_3, AB, A_2B_7, A_6B_{23}, and AB. Table 1.1 shows the representative of different intermetallic compounds. The intermetallic hydrides exhibit poor gravimetric storage density (< 2 wt.%) owing to the presence of heavy elements. An exceptional metallic hydride that offers gravimetric storage density exceeding the US-DOE (US DoE, 2017) target is MgH_2. Due to its low weight, it offers a storage capacity of 7.6 wt.%. However, the reaction enthalpy of MgH_2 is so high that hydrogen desorption can only take place beyond 290 °C.

Table 1.1: Examples of intermetallic hydrides (Makridis, 2016)

Stoichiometry	**Representative of ‘A’ element**	**Representative of ‘B’ element**	**Intermetallic compound**
AB_5	Ca, La, rare earth	Ni, Cu, Co, Pt, Fe	$CaNi_5$, $LaNi_5$, $CeNi_5$, $LaCu_5$, $LaPt_5$, $LaFe_5$
AB_2	Zr, Ti, Y, La	V, Cr, Mn, Fe, Ni	$LaNi_2$, YNi_2, YMn_2, $ZrCr_2$, $ZrMn_2$, ZrV_2, $TiMn_2$
AB_3	La, Y, Mg	Ni, Co	$LaCo_3$, YNi_3, $LaMg_2Ni_9$
A_2B_7	Y, Th	Ni, Fe	Y_2Ni_7, Th_2Fe_7
A_6B_{23}	Y	Y	Y_6Fe_{23}
AB	Ti, Zr	Ni, Fe	TiNi, TiFe, ZrNi
A_2B	Mg, Zr	Ni, Fe, Co	Mg_2Ni, Mg_2Co, Zr_2Fe

Complex hydrides

Complex hydrides attracted great attention as they offer substantially high gravimetric storage density compared to intermetallic hydrides. Complex hydrides are salt-like materials in which hydrogen is covalently bound to the central atoms, resulting in the formation of a crystal structure composed of complex anions. A wide range of metal-hydrogen complexes are formed by Group I, II, and III elements, such as Li, Mg, B, and Al. When some transition metals combine with group IA or IIA in the presence of hydrogen, transition metal complex hydrides are formed (Srinivasan et al., 2020b). The formation and decomposition features of transition metal complex hydrides are such that they usually require some metal atom diffusion. The reaction kinetics of these hydrides is slower kinetics compared to intermetallic hydrides and require high temperature for desorption. A typical example of a transition metal complex hydride is Mg_2FeH_6 which offers 5.5 wt.% storage capacity (Sandrock, 1999). Another set of complex hydrides constitutes non-transition metal complexes. Typical examples include aluminates $[AlH_4^-]$, borohydrides $[BH_4^-]$, and amides $[NH_2^-]$. For example, $LiBH_4$ offers a theoretical storage capacity of 18.5 wt.%. However, the reaction is not reversible, and hydrogen desorption starts at 320 °C and complete dehydrogenetaion is only possible beyond 400 °C (Rusman and Dahari, 2016). Alanates are also outstanding hydrogen storage material; however, the decomposition requires cascading steps. $NaAlH_4$ grabbed a lot of attention for its theoretical storage capacity of 5.6 wt.%. With the aid of Ti-based catalysts, the decomposition of $NaAlH_4$ offers 4 wt.% reversible capacities below 150 °C. Similarly, $LiAlH_4$ has a theoretical hydrogen storage capacity of 10.5 wt.%, although the two-step decomposition provides 5.3 wt.% and 2.65 wt.% hydrogen release between 160-200 °C. A few classical complex hydrides and their absorption/desorption conditions are presented in Table 1.2.

Table 1.2: A few complex hydrides and their hydrogen storage properties (Prachi R. et al., 2016; Rusman and Dahari, 2016)

Complex hydrides	Desorption temperature (°C)	Storage capacity (wt.%)
$LiBH_4$	320	18.4
$NaBH_4$	45	10.6
KBH_4	584	7.4
$LiAlH_4$	170	10.6
$NaAlH_4$	230	7.5
$NaAlH_4$ + 4 mol% Ti	100	5.6
$NaAlH_4$ + 1.0 mol% Ti	150	5.6

Chemical hydrides

The term chemical hydrides refer to disposable compounds which release hydrogen one time when subjected to a chemical reaction. A typical example of a chemical hydride is ammonia borane (NH_3BH_3) which possesses a gravimetric storage capacity of 19.6 wt.% (Rusman and Dahari, 2016). Hydrogen can be released from ammonia borane either by thermolysis or solvolysis. The hydrogen discharge rate is slow at temperatures below 100 °C as the hydrogen gets trapped by by-products generated from parallel reactions. The sluggish discharge can be augmented by the use of catalysts like LiH or $LiNH_2$. Many chemical hydrides react exothermally with water, and often the by-product is thermodynamically stable. For example, hydrolysis of $NaBH_4$ creates $NaBO_2$, which is a highly stable compound, and hence regeneration of the feed stock material becomes expensive. Due to their irreversible nature, chemical hydrides are utilized as single-use fuels.

Elemental hydrides

Elements like magnesium and aluminium form a binary compound with hydrogen and offer significantly large hydrogen storage capacity. Magnesium hydride is a very attractive choice as a hydrogen storage material as it has a substantially high hydrogen storage capacity (7.6 wt.%), and the feedstock is cheap. However, the Mg-H bond strength (~75 $kJ.mol^{-1}$) is so high that hydrogen absorption and desorption can take place only around 300 °C. Also, the both-way reaction kinetics are quite slow, which can be enhanced by nano-confinement, ball milling, alloy doping or a combination measure. On the other hand, aluminium hydride (AlH_3) has an enthalpy of dehydrogenetaion that is quite less ($7\ kJ.mol^{-1}$), which enables rapid desorption of 10.1 wt.% hydrogen below 100 °C. However, this reaction is irreversible as AlH_3 can only be formed at extreme pressure (Andersson and Grönkvist, 2019).

1.4.3. Engineering applications of metal hydrides

A number of engineering applications (shown in Fig. 1.9), viz. hydrogen storage, hydrogen compression, hydrogen purification, heat storage, heat pump, refrigeration, isotope separation, sensors and actuators etc., can be derived out of the MH-H_2 combination. The heat interactions during the formation (exothermic) and dissociation (endothermic) of MH form the basis of all these applications. High resistance to impurity infiltration, easy activation, and decent cyclic capability are common desired attributes for almost all the applications.

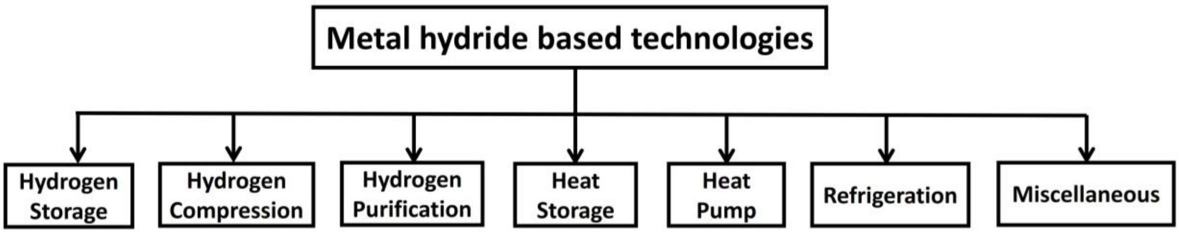

Fig. 1.9: Engineering application of metal hydrides.

Hydrogen storage

Hydrogen storage by intermetallic MH offers several advantages over compressed and liquefied storage methods. The key advantages of storing hydrogen in MH are high volumetric density, low storage pressure, ultra-high purity of desorbed gas and tunability of thermodynamics. While designing a MH-based hydrogen storage system, the first and foremost criteria should be the affirmation of large reversible storage capacity and low to moderate reaction enthalpy. Hydrogen should be conveniently stored at low pressure (below 50 bar) at near ambient temperature, while hydrogen discharge should be made possible with the available waste heat or other heat sources (60-80 °C, typically). MH, in general, is not a great choice for automotive uses as the necessary refilling time (5 kg H_2 storage within 3-5 min, as per US-DOE goals) sets a constraint on the capacity of the chiller (>2 MW) used for cooling the MH system. To date, no such MH material is available which can simultaneously fulfill all the US-DOE targets for automotive applications. However, stationary storage using intermetallic hydrides is a viable option, as system weight is not a concern. One of the key limitations of hydrogen storage by MH is the very high cost of the material and associated investment in heat exchangers.

Hydrogen compression

Hydrogen compression using MH can be achieved by thermal swing, i.e., by adjusting the absorption and desorption temperatures. Such compression devices do not include any moving parts unlike mechanical compressors and hence are vibration free. Another advantage of hydrogen compression using MH is that the desorbed hydrogen is of high purity. In such devices, hydrogen is preferably charged at near ambient temperature, and depending upon the required discharge pressure, the MH bed is heated to 60-80 °C with the availability of low-grade heat input. In single-stage hydrogen compression, typically 3-10 (Bhuiya et al., 2015) compression ratio is achieved. To improve the compression ratio, two to three or even more stages can be connected in series**.** The desired features of MH materials for compression applications are high impurity resistance and cyclic stability. Among the intermetallic alloys, AB_5 and AB_2 are best suited for compression application owing to favourable absorption temperatures.

Hydrogen purification

By virtue of the strong affinity for hydrogen in intermetallic alloys, hydrogen purification can be achieved from a mixture of gases containing hydrogen and other undesirable species, viz., CO_2, CH_4, N_2, etc. (Kumar and Muthukumar, 2022a; Kumar and Muthukumar, 2022b). When such a mixture of gases is supplied to the MH bed, the impurity species occupy the void spaces while hydrogen forms MH by occupying the interstitial sites. In order to obtain pure hydrogen gas, the impurity species are flushed first, followed by desorption at high temperatures (60-80 °C). From an infeed mixture containing 99.99% pure H_2 to obtain 99.9999% pure H_2 has been demonstrated in the literature (Sandrock et al., 1992). The PCT property of the intermetallic alloy should be such that the equilibrium absorption pressure at ambient temperature should be less than ambient pressure to minimize hydrogen losses during flushing.

Heat storage

Thermochemical heat storage can be accomplished by utilizing a pair of MH reactors. The basic concept is to utilize heat at high temperature (e.g., solar, industrial waste) to drive endothermic decomposition of MH in a high-temperature reactor (low pressure) during daytime or generation period and storing it in a low-temperature MH reactor (high pressure). Later, on demand, the hydrogen can be sent back to the high-temperature reactor to drive the exothermic re-combination reaction and thus yield the required heat. Such thermochemical heat storage offers high energy density and prolonged storage duration. Mg-based hydrides are often employed as high-temperature heat storage material. In such systems, the high-temperature and low-temperature MH alloys must be carefully screened to allow sufficient hydrogen flow between the coupled reactors at designed operating temperatures.

Heat pump

MH-based heat pump operates in a closed loop with two dissimilar MH alloys (usually intermetallic) tuned to allow hydrogen transfer back and forth between them. One of the alloy operates at high pressure at low-temperature levels, while the other alloy operates at low pressure at high-temperature levels. In the first half-cycle, the low-pressure hydride (initially saturated) desorbs hydrogen by taking heat at high temperature (120-160 °C), and the hydrogen is absorbed by the other hydride (initially unsaturated) at medium temperature (40-60 °C). Now the low-pressure hydride is cooled to medium temperature, and the high-pressure hydride is cooled to low temperature (25-35 °C). In the second half-cycle, hydrogen desorbed from the high-pressure hydride at low temperature is absorbed the low-pressure hydride at medium temperature. Subsequently, both reactors are sensibly heated to their respective initial states to proceed with the next cycle. Thus, during the complete cycle, heat input is given at high temperature and low temperature while heat output is obtained twice at medium temperature. To achieve quasi-continuous heat pumping, two identical pairs of MH reactors should be operated 180° out of phase.

Refrigeration

The operation of a closed loop thermally driven MH-based refrigeration system is similar to the heat pump operation described above. The only difference is that the pair of alloys screened should be able to facilitate hydrogen transfer from high-pressure reactor to low-pressure reactor at a temperature below ambient temperature. In such a thermally driven system, cooling is produced at refrigeration temperature at the expense of heat input at high temperature. Another variant of closed-loop refrigeration system can be operated with the aid of a mechanical compressor discarding the need for high-temperature heat source. Such a mechanically driven system requires two identical MH reactors filled with the same alloy. Hydrogen desorbed from one reactor is pumped to the other reactor in each half-cycle. In this system, cooling is produced at the expense of electrical energy input to the compressor. Although the maximum COP reported for MH-based cooling systems is still limited to 0.5-2.5, it has been demonstrated by prototype experiments that the compressor-operated refrigeration system can compete the conventional vapour compression refrigeration system (VCRS) systems with the cautious design of MH reactor and hydrogen compressor.

Miscellaneous applications

Apart from the applications cited above, hydrogen interaction with MH can be engineered to serve a variety of other applications, viz. heat engines, gas sensors and actuators, rechargeable battery electrodes etc. Hydrogen desorbed from MH at high temperature in a closed containment can be used to displace a piston assembly to provide mechanical work, or the gas pressure can be used to trigger actuation systems (metal bellow, artificial muscle, etc.). The high surface concentration of atomic hydrogen in intermetallic hydrides can also facilitate the role of a catalyst for methanation, ammonia synthesis, hydrogenation, etc. (Sandrock et al., 1992). Intermetallic MH (AB_2, AB_5) are also extensively used as cathode material for Ni-MH batteries.

1.5. Motivation of the thesis

Climate crisis and population growth are setting a combined stress on the present energy sector. With the continuous improvement in living standards of the growing population, the need for heat, electricity and cooling will be increased by multi-fold by the end of mid-21st century. Metal hydrides are a class of materials which, when paired with hydrogen, can provide sustainable engineering solutions to the ongoing climate crisis. The duo can offer a very safe and compact hydrogen storage. MH-based hydrogen storage can be especially beneficial for decentralized electricity generation utilizing fuel cells. It can be used to power up households, data centres, telecom networks etc. Alongside, by virtue of MH formation (exothermic) and dissociation (endothermic) it can offer heating, cooling, hydrogen compression, thermal energy storage, etc. Open-cycle systems can offer both hydrogen storage and heating/cooling, whereas closed-cycle systems can offer only heating/cooling effects. Open cycle systems can be integrated in stationary as well as mobile applications, where the MH unit would act as an intermediate hydrogen storage option. The use of MH based cooling system can mitigate the issue of greenhouse gas

(GHG) emissions substantially also, such a cooling system would be free from noise and vibration. Therefore, the present thesis work is focused on the design, development and testing of metal hydride reactors for stationary hydrogen storage and cooling applications targeted to be deployed in off-grid locations.

1.6. Outline of the thesis

In line with the formulated thesis objectives, the thesis work is structured in eight chapters, which are described below.

Chapter 1: Introduction

The background of the thesis work is described in this chapter, followed by scope and motivation. It starts with a brief overview of the worldwide energy consumption pattern over a span of half-decade and reflects on why a renewable-based energy economy must be considered to mitigate the calamitous effect of climate change. Alongside the context of hydrogen-based energy economy is also contemplated briefly to tackle the future heating, cooling and electricity demand. It is then followed by the introduction to MH-based hydrogen storage and concomitant thermal engineering applications emphasizing the safety, compactness and simplicity of end usage.

Chapter 2: Literature review

This chapter presents an exhaustive review of the MH systems from an engineering perspective. It broadly covers the fundamental aspects of heat and mass transfer within the MH bed, chemical kinetics, heat transfer intensification strategies and different reactor configurations considered for hydrogen storage as well cooling applications. It is followed by the identification of the research gap and formulation of thesis objectives.

Chapter 3: Design and fabrication of metal hydride reactors

In this chapter, the design and fabrication of the MH reactors is discussed in detail. Two major reactor configurations are considered, i.e., tube bundle and embedded tube configuration. The design procedure for the tube bundle reactor (TBR) was supported by the numerical results obtained from simulating COMSOL models. Whereas, the design of the embedded cooling tube reactors (ECTR) was followed from guidelines proposed by Raju et al., (2019). A number of lab-scale (up to 3.5 kg alloy) and large-scale (up to 25 kg alloy) MH reactors were fabricated.

Chapter 4: Experimental studies on MH based hydrogen storage systems

This chapter discusses the experimental studies conducted on MH-based hydrogen storage system for both lab-scale and large-scale reactors. The particulars of the MH alloys, reactors, experimental apparatus, and experimental procedure are presented in this section. The experimental results were analysed in terms of the amount of hydrogen stored, rate of heat input and heat output, energy efficiency and desorption condition with respect to fuel cell application.

Chapter 5: Experimental studies on MH based open cycle cooling systems

This chapter deals with the experimental studies conducted on open-cycle cooling systems with and without the aid of a compressor. The particulars of the MH alloy, reactors, test setup and experimental method are discussed in detail in this segment. For open cycle tests without compressor, the results were analysed in terms of the rate of cooling produced and cumulative cold output at varied desorption temperatures. Whereas, for tests with compressor, two primary performance metrics, i.e., COP and specific cooling power (SCP), were analysed by altering cooling temperature and cycle time.

Chapter 6: Experimental studies on MH based closed cycle cooling systems

This chapter discusses the experimental studies conducted on the closed-cycle compressor-driven cooling system. The particulars of the test setup and apparatus are also presented in this chapter. Test runs were performed by altering refrigeration temperature, sink temperature, and half-cycle time. The effect of altered operating conditions on the amount of hydrogen transferred, COP and SCP are deliberated in this segment.

Chapter 7: Numerical studies on hydrogen storage and cooling systems

In this chapter, the numerical part of the thesis work is discussed. It essentially comprises of two different numerical studies. In the first study, an extended numerical model has been developed and implemented in COMSOL Multiphysics 5.5 to accommodate the HTF flow and heat transfer effects by specifying the mass, momentum and energy equations and appropriate initial and boundary conditions. This model is further used to predict the constant mass flow rate desorption behaviour of the 19 TBR module. In the second study, a lumped model has been developed for a compressor-operated MH-based closed loop cooling system. This model is used to predict the system performance (viz. COP and SCP) under a variety of operational and design conditions.

Chapter 8: Thesis Summary, Conclusions and Recommendations

This chapter sums up the major conclusions of the numerical and experimental work carried out on hydrogen storage and cooling systems. Furthermore, the prospect of extension of the present thesis work and a few more future research directions is also indicated.

2. Literature Review

2.1. Introduction

The use of metal hydrides for any engineering application primarily necessitates an in-depth understanding of the material properties of the porous bed (e.g., particle shape, size, porosity, permeability, effective thermal conductivity, etc.) and thermodynamic as well as chemical kinetic parameters. Besides, the storage/thermal performance of metal hydride-based devices also depends on the design of the containment vessel, heat exchange preferences, and operating conditions. In this chapter, a comprehensive review of the reported works on chemical kinetics, heat and mass transfer aspects, and state-of-the-art developments on heat exchange options for hydrogen storage and cooling applications are presented.

2.2. Studies on the chemical kinetics of metal hydrides

Goodell et al., (1980) performed reaction rate measurements on $LaNi_5$ (15-45 °C) and FeTi (-20-45 °C) alloys using thin disc reactors. They reported the intrinsic reaction rates of $LaNi_5$ at 25 °C to be significantly faster compared to FeTi at the same temperature. However, it was also inferred that the reaction kinetics of both these alloys still could be inhibited by heat transfer limitation even in a high conductivity reactor. Compared to static test results, higher hysteresis was observed during dynamic tests conducted in their study. Suda et al., (1980) studied the hydriding and dehydriding reaction rates of binary mixture of few alloys ($LaNi_5$, $MmNi_5$, aluminium-substituted mischmetal nickels, $TiMn_{1.5}$ and $Ti_{0.8}Zr_{0.2}Cr_{0.8}Mn_{1.2}$) to assess the influence of alloy mixing on reaction rates. With the use of an inclusive reaction parameter, they concluded that hydriding and dehydriding to be most sensitive to pressure and temperature, respectively. It was inferred from their study that a suitable mixture (high reactive and less reactive) of alloys could improve the kinetic properties as well widen the available temperature range of practical application. Goudy et al., (1983) experimentally determined the hydrogen desorption rates of $LaNi_5$ alloy mixed with different Al percentages (70-97.5 wt.%) in the form of compressed pellets and powder mixtures. It was observed that for compressed pellets, with an increase in aluminium content from 80-95 wt.%, the hydrogen desorption rates increased steadily, indicating heat transfer to be the rate controlling factor. Moreover, for a small quantity of $LaNi_5$ (2.5-5 wt.%), the desorption rates did not vary significantly which reiterated the influence of heat transfer on desorption kinetics. The study also advocated that under quasi-isothermal conditions, the overall hydrogen desorption process can be modelled as first order reaction. Miyamoto et al., (1983) measured hydriding rates of $LaNi_5$ under constant supply pressure in the temperature range of 15-80 °C. They concluded that a logarithmic pressure difference correctly describes the pressure dependence on absorption kinetics expression. Supper et al., (1984) carried out reaction kinetics measurements for $LaNi_{4.7}Al_{0.3}$ and $CaNi_5$ alloys using fast reaction beds. The motive of the experiments was to gauge the influence of bed thickness, heat transfer enhancer, and mass transfer enhancer on reaction kinetics. For $LaNi_{4.7}Al_{0.3}$ alloy, absorption rates measured under identical equilibrium distance condition (ΔP) for 1-6 mm bed thickness indicated an increase in bed thickness beyond 1 mm restricted heat and mass transfer. An improvement of 2.24-3 fold in reaction rates was observed when the $LaNi_{4.7}Al_{0.3}$ bed was filled with aluminium foam (94% porosity, 1 mm pore size) to the case where no foam was used. Moreover, it was reported that the use of hydrogen transfer arteries could minimize 50% reaction time by 2.5-2.9 fold compared to the case where no arteries were used. Han and Lee, (1987) reported the reaction kinetics data of Mg_2Ni in near isothermal conditions using a copper tube reactor with the aid of Ni thermal ballast. It was inferred that above allotropic transformation temperature of Mg_2NiH_4, reaction kinetics was influenced by forced hydrogen flow, but chemisorption dominates the same at later stage. Whereas for temperature below allotropic transformation, the hydriding rate was controlled by chemisorption (higher temperature) and bulk reaction (lower temperature), respectively. Later the same researchers (Han and Lee, 1989) experimentally measured the hydriding kinetics data of $LaNi_5$ and $LaNi_{4.7}Al_{0.3}$ at constant pressure. A large quantity of Al powder was mixed with the samples inside Cu tube reactors to ensure near isothermal conditions. Experimental results suggested that the critical reaction mechanism was transformed from chemisorption (low pressure) or nucleation and growth (high pressure) to hydride diffusion for both the alloys. Koh et al., (1989) conducted experiments to identify the rate-controlling steps for hydriding and dehydriding of $LaNi_5$. It was inferred in both processes; reaction rate was controlled by phase transformation at the α-β interface. The importance of a sufficient number of sample cycling to obtain a coherent and unambiguous reaction rate model was highlighted in their study. Wang and Suda, (1990a; 1990b; 1990c) proposed a step-wise method of maintaining isothermal conditions for the measurement of hydriding and dehydriding kinetics of $LaNi_{4.7}Al_{0.3}$. This method employs gradual change in hydrogen concentration by controlling the hydrogen pressure, and therefore it was possible to measure reaction rate controlling steps across hydride phase changes from α to β. Skripnyuk and Ron, (1999; 2003) evaluated the reaction kinetics of several high-pressure alloys ($Ti_{0.95}Zr_{0.05}Mn_{1.48}V_{0.43}Fe_{0.08}Al_{0.01}$,$Ti_{0.98}Zr_{0.02}Mn_{1.46}V_{0.41}Cr_{0.05}Fe_{0.08}$,$Ti_{0.95}Zr_{0.05}Mn_{1.48}V_{0.43}Fe_{0.08}Al_{0.01}$, $Ti_{0.955}Zr_{0.045}Mn_{1.52}V_{0.43}Fe_{0.12}Al_{0.03}$) using normalized pressure dependence method. In this method, the pressure dependence function ($f(P)=|P_{eq}-P|/P_{eq}$) is inserted into an integral rate equation of a particular mechanism. The desorption kinetics of the alloys were studied in the temperature range of -20-20 °C, which exhibited very fast hydrogen discharge, exemplifying their suitability for MH-based cooling applications. Muthukumar et al., (2009) measured the hydriding rates of three different AB_5-type alloys, namely $LaNi_5$, $LaNi_{4.7}Al_{0.3}$ and $LmNi_{4.91}Sn_{0.15}$, in the temperature range 20-80 °C maintaining supply pressure to an equilibrium pressure ratio of 2. Further, they checked the kinetic data for fitting using two models viz. Johnson–Mehl–Avrami (JMA) model and the Jander diffusion model (JDM) model reported that the JDM predictions closely resemble the experimental outcomes for all three alloys. Sharma and Anil Kumar, (2014) reported kinetic and P-C-T data of four different alloys ($La_{0.9}Ce_{0.1}Ni_5$, $La_{0.8}Ce_{0.2}Ni_5$, $LaNi_{4.7}Al_{0.3}$ and $LaNi_{4.6}Al_{0.4}$) targeting MH based cooling application. They concluded that the addition of Ce improves kinetics (hydride stability reduced) while the addition of Al impairs the kinetics (hydride stability improved) of $LaNi_5$. It was reported that among the two employed kinetic models (Jander-Diffusion and Park-Lee models), the PLM predictions were more accurate compared to JDM.

2.3. Studies on heat and mass transfer description of metal hydrides

Lucas and Richards, (1984) recommended a 1-D mathematical model to describe the heat and mass transfer characteristics inside a cylindrical metal hydride container using alloy-specific heat transfer and mass diffusion data. It was concluded that the rate of heat transfer is the rate-limiting factor for practical storage systems. Mayer et al., (1987) established a 1-D mathematical model considering constant MH bed pressure conditions to predict the transient heat and mass transfer behaviour inside tubular reaction beds employing $LaNi_{4.7}Al_{0.3}$ and $LmNi_5$. As a mean of improving heat and mass transfer within the bed, aluminium foam (94% porosity) and steel screen arteries were used. Groll et al., (1987) experimentally established favourable heat and mass transfer criteria for periodically operating thermal machines deploying tubular reaction beds. With provision for hydrogen flow through porous metallic networks, significant improvement in hydrogen absorption time (3.6-4.2 times shorter) and desorption time (11 times shorter) were observed compared to the case where no mass transfer network was provided. Experimental results also advocated for attaining high external heat transfer coefficient and minimized the thermal gap between the reactor wall and material to improve heat transfer. Da-Wen and Song-Jiu, (1989) developed a 2-D mathematical model to assess the heat and mass transfer behaviour using a variable thermal conductivity model. The heat transfer features of rectangular, cylindrical geometries for different aspect ratios were analysed in their study, and it was reported that heat transfer rates across thinner sections were faster. It was also reported that increase in wall temperature and reaction time increases the cumulative hydrogen discharged. Bjurström and Suda, (1989) studied the hydrogen transfer characteristics in a paired metal hydride bed of a heat pump using a lumped parameter model. Two different alloy pairs were considered i.e., $LaNi_{4.8}Al_{0.2}$-$MmNi_{4.5}Al_{0.5}$ and $MmNi_{4.5}Al_{0.5}$-$MmNi_{4.2}Al_{0.1}Fe_{0.7}$. It was concluded that the hydrogen transfer rate between paired reactors is mainly influenced by heat transfer rate rather than intrinsic kinetics. It was also shown that bed conduction resistance and heat transfer fluid capacity rate play very crucial role in heat transfer. Choi and Mills, (1990) developed a 1-D mathematical model to predict heat and mass transfer behaviour accounting for heat convection due to hydrogen flow. For $LaNi_{4.7}Al_{0.3}$ alloy, it was inferred that, for a bed thickness of 10 mm, effective thermal conductivity increment up to 4 $W.m^{-1}.K^{-1}$ gives improved result; beyond 4 $W.m^{-1}.K^{-1}$, hydrogen flow and reaction kinetics limit the hydrogen transfer rate. The optimum bed thickness for heat pump application was recommended to be 10-15 mm for a thermally unenhanced bed. Ramgopal and Srinivasa Murthy, (1992) developed a 1-D mathematical model to predict the effect of various operating parameters and bed properties on heat and mass transfer characteristics using $LaNi_{4.7}Al_{0.3}$. It was inferred that a thinner bed with superior effective thermal conductivity augments heat and mass transfer to a great extent. In addition, a greater pressure ratio between exterior and bed, large temperature difference between heat transfer fluid and bed, higher reaction rate constants, and lower activation energy ensures enhanced heat and mass transfer. Nasrallah and Jemni, (1997) verified the reasoning of several hypotheses related to heat and mass transfer models of MH-H_2 system. Based on the outcomes of a 2-D numerical model applied to $LaNi_5$ system, they testified for the existence of local thermal equilibrium conditions and negligible gas convection effects. Nakagawa, (2000) developed a 2-D numerical model of tubular $LaNi_5$ bed considering the influence of reaction fraction on hydride thermophysical properties. Their study emphasized on correct estimation of particle Reynolds number and interphase heat transfer coefficient to confirm the applicability of local thermal equilibrium conditions. It was also inferred that the inclusion of the convective heat transfer term in the numerical model leads to favourable hydrogen sorption in the beginning, however; later, it encumbers the sorption rate. Ha et al., (2004) developed a 2-D mathematical model to study the effect of thermal conductivity, bed diameter and internal fins on thermo-fluidic phenomena of hydriding reaction. It was inferred that the hydriding reaction occurs in two steps; while the initial step is governed by the pressure difference between supply and bed, which is very swift, in the subsequent step, the hydriding rate is impeded by slow heat diffusion from bed to cooling fluid. They recommended use of thinner beds with enhanced thermal conductivity and fins to boost the heat transfer. Kumar Phate et al., (2007) studied the influence of length-to-diameter ratio (L/D), and porosity on the hydriding of $LaNi_5$ inside a cylindrical bed using 2-D numerical model. The model accounted for changes in effective thermal conductivity with porosity. In their simulation, for a given L/D value, porosity change was reflected by varying the reactor dimensions, which also influenced the heat exchange surface area and the effective thermal conductivity. It was reported that with an increase in porosity, the corresponding reduction in effective thermal conductivity shades the effect of the corresponding increment in surface area. Yang et al., (2007) introduced two comprehensive parameters, viz. heat transfer dictated sorption rate and mass transfer dictated sorption rate, to characterize the dynamic performance of MH reactors. These parameters took into account the thermodynamic and kinetic properties of the MH alloy as well as the operating conditions and geometrical attributes of the MH reactors. Further, the validity of these parameters were tested with 2-D numerical model results. Results of the parametric study favoured for thinner MH beds, higher hydrogen feed pressure, and lower HTF temperature for improving hydrogen absorption. Similar criteria of operating parameters for favourable hydrogen absorption and desorption were recognized in other reported parametric studies (Muthukumar et al., 2007; Muthukumar and Ramana, 2009; Muthukumar and Venkata Ramana, 2010). The influence of heat transfer fluid temperature variation along the length on hydriding performance was reported by Muthukumar and Ramana, 2009 in their numerical study**.** The effect of considering variable wall temperature was more pronounced for bed thickness greater than 7.5 mm for $MmNi_{4.6}Al_{0.4}$. For a bed thickness of 17.5 mm, at 20 bar supply pressure, they reported a reduction in predicted absorption time of 300 s when constant wall temperature was considered instead of variable wall temperature conditions. The same authors Muthukumar and Venkata Ramana, (2010) later reported the effect of variable wall temperature conditions on hydrogen desorption of $MmNi_{4.6}Al_{0.4}$. At a hot fluid temperature of 30 °C, the difference in desorption times between constant wall temperature and variable wall temperature was as high as 375 s (17.5 mm bed thickness). Yang et al., (2012) investigated the effect of gas permeability, thermal conductivity, PCT properties, and reaction kinetics on the hydriding behaviour of $LaNi_5$ storage tank with increase in number of absorption-desorption cycles. They reported that gas permeability drops with cycling but has insignificant consequences on hydriding rate. However, a reduction in effective thermal conductivity with cycling leads to impaired hydriding performance. Slope and hysteresis change with a number of cycles, though they have a trivial influence on hydriding and finally, reaction kinetics of $LaNi_5$ was reported to be improved with cycling and it augmented the hydriding rate. Bao et al., (2013) developed a 3-D numerical model to analyse the effect of fluid flow parameters and MH bed properties on hydrogen absorption behaviour. They concluded that absorption is most sensitive to bed thermal conductivity followed by heat transfer fluid flow rate, contact resistance between bed and heat exchanger tube wall and finally heat exchanger tube material. A reformed numerical model accounting for the practical operation of large-scale metal hydride tank was developed by Mohammadshahi et al., (2016). The model accounted for flexible hydrogen charging/discharging demand, periodic operation of the MH reactor subjected to fixed and variable heat transfer fluid temperature. The model also verified the applicability of the non-ideal gas assumption for $LaNi_5$. It was reported that the ideal gas assumption for $LaNi_5$-H_2 system holds good up to 100 bar at 300 K. Afzal and Sharma, (2018a) performed a sensitivity analysis to gauge the impact of operating (supply pressure, HTF temperature, heat transfer coefficient) and design parameters (effective thermal conductivity, porosity) on hydrogen absorption and desorption behaviour using a 2-D numerical model. Effective thermal conductivity was inferred to be the most vital parameter influencing hydrogen desorption, whereas, absorption was influenced majorly by variations in gas feed pressure, porosity as well as thermal conductivity. The effect of reactor wall material on hydrogen absorption was experimentally studied by Briki et al., (2018). Three different lab-scale MH reactors (30 g $LaNi_5$) composed of steel, aluminium and copper were subjected to a set of parametric tests. Out of the three configurations, aluminium reactor demonstrated the fastest hydrogen storage under similar operating conditions (8 bar, 20 °C).

2.4. Studies on heat transfer intensification strategies adopted for metal hydride systems

2.4.1. Studies on effective thermal conductivity enhancement

Kim et al., (2001) demonstrated that use of a tiny amount (2.1 mass%) of expanded graphite (EG) with $LaNi_5$ and compaction of the mixture could yield up-to 3 $W.m^{-1}.K^{-1}$ effective thermal conductivity. Simulation outcomes reported by Lozano et al., (2012) on the optimization of tubular MH tanks re-confirmed the importance of MH compaction with EG for boosting hydriding/de-hydriding performance. Delhomme et al., (2012) tested a large-scale MgH_2 tank (0.6 kg H_2) where 10 wt.% EG was used as a binding agent with Mg powder. A significant reduction in hydrogen loading time (35 min) and discharging time (105-180 min) were reported in their study. Nagel et al., (1986) used a corrugated copper wire structure as a means to improve the effective thermal conductivity of $MmNi_{4.46}A1_{0.54}$ powdered bed. The reported effective thermal conductivity was in the range of 0.5-2.5 $W.m^{-1}. K^{-1}$. Lee et al., (1995) experimented on a prototype MH-based heat pump using tubular reactors with brass screens as thermal conductivity enhancers. Two brass screens (120 mesh size, mass ratio to MH = 0.12) were inserted in the tubular reactors. The reported effective thermal conductivity of the MH bed was 6 $W.m^{-1}.K^{-1}$. Klein and Groll, (2002) deployed aluminium foamed (92% porosity, 8 $W.m^{-1}.K^{-1}$ thermal conductivity) cylindrical reaction beds for cascaded sorption systems for cold generation. Laurencelle and Goyette, (2007) performed 1-D simulations on cylindrical reactors equipped with aluminium foam. Their model predictions advocated that use of aluminium foam can uphold the hydriding performance while allowing the reactor diameter to be increased by as high as 7.5 times. Singh et al., (2017) used copper flakes as thermal conductivity enhancers in the experimental study on a 1 kg $LaNi_5$ based MH reactor. They reported an 11% reduction in hydrogen charging time with the use of copper flakes compared to the case with no copper flakes. Afzal et al., (2017) reviewed and summarized various heat transfer augmentation techniques adopted for MH systems. The key takeaway from their study was that simultaneous improvement in effective thermal conductivity and convective heat transfer coefficient must be incorporated to mitigate the poor thermal performance of MH systems. Therefore, they recommended the use of coils/fins along with metal foam/EG, etc. together. Also it was suggested that for tube diameter less than 10 mm, property improvement is not obligatory.

2.4.2. Studies on heat exchanger design for MH reactors

Simple tubular MH reactors have been reported by (Muthukumar et al., 2005, Kikkinides et al., 2006, Melnichuk et al., 2008, Førde et al., 2009) and many others. Muthukumar et al., (2005) experimentally investigated the hydrogen storage behaviour of two alloys, namely $MmNi_{4.6}Fe_{0.4}$ and $MmNi_{4.6}Al_{0.4}$ in an annular cylindrical reactor attached with radial copper fins. The inner tube (φ 33×3 mm) and outer tube (φ 40×1.5 mm) dimensions were chosen to yield a 2 mm annular passage for HTF flow. At 35 bar supply pressure and 288 K cooling fluid temperature, the reactors filled with $MmNi_{4.6}Fe_{0.4}$ and $MmNi_{4.6}Al_{0.4}$ stored 1.6 wt.% and 1.3 wt.% of hydrogen in approximately 569 s and 170 s, respectively. Kikkinides et al., (2006) developed a 2-D mathematical model to optimize the hydrogen storage characteristics in a cylindrical metal hydride bed with outer jacket. They explored the effect of incorporating an additional annular cooling channel and a central cooling tube inside the bed. It was reported that the addition of an annular cooling fluid ring with a central cooling tube minimizes storage time by 60% compared to the base case without a central tube or concentric ring. Melnichuk et al., (2008) conducted constant flow rate desorption tests on a simple cylindrical MH reactor filled with 0.5 kg $MmNi_{4.7}Al_{0.3}$. Tests were conducted at room temperature (~20 °C) by varying the outflow rate and initial reactor pressure. It was inferred from the tests that for a given cut-off pressure, a smaller set outflow rate would result in an increased amount of hydrogen desorption owing to a gradual reduction in dynamic pressure. The reactor could desorb hydrogen at constant flow rates of 1.5-2 LPM for 26-35 min at room temperature. Førde et al., (2009) investigated the charging-discharging characteristics of a cylindrical reactor filled with 850 g of $La_{0.83}Ce_{0.10}Pr_{0.04}Nd_{0.03}Ni_{4.4}Al_{0.60}$. The reactor was immersed in a constant-temperature water bath. It was reported that the reactor could desorb at a rate of 1.9 Nl.(min-kg of MH)$^{-1}$ reaching 80% of its total capacity at 1.1 bar outlet pressure and 293 K bath temperature.

Finned tube heat exchangers are widely used in MH reactor configurations. Oi et al., (2004) investigated the heat transfer characteristics of metal hydride storage vessel using plate fins. An AB_2-type alloy $Ti_{0.42}Zr_{0.58}Cr_{0.78}Fe_{0.57}Ni_{0.2}Mn_{0.39}Cu_{0.03}$ with a storage capacity of 0.92 wt.% was used for experiments. The rectangular-shaped vessel was made up of aluminium alloy, where powdered alloy was filled inside three packed beds accompanied by fins, and there were four water circulation passages. Botzung et al., (2008) developed and tested a metal hydride reactor equipped with plate-fin heat exchanger for hydrogen supply to a 40 kW PEMFC. The reactor was packed with 10.3 kg $La_{0.9}Ce_{0.05}Nd_{0.04}Pr_{0.01}Ni_{4.63}Sn_{0.32}$. The reactor charged with hydrogen at 3.5 bar at 65 °C could desorb 119 g hydrogen at 125 LPH flow rate at 85 °C. Mellouli et al., (2010) put up a 2-D numerical model and studied the effect of length, thickness, pitch, and arrangement of circular fins on hydrogen absorption/desorption characteristics of a cylindrical MH reactor (1 kg $LaNi_5$) equipped with spiral coil. Projected model results favoured for long, thick, and densely packed fins with a staggered arrangement. Furthermore, they recommended a dual-layered spiral-finned MH reactor for fast hydrogen charging and discharging. Ma et al., (2014) presented a tubular manifold MH reactor furnished with circular fins and performed sensitivity analysis using 3-D numerical model. Out of the three fin parameters (number, radius and thickness) studied, they observed that addition in the number of fins brings the most significant improvement in absorption performance. Nyamsi et al., (2012) put forward an analytical model to optimize the heat transfer in finned tube heat exchangers for MH reactors. Their study promoted use of thin and longer fins to reduce thermal resistance effectively. Visaria and Mudawar, (2012) experimentally evaluated the dehydriding characteristics of two different heat exchanger configurations (coiled tube and finned tube) for fuel cell applications using $Ti_{1.1}CrMn$ alloy (2.6-4 kg). Their study reported improved heat transmission characteristics in finned tube heat exchangers compared to the coiled tube configuration. Bhouri et al., (2012) performed geometric optimization on a compound tube reactor with end-to-end fins using a numerical model. The MH reactor was simulated for a capacity of 6 kg sodium alanate. As per their study, fin tip clearance was the most influential parameter governing the hydrogen charging rate. Garrison et al., (2012) performed geometry optimization studies on finned tubes involving transverse fins and longitudinal fins for MH reactors. The planned storage capacity of the proposed shell and tube reactor (packed with sodium alanate) was 1 kg hydrogen at 50 bar pressure. Optimization results favoured for small diameter and narrowly spaced cooling tubes. Andreasen et al., (2013) conducted hydrogen desorption experiments on a prototype MH vessel built with interior and exterior fins. Desorption trials were conducted under static bath, natural and forced air convection conditions, which indicated the inclusion of fins improved the discharge characteristics significantly. The storage unit could deliver 70 L hydrogen at a discharge rate of 0.5 LPM at 20 °C, which could feed a 50 W PEMFC for 140 min. Souahlia et al., (2014) built and tested lab-scale MH reactors fitted with a finned-spiral tube and a circumferential jacket. The results of the parametric studies displayed the superiority of the finned tube heat exchanger over the lateral one. Lototskyy et al., (2015) demonstrated the hydrogen storage performance of multiple MH canisters equipped with copper and aluminium fins for LT-PEMFC applications. The hydrogen storage capacity of the MH reactors was in the range of 10-10000 NL. The storage performance of these liquid/air-cooled MH canisters highlighted that a combination of MH compaction and the addition of extended surfaces is essential to realize a steadier hydrogen discharge. Keshari and Maiya, (2018) numerically investigated the performance of a cylindrical metal hydride reactor employing a pin finned copper tube heat exchanger. They concluded increase in fin diameter and the number of fin arrays augment the hydrogen absorption rate. The reactor was predicted to attain a storage capacity of 1.4 wt.% within 636 s subjected to 15 bar, 298 K at 6.75 LPM HTF flow rate. Sunku prasad and Muthukumar, (2021) designed a compact MH reactor (filled with 9 kg $LaNi_5$) of annular finned-tube configuration and performed hydrogen storage performance tests. The reported system gravimetric and volumetric storage capacities were 0.73% and 20 kg-H_2.m^{-3}, correspondingly. Three distinct finned MH reactor configurations (longitudinal, transverse and spiral fins) were simulated by Parida and Muthukumar, (2023) aiming single stage hydrogen compression application. The heat transfer performance of all three configurations was found to be comparable under identical operating conditions, although spiral fins were recommended considering ease of availability and fabrication.

Usage of multiple small-diameter HTF tubes in MH reactors has been extensively explored (Mohan et al., 2007, Freni et al., 2009, Linder et al., 2010a, Muthukumar et al., 2012, Raju et al., 2019) to date**.** Large specific heat transfer surface area (m^2.m^{-3}) distinguishes such heat exchangers. Mohan et al., (2007) performed simulation on a cylindrical MH reactor with multiple cooling tubes and filter elements distributed over the bed. It was reported in their study that there lies an optimum number of cooling tubes and their corresponding diameter, beyond which improvement in hydrogen absorption/desorption becomes marginal. Freni et al., (2009) added an outer HTF sleeve to embedded tube reactor model and carried out 3-D simulation. Out of the three arrangements considered, which differed by the number of tubes, the model with 12 embedded tubes and an outer sleeve delivered the fastest hydrogen charging time of 15 min. A rapid response prototype MH reactor (<1 kg $LmNi_{4.91}Sn_{0.15}$) comprising 372 capillary tubes (inner diameter = 1.4 mm) was demonstrated by Linder et al., (2010a). The reported absorption/desorption reaction completion time was around 120-200 s only. Furthermore, they testified that bed reaction dynamics was at par with the inherent reaction kinetics of $LmNi_{4.91}Sn_{0.15}$. Muthukumar et al., (2012) developed a 2-D numerical model and performed optimization studies on ECT-based MH reactors by varying the quantity and spatial organization of tubes within the MH bed. Furthermore, they proposed an industrial-scale MH container of 150 kg alloy capacity, which would be refilled up to 96% of the maximum hydrogen storing capacity within 2120 s. Meng et al., (2013) suggested a miniature channel MH reactor configuration and compared its storage performance with conventional disc and tubular reactors using simulation. Simulation results showed the mini-channel reactor could outperform disc and tubular reactors owing to high specific surface area distribution. Raju et al., (2019) recommended detailed design guidelines for ECT-based MH reactor configurations and proposed a 99 ECT reactor which is capable of holding 50 kg $LaNi_{4.7}Al_{0.3}$. The designed MH reactor was predicted to attain 4/5th of the peak storage capacity within 430 s (30 bar, 25 °C). Kumar et al., (2019) carried out parametric studies on an industrial scale metal hydride reactor containing 40 kg $LaNi_{4.7}Al_{0.3}$. A 700 mm long cylindrical reactor embedded with 99 cooling tubes was used for the experimental study. At 40 bar supply pressure and 30 °C cooling fluid temperature, the MH reactor stored 552.356 g of hydrogen within 500 s. Karmakar et al., (2021) built and tested an ECT-type MH reactor with an outer cooling jacket filled with 10 kg $LaNi_5$. Parametric tests were conducted on the MH reactor to establish the best-suited operating conditions for hydrogen charging and discharging. The reactor could store 1.13 wt.% hydrogen within 1620 s subjected to 25 bar and 10 °C absorption conditions.

Another variant of shell and tube MH reactor configuration is usually recognized as tube bundle or multi-tubular reactor, where MH is filled inside tubes, and HTF flow is contained by the shell. Krokos et al., (2009) designed and optimized a multi-tubular reactor for hydrogen storage using a 3-D mathematical model. They reported that an increase in number of tubes by keeping the alloy amount unchanged improves the charging performance, as heat transfer is augmented due to the availability of enhanced surface area. It was also reported that the arrangement of hydride tubes inside fluid containers also plays a major role as heat transfer is influenced by the availability of space shared by cooling fluid. The hydrogen storage performance was improved by 88.7% for the multi-tubular tank compared to base tank, where hydride was stored in a single container. Na Ranong et al., (2009) designed and manufactured a tube bundle type storage tank for filling 8 kg sodium alanate. They used one tube bundle consisting of 7 tubes. Based on the designed prototype, they proposed a scaled-up reactor that can accommodate 100 kg alanate with 82 elements for 5 kg hydrogen storage. Bao et al., (2013) established a 3-D numerical model and performed sensitivity analysis on a multi-tubular MH reactor. The results pointed to effective thermal conductivity as the key factor influencing hydrogen storage, followed by HTF flow rate. Blinov et al., (2014) experimentally examined the discharge rate of a multi-tubular reactor packed with 5 kg $LaFe_{0.5}Mn_{0.3}Ni_{4.8}$. In the hot fluid temperature range of 60-80 °C, discharge rates of 12-75 SLPM were demonstrated. Afzal and Sharma, (2018b) proposed an industrial-scale hydrogen storage reactor (210 kg Ti-Mn alloy) with a tube bundle layout based on simulation outcomes. The proposed multi-tubular storage unit was predicted to attain 80% storage capacity within 900 s.

Helical coils as HTF flow channels within the MH reactors have been practiced in many works (Mellouli et al., 2007; Raju and Kumar, 2012; Nakano et al., 2013 etc.) Heat transfer in these helical coils is better due to the manifestation of secondary flow circulation. Mellouli et al., (2007) experimented on a cylindrical metal hydride vessel equipped with a spiral-coiled heat exchanger. The reactor filled with 1 kg $LaNi_5$ was tested for variation in supply pressure, cooling temperature, tank volume, and heat transfer coefficient. The reported hydrogen charging time (80% filling) was reduced by 5 fold with the addition of a spiral coil compared to the case where no coil was used**.** Raju and Kumar, (2012) performed a simulation on three industrial-scale MH reactor configurations (coiled tube and straight tube) targeting to store 5 kg hydrogen within 630 s. They performed geometric optimization on the configurations and predicted that the coiled tube configuration could provide superior storage densities (gravimetric & volumetric) compared to the rest of the arrangements. Nakano et al., (2013) manufactured and tested a 50 kg MH reactor reinforced with a double spiral coil heat exchanger. The reactor could supply approximately 6400 NL hydrogen within 5.5 hours at an average rate of roughly 20 LPM to an FC. Tong et al., (2019) numerically investigated the effect of adding coiled heat exchanger in a metal hydride hydrogen storage vessel. They explored both single-coil and dual-coil heat exchangers and concluded dual coiled reactor has very effective thermal management characteristics as compared to single-coil and single-tube configurations. The dual-coiled configuration could achieve 90% hydrogen saturation within 271 s. Recently, Bao and Mou, (2021) built and tested a lab-scale MH reactor incorporating a helical coil. A number of parametric tests were executed on the reactor to understand the effect of operating constraints on hydrogenation performance. Parida and Muthukumar, (2022) built a 3-D numerical model and compared the thermal performance of ECT reactor with helical coiled reactor of equal alloy capacity and heat transfer surface area. Simulation results indicated helical coiled reactor could minimize the absorption (30 bar, 298 K) and desorption (1 bar, 323 K) times by ~65% and 25% compared to ECT configuration.

Passive thermal management of MH reactors by heat pipe was demonstrated in the works of Chung et al., (2013); Liu et al., (2014) and many others. Chung et al., (2013) experimentally verified the effectiveness of adding heat pipe in MH canister using a lab-scale model. They reported a 44% reduction in hydrogen discharge time at 1 LPM flow rate compared to the case where no heat pipe was incorporated. Liu et al., (2014) built a 2-D numerical model to study the influence of heat pipe addition in MH tank on hydrogen charging rate. One of the significant inference from their study was addition of large number of small-diameter heat pipes would result in better hydrogen charging rate than fewer heat pipes with larger diameters. At 10 bar supply pressure, for the up-scaled model (280 kg $LaNi_5$), they reported a sweeping reduction of 46% storage time when heat pipe was used compared to the case without heat pipe.

Mellouli et al., (2016) performed a simulation on Mg_2Ni reactor surrounded with $NaNO_3$ (PCM) filled inside different enclosures. They considered spherical shells, hexagonal tubes, and straight tubes as shell structures for PCM. While assessing the effect of thermal conductivity, heat capacity, supply pressure and operating temperature on charging, they found that an increase in effective thermal conductivity of the MH-PCM system returns maximum improvement. For the configuration with PCM filled inside straight tubes, 90% charging time was predicted to 19335 s, which marked a 58.1% reduction in charging time compared to the case where PCM was filled in the annular layer. The concept of cascaded PCM jackets for thermal management of MH was numerically explored by Alqahtani et al., (2020). They built a numerical model to assess the impact of introducing a cascaded PCM jacket for the thermal management of MH beds. Simulation results suggested that the cascaded system could shorten the charging and discharging duration of the MH bed by 26% and 51%, respectively, compared to the case where only a single PCM was used. El Mghari et al., (2020) numerically inspected the influence of different PCMs on the absorption behaviour of a $LaNi_5$-based MH reactor. Out of the 5 PCM compositions studied, $LiNO_3.3H_2O$ offered the fastest loading time. Moreover, the study reiterated the importance of mixing PCM with high-conductive metal foams (Al, Cu, and Zn) to improve PCM's effective thermal conductivity.

Weckerle et al., (2017) designed an innovative stacked plate heat exchanger for metal hydride-based cooling system. The reactor engaged alternative stacks of MH and HTF passage on primary and secondary sides with a miniature gap of 1.5 mm. They reported very short desorption time ($t < 60$ s) with 0.353 kg alloy inventory in the temperature range of 0-40 °C**.** Wang et al., (2019) compared seven different minuscule channel MH reactor configurations using 3-D numerical model and recommended two mini-channel MH reactors with enhanced radial heat transfer. The studied configurations included i) tank reactor with no tube, ii) straight tube reactor, iii) converging-diverging channel reactor, iv) coiled tube reactor, v) composite coiled tube reactor, vi) coupling linkage coiled tube reactor and vii) radiation tube reactor. Sensitivity analysis pointed out transverse pitch and mounting span to be the utmost influential geometrical factors affecting hydrogen absorption. Afzal et al., (2021) experimentally characterized a large-scale MH reactor (47.5 kg $La_{0.9}Ce_{0.1}Ni_5$) with a honeycomb shaped extended surface rooted inside the pressure chamber. The stated complete absorption and desorption durations were in the order of 120–200 min when aided with natural convection with water.

Table 2.1: Summary of various heat exchange options opted for metal hydride reactors

Authors (Reference)	**Type of investigation**	**Alloy used (amount)**	**Reactor details/heat exchange option**	**Operating conditions**	**Hydriding/dehydriding performance**
Oi et al., (2004)	Experimental and Numerical	$Ti_{0.42}Zr_{0.58}Cr_{0.78}Fe_{0.57}Ni_{0.2}Mn_{0.39}Cu_{0.03}$ (11.3 kg)	Rectangular vessel with plate-fin type heat exchanger	P_s = 2-8 bar, T_c = 293 K, T_d = 313 K, Q_f = 0.6-1.2 $m^3.h^{-1}$	The reactor was able to absorb/desorb hydrogen at a near constant flow rate of 2.1 $Nm^3.h^{-1}$ for 1200 s at 293/313 K.
Muthukumar et al., (2005)	Experimental	$MmNi_{4.6}Fe_{0.4}$, $MmNi_{4.6}Al_{0.4}$ (0.5 kg)	Annular cylindrical reactor with radial copper fins	P_s = 5-35 bar, T_c = 288-298 K, T_d = 313-333 K, U_o = 750-1250 $W.m^{-2}.K^{-1}$	At 35 bar, 288 K, the reactors filled with $MmNi_{4.6}Fe_{0.4}$ and $MmNi_{4.6}Al_{0.4}$ stored 1.6 wt.% and 1.3 wt.% of hydrogen in approximately 569 s and 170 s, respectively.
Kikkinides et al., (2006)	Numerical	$LaNi_5$ (1 kg)	Annular cylindrical reactor with concentric tube/concentric ring	P_s =10 bar, T_c = 290 K, U_o = 1650 $W.m^{-2}.K^{-1}$	The configuration with concentric tube and annular ring was able to attain 99 % of the maximum storage capacity within 620 s.
Mohan et al., (2007)	Numerical	$LaNi_5$ (1 kg)	Cylindrical reactor with multiple cooling and filter tubes	P_s = 8-15 bar, T_c = 293-323 K, U_o = 500-1000 $W.m^{-2}.K^{-1}$	The configuration with 55 cooling tubes attained 1.22 wt.% storage capacity within ~5000 s at 15 bar, 293 K.
Mellouli et al., (2007)	Experimental	$LaNi_5$ (1 kg)	Cylindrical reactor with spiral coil	P_s = 6-10 bar, T_c = 283-293 K, T_d = 313-323 K, U_{ov} = 750-1150 $W.m^{-2}.K^{-1}$	At 10 bar, 293 K, the reactor was able to store 1.06 wt.% of hydrogen in nearly 4000 s.
Melnichuk et al., (2008)	Experimental	$MmNi_{4.7}Al_{0.3}$ (0.5 kg)	Cylindrical vessel with lateral surface cooling	T_c = 293 K, T_d = 296 K	With initial reactor pressure of 24 bar, the reactor was able to desorb hydrogen at a maximum constant flow rate of 1.5 LPM for 38 min.

Botzung et al., (2008)	Experimental and Numerical	$La_{0.90}Ce_{0.05}Nd_{0.04}Pr_{0.01}Ni_{4.63}Sn_{0.32}$ (10.3 kg)	Rectangular vessel with aluminium fins and aluminium foam	P_s = 3.5 bar, T_c = 293 K, P_d = 1.5 bar, T_d = 348 K, Q_f = 10 $m^3.hr^{-1}$	The reactor desorbed 119 g hydrogen at a constant flow rate of 125 LPH at 85 °C.
Freni et al., (2009)	Numerical	$LaNi_5$ (~70 kg)	Cylindrical reactor with multiple cooling tubes and outer jacket	P_s = 8 bar, T_c = 293 K, U_c = 1650 $W.m^{-2}.K^{-1}$	The configuration with 12 cooling tubes and outer jacket attained 1.3 wt.% capacity within 15 min.
Krokos et al., (2009)	Numerical	$LaNi_5$ (Not specified)	Multi-tubular reactor	P_s =10 bar, T_c = 290 K, U_o = 1650 $W.m^{-2}.K^{-1}$	At 10 bar, 290 K, the time taken for 99 % storage for the 9 tube bundle reactor was estimated to be 1030 s.
Na Ranong et al., (2009)	Experimental and Numerical	$NaAlH_4$ (8 kg)	Cylindrical reactor with helical coil/ tube bundle	P_s = 100 bar, T_c = 373 K, Q_f = 1.2 $m^3.hr^{-1}$	The tube bundle reactor was able to store 80% of the maximum hydrogen storage capacity in 540 s.
Førde et al., (2009)	Experimental and Numerical	$La_{0.83}Ce_{0.10}Pr_{0.04}Nd_{0.03}Ni_{4.4}Al_{0.60}$ (0.85 kg)	Cylindrical vessel with water bath cooling	P_s = 10 bar, T_c = 293 K, T_d = 293-313 K	The reactor was able to desorb more than 80% of the maximum storage capacity at a constant flow rate of 1.9 Nl/ (min kg MH) at 293 K.
Mellouli et al., (2010)	Numerical	$LaNi_5$ (1 kg)	Cylindrical reactor with single and dual-layer spiral coils and fins	P_s = 10 bar, T_c = 297 K	The predicted hydrogen absorption times ($t_{90\%}$) were in the range of 420-500 s for dual layered spiral configurations.
Linder et al., (2010)	Experimental	$LmNi_{4.91}Sn_{0.15}$ (0.9 kg)	Cylindrical reactor with multiple capillary tubes	P_s = 11.2 bar, T_c/T_d = 28-60 °C, P_d = Vacuum, Q_f = 2.5-5 LPM	At 28 °C, the absorption and desorption times were 120 s and 200 s, respectively.

Visaria and Mudawar, (2012)	Experimental and Numerical	$Ti_{1.1}CrMn$ (2-6.4 kg)	Cylindrical reactor with finned tube and coiled tube	T_d = 17-32 °C, Q_f = 12.5-17.5 LPM	At a set hydrogen flow rate of 0.14-0.15 $g.s^{-1}$, the constant flow discharge were maintained between 6.2-7.2 min.
Bhouri et al., (2012)	Numerical	$NaAlH_4$ (18 kg)	Multi-tubular reactor with internal longitudinal fins	P_s = 100-300 bar, T_c = 80-140 °C, U_c = 185-3110 $W.m^{-2}.K^{-1}$	The reactor configuration with six fins attained a storage capacity of 2.45 wt.% in 720 s.
Garrison et al., (2012)	Numerical	$NaAlH_4$ (126 kg)	Shell and tube reactors with transverse and longitudinal fins	P_s = 50 bar T_c = 100 °C, U_c = 1500 $W.m^{-2}.K^{-1}$	The longitudinal finned configuration could yield 0.7 wt.% storage capacity within 12 min.
Muthukumar et al., (2012)	Numerical	$MmNi_{4.6}Al_{0.4}$ (150 kg)	Cylindrical reactor with multiple cooling tubes	P_s = 15-35 bar, T_c = 15-35 °C, U_o = 500-1250 $W.m^{-2}.K^{-1}$	The reactor could reach 96 % of the maximum hydrogen storage capacity within 2120 s.
Meng et al., (2012)	Numerical and Experimental	$LaNi_5$ (0.4 kg)	Rectangular vessel with multiple miniature cooling channels	P_s = 6-10 bar, T_c = 293 K, P_d = 1.5 bar, T_d = 353 K, U_o = 1000-11000 $W.m^{-2}.K^{-1}$	At 8 bar, 293 K, the reactor could complete hydrogen absorption within 500 s.
Raju and Kumar, (2012)	Numerical	$NaAlH_4$ (177 kg)	Shell and tube configurations/helical coiled reactor	P_s = 150 bar, T_c = 380 K, Q_f = 20 LPM	At 150 bar, the helical coiled configuration was able to store 3.07 wt.% hydrogen within 630 s.
Nyamsi et al., (2012)	Numerical (2-D model)	$LaNi_5$ (1 kg)	Cylindrical reactor with central finned tubes for HTF flow	P_s = 10 bar, T_c = 293 K, U_c = 1000 $W.m^{-2}.K^{-1}$	The predicted hydrogen absorption time was approximately 3000 s.
Andreasen et al., (2013)	Experimental	$MmNi_{4.7}Al_{0.3}$ (0.5 kg)	Cylindrical reactor with circular internal and longitudinal external fins.	P_s = 25 bar, T_c = 20-40 °C, T_d = 0-50 °C, P_d = 1 bar	The prototype reactor could feed a 50 W fuel cell for 140 min at 0.5 LPM flow rate.

Bao et al., (2013)	Numerical	$LaNi_5$, $MmNi_{4.6}Fe_{0.4}$ (0.36-0.6 kg)	Cylindrical reactor with MH tubes and filters	P_s = 8-45 bar, T_c = 293 K, , U_o = 1000 $W.m^{-2}.K^{-1}$	The absorption completion time was around 3500 s.
Nakano et al., (2013)	Experimental	$MmNi_5$ (50 kg)	Cylindrical reactor with double helical coil	P_s = 20 bar, T_c/T_d = 12-32 °C, Q_f = 1.15-1.72 LPM	At 22 °C, the reactor could supply approximately 6400 L hydrogen within 5.5 hours at an average rate of roughly 20 LPM to an FC.
Chung et al., (2013)	Experimental	$LaNi_5$ (0.295 kg)	Cylindrical tank with finned heat pipe	P_s = 10 bar, T_c=20 °C, P_d = 1 bar, T_d = 50 °C	At 10 bar, 20 °C, the reactor could attain 95% hydrogen saturation within 900 s.
Ma et al., (2014)	Numerical (3-D model)	$LaNi_5$ (1 kg)	Cylindrical reactor with multiple finned tubes for HTF flow	P_s = 5-10 bar, T_c = 293 K, U_{ov} = 500-1500 $W.m^{-2}.K^{-1}$	The projected hydrogen absorption times were in the range of 1720-2000 s.
Souahlia et al., (2014)	Experimental	$LaNi_5$ (1 kg)	Cylindrical reactor with internal spiral coil and outer jacket.	P_s = 3-11 bar, T_c = 20-40 °C, m_f = 3-13 $g.s^{-1}$	The prototype unit could store 1.33 wt.% hydrogen within 420 s at 11 bar, 20 °C.
Blinov et al., (2014)	Experimental and Numerical	$LaFe_{0.5}Mn_{0.3}Ni_{4.8}$ (5kg)	Multiple cartridge reactor	T_c/T_d = 10-95 °C, m_f = 0.05-0.3 $kg.s^{-1}$	The storage unit was able to deliver nearly 80% of the maximum storage capacity at a constant flow rate of 12.8 LPM in 2151 s.
Liu et al., (2014)	Numerical	$LaNi_5$ (280 kg)	Cylindrical reactor with outer jacket and embedded heat pipe	P_s = 10 bar, T_c = 275-320 K, U_c = 600-2000 $W.m^{-2}.K^{-1}$	The time required to 95% hydrogen storage capacity was around 840 min.
Lototskyy et al., (2015)	Experimental	AB_2 type alloy (Ti, Zr, Fe, Mn, Cr, Ni) (0.07-12.2 kg)	Cylindrical reactors with internal and external fins	P_s = 20-80 bar, P_d = 1-15 bar, T_c/T_d=10-40 °C, m_f = 0.3-0.5 $kg.min^{-1}$	The reactor with 12.2 kg alloy capacity could run a 1.2 kW LT-PEMFC for ~100 min.

Mellouli et al., (2016)	Numerical	Mg_2Ni (Not specified)	Cylindrical reactor with PCM filled in spherical elements/hexagonal tubes/straight tubes	P_s = 15-20 bar, T_c/T_d = 560-580 K, P_d = 2 bar	For the straight tube configuration with 60% aluminium foam, the time required for 90% hydrogen storage was 9130 s.
Bhogilla, (2017)	Numerical	$Ti_{0.98}Zr_{0.02}V_{0.43}Fe_{0.09}Cr_{0.05}Mn_{1.5}$ (~60 kg)	Cylindrical reactor with helical coil	P_s = 10-30 bar, T_c = 293 K, U_o = 500-1500 $W.m^{-2}.K^{-1}$	At 20 bar, 293 K, the reactor attained a storage capacity of nearly 1.8 wt.% in approximately 1800 s.
Weckerle et al., (2017)	Experimental	Hydralloy C5 (0.353 kg)	Plate finned reactor with alternative stacks for MH and HTF	P_s = 30 bar, T_c/T_d = 0-40 °C, Q_f = 4.5 LPM	The complete absorption and desorption times were in the range of 60-80 s.
Keshari and Maiya, (2018)	Numerical	$LaNi_5$ (1 kg)	Cylindrical reactor with internal pin fins and tubes	P_s = 5-15 bar, T_c = 288-308 K, Q_f = 3-6.75 LPM	The reactor could store 1.4 wt.% hydrogen within 636 s at 15 bar, 298 K.
Afzal and Sharma, (2018b)	Numerical	Ti-Mn based (Hydralloy C5) (210 kg)	Multi-tubular reactor	P_s = 25-50 bar, T_c = 278-298 K, T_d = 308-333 K, U_o = 4-500 $W.m^{-2}.K^{-1}$	At 40 bar, the reactor configuration with 14 tubes was able to reach 80% of the maximum hydrogen storage capacity in 900 s.
Raju et al., (2019)	Theoretical and Numerical	$LaNi_{4.7}Al_{0.3}$ (50 kg)	Cylindrical reactor with multiple cooling tubes	P_s = 5-35 bar, T_c = 293-308 K, Q_f=10-35 LPM	At 30 bar, 298 K, the reactor could attain 1.29 wt.% hydrogen storage capacity within 2060 s.
Tong et al., (2019)	Numerical	$LaNi_5$ (~0.4 kg)	Cylindrical reactor with single/double helical tube	P_s = 8 bar, T_c = 293 K, U_c = 1652 $W.m^{-2}.K^{-1}$	The dual coiled configuration attained 90% hydrogen storage capacity within 271 s.
Wang et al., (2019)	Numerical	$LaNi_5$ (Not specified)	Cylindrical reactor with straight tube/converging-	P_s = 6-14 bar, T_c = 273-313 K, U_c = 1000 $W.m^{-2}.K^{-1}$	The radiation tube reactor attained 99.3% hydrogen saturation within 1040 s.

			diverging channel/coiled tube/composite coiled tube/coupling linkage coiled tube/radiation tube		
Kumar et al., (2019)	Experimental	$LaNi_{4.7}Al_{0.3}$ (40 kg)	Cylindrical reactor with embedded cooling tubes	P_s = 2-25 bar, T_c = 30 °C, T_d = 60-90 °C, Q_f = 8-30 LPM	At 40 bar, 30 °C the reactor stored 552.356 g of hydrogen within 500 s.
Alqahtani et al., (2020)	Numerical	Mg_2Ni (Not specified)	Cylindrical reactor with cascaded PCM envelope/sandwiched PCM structure	P_s =12 bar, T_c/T_d = 579 K, P_d = 3 bar	The configuration with a cascaded PCM sandwich bed could attain hydrogen saturation within 2025 s.
Mghari et al., (2020)	Numerical	$LaNi_5$ (0.424 kg)	Cylindrical and Spherical reactors with PCM	P_s = 8 bar, T_c = 293 K, T_d = 313 K	The concentric spherical reactor attained 1.32 wt.% storage capacity within 60 min.
Karmakar et al., (2021)	Experimental	$LaNi_5$ (10 kg)	Cylindrical reactor with multiple cooling tubes and outer jacket	P_s = 10-30 bar, T_c = 5-30 °C, P_d = 1 bar, T_d = 50-80 °C, Q_f = 20 LPM	At 25 bar, 25 °C, the reactor could store 1.13 wt.% hydrogen within 1620 s.
Prasad and Muthukumar, (2021)	Experimental	$LaNi_5$ (9 kg)	Cylindrical reactor with internal finned tube and outer jacket	P_s = 10-30 bar, T_c = 15-30 °C, P_d = 1 bar, T_d = 40-70 °C, Q_f = 2.5 LPM	At 30 bar, 25 °C, the reactor could store 104.5 g hydrogen within 475 s.
Bao and Mou, (2021)	Experimental	$LaNi_5$ (0.64 kg)	Cylindrical reactor with helical coil	P_s = 8-12 bar, T_c = 20-40 °C, Q_f = 10-50 LPH	The hydrogen absorption time of the reactor was approximately 3000 s.
Afzal et al., (2021)	Experimental	$La_{0.9}Ce_{0.1}Ni_5$ (47.5 kg)	Cylindrical reactor with honeycomb-shaped heat structure	P_s = 25-35 bar, T_c = 5-25 °C, P_d = 1 bar, T_d = 25-	At 35 bar, 5 °C, the reactor was able to attain 90% hydrogen saturation within 3600 s.

				60°C, U_c = 4-1112 W.m^{-2}.K^{-1}	
Parida and Muthukumar, (2021)	Numerical	$MmNi_{4.6}Al_{0.4}$ (20 kg)	Cylindrical reactor with multiple tubes/ helical coil	P_s = 10-30 bar, T_c = 283-298 K, P_d =1-3 bar, T_d = 298-323 K	At 30 bar, 298 K, the helical coiled reactor took 1360 s for complete absorption.
Parida and Muthukumar, (2022)	Numerical	$MmNi_{4.6}Al_{0.4}$ (0.5 kg)	Cylindrical reactor with longitudinal/transverse/spiral fins	P_s = 20 bar, T_c = 293-303 K, P_d = 10-50 bar, T_d = 353-373 K, U_c = 1515 W.m^{-2}.K^{-1}	The reactor could deliver hydrogen at an average rate of 2.27 LPM for 2000 s at 10 bar discharge pressure.

P_s/P_d: Hydrogen supply/desorption pressure, T_c/T_d: Absorption/Desorption temperature, HTF: Heat transfer fluid, U_o: Overall heat transfer coefficient, U_c: Convective heat transfer coefficient, Q_f/m_f: Volume/Mass flow rate of heat transfer fluid

Figure 2.1 shows some of the distinct choices of heat exchange options adopted to date for MH-based thermal devices.

2.5. Studies on metal hydride based cooling systems

2.5.1. Studies on thermally driven systems

Gruen et al., (1978) first demonstrated the idea of a chemical heat pump which utilizes solar thermal energy to drive a coupled MH system for cooling applications. They performed thermodynamic analysis on $CaNi_5$/$LaNi_5$ pair as high-temperature metal hydride (HTMH)/low-temperature metal hydride (LTMH) and reported a static enthalpy based COP of 0.95. Later, Nishizaki et al., (1983) performed mathematical calculations on a thermally driven MH-based cooling system (TDMHCS), introducing the concept of sensible heat exchange between reactors as a means to improve the system COP. They paired up $LaNi_{4.7}Al_{0.3}$/$LaNi_5$ as HTMH/LTMH, respectively.

Helical coiled reactor (Mellouli et al., 2007)

Finned 'U' tube reactor (Singh et al., 2017)

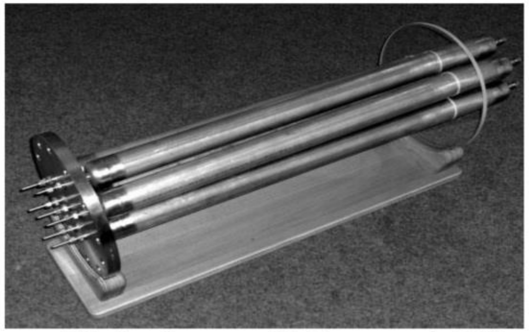

Tube bundle reactor (Na Ranong et al., 2009)

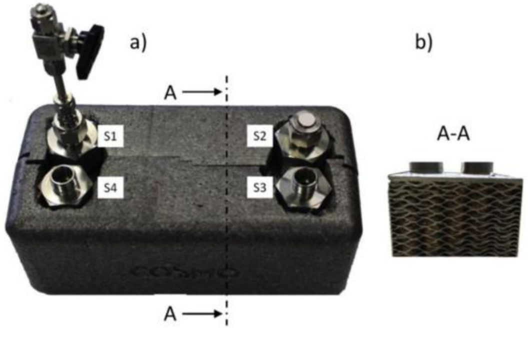

Stacked plate reactor (Weckerle at al., 2017)

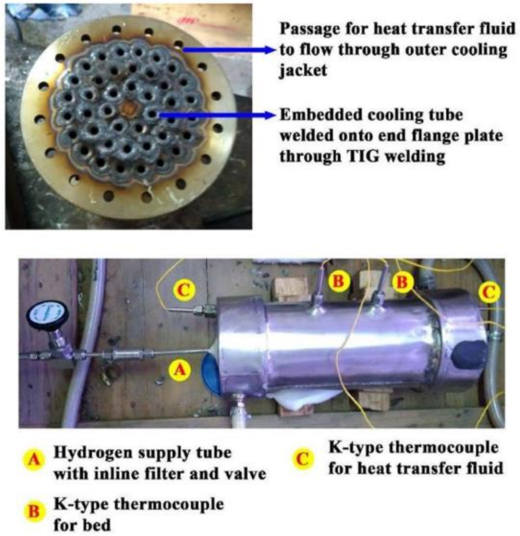

Embedded cooling tube reactor (Raju et al., 2022)

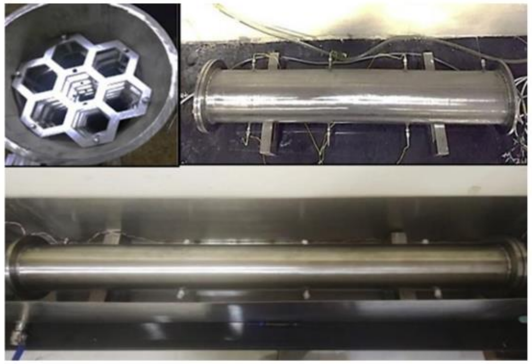

Honeycomb cell reactor (Afzal et al., 2021)

Conical finned reactor (Chandra et al., 2022)

Fig. 2.1: Pictorial representation of a few MH reactors with diverse heat exchange options.

Since then, a plentiful of experimental investigations on TDMHCS have been carried out. These investigations were primarily aimed at assessing the dependence of performance indices like COP and specific cooling power (SCP) on the operating and design parameters. Nagel et al., (1984) performed experiments on a TDMHCS employing $LaNi_{4.65}Al_{0.3}/MmNi_{4.0}Fe_{1.0}$ pair (HTMH/LTMH) at an operating temperature of 423/303/298 K ($T_h/T_m/T_c$). Where 'T_h', 'T_m' and 'T_c' denote source temperature, sink temperature, and cooling temperature, respectively. They reported an optimum cooling output of 1.7 kW for a cycle time of 13 min. It was inferred that a mere increase in charged hydrogen does not necessarily increase cooling output, as the amount of hydrogen transferred between the reactors was constant for a fixed cycle time. They put emphasis on the dynamic characterization of hydrogen transfer between coupled reactors for designing MH-based cooling systems. Ron, (1984) designed and demonstrated a 3.6 kW bus air conditioning unit using $LaNi_{4.7}Al_{0.3}/MmNi_{4.15}Fe_{0.85}$ pair (HTMH/LTMH) intended to be run by exhaust gas (150-300 °C). The low-temperature hydride was used in the form of Porous Metal Hydride (PMH) compacts comprising of 18 wt.% Al matrix, which yielded a thermal conductivity of the order 17-20 $W.m^{-1}$. K^{-1}. A cooling power of 250 $W.kg^{-1}$ of desorbing alloy and a COP of 0.35 was reported for 6 min cycle time operation. Lee et al., (1995) investigated the performance of a prototype heat pump intended for cooling at different operating conditions employing $Zr_{0.9}Ti_{0.1}Cr_{0.9}Fe_{1.1}$/ $Zr_{0.9}Ti_{0.1}Cr_{0.6}Fe_{1.4}$ pair as HTMH/LTMH. They used brass screen inside the MH bed to improve the effective thermal conductivity (6 $W.m^{-1}.K^{-1}$). At an operating temperature of 493/303/291 K ($T_h/T_m/T_c$) the reported cooling power was around 151 $W.kg^{-1}$ for 7 min cooling cycle time. Imoto et al., (1996) demonstrated a solar-driven (140 °C) cooling system intended to attain a freezing temperature of -20 °C. For a designed cooling capacity of 1.86 kW, 90 kg of total alloy inventory was used pairing $LaNi_{4.6}Mn_{0.3}Al_{0.1}$ and $La_{0.6}Y_{0.4}Ni_{4.8}Mn_{0.2}$ as high and low-temperature hydride respectively. They reported a system COP of 0.42 for a cooling cycle time of 1140 s. Izhvanov et al., (1996) demonstrated a working prototype of water heating (40-45 °C) and cooling system (0-4 °C) utilizing $LaNi_{4.6}Al_{0.4}/MmNi_{4.15}Fe_{0.85}$ alloy pair. For a designed heating/cooling capacity of 500 W, the reported COP was in the range of 0.17-0.2. Chernikov et al., (2002) tested a similar cold water production unit (18 L water tank) pairing $LaNi_{4.6}Al_{0.4}$ and $MmNi_{4.85}Fe_{0.15}$. Longitudinally finned corrugated aluminium foil was used to enhance the thermal conductivity of the MH bed up to 8 $W.m^{-1}.K^{-1}$. They reported average cooling capacity of 154 W and a COP of 0.11 for a half-cycle time of 20 min. Ni and Liu, (2007) performed refrigeration experiments on

$LaNi_{4.61}Mn_{0.26}Al_{0.13}/La_{0.6}Y_{0.4}Ni_{4.8}Mn_{0.2}$ pair (LTMH/HTMH) in the temperature range of 115-150/30-35/20 °C ($T_h/T_m/T_c$) to understand the actual system performance. At 150°C hot source temperature, they achieved a COP of 0.3, yielding 245 W cooling output for 64 min cycle time. The same alloy pair was employed by Qin et al., (2007) to develop an automobile air condition system driven by exhaust gas. For 2.75 kg alloy inventory, in the experimented temperature range of 120–200/20–50/-10-0 °C, the achieved cooling power was 61-238 W. Kang et al., (1996) performed experiments on a coupled bed TDMHCS engaging $LaNi_{4.7}Al_{0.3}$/ $MmNi_{4.15}Fe_{0.85}$ as HTMH/LTMH pair. The focus of their study was to understand the mechanism of hydrogen transfer between coupled reactors at varied operating conditions. For 5.7 kg cooling alloy inventory, the reported optimum hydrogen transfer amount was 520 NL for 10 min half cycle time. They reported a maximum COP of 0.2. Linder et al., (2010b) conducted experiments on a compact TDMHCS using $LmNi_{4.91}Sn_{0.15}/Ti_{0.99}Zr_{0.01}V_{0.43}Fe_{0.09}Cr_{0.05}Mn_{1.5}$ pair (HTMH/LTMH). They demonstrated a very fast cooling cycle (Half-cycle (HC) time: 100-120 s) with the use of capillary tube bundle reactors and reported SCP up to 780 $W.kg^{-1}$ of desorbing alloy. Yasuda et al., (2013) experimentally explored the effect of the addition of metal hydride sheets on the performance of MH based cooling system. MH sheets were prepared by mixing aramid pulp and carbon fibre to MH powder in the ratio of 1:2:7. They achieved 20% lift in SCP with use of MH sheets compared to the case when only MH powder was used.

Numerical studies on TDMHCS are somewhat less reported in the literature. 1-D numerical models on TD-MHCS have been demonstrated by Ramgopal and Srinivasa Murthy, (1992); Dehouche et al., (1998); Fedorov et al., (1999); and Jang et al., (2001). Ramgopal and Srinivasa Murthy, (1992) built 1-D numerical model to predict coupled bed ($ZrMnFe/MmNi_{4.5}Al_{0.5}$) performance under varied bed thickness, thermal conductivity, and operating temperatures. It was inferred that bed thickness and effective thermal conductivity controls cycle time and specific power significantly; however, they have minor influence on system COP. Also, it was shown that change in heat source and refrigeration temperature bears negligible influence on COP; however, specific output increases significantly with rise in refrigeration temperature. Dehouche et al., (1998) built and simulated a 1-D mathematical model describing conjugate heat and mass transfer phenomena of coupled MH bed considering fast reaction cell designs. For operating temperature range of 213/40/2 °C, the reported COP and SCP were in the range of 0.5-0.6 and 23-30 $W.kg^{-1}$. Fedorov et al., (1999) numerically solved a 1-D mathematical model for

MH-based heat pump employing $LaNi_{4.5}Al_{0.25}/TiFe_{0.8}Mn_{0.2}$ pair. The objective of the simulation was to comprehend the heat and hydrogen transfer between the reactors and to assess the influence of operating temperatures, heat flow patterns, heating and cooling times on thermal efficiency and COP. Jang et al., (2001) carried out 1-D simulation of MH based heat pump system with $Zr_{0.9}Ti_{0.15}Cr_{0.6}Fe_{1.45}$ (HTMH) and $Zr_{0.9}Ti_{0.1}Cr_{0.9}Fe_{1.1}$ (LTMH) alloys. Simulation outcomes suggested to have increased plateau pressure difference between the coupled pair and reduced individual hysteresis to improve cooling power. Payá et al., (2009) studied the dynamic behaviour of the TD-MHCS using a lumped parameter model with $LmNi_{4.91}Sn_{0.15}/Ti_{0.99}Zr_{0.01}V_{0.43}Fe_{0.09}Cr_{0.05}Mn_{1.5}$ alloy pair. They proposed a novel correlation to account for hysteresis in PCT modelling. Later the model was improved by Payá et al., (2011) by incorporating measured reaction kinetics data and experiential correlations capturing PCT data beyond the plateau on both side (α and β phases). They performed a sensitivity analysis of several operating parameters (operating temperatures, hydrogen charged amount, cycle time, etc.). Simulation results pointed toward smaller thermal mass, reduced cycle time, and increased hydrogen inventory to obtain higher cooling power. A similar sensitivity analysis of operating parameters on the cooling performance of a TDMHCS was performed by Mellouli et al., (2009) using lumped parameter model. The low value of COP (0.45-0.5) obtained in their study was attributed to the low enthalpy of the cooling alloy. Satheesh et al., (2009) built a 2-D numerical model and studied the effect of constant and variable wall temperature boundary conditions on the performance of a TDMHCS comprising $MmNi_{4.6}Al_{0.4}/MmNi_{4.6}Fe_{0.4}$ pair. It was concluded that the assumption of constant wall temperature boundary conditions overestimates the actual system performance. Later, the same research group (Satheesh and Muthukumar, 2010) performed a performance investigation on five different alloy pairs for MH-based cooling applications using their previous numerical model (Satheesh et al., 2009).

2.5.2. Studies on compressor driven systems

The COP of the MH-based cooling systems can be improved significantly by including a mechanical compressor which eliminates the need for a regeneration alloy. In 1997, Kim et al., (1997) theoretically investigated the performance of few hydrides for MH-based compressor-driven cooling systems (MH-CDCS) application. The estimated COP for 26 different MH alloys was in the ranges of 3.6-4.4 for 4 min cycle time and 6 °C refrigeration temperature. They also demonstrated a lofty specific cooling power of 1.5 $kW.kg^{-1}$ (130 s) for $LaNi_5$ compacts under vacuum desorption conditions. A set of experiments on MH-CDCS were conducted by Park et al., (2001) using $Zr_{0.9}Ti_{0.1}Cr_{0.55}Fe_{1.45}$ alloy (4.2 kg) with the aid of an oil-free air-propelled compressor (1-18 atm). The maximum specific cooling power (SCP) achieved at 11 $m^3.min^{-1}$ air flow rate, 24°C ambient temperature for 2.6 min cycle time was 292 $W.kg^{-1}$. Later Park and co-workers (Park et al., 2002) tested the cooling capability of the same alloy (3.5 kg) in a finned tube heat exchanger assembly with the aid of an oil-type compressor (1-hp motor). For 3 min half-cycle time and 7 $m^3.min^{-1}$ air flow rate, the reported system SCP and COP were 411 $W.kg^{-1}$ and 1.8, respectively. The minimum cooled air outlet temperature achieved was 6 °C. Mazumdar et al., (2005) built and simulated the numerical model of a MH-CDCS considering the dynamic characteristics of a 50 cc reciprocating compressor, finned reactors, and cooled space. Subjected to 1 kW cooling load, for considered 3.2 kg $Zr_{0.9}Ti_{0.1}Cr_{0.55}Fe_{1.45}$ alloy, the projected SCP was 167 $W.kg^{-1}$. The predicted cycle COP was in the range of 1.7-2.2 for 6 min cycle time. Bedbak and Ramgopal, (2005) performed thermodynamic studies (1st Law and 2nd Law analysis) on a MH-CDCS system as room air conditioner unit. Their analysis emphasized on minimizing temperature drop at the high and low-temperature MH reactor to improve system COP. The study outcomes also advocated internal heat recovery to be of paramount importance for such systems to be able to be competitive with conventional VCRS. Magnetto et al., (2006) built and demonstrated a prototype MH-CDCS as an air conditioning unit employing Mm based alloy with small hydrogen inventory (27 g only). The spiral-shaped hydride heat exchanger used in the experiments was formed by coupling multiple copper tubes (diameter 3.175 mm). For 3.5 min half-cycle time, the miniature system yielded impressive COP (2.57-2.85) in the ambient temperature range of 21-35 °C. Muthukumar et al., (2016) demonstrated the performance of a lab-scale MH-CDCS using 2.75 kg $LmNi_{4.91}Sn_{0.15}$ filled inside embedded cooling tube reactor (60 tubes). Tests were conducted by altering refrigeration temperature, sink temperature, cold fluid flow rates and half-cycle time. The testified maximum COP and SCP values were 2.2 and 53.5 $W.kg^{-1}$ at 20 °C refrigeration temperature and 25 °C sink temperature.

Table 2.2: Summary of experimental studies conducted on metal hydride based closed-cycle cooling systems

Author (Reference)	**Alloy pair used (HTMH /LTMH)**	**Drive type**	**Operating temperature**	**Cooling Capacity**	**COP**	**Specific Cooling Power**
Ron, (1984)	$LaNi_{4.7}Al_{0.3}/MmNi_{4.15}Fe_{0.85}$	Thermal	$T_h/T_m/T_c$ = 150-200/35/20 °C	3.5 kW	0.22-0.35	200-250 $W.(kg\text{-}alloy)^{-1}$
Nagel et al., (1984)	$LaNi_{4.65}Al_{0.3}/MmNi_{4.0}Fe_{1.0}$	Thermal	$T_h/T_m/T_c$ = 423/303/298 K	1.7 kW	-	128.3 $W.(kg\text{-}alloy)^{-1}$
Lee et al., (1995)	$Zr_{0.9}Ti_{0.1}Cr_{0.9}Fe_{1.1}/Zr_{0.9}Ti_{0.1}Cr_{0.6}Fe_{1.4}$	Thermal	$T_h/T_m/T_c$ = 220/30/18 °C	-	-	151 $W.(kg\text{-}alloy)^{-1}$
Imoto et al., (1996)	$LaNi_{4.6}Mn_{0.3}Al_{0.1}/La_{0.6}Y_{0.4}Ni_{4.8}Mn_{0.2}$	Thermal	$T_h/T_m/T_c$ = 150/20/-20 °C	1.86 kW	0.42	40 $W.(kg\text{-}alloy)^{-1}$
Izhvanov et al., (1996)	$LaNi_{4.6}Al_{0.4}/MmNi_{4.15}Fe_{0.85}$	Thermal	$T_h/T_m/T_c$ = 158/45/(0-4) °C	0.2 kW	0.2	133 $W.(kg\text{-}alloy)^{-1}$
Kang et al., (1996)	$LaNi_{4.7}Al_{0.3}/MmNi_{4.15}Fe_{0.85}$	Thermal	$T_h/T_m/T_c$ = 413/308/288 K	-	0.2	-
Kim et al., (1997)	$LaNi_5$	Compressor /Theoretical	T_c = 22 °C	-	-	1500 $W.(kg\text{-}alloy)^{-1}$ (Desorption through vacuum)
Willers et al., (1999)	$LaNi_{4.3}Al_{0.4}Mn_{0.3}$, $LaNi_{4.4}Al_{0.34}Mn_{0.26}$, $LaNi_{4.5}Al_{0.29}Mn_{0.21}$, $LaNi_{4.7}Sn_{0.3}$, $LaNi_{4.75}Al_{0.25}$, $LaNi_{4.85}Al_{0.15}$, $LaNi_5$ /$La_{0.555}Co_{0.03}Pr_{0.12}Nd_{0.295}Ni_5$, $Ti_{0.98}Zr_{0.02}V_{0.43}Fe_{0.09}Cr_{0.05}Mn_{1.5}$	Thermal	$T_h/T_m/T_c$ = 235/33/18 °C	0.36 kW	0.6	10 $W.(kg\text{-}alloy)^{-1}$

Gopal and Murthy, (1999)	ZrMnFe/$MmNi_{4.5}Al_{0.5}$	Thermal	$T_h/T_m/T_c$ = 110-130/25-30/5-15 °C	0.35 kW	0.35	45 W.(kg-alloy)$^{-1}$
Park et al., (2001)	$Zr_{0.9}Ti_{0.1}Cr_{0.55}Fe_{1.45}$	Compressor	T_m/T_c = 22-24 °C	0.29 kW	-	292 W.(kg-alloy)$^{-1}$
Chernikov et al., (2002)	$LaNi_{4.6}Al_{0.4}$/$MmNi_{4.85}Fe_{0.15}$	Thermal	$T_h/T_m/T_c$ = 200/45/0-4 °C	0.154 kW	0.11	103 W.(kg-alloy)$^{-1}$
Park et al., (2002)	$Zr_{0.9}Ti_{0.1}Cr_{0.55}Fe_{1.45}$	Compressor	T_m/T_c = 27 °C	0.41 kW	1.8	411 W.(kg-alloy)$^{-1}$
Ni and Liu, (2006)	$LaNi_{4.61}Mn_{0.26}Al_{0.13}$/$La_{0.6}Y_{0.4}Ni_{4.8}Mn_{0.2}$	Thermal	$T_h/T_m/T_c$ = 115-150/30-35/20 °C		0.22-0.3	88.8 W.(kg-alloy)$^{-1}$
Magnetto et al., (2006)	Rare earth composition	Compressor	T_m/T_c = 21-35 °C	1.5-2 kW	2.57-2.85	
Qin et al., (2007)	$LaNi_{4.61}Mn_{0.26}Al_{0.13}$/$La_{0.6}Y_{0.4}Ni_{4.8}Mn_{0.2}$	Thermal	$T_h/T_m/T_c$ = 120–200/20–50/-10–0 °C	0.085 kW	0.26	7.7 W.(kg-alloy)$^{-1}$
Linder et al., (2010)	$LmNi_{4.91}Sn_{0.15}$/$Ti_{0.99}Zr_{0.01}V_{0.43}Fe_{0.09}Cr_{0.05}Mn_{1.5}$	Thermal	$T_h/T_m/T_c$ = 130/28/20 °C	-	-	780 W.(kg-alloy)$^{-1}$
Yasuda et al., (2013)	$TiFe_{0.9}Ni_{0.1}$/$La_{0.6}Y_{0.4}Ni_{4.9}Al_{0.1}$	Thermal	$T_h/T_m/T_c$ = 125/15/5 °C	-	-	195 W.(kg-alloy)$^{-1}$
Muthukumar et al., (2016)	$LmNi_{4.91}Sn_{0.15}$	Compressor	T_m/T_c = 10-20/25-35 °C	-	2.2	53.5 W.(kg-alloy)$^{-1}$

$T_h/T_m/T_c$: Hot/Medium/Low temperature

2.6. Literature Closure

From the set of literature studied, the following inferences can be deduced:

- Heat transfer in the MH-hydrogen system is the most critical factor influencing the hydrogen sorption rate.
- Heat transfer in MH bed can be improved by augmenting the effective thermal conductivity (conjugate property of metal hydride and hydrogen). Improvement can be accomplished by densification/compaction of MH powder with conductive additives, use of extended natural graphite, and reinforcement of conductive structures, e.g., mesh, wire, foam, flakes, etc. However, all these methods inevitably incur a loss in gravimetric storage capacity at the expense of improvement in reaction dynamics. Another basic exercise for improving the heat transfer is to minimize the heat conduction path i.e. to reduce the MH bed thickness.
- Heat transfer in MH beds can also be augmented by engaging a heat exchanger either externally or internally. The heat exchanger used so far ranges from a basic cooling tube with an outer jacket to complex coiled heat exchangers. However, the design of heat exchangers often involves simulation, which incurs increased computation cost with the intricacy of heat exchangers.
- While a large number of studies on numerous heat exchanger designs have been reported in the literature, most of these studies are computational in nature, where hydrogen storage performance or parametric investigation has been carried out subject to a set of model assumptions. Recent studies indicate that the number of numerical studies documented in the literature are approximately 20% higher than that of experimental studies (Sreeraj et al., 2022). Nonetheless, a few intricate designs have been proposed that result in better performance; however, their practical implementation has been limited.
- Despite the fact that a significant number of studies on lab-scale prototypes (up to 5 kg MH alloy), including experimental and numerical works, are reported in the literature, experimental characterization of large-scale MH reactors (alloy capacity > 10 kg) is fewer in number. Simulation studies intended to optimize operational, design, and material parameters of MH-based thermal devices often do not reflect actual system performance owing to lack/inaccuracy in the estimation of the thermo-physical, kinetic, and Pressure-Concentration-Temperature (PCT)

parameters of the MH alloys involved. To expedite the hands-on implementation of large-scale MH based thermal devices, more testing and system characterization is necessary.

- MH-based engineering systems for cooling/air conditioning is a sustainable solution as the refrigerant is hydrogen which does not harm the ozone layer and possess a low GWP compared to conventional refrigerants. Thermally driven cooling systems utilizes low-grade heat input but offer COP in the range of 0.2-0.6 typically. On the other hand, MH-CDCS utilizes high grade energy and offers COP in the range of 1.7-2.5. However, selection of compressors for MH-CDCS is a critical issue owing to the requirement of low flow rate (0.9-12 $m^3.h^{-1}$) at moderate pressure (1-15 bar). A few researchers have claimed that MH-CDCS can be competitive to existing VCRS with a proper selection of compressor and minimizing parasitic thermal penalties. Nonetheless, only a limited number of works on MH-CDCS employing lab-scale reactors have been reported in the literature till date.

2.7. Thesis Objectives

The following objectives were formulated for the present thesis work.

- To select appropriate MH alloys for hydrogen storage and cooling applications using PCT properties
- To build a numerical model to predict the hydrogen absorption and desorption performances of MH reactors
- To build a numerical model to predict the performance of compressor driven MH based cooling system
- To design and construct MH reactor configurations with improved heat transfer characteristics and reduced parasitic mass
- To conduct exhaustive experimental studies on developed MH reactors at near-ambient operating conditions and assess the hydrogen storage performance in terms of hydrogen discharging time and energy efficiency
- To conduct exhaustive experimental studies on developed MH reactors at varied operating conditions and assess the cooling performance in terms of COP and SCP

2.8. Summary

In this chapter, state-of-the-art developments in metal hydride-based hydrogen storage and cooling devices are discussed. Apart from overviewing the chemical kinetics, heat and mass transfer aspects of metal hydrides, the chapter also includes a tabulated summary of various heat exchange options adopted for metal hydride reactors over the last two decades. Additionally, the chapter embodies the systematic review of the research work carried out towards the development of thermally driven as well as compressor-driven cooling systems. Founded on the in-depth literature review, the objectives of the present thesis work have been composed.

3. Design and fabrication of metal hydride reactors

3.1. Introduction

The design of a metal hydride reactor for a specific application, first and foremost, obliges the amount of hydrogen required to be known. Then based on the nature of the application, the type of metal hydride must be chosen to serve within the operating temperature and pressure regime. For example, AB_5-type intermetallic hydrides are usually preferred for near ambient hydrogen storage intended for stationary application. Again to serve high-temperature thermal energy storage (350-400 °C), usually, Mg-based hydrides are preferred because of their high enthalpy of formation. Once the type of metal hydride is finalized, the total amount of alloy required can be calculated from known reversible capacity (wt.%). The next step involves the estimation of storage volume based on alloy density, porosity and volume expansion allowance. The shape and size of the containment vessel can be decided based on mechanical strength in the operating regime and the type of fabrication method opted. Once the reactor dimensions are calculated, the heating/cooling load and peak required rate of heat transfer dictates the heat exchange option that needs to be incorporated. After the selection of heat exchanger, the hydrogen absorption/desorption performance may be checked by means of numerical modelling at the desired operating conditions. If satisfactory hydrogen absorption/desorption is not achieved, any of the heat transfer augmentation techniques mentioned in the previous chapter can be applied. A flow chart indicating the design of metal hydride reactors is shown in Fig. 3.1.

3.1.1. General design criteria

The design of the MH reactors was further subjected to the following general conditions.

- Simple in design and construction
- Improved heat transfers without thermal enhancement or addition of thermal structure
- Improved alloy to empty reactor weight ratio
- Ease of transportation and operation

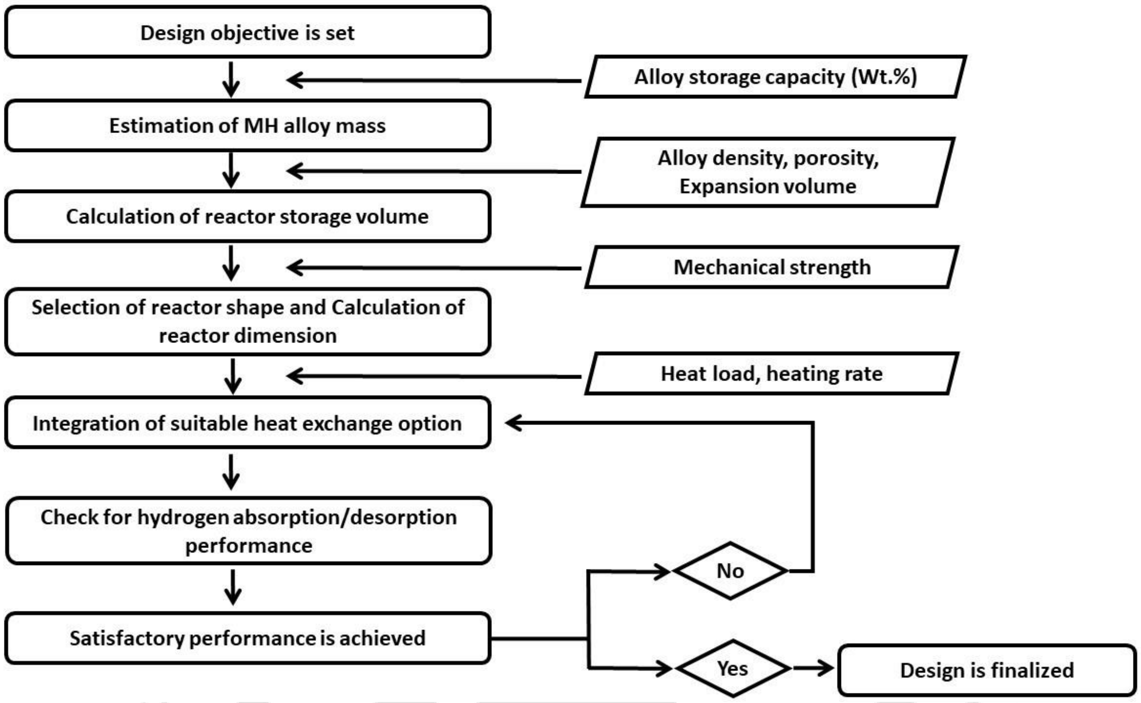

Fig. 3.1: Flow chart indicating steps involved in MH reactor design.

3.2. Reactor description

Two different reactor configurations were considered for experimental studies. In the first configuration, the MH alloy could be filled inside the shell and heat transfer fluid (HTF) could flow through the tubes. This configuration is called as the Embedded Cooling Tube reactor. From now onwards, this configuration will be referred to as ECTR. In the other configuration, the MH alloy could be filled inside tubes while the HTF could flow over the tube bundles. This configuration is called as the Tube Bundle reactor. From now onwards, this configuration will be referred to as TBR. The schematic diagram of the ECTR and TBR is represented in Fig. 3.2.

3.3. Design objectives

For large-scale reactors, the objective was to store 1 kg of hydrogen at near ambient conditions and provide 3.5 kW cooling. On the other hand, the lab-scale reactors were designed to study the alloy behaviour.

3.3.1. Design constraints

The following constraints were imposed considering ease of fabrication, installation and operation.

- The metal hydride alloy to empty reactor weight ratio should be at least 1.25
- The length of reactor should not exceed 1 m.
- The diameter of reactor should not exceed 0.25 m.
- There should be minimum number of welded joints.

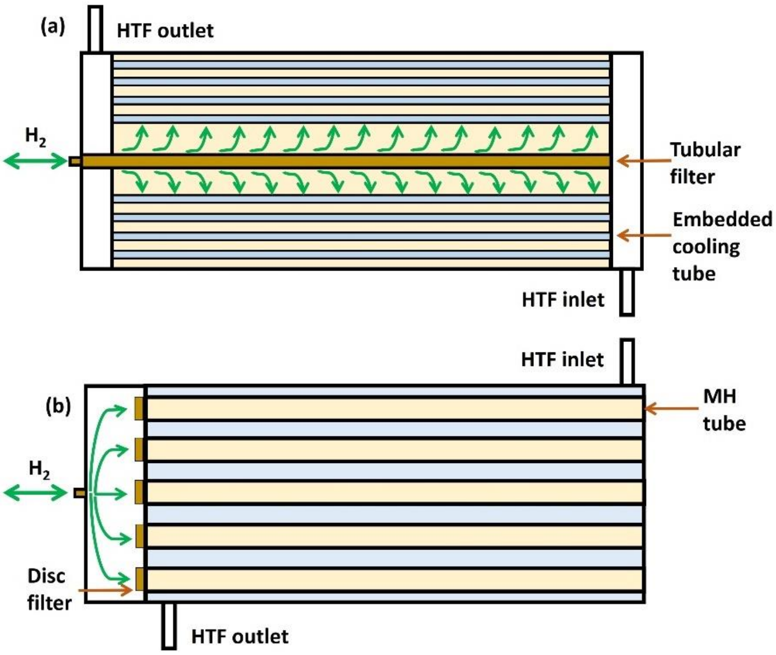

Fig. 3.2: Schematic diagram of the reactors (a) ECTR and (b) TBR.

3.4. Design of the TBR

The TBR configuration is a very simple yet effective design concept that leverages the following advantages when it comes to MH-based hydrogen storage:

- A cylindrical shape offers uniform stress distribution and excellent sealing.
- The availability of standardized tubes makes fabrication easier.
- The bed thickness can be varied independently just by varying the tube diameter.

3.4.1. Selection of tube dimension for TBR

The selection of tube dimensions was based on mechanical strength, weight, and heat transfer performance. Considering AB_5-type alloy with an approximate packing density of 4200 kg.m^{-3} (50% porosity) and 20% expansion allowance, the dimension of different tube sizes and the corresponding performance parameters are shown in Table 3.1.

Table 3.1: Selection of tube dimension for TBR

Outer diameter (mm)	**Thickness (mm)**	**Maximum working pressure (bar)**	**Mass of alloy filling per meter length ($kg.m^{-1}$)**	**MH alloy to tube weight ratio**
12.7	1	161.41	0.28	0.99
15.875	1	129.13	0.48	1.31
19.05	1	107.61	0.72	1.63
25.4	***1.2***	***96.85***	***1.31***	***1.84***
31.25	1.65	108.24	1.93	1.62
38.1	2.1	112.9	2.84	1.54
50.8	2.6	104.9	5.14	1.68

Based on above stated criteria, the tube dimension of φ 25.4×1.2 mm was selected for further study.

3.4.2. Determination of Shell dimension for TBR

Once the tube dimension was determined, a circular arrangement of tubes inside the shell was decided, allowing for a minimum 8 mm distance between two neighbouring tube surfaces for ease of welding. Once again, a cylindrical shell was decided, and the corresponding shell dimension (cylindrical) would vary depending on capacity. The dimension of the shell is given in subsequent sections.

3.5. Design of the ECTR

The design methodology of the ECTR was adopted from the work of Raju et al. 2019. The proposed methodology provides mathematical correlations to determine the optimum number of stacks and tubes per stack so that the yielded bed thickness takes the least possible value without increasing reactor weight.

3.5.1. Selection of tube dimension for ECTR

The tube dimension for HTF flow in an ECTR was chosen as standard available Swagelok 1/4 inch tubes (φ 6.35×0.89 mm). This tube thickness is optimum for welding purposes and also does not cause severe pressure drop.

3.5.2. Determination of Shell dimension for ECTR

In case of an ECTR configuration, the cylindrical shell is the principle pressure chamber where MH alloy would be filled. Hence, depending on the alloy capacity and a number of embedded tubes, and necessary pressure rating, usually nominal pipes (seamless) are employed. The detailed dimension of the shell for lab-scale and large-scale ECTRs are provided in subsequent sections. Table 3.2 summarizes the tube stack details and other performance parameters for available nominal pipe sizes available chosen as shell.

3.6. Numerical modelling

The behaviour of the metal hydride during absorption and desorption of hydrogen can be predicted with reasonable accuracy by solving a numerical model. The model essentially involves continuity equation for solid and gas phase, momentum equation for gas phase, and a combined energy equation for gas and solid. Apart from these fundamental governing equations, the reaction kinetics expression, the expression for equilibrium pressure calculation, and an equation of state are required to solve the complete model subjected to suitable initial and boundary conditions.

3.6.1. Description of the physical system

Two different physical models are considered for simulation, i.e., the TBR configuration and the ECTR configuration. The dimensional details of the physical models are provided in Table 3.3. The ECTR and TBR models have been designed as per the corresponding design methodologies described in the above section to contain the same amount of MH alloy. The sectional and isometric views of the models are depicted in Fig. 3.3.

Table 3.2: Estimation of the number of stacks for ECTR

Nominal pipe size (inch)	**Outer diameter (mm)**	**Thickness**	**Maximum Working Pressure (bar)**	**Radial location of each stack**	**No. of tubes at each stack**	**Mass of alloy filling per meter length (kg.m^{-1})**	**MH alloy to reactor weight ratio**
4	114.3	6.02	108	15.96	7	22.72	1.07
				30.03	14		
				44.10	20		
5	141.3	6.55	95	15.77	7	35.72	1.19
				29.58	14		
				43.39	20		
				57.20	26		
6	***168.28***	***7.12***	***86.7***	***15.64***	***7***	***51.57***	***1.29***
				28.28	***14***		
				42.92	***20***		
				56.56	***26***		
				70.2	***32***		
8	219.08	8.18	76.5	16.93	7	93.46	1.58
				32.28	13		
				47.63	20		
				62.98	26		
				78.33	32		
				93.68	38		

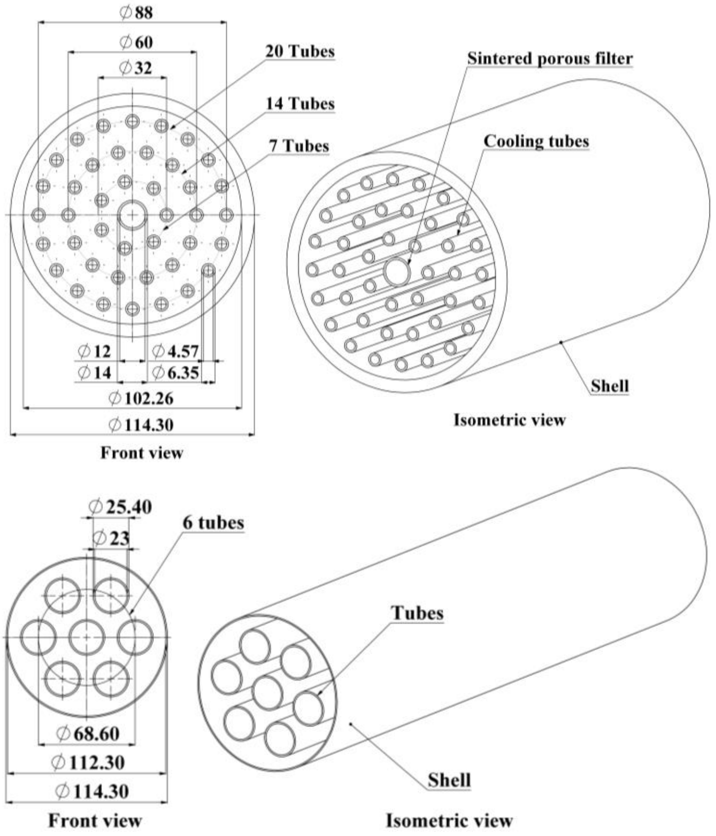

Fig. 3.3: The sectional and isometric view of the models (a) ECTR configuration and (b) TBR configuration.

Table 3.3: Dimensional details of the physical models

Parameter/Attribute	**ECTR configuration**	**TBR configuration**
Tube OD (mm)	6.35	25.4
Tube thickness (mm)	0.89	1.2
Number of tubes	41	7
Length of reactor (mm)	222	520
Shell OD (mm)	114.3	114.3
Amount of alloy filling (kg)	6.3	6.33
Heat transfer surface area (m^2)	0.18	0.29

3.6.2. Mathematical model

Assumptions

1. Hydrogen behaves as an ideal gas within the temperature and pressure range studied.
2. The solid phase is isotropic and has a uniform porosity.
3. Local thermal equilibrium between the hydrogen gas and metal hydride is valid.
4. The thermo-physical properties of the metal hydride are independent of temperature, concentration and hydrogen pressure.

5. The reactor outer surface is well insulated.
6. Radiative heat transfer is negligible.

Governing Equations

Continuity Equation

a) Gas phase

Considering the sink term as the amount of hydrogen absorbed/desorbed, the continuity equation (Shahrzad S Mohammadshahi et al., 2016) can be expressed as:

Absorption
$$\varepsilon \frac{\partial \rho_g}{\partial t} + \nabla.(\rho_g \vec{u}) = -\zeta_a \tag{3.1}$$

Desorption
$$\varepsilon \frac{\partial \rho_g}{\partial t} + \nabla.(\rho_g \vec{u}) = \zeta_d \tag{3.2}$$

b) Solid phase

The mass balance for the solid phase (Anbarasu et al., 2014) considering source during absorption, and sink during desorption are expressed as:

Absorption
$$(1-\varepsilon)\frac{\partial \rho_s}{\partial t} = \zeta_a \tag{3.3}$$

Desorption
$$(1-\varepsilon)\frac{\partial \rho_s}{\partial t} = -\zeta_d \tag{3.4}$$

Here 'ε' denotes porosity of the hydride bed. 'ζ_a' and 'ζ_d' denotes mass of hydrogen absorbed/desorbed by the metal hydride, per unit time and per unit volume.

Momentum Equation

For saturated porous media with low fluid velocity ($Re_P < 1$), the inertia term can be neglected and the velocity of hydrogen gas through the porous media (metal hydride bed), '$\vec{u}$' can be calculated using Darcy's law (Muthukumar et al., 2012) given by:

$$\vec{u} = -\left(\frac{K}{\mu_g}\right)\nabla P \tag{3.5}$$

Where 'K' is the permeability of the hydride bed, and 'μ_g' is the dynamic viscosity of hydrogen gas.

Energy Equation

Owing to the high thermal conductivity of hydrogen gas, a local thermal equilibrium between the solid and gas phase can be considered reasonably, and a combined energy equation (Muthukumar et al., 2012) can be written as:

$$(\rho c_p)_e \frac{\partial T}{\partial t} + (\rho_g c_{pg})(\vec{u}.\nabla T) = k_e \nabla^2 T + Q_g \tag{3.6}$$

Where *'Q_g'* is the heat source/sink term given by:

Absorption $$Q_{g,a} = \zeta_a \left(\frac{\Delta H}{M_g} \right) \tag{3.7}$$

Desorption $$Q_{g,d} = \zeta_d \left(\frac{\Delta H}{M_g} \right) \tag{3.8}$$

Where *'ΔH'* is the enthalpy of formation. In the energy balance equation, effective heat capacity *'$(\rho c_p)_e$'* is given by,

$$(\rho c_p)_e = (1-\varepsilon)(\rho c_p)_s + \varepsilon(\rho c_p)_g \tag{3.9}$$

Where *'$(\rho c_p)_g$'* denotes the heat capacity of the gas phase, while *'$(\rho c_p)_s$'* represents the heat capacity of the solid phase. Similarly, the effective thermal conductivity is obtained as,

$$k_e = (1-\varepsilon)k_s + \varepsilon k_g \tag{3.10}$$

Equation of state

The density of hydrogen gas *'ρ_g'* can be evaluated from the ideal gas equation as:

$$\rho_g = \frac{P_g M_g}{R_u T} \tag{3.11}$$

Where *'P_g'* is the gas pressure and *'T'* is the temperature within MH bed while *'M_g'* is the molecular weight of gaseous hydrogen and *'R_u'* is the universal gas constant.

Ancillary Equations

Reaction rate expression

The rate of mass of hydrogen absorbed/desorbed *'ζ_a/ζ_d'* per unit volume per unit time is related to rate of reaction (Anbarasu et al., 2014) as expressed by:

Absorption $$\zeta_a = C_a \exp\left(-\frac{E_a}{R_u T}\right) \ln\left(\frac{P_g}{P_{eq}}\right)(\rho_{ss} - \rho_t) \tag{3.12}$$

Desorption $$\zeta_d = C_d \exp\left(-\frac{E_d}{R_u T}\right)\left(\frac{P_{eq} - P_g}{P_{eq}}\right)(\rho_t) \tag{3.13}$$

Where 'C_a/ C_d' designates the reaction rate constant, 'E_a/E_d' is the activation energy, and 'P_{eq}' stands for the equilibrium pressure of MH alloy. Similarly, 'ρ_{ss}' is the saturated MH density, and 'ρ_t' is the density of MH alloy at any time 't'.

Modified van't Hoff equation

The formation of MH can be explained using the PCT plots in the phase transformation diagram. The pressure-temperature dependency within the two-phase region is mathematically expressed by the ideal van't Hoff equation. During the absorption/desorption process, the equilibrium pressure inside the MH bed is calculated using the modified van't Hoff equation (Anbarasu et al., 2014):

$$\frac{P_{eq}}{P_0} = \exp\left[\frac{\Delta S}{R_u} - \frac{\Delta H}{R_u T} + (\varphi_s \pm \varphi_o) \times \tan\left(\pi\left(\frac{X}{X_{\max}} - \frac{1}{2}\right)\right) \pm \frac{\varphi}{2}\right] \tag{3.14}$$

In Eq. (3.14), '+' sign indicates absorption, while '-' sign indicates desorption. 'P_0' stands for atmospheric pressure, 'ΔS' is the entropy of formation, while 'φ_s', 'φ_o' and 'φ' respectively denote slope factor, slope constant and hysteresis factor. Concentration is the ratio of the number of hydrogen atoms absorbed/desorbed over the total number of metal atoms present per mole of alloy. Concentration at any given time 't' is designated by 'X' while the maximum concentration is represented as 'X_{max}'.

Initial and boundary conditions

Initial conditions

Initially (at $t = 0$), the hydride bed temperature, gas temperature and HTF temperature are uniform and equal to set initial temperature.

$$T_m = T_g = T = T_f = T_0 \tag{3.15}$$

Also the gas pressure and hydride density, are assumed to be uniform. For absorption, the initial hydride density is equal to metal density, whereas, for desorption, the initial hydride density is equal to saturated hydride density. The initial gas pressure for both absorption and desorption is equal to initial hydride equilibrium pressure at a given temperature.

Absorption $\rho_m = \rho_{emp}$ (3.16)

Desorption $\rho_m = \rho_{ss}$ (3.17)

Absorption/Desorption $P_g = P_{eqi}$ (3.18)

Boundary conditions

As illustrated in Fig. 3.4, heat transfer takes place from the hydride bed to HTF across the tube wall via convective heat transfer. At the heat transfer interface,

$$-k\left.\frac{\partial T}{\partial r}\right|_{r=r_i} = U_c(T_s - T_f) \tag{3.19}$$

The constant pressure boundary condition is implemented at the top surface, through which hydrogen is absorbed or desorbed.

Absorption $$P_g = P_s \tag{3.20}$$

Desorption $$P_g = P_d \tag{3.21}$$

The outer boundary of the metal hydride container is assumed adiabatic.

$$-k\left.\frac{\partial T}{\partial r}\right|_{r=r_c} = 0 \tag{3.22}$$

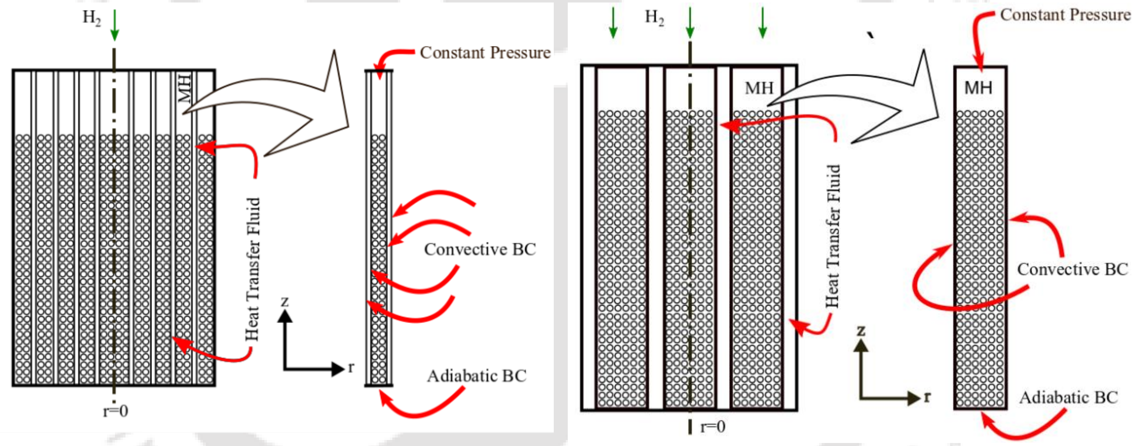

Fig. 3.4: Depiction of boundary conditions implemented in model (a) TBR configuration and (b) ECTR configuration.

3.6.3. Solution methodology

The set of governing equations subjected to the initial and boundary conditions are implemented and solved using COMSOL Multiphysics 5.5. COMSOL Multiphysics is a commercial simulation software that uses the Finite Element Method (FEM) for solving a system of equations. It specializes in multi-physics coupling. A direct linear solver (MUMPS) is employed to solve the system of equations. Time stepping is done using Euler backward difference formula (BDF) with an adaptive technique where time steps vary with error values calculated at the previous iteration. During simulation, relative and absolute tolerances are set to 10^{-4} and 10^{-3}, respectively.

Table 3.4: Model input parameters for $MmNi_{4.6}Al_{0.4}$-H_2 system

Parameters	**Value**
Properties of $\boldsymbol{MmNi_{4.6}Al_{0.4}}$	
Density of metal alloy	$8400\ kg.m^{-3}$
Specific heat capacity of metal (c_{ps})	$419\ J.kg^{-1}.K^{-1}$
Thermal conductivity of metal (k_s)	$1.6\ W.m^{-1}.K^{-1}$
Porosity (ε)	0.5
Effective density of metal alloy (ρ_{emp})	$4200\ kg.m^{-3}$
Effective density of saturated MH (ρ_{ss})	$4259\ kg.m^{-3}$
Activation energy (E_a)	$21170\ J.(mol\ H_2)^{-1}$
(E_d)	$22000\ J.(mol\ H_2)^{-1}$
Reaction entropy (ΔS_a)	$107.2\ J.(mol\ H_2)^{-1}.K$
(ΔS_d)	$100\ J.(mol\ H_2)^{-1}.K$
Reaction enthalpy (ΔH_a)	$28000\ J.(mol\ H_2)^{-1}$
(ΔH_d)	$27500\ J.(mol\ H_2)^{-1}$
Properties of hydrogen	
Thermal conductivity (k_g)	$0.1272\ W.m^{-1}.K^{-1}$
Specific heat capacity (c_{pg})	$14{,}283\ J.kg^{-1}.K^{-1}$
Molecular weight (M_g)	$2.016\ g.mol^{-1}$
Constants used	
Universal gas constant (R_u)	$8.314\ J.mol^{-1}.K^{-1}$
Reaction constant (C_a)	$75\ s^{-1}$
(C_d)	$100\ s^{-1}$
Slope factor (φ_s)	0.35
Slope constant (φ_o)	0.15
Hysteresis factor (φ)	0.2

To simplify the model, the wall thickness of the tubes as well as the shell were neglected for both reactor configurations during the simulation. For simulation of the hydrogen storage, $MmNi_{4.6}Al_{0.4}$ is selected as filling alloy as the PCT properties and kinetic parameters are widely available in the literature (Muthukumar et al., 2012; Muthukumar and Venkata Ramana, 2010). The model input parameters are given below in Table 3.4.

3.6.4. Mesh independence test

To confirm that the model simulation results are not influenced by changes in mesh size or number or mesh elements, the present numerical model is checked from the mesh independence test. The details of the mesh configurations chosen including quality parameters are shown in Table 3.5. The results of the mesh independence test for both configurations at 20 bar, 25 °C hydrogen absorption condition is shown in Fig. 3.5. Based on the mesh independence test outcomes it was decided to go for Mesh 2 and Mesh 1 for TBR and ECTR configurations, respectively.

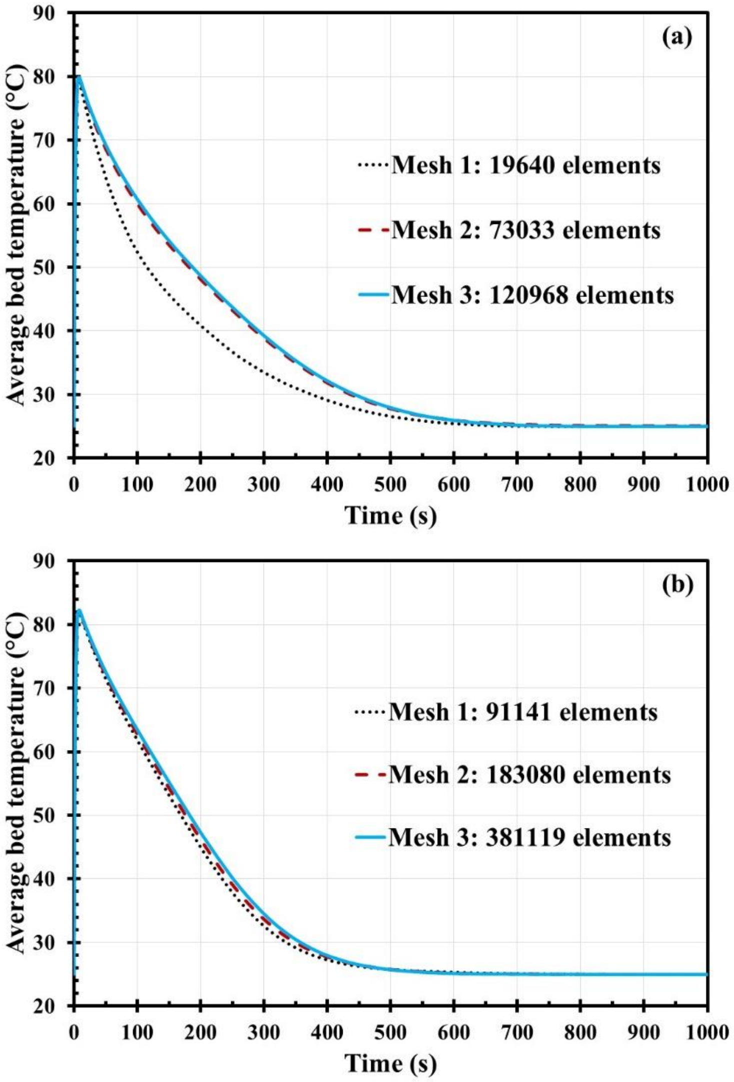

Fig. 3.5: Mesh independence test for reactor models (a) TBR configuration and (b) ECTR configuration.

Table 3.5: Details of the mesh independence test

Reactor configuration	**Mesh configuration**	**Minimum element size (mm)**	**Maximum element size (mm)**	**No. of elements**
TBR (7 tubes)	Mesh 1	9.36	52	19640
	Mesh 2	5.2	41.6	73033
	Mesh 3	2.08	28.6	120968
ECTR (41 tubes)	Mesh 1	4	22.2	91141
	Mesh 2	3	18.5	183080
	Mesh 3	2.22	17.8	381119

3.6.5. Model Validation

For validation of the present model, the reactor geometry used by Muthukumar et al., (2005) was adopted, and simulations were performed accordingly. The annular cylindrical MH reactor studied (Muthukumar et al., 2005) had an inner tube of 33 mm outer diameter and 3 mm wall thickness, where MH alloy was filled and a 2 mm annular passage for HTF circulation. The reactor was 450 mm long with 8 radial copper fins arranged within the MH bed.

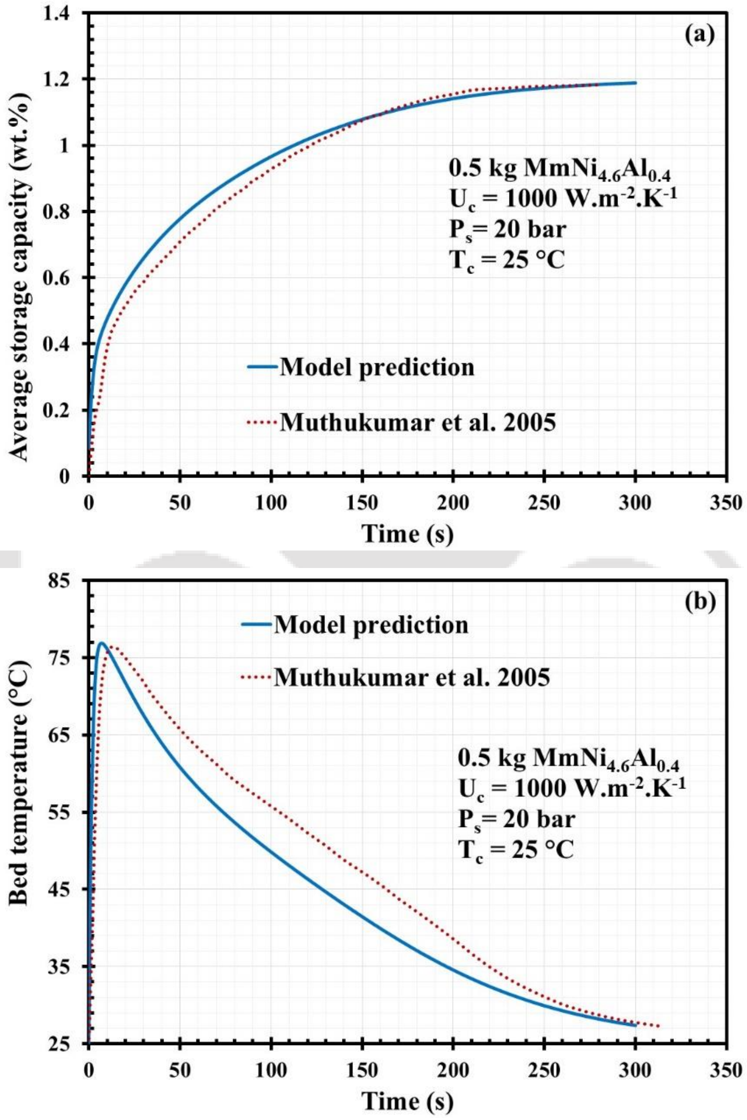

Fig. 3.6: Model validation (a) storage capacity (wt.%) and (b) bed temperature.

3.6.6. Comparison of hydrogen absorption behaviour

In this section, the results of the hydrogen absorption performance comparison of the prototype TBR and ECTR configurations are presented. The hydriding performance is compared in terms of volume-averaged bed temperature and volume-averaged hydrogen storage capacity. Simulation is carried out at a supply pressure of 20 bar and 40 bar, while the convective heat transfer coefficient and the cooling fluid temperature are set at 500 W.m^{-2}.K^{-1} and 25 °C, respectively.

Effect of reactor configuration on hydrogen absorption characteristics

Figure 3.7(a) shows the effect of heat exchanger configuration on average bed temperature at different supply pressures.

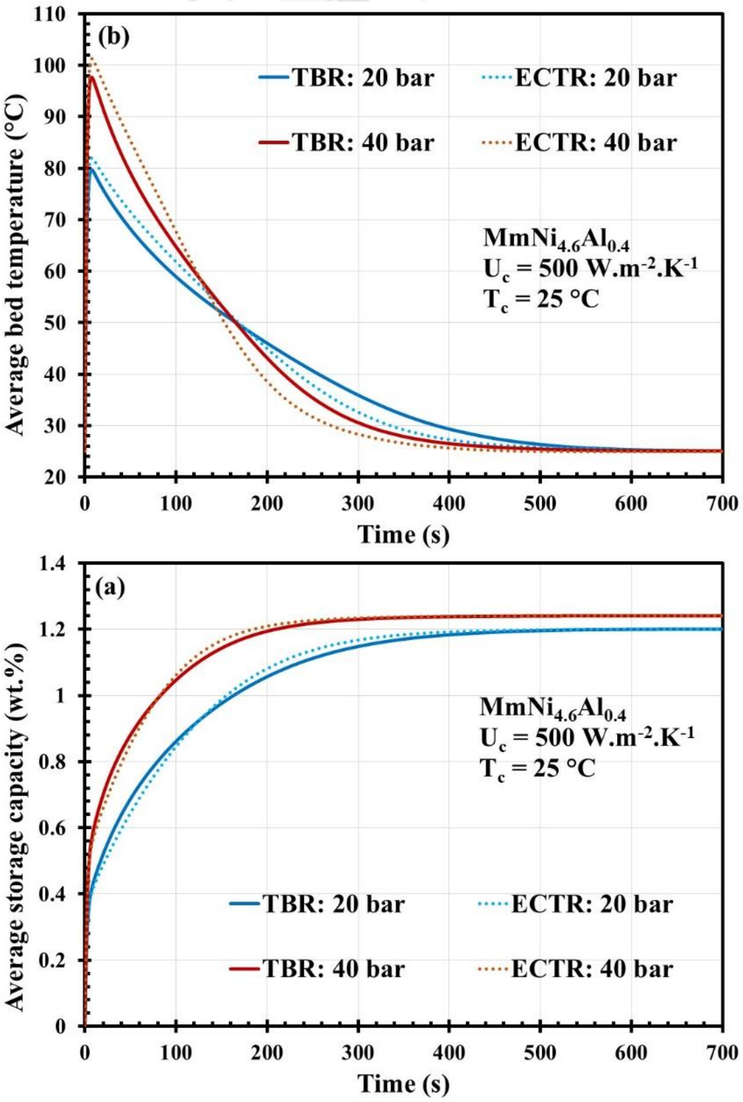

Fig. 3.7: Hydrogen absorption comparison of ECTR and TBR (a) bed temperature and (b) storage capacity (wt.%).

As soon as the hydriding reaction is initiated, the rate at which reaction heat evolved within the first 5-10 seconds surpasses the rate at which heat is dissipated to the cooling fluid, which causes the temperature peak. The large initial rate of heat generation is due to the ample pressure differential between supply pressure and equilibrium pressure at the beginning of absorption. As the reaction progresses, the reaction rate slows down owing to the diminishing pressure differential between supply pressure and hydride equilibrium pressure, and gradually, the hydride bed attained the cooling fluid temperature.

From Fig. 3.7(a), it can be appreciated that the bed temperature profiles are similar in both reactor configurations. The peak temperatures attained by ECTR configuration were 2.3 °C and 3.6 °C higher than that of TBR configuration under supply pressure of 20 bar and 40 bar, respectively, implying marginally better heat transfer in the initial hydriding stage in the case of TB configuration. However, the cooling rate was slightly faster in the later phase of the hydriding reaction for ECT configuration. This happened because the hydride bed thickness of the TB configuration is higher than ECT configuration, which is responsible for reduced heat transfer in the later reaction phase. Both the configurations attained the cooling fluid temperature of 25 °C at the end of 600 s. The variation in hydrogen storage capacity for the ECTR and TBR configurations at different supply pressures is illustrated in Fig. 3.7(b). At the beginning of hydrogen absorption, the mass transfer driving potential is the highest, which results in fast absorption. As this driving potential weakens over time, the absorption rate slows down, and eventually, the hydride bed attains its maximum storage capacity for the given absorption condition. As it can be seen from Fig. 3.7(b), the initial hydrogen absorption rate is marginally better in the case of TB configuration as compared to the ECT configuration. However, both configurations reached a maximum storage capacity of 1.2 wt.% and 1.24 wt.% at the end of 600 s when subjected to 20 bar and 40 bar supply pressure, respectively.

3.7. Proposed reactor configurations

From the hydrogen absorption performance comparison, it is evident that both TBR and ECTR configurations offer identical hydrogen absorption characteristics. For the considered physical models in this study, the calculated MH weight ratio (ratio of MH alloy weight to empty reactor weight) for TBR configuration is 1.17 times higher than that of the ECTR configuration. Based on the design methodology of TBR and ECTR configurations, a number of lab-scale (up to 3.5 kg alloy) and large-scale (up to 25 kg alloy) MH reactors were devised and fabricated. The design particulars of the reactors are discussed in the subsequent section. The design specification of all the fabricated reactors is shown in Table 3.6.

3.7.1. Design and fabrication of large-scale reactors

TBR configuration

A 19-tube model is proposed, which can hold up to 26.5 kg of alloy. As described in Table 3.1, the standard-sized seamless SS-316 tube (φ 25.4×1.2 mm) was chosen, which offers a bearing pressure of 96 bar with safety factor of 2.

Table 3.6: Design specification of the proposed reactor configurations

Design Parameter	19 TBR	99 ECTR with OCJ	Tube in tube reactor	48 ECTR with OCJ
Designed alloy filling capacity (kg)	33.15	30	3.46	4.4
Actual alloy filling capacity with 20% expansion (kg)	26.5	24	2.77	3.5
Tube outer diameter (mm)	25.4	6.35	*(Inner tube)* 42.6	6.35
Tube thickness (mm)	1.2	0.89	*(Inner tube)* 3.2	0.89
Length of tube (mm)	1000	465	800	160
Number of tubes	19	99	1	48
Shell outer diameter (mm)	186	168.28	*(Outer tube)* 63.5	114.3
Shell thickness (mm)	1.5	7.11	*(Outer tube)* 1	6.02
Jacket outer diameter (mm)	-	192.28	-	141.3
Jacket thickness (mm)	-	2	-	6.55
Total heat transfer surface area (m^2)	1.37	1.16	0.11	0.21
Total tube weight (kg)	13.51	2.62	2.47	1.27
Shell weight (kg)	6.78	13.06	1.82	2.55
Weight of outer jacket (kg)	-	4.33	-	3.46
Weight of reactor (including shell, tubes and jacket)	20.29	20	4.29	7.28
MH weight ratio	1.31	1.2	0.64	0.48

The length of each MH tube was considered to be 1 m, which holds approximately 1.7 kg MH alloy. Total of 19 tubes were organizationally positioned in two circular stacks and at the centre. The first and second stacks contained 6 and 12 tubes, respectively, whereas one tube was positioned in the middle. The designed tube pitch ratio was 1.35, which falls under the recommended range issued by Tubular Exchanger Manufacturers Association. Sintered porous SS 316 disc filters (φ 25×3 mm) of 2 µm porosity were welded on the top of each of these tubes to refrain MH powders inside the tubes. Hydrogen gas would be supplied/collected from a common chamber via a branched 1/4-inch SS-316 tube. The MH tubes were welded on the front and rear tube sheets. Nineteen Swagelok tube fittings (SS-400-1-4W) were welded on the end closing plate corresponding to each MH tube to accommodate thermocouples and pressure transducer and also to facilitate MH powder filling. The model sectional view and photograph of the fabricated unit are displayed in Fig.3.8.

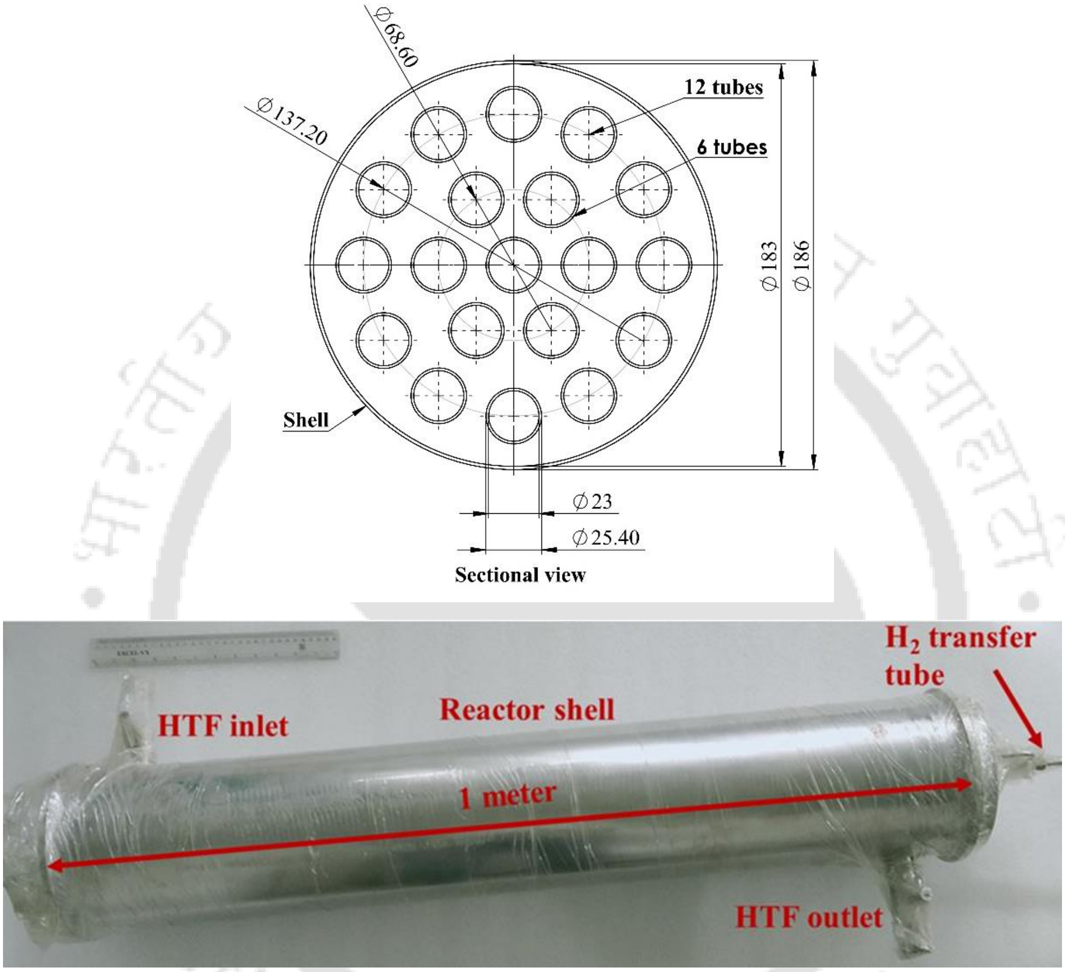

Fig. 3.8: (a) 19-TBR model sectional view and (b) photograph of the fabricated unit.

ECTR configuration

A 99 ECT model with an outer cooling jacket (OCJ) is proposed, which can hold up to 25 kg of alloy. As designated in Table 3.2, a total of 99 tubes are embedded evenly inside the shell yielding a maximum distance between two tube surfaces of 7.3 mm only. The shell dimension (φ 168.28×7.11 mm) is chosen to ensure a maximum bearing pressure of 86 bar with a Factor of Safety of 2. The length of the shell was determined as 465 mm to accommodate around 25 kg alloy considering a filling density of 4200 kg.m^{-3} and 20% expansion volume. A tubular (φ 14×2 mm) porous filter (porosity 2-µm) was positioned in the middle to refrain the powder particles from getting out of the containment and to facilitate even distribution of hydrogen along the length of the reactor.

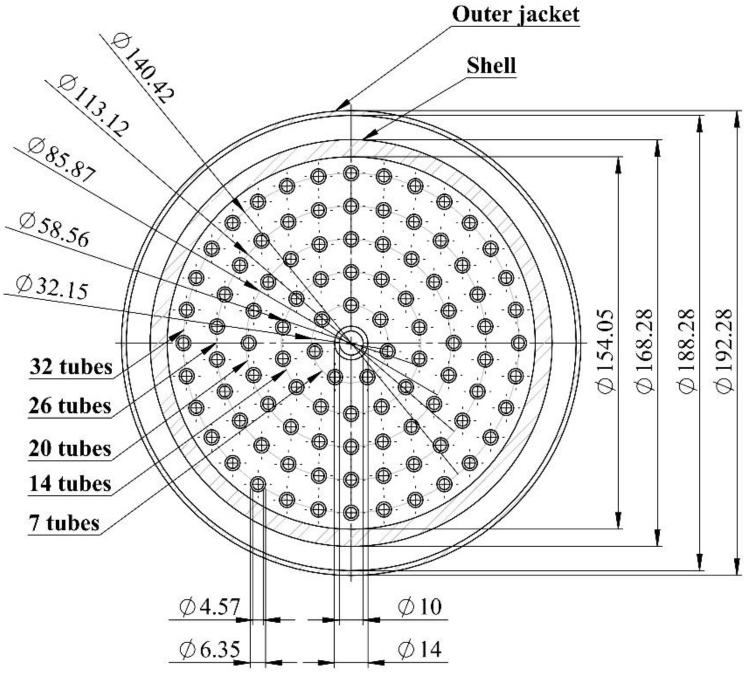

Sectional view

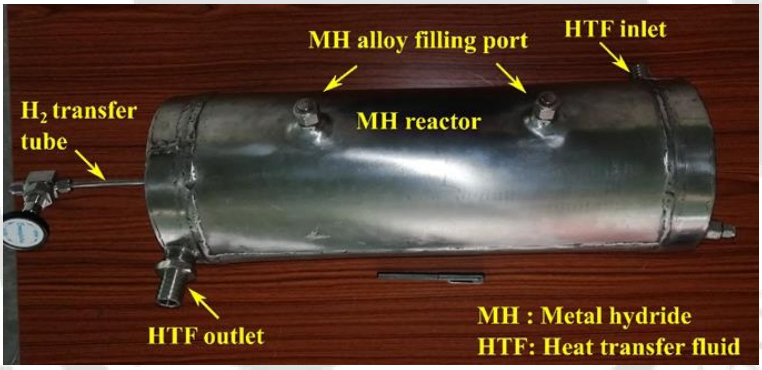

Fig. 3.9: (a) 99 ECTR-OCJ model sectional view and (b) photograph of the fabricated unit.

To maximize the heat transfer around the reactor wall, an outer jacket of 10 mm HTF flow passage was provided. The complete reactor was constructed using SS-316. The reactor was equipped with two 1/2-inch ports for MH alloy filling and three 1/4-inch ports for thermocouple and pressure transducer fitting. The model sectional view and the photograph of the fabricated unit are shown in Fig. 3.9.

3.7.2. Design and fabrication of lab-scale reactors

Tube-in-tube reactor configuration

A simple concentric tube reactor is designed, which can hold approximately 2.8 kg alloy. The design is similar to TBR configuration except that TBR contains multiple MH tubes. In this reactor, the inner tube dimension was chosen (φ 42.6×3.2) to provide a working pressure of 154 bar with factor of safety 2. Whereas, the outer tube dimension was φ 63.5×1 mm. The length of the inner tube and outer tube was 800 mm and 780 mm, respectively. One end of the inner tube was welded with a sintered porous disc filter (2 µm), and the other end was welded with a circular plate attached with tube fittings (1/4-inch) for alloy filling and thermocouple fitting. The inner tube and outer tube materials were SS-316 and SS-202, respectively. The sectional view and the photograph of the fabricated unit are shown in Fig. 3.10.

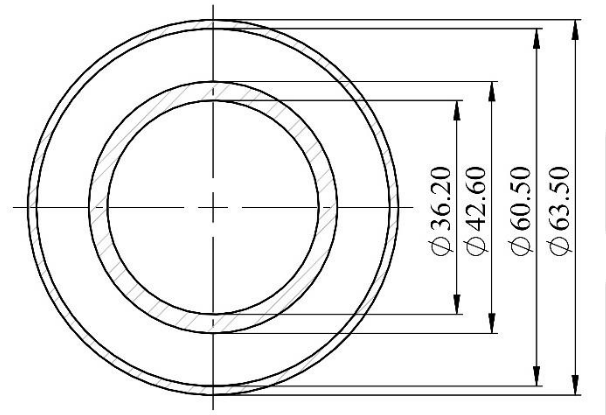

Sectional view

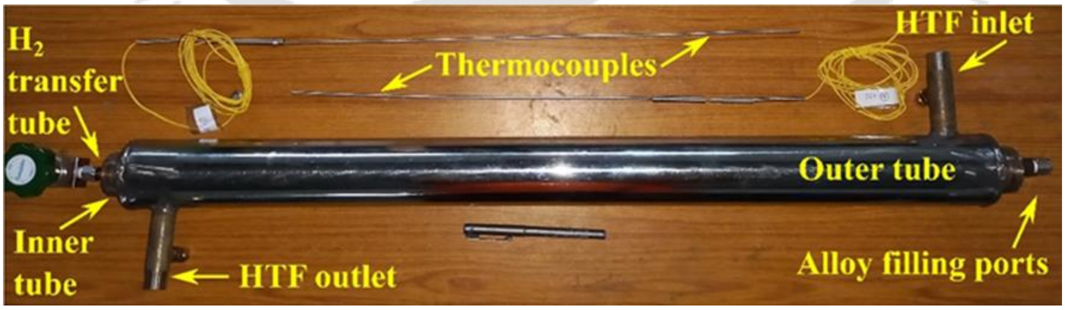

Fig. 3.10: (a) Tube-in-tube reactor model sectional view and (b) photograph of the fabricated unit.

ECTR configuration

A 48 ECT model with an outer jacket is proposed, which can hold up to 3.5 kg alloy. In this reactor, a total of 48 tubes are arranged in a circular conformation inside the shell to ensure the even distribution of heat transfer surfaces within the MH bed. A sintered porous tube of 2 µm porosity was positioned at the centre to facilitate hydrogen transfer to and from the MH bed. The material of construction of all the reactor components, including the porous filter element, is chosen as SS-316. The reactor is equipped with two 1/4-inch ports for attaching metal-sheathed thermocouples and a 1/2-inch port for MH alloy filling. The sectional view and the photograph of the fabricated unit are shown in Fig. 3.11.

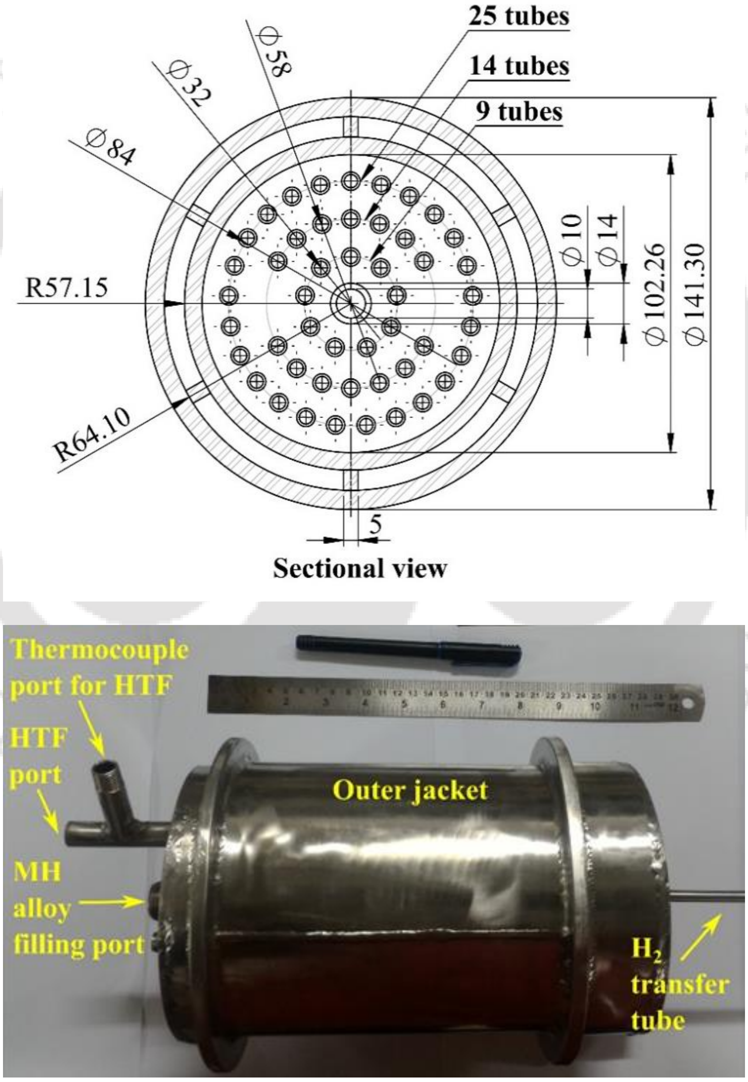

Fig. 3.11: (a) 48 ECTR-OCJ model sectional view and (b) photograph of the fabricated unit.

3.8. Summary

In this chapter, the design basis of the metal hydride reactors used for experiments is deliberated step by step. The design basis is primarily established on the criteria of heat load and rate of heat transfer necessitated by the metal hydride reactor. Two basic cylindrical shell and tube heat exchangers, namely the tube bundle configuration and the embedded tube configuration, have been explored considering mechanical strength, MH bed thickness, alloy filling capacity, ease of manufacturing, portability and operational ease. The design of the reactor configurations is supported by simulation predictions. The TBR and ECTR configurations are predicted to offer similar heat transfer and hydrogen absorption performance subjected to identical operational conditions. Further, the design methodology of the TBR and ECTR has been exploited to design a number of lab-scale and large-scale metal hydride reactors.

4. Experiments on MH based hydrogen storage systems

4.1. Introduction

Following by design and fabrication of the MH reactors stated in the preceding chapter, in this chapter, the hydrogen storage experiments carried out on both large-scale and lab-scale MH reactors are presented. The studies are divided into three categories based on the reactor used for experiments.

4.2. Experiments on 19-TBR module

4.2.1. Description of MH alloy

The MH alloy used in this experiment is AB_5 type; the exact composition is $La_{0.8}Ce_{0.2}Ni_5$. The PCT data is reflected in Fig. 4.1. The alloy was procured from M/s Zhongke Scientific & Technical Co., Ltd., China. It has excellent hydrogen absorption and desorption characteristics in the near ambient temperature. It was originally received in the form of small chunks (3-6 mm) which were ball milled to obtain powdered form (150-200 µm) before filling inside the reactor. Each of the MH tubes was filled with 1.35 kg of the alloy, constituting 26.5 kg powder packed inside the reactor.

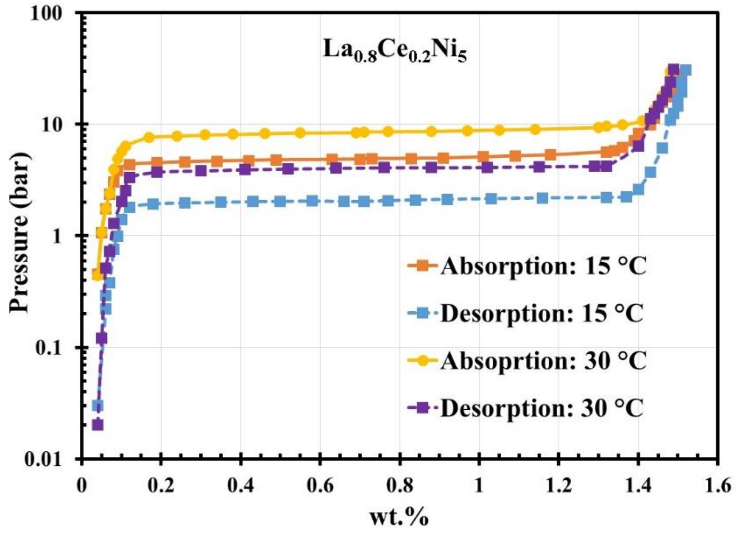

Fig. 4.1: PCT data of $La_{0.8}Ce_{0.2}Ni_5$.

4.2.2. Components of the experimental setup

The experimental facility consists of an MH reactor, gas flow circuit, HTF flow circuit, mass flow meter, vacuum pump, constant temperature HTF baths, argon and hydrogen cylinder, HTF flowmeters and data acquisition unit (DAQ). The photograph of the experimental setup indicating the major components is portrayed in Fig. 4.2. The gas flow circuit is made of bellow-sealed valves,1/4-inch braided SS-316 hoses, 1/4-inch SS-316 tubes, and tube fittings. Likewise, the HTF flow circuit is made of 1-inch flexible PVC hoses, two constant temperature baths (cold and hot), a flowmeter, ball valves, and necessary tube fittings. A Coriolis mass flow meter (accuracy ± 0.35% of measured quantity) is engaged in the gas circuit to measure the mass flow rate of the hydrogen inflowing or outflowing the MH reactor. A rotary vacuum pump is utilized to degas the gas circuit and the MH reactor down to a vacuum of 6.5 Pa (abs). Temperature and pressure readings are monitored at an interval of 1 s, using the DAQ connected to a computer. Water is used as HTF throughout the experimental study. For temperature measurement, six ‘K type’ thermocouples (TC1, TC2: 750 mm, TC3, TC4: 500 mm, TC5, TC6: 350 mm) were placed in six MH tubes of the outermost stack of the 19 TBR; also, an additional pair of ‘K type’ thermocouple was used to measure the inlet and outlet temperature of the HTF. For pressure measurement, a gauge pressure transducer (PT: 0-100 bar) was fitted to one of the weld fittings. Figure 4.3 shows the pictorial views of the 19 TBR module and the positions of the thermocouples and pressure transducer.

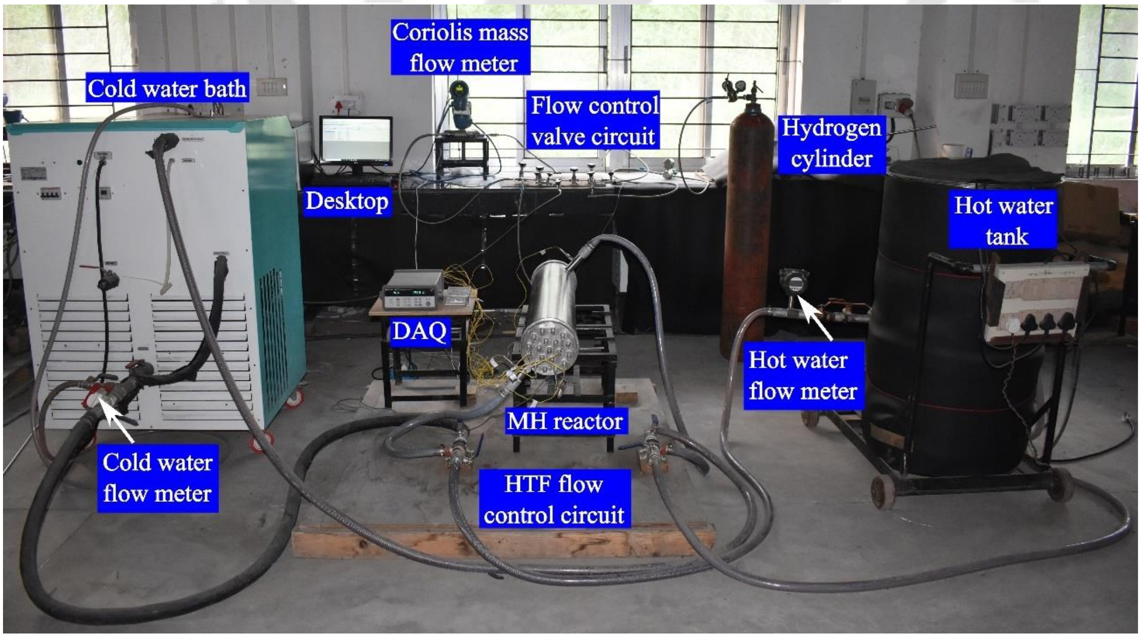

Fig. 4.2: Photograph of the experimental setup of 19 TBR module.

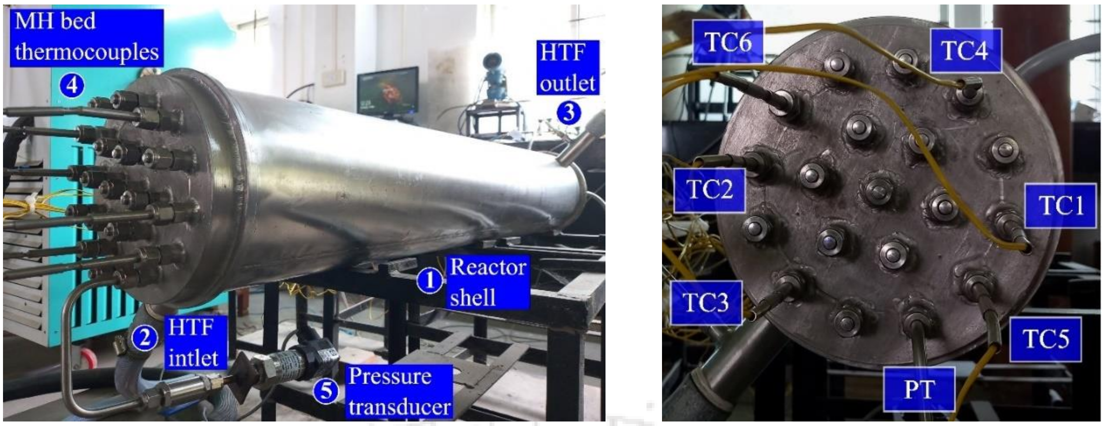

Fig. 4.3: (a) Photograph of the 19 TBR module and (b) position of thermocouples and pressure transducer.

4.2.3. Description of the experimental protocol

Prior to conducting experiments, the MH reactor and the gas circuit were verified for leak-sealing using argon gas at 60 bar and kept for 24 h. The experiments consist of two balancing cycles, i.e., absorption and desorption. The diagrammatic illustration of the experimental setup is demonstrated in Fig. 4.4.

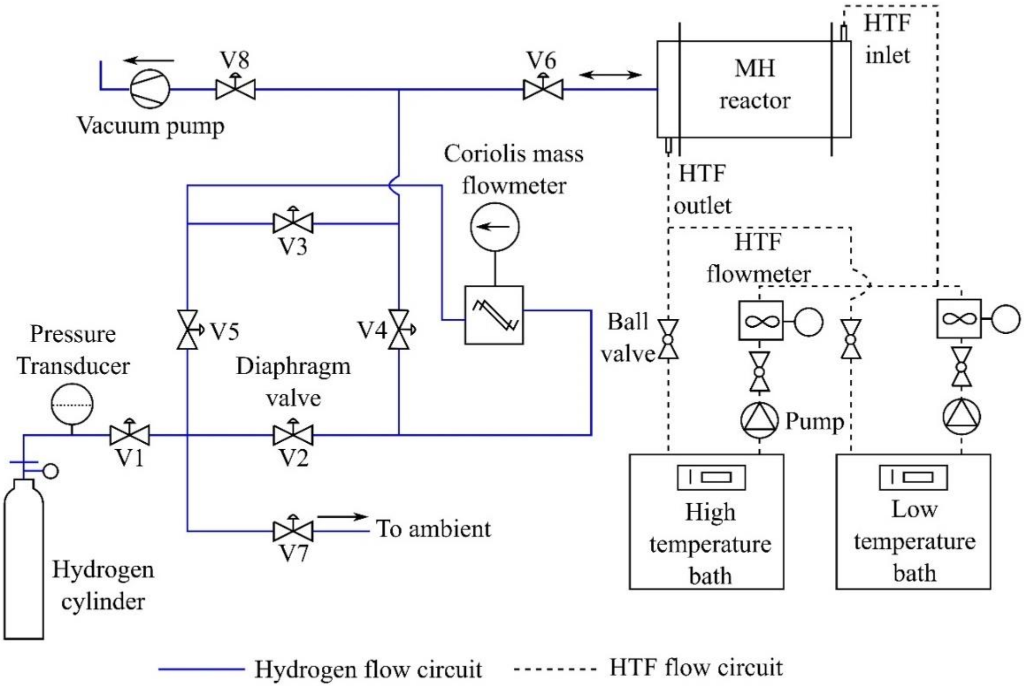

Fig. 4.4: Diagrammatic representation of the experimental setup.

Before absorption begins, the MH bed is maintained at an intended temperature by flowing water from the low-temperature bath. The supply pressure is set using the cylinder regulator and a pressure transducer connected to the gas circuit. In the course of absorption, the valves V1, V2, and V3 are opened, whereas the rest of the valves are shut. Absorption initiates as soon as the reactor valve (V6) is opened. The end of absorption is prominently indicated by the falling mass flow rate as recorded by the mass flow meter and also the shrinking difference between the HTF temperatures at the inlet and exit. After completion of absorption, the valves V6, V1, V2, and V3 are shut. Before desorption could take place, the MH bed is sensibly heated to an intended temperature and maintained thereafter by flowing water from the high-temperature bath. In the course of desorption, the valves V4, V5, and V7 are opened, and all other valves are closed. Desorption is initiated as soon as the reactor valve (V6) is opened, and the gas is sent out to the ambient. Similar to the absorption case, completion of desorption is markedly indicated by the dipping rate of mass flow and near-zero temperature difference between HTF inflow and outflow. After completion of desorption, the valves V6, V4, V5, and V7 are shut. The successive sequences of absorption-desorption tests are carried out accordingly.

4.2.4. Activation of the MH alloy

To begin activation, the MH reactor was first heated to 70 °C, and outgassed using the vacuum pump to a value of 6.5 Pa (abs). The first hydrogen charging was carried out at 40 bar and 10 °C. Thereafter, it was again heated to 70 °C and evacuated to 6.5 Pa (abs). During the 3rd absorption cycle, the MH alloy took in 379.62 g hydrogen resulting in 1.43 wt.% storage. Alloy activation was concluded in 4 sequential absorption/desorption phases. In the fourth absorption, the absorbed quantity of hydrogen was 385.75 g.

4.2.5. Hydrogen storage characterization of the reactor

Hydrogen absorption behaviour

The hydrogen absorption behaviour of the MH reactor at 20 bar, 20 °C absorption condition is illustrated in Fig. 4.5. At this absorption condition, the MH reactor absorbed 369.08 g hydrogen within 1372 s. As shown in Fig. 4.5(a), the hydrogen supply pressure falls from 20 bar to 8.5 bar within 4 s owing to the filling of hydrogen gas within the large volume of the storage vessel resulting from the initial hefty pressure differential. At this moment, the hydrogen absorption rate gains momentum, and it continues till around 45 s, and gas pressure within the reactor is yet to increase. Thereafter, as the hydrogen supply pressure is fully restored to its initial set value, it results in a large pressure differential and causes rapid absorption. However, as the quantity of absorbed mass increases, the reactor pressure again increases, leading to shrinking rate of absorption. The rate of absorption further shrinks continuously as absorption progresses, and by the end of the absorption process, it becomes almost zero.

The hydrogen absorption behaviour can also be understood from the temperature profiles of the MH bed and the HTF. As the absorption reaction is initiated, enormous heat is liberated which causes the MH bed temperature to escalate (Fig. 4.5(b)). The highest bed temperature recorded by TC5 was 42.4 °C at 207 s. Nevertheless, the highest temperature difference between the HTF outlet and the inlet was recorded to be 6.1 °C at 223 s.

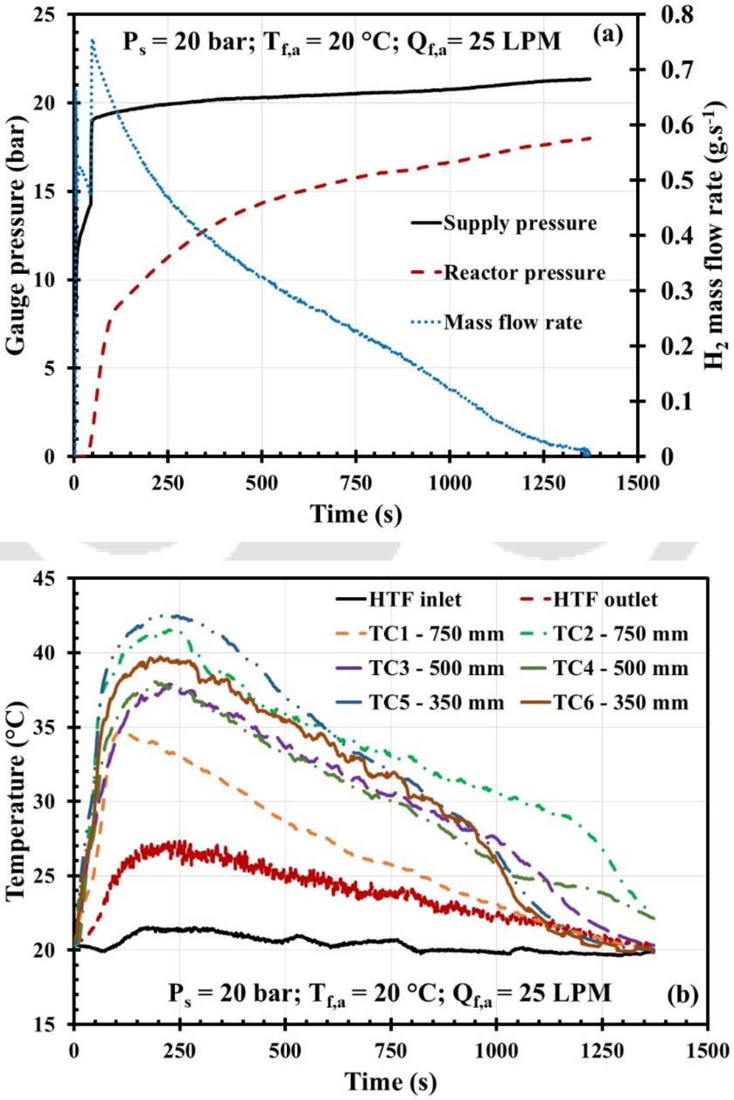

Fig. 4.5: Depiction of absorption characteristics (a) variation of pressure and mass flow rate and (b) variation of temperature.

As the absorption reaction moved forward, due to the continuously dropping absorption rate, the rate of heat generation also reduced, and bed temperatures gradually came down and almost attained the HTF inlet temperature. The temperature profile recorded by the thermocouples at different axial locations shows that heat transfer within the reactor along the length is almost uniform.

Hydrogen desorption behaviour

The hydrogen desorption behaviour of the MH reactor at 50 °C HTF temperature is shown in Fig. 4.6. Before the beginning of desorption, the reactor pressure was recorded to be around 38 bar.

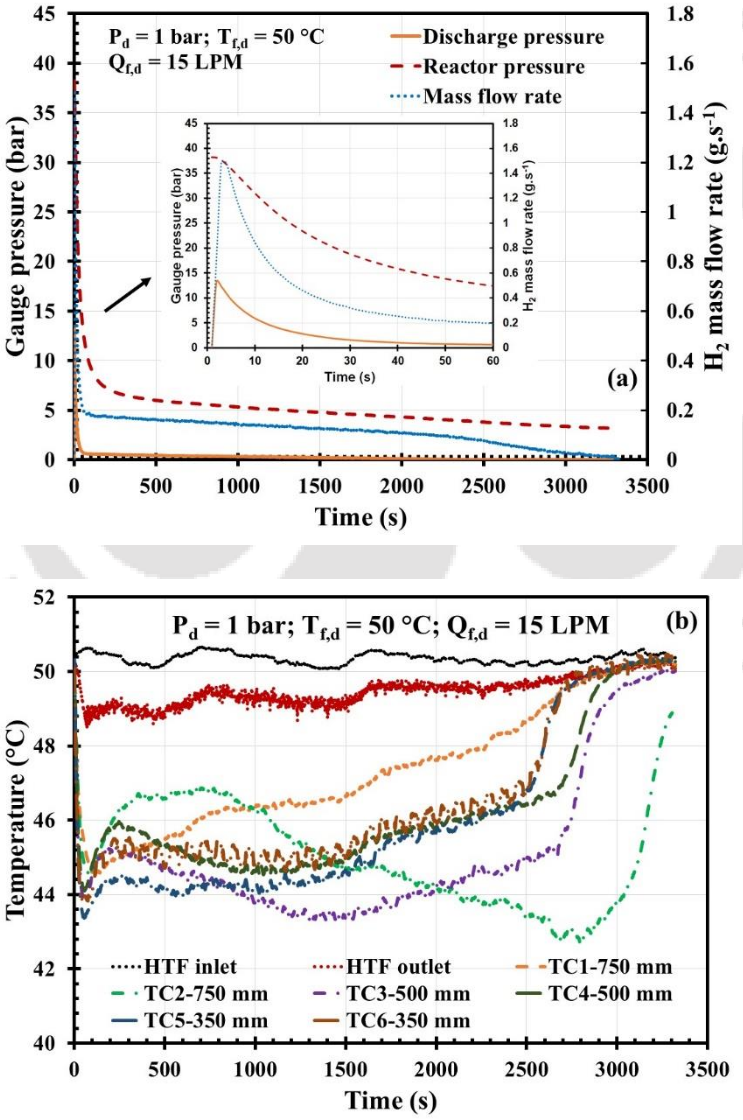

Fig. 4.6: Depiction of desorption characteristics (a) variation of pressure and mass flow rate and (b) variation of temperature.

As desorption started, the reactor pressure drops to 31 bar within 10 s, whereas the discharge line pressure increases from 0 to 13 bar within 1 s and then reduced to 5.9 bar within 10 s. The maximum rate of hydrogen desorption recorded was 1.49 $g.s^{-1}$ at 3 s. By the end of 10 s, the rate of desorption dropped to 0.84 $g.s^{-1}$. As desorption progresses, due to removal of hydrogen from the reactor, the bed pressure decreases continuously which decelerates the rate of desorption. At the end of the desorption, the recorded reactor pressure was 3.2 bar, whereas the discharge line pressure was maintained at a pressure slightly above zero (not captured by the pressure transducer). At this desorption condition, the amount of hydrogen desorbed by the reactor was 377.51 g within 3322 s. The significance of hydrogen desorption is also translated in the temperature profile of the MH bed as well as HTF temperature (inlet and outlet) as can be seen in Fig. 4.6(b). During the initial phase of desorption, the lowest MH bed temperature recorded by TC5 was 43.3 °C (at 55 s). However, the lowest temperature recorded during the entire desorption period was 42.6 °C by TC2 at the end of 2796 s. This phenomenon signifies that the MH tube where TC2 was fitted was among the last to complete desorption. The largest temperature drop from inlet to outlet section during desorption was recorded to be 2.1 °C at 67 s.

4.2.6. Parametric study

A set of experiments were conducted to assess the influence of operating parameters on hydrogen absorption and desorption. The designated operating parameters and their operation range are provided in Table 4.1.

Table 4.1: Scheme of the parametric study for 19 TBR module

Process	Operating parameter	Range	Remarks
Absorption	Supply Pressure (P_s):	5-20 bar	HTF temperature ($T_{f,a}$) set at: 20 °C; HTF flow rate ($Q_{f,a}$) set at: 25 LPM
	HTF temperature ($T_{f,a}$):	10-30 °C	Supply Pressure (P_s) set at: 15 bar; HTF flow rate ($Q_{f,a}$) set at: 25 LPM
Desorption	HTF temperature ($T_{f,d}$):	40-70 °C	Desorption Pressure (P_d) set at: 1 bar; HTF flow rate ($Q_{f,d}$) set at: 15 LPM

Influence of supply pressure alteration on absorbed mass and rate of required cooling

Figure 4.7 shows the effect of supply pressure variation on the amount of hydrogen absorbed and the rate of cooling required. As supply pressure was varied from 5-20 bar, the absorption condition was set at 20 °C, 25 LPM. At 5 bar supply pressure, the MH reactor absorbed 99.72 g hydrogen within 5228 s, which corresponds to 0.39 wt.%. When supply pressure was ramped to 5 bar to 10 bar, the quantity of absorbed hydrogen increased by approximately 3.5 times, with a reduction in absorption time by 1.15 fold.

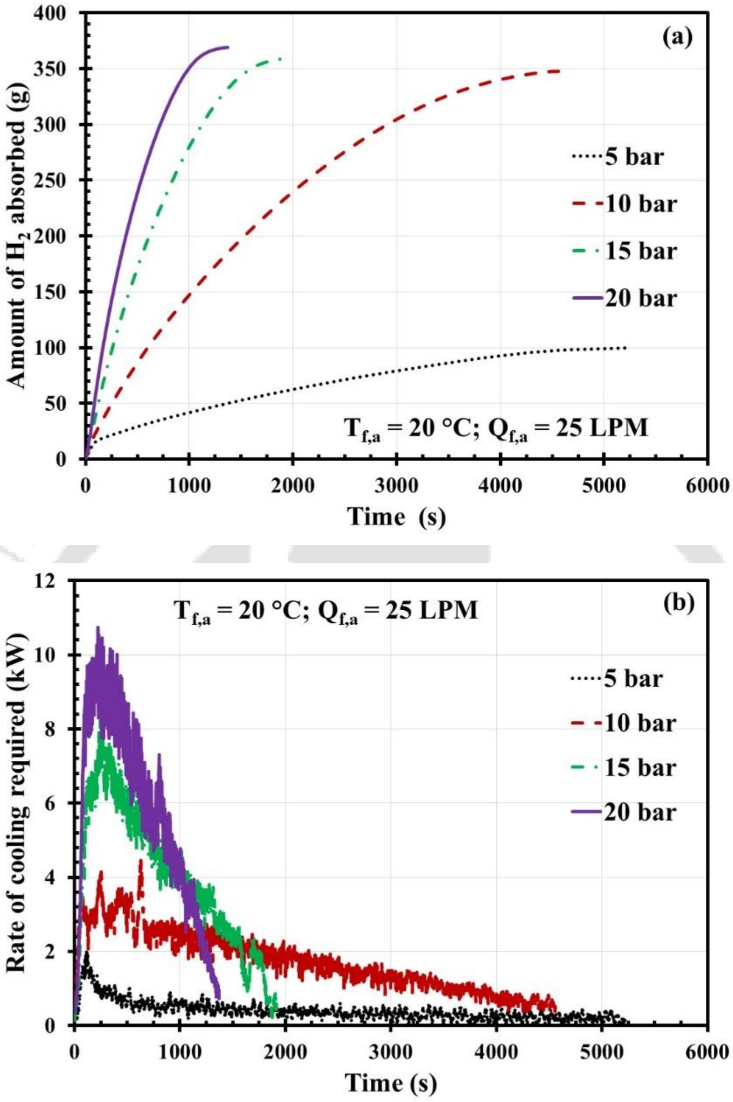

Fig. 4.7: Influence of supply pressure on (a) absorbed mass (b) rate of required cooling.

With a further boost in supply pressure from 10 bar to 15 bar and 20 bar, absorbed hydrogen amount was increased by merely 3.3% and 6.2%, individually; however remarkable reductions in absorption time (58% and 70%, correspondingly) were observed (Fig. 4.7 (a)). With an increase in hydrogen supply pressure, the quantity of hydrogen absorbed also increases till the maximum hydrogen storage capacity at that given temperature is reached. Also, the rate of hydrogen absorption is faster at higher supply pressure owing to the greater pressure difference between supply pressure and equilibrium pressure.

The rate of cooling needed for hydrogen absorption at altered feed pressures are presented in Fig. 4.7(b). The peak rates of cooling required were 2 kW, 4.4 kW, 8.4 kW and 10.7 kW, respectively, at 5,10, 15 and 20 bar. However, the average rates of required cooling were 0.4 kW, 1.7 kW, 3.9 kW and 5.6 kW, respectively. At elevated feed pressure, the peak rate of required cooling increases as the absorption rate of hydrogen increases, and therefore the heat generation rate is also increased.

Influence of HTF temperature alteration on absorbed mass and rate of required cooling

Figure 4.8 shows the influence of HTF temperature variation on the amount of hydrogen absorption and rate of required cooling.

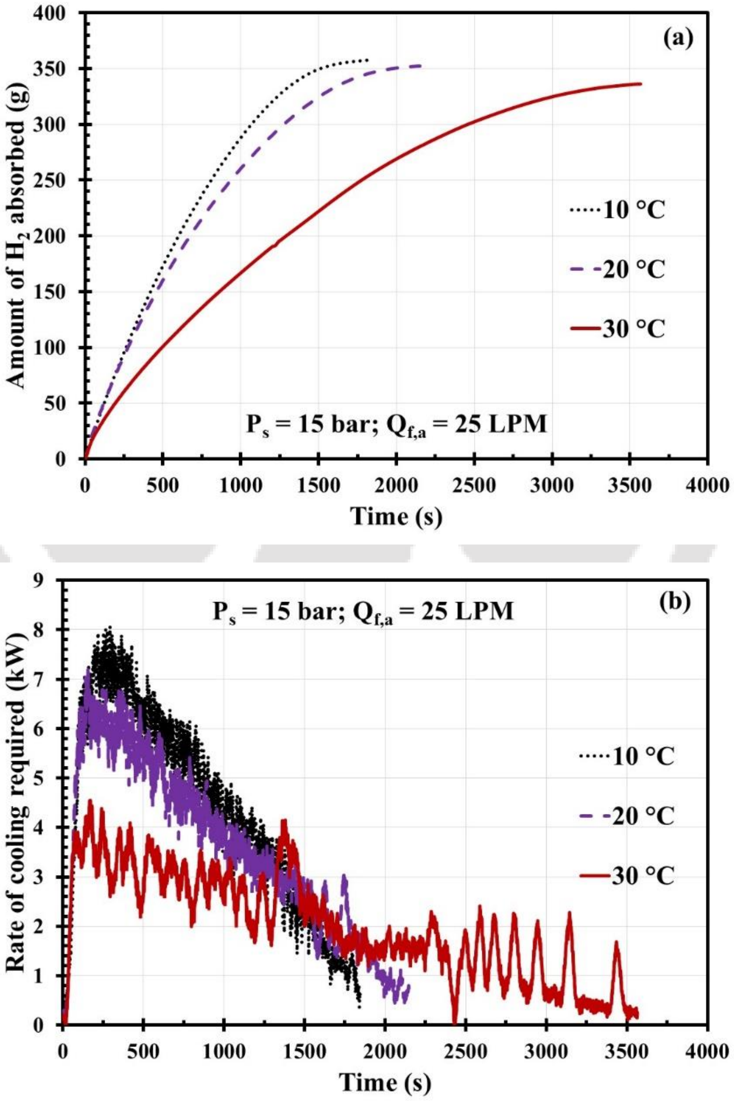

Fig. 4.8: Influence of HTF temperature alteration on (a) absorbed mass and (b) rate of required cooling.

While evaluating the effect of HTF temperature variation on absorption performance, the absorption condition was set at 15 bar, 25 LPM. At 20 °C, the amount of hydrogen absorbed was 352.25 g in 2150 s. When HTF temperature was reduced to 10 °C, the increment in the amount of hydrogen stored was only 1.6%, while absorption time was reasonably reduced by 14.2%. On the other hand, when HTF temperature was increased from 20 °C to 30 °C, the reduction in the absorbed amount of hydrogen was 4.5% although a whooping increase of nearly 40% in absorption time was witnessed (Fig. 4.8(a)). The influence of HTF temperature alteration on required rate of cooling is reflected in Fig. 4.8(b). The peak rates of the required cooling rate at 10 °C, 20 °C and 30 °C were 8 kW, 7.2 kW and 4.5 kW, correspondingly. While, the average rate of required cooling was estimated to be 4.3 kW, 3.5 kW and 2 kW, respectively at 10 °C, 20 °C and 30 °C. At any given supply pressure, the peak rate of required cooling goes down with an increase in absorption temperature owing to a reduction in peak hydrogen absorption rate.

Influence of HTF temperature alteration on desorbed mass and rate of required heating

Figure 4.9 elucidates the influence of HTF temperature alteration on the amount of hydrogen desorbed and rate of heating required. While weighing the impact of HTF temperature, the desorption pressure was set to 1 bar (i.e., reactor outlet was open to the atmosphere) and the flow rate of the HTF was set to 15 LPM. At 50 °C HTF temperature, the amount of hydrogen desorbed was 350.56 g in 4740 s. In due course, as the temperature of HTF was raised to 50 °C, 60 °C and 70 °C, the desorbed quantity of hydrogen stayed almost equal (± 1% variation) while the time required for desorption reduced massively by 31%, 49.5% and 63.4%, respectively (Fig. 4.9(a)). With a rise in HTF temperature, it is anticipated that the rate of hydrogen desorption will increase; however, such ample reduction in desorption periods at elevated temperatures is explained with the interpretation of reactor pressure and mass flow rate data in Fig. 4.10. The required rate of heating required at altered HTF temperatures is illustrated in Fig. 4.9(b). The highest rates of heating required for desorption at 40 °C, 50 °C, 60°C and 70 °C were 1.58 kW, 1.72 kW, 2.3 kW and 3.16 kW accordingly. Whereas the average rate of heating required at 40 °C, 50 °C, 60 °C and 70°C were 0.64 kW, 0.8 kW, 1.24 kW, 1.72 kW, respectively. The peak rate of heating required for hydrogen desorption at any given hot fluid temperature is an important parameter which not only decides the heater capacity but also determines the storage efficiency of the system, which has been deliberated in the subsequent section.

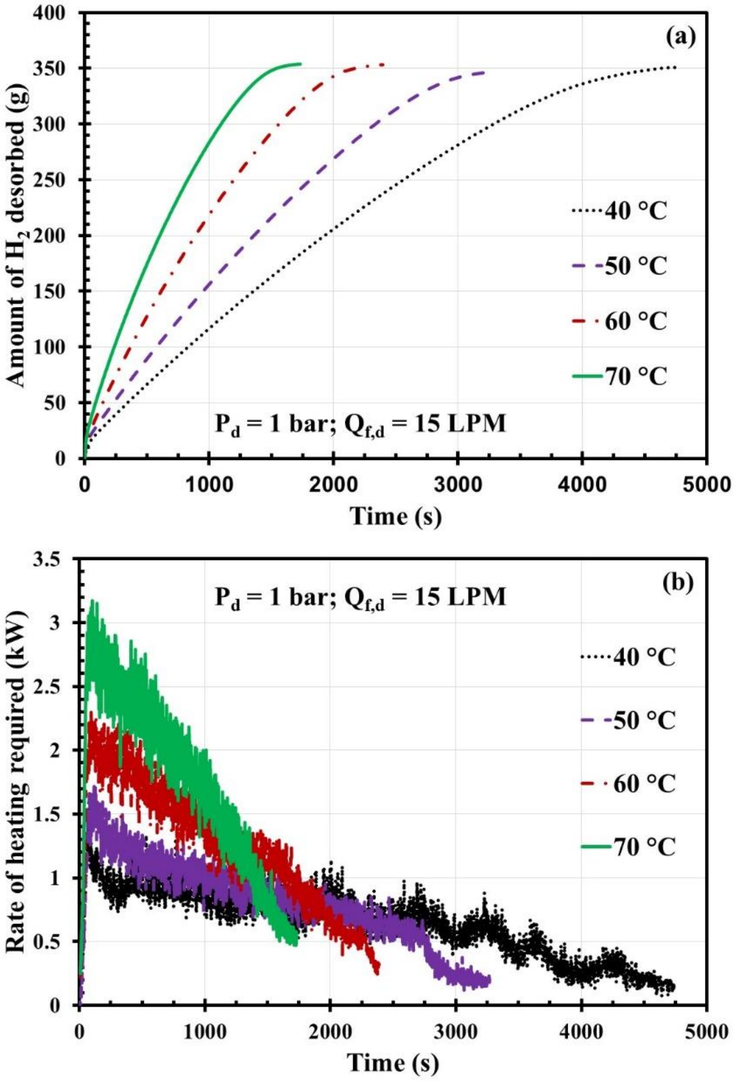

Fig. 4.9: Influence of HTF temperature alteration on (a) desorbed mass and (b) rate of required heating.

Influence of HTF temperature alteration on reactor pressure and mass flow rate during desorption

Figure 4.10 shows the influence of HTF temperature alteration on reactor pressure and desorption mass flow rates. As the MH reactor is taken (sensible heating) to desired hot fluid temperature after completion of absorption, the bed pressure rises exponentially as per van't Hoff law. Before the commencement of desorption, the measured gauge pressures at HTF temperatures 40 °C, 50 °C, 60 °C and 70°C were 21.6 bar, 32.6 bar, 38 bar and 54.9 bar, respectively (Fig. 4.10(a)). As desorption started, within the first 60 s, the reactor pressure dropped to 11.68 bar (40 °C), 14.36 bar (50 °C), 15.06 bar (60 °C), and 17.54 bar

(70 °C), respectively. Such a drastic drop in reactor pressure occurs owing to very high initial desorption rates, as witnessed in Fig. 4.10(b).

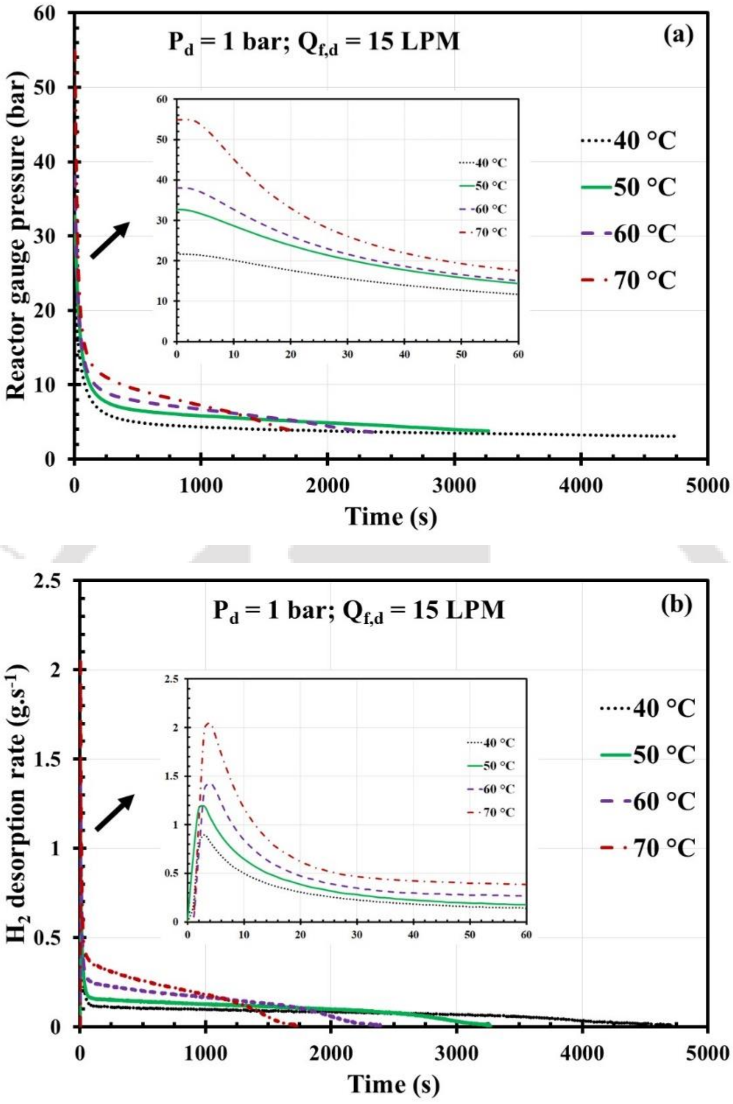

Fig. 4.10: Impact of HTF temperature alteration on (a) reactor pressure and (b) desorption rate.

The initial maximum desorption rate recorded at 40 °C, 50 °C, 60 °C and 70 °C were 0.89 g.s^{-1} (3 s), 1.18 g.s^{-1} (3 s), 1.43 g.s^{-1} (4 s), 2.05 g.s^{-1} (4 s). Within 60 s, the desorption rates descended to 0.139 g.s^{-1}, 0.177 g.s^{-1}, 0.269 g.s^{-1}, 0.387 g.s^{-1}, correspondingly. The recorded reactor pressure at the end of desorption were 3.05 bar (40 °C), 3.79 bar (50 °C), 3.60 bar (60 °C), and 3.82 bar (70 °C), respectively. The average mass flow rate achieved during desorption at 40 °C, 50 °C, 60 °C and 70 °C were 0.075 g.s^{-1}, 0.107 g.s^{-1}, 0.148 g.s^{-1} and 0.205 g.s^{-1}. The drop in bed pressure and mass flow rate with time is only logical as the amount of hydrogen is a finite quantity. With the realized average mass flow rate at 40 °C, a 4.6 kW low temperature polymer electrolyte membrane fuel cell (LT-PEMFC) could be run for 4740 s (if desorbed by means of a mass flow controller). The mass flow rate requirement for PEMFC for rated power output has been estimated using the following equation (Larminie and Dicks, 2013).

$$\dot{m}_{H_2} = 1.05 \times 10^{-8} \times \frac{P_e}{V_c} \tag{4.1}$$

In Eq. (4.1), 'P_e' and 'V_c' denotes electrical power of the fuel cell stack in watts and average cell voltage of the stack.

4.2.7. Energy efficiency of hydrogen storage

The hydrogen storage efficiency of any storage system can be stated as the fraction of energy obtained from the system (energy output) to the energy provided to the system (energy input). The energy output is essentially the product of the amount of hydrogen delivered by the system and its calorific value. Whereas, the energy input comprises of the energy content (product of mass and calorific vale) of the stored amount, energy required to store the hydrogen as well as energy required to deliver the stored hydrogen. While accounting for any electrical energy input during operation of the system (e.g. pumps, chiller etc.), conversion to equivalent amount of thermal energy has been performed by including overall utilization efficiency (η_{ut}) at user point and the coefficient of performance of the chiller (COP_c). During the course of the calculation, the values of 'COP_c' and 'η_{ut}' are assumed as 7 and 0.2, respectively. The different energy contents are quantified as follows:

Energy output: $E_{out} = \dot{m}_{H2,out}\, LHV_{H2}$ (4.2)

Energy input: $E_{in} = \dot{m}_{H2,in}\, LHV_{H2}$ (4.3)

Energy required to store hydrogen

The temperature at which hydrogen is stored contributes to the energy efficiency of the storage system. In the present work, the reference absorption temperature is considered as 20 °C, which is below the ambient temperature (25 ± 2 °C). Hence, the amount of energy required to sensibly cool the MH reactor from ambient temperature to 20 °C and thereby to maintain the absorption temperature during the complete absorption period has been accounted in the energy demand. However, if the absorption is performed at ambient temperature, no external cooling is required.

$$E_{st} = E_{sc} + E_a + E_{pump,st} \tag{4.4}$$

$$= \frac{1}{COP_c\left(\eta_{ut}\right)}\left[\int_{t_{sc}+t_{cy,a}} \dot{m}_f c_{p,f}\left[T_{f,out}(t) - T_{f,in}(t)\right]dt\right] + \frac{1}{\eta_{ut}}\left(\int_{t_{sc}+t_{cy,a}} P_{pump}\,dt\right)$$

$$= \frac{\dot{m}_f c_{p,f}}{COP_c\left(\eta_{ut}\right)}\left[\int_{t_{sc}}\left[T_{f,out}(t) - T_{f,in}(t)\right]dt + \int_{t_{cy,a}}\left[T_{f,out}(t) - T_{f,in}(t)\right]dt\right] + \frac{P_{pump}}{\eta_{ut}}\left(t_{sc} + t_{cy,a}\right)$$

Energy required to deliver hydrogen

$$E_{del} = E_{sh} + E_d + E_{pump,del} \tag{4.5}$$

$$= \int_{t_{sh}+t_{cy,d}} \dot{m}_f c_{p,f}\left[T_{f,in}(t) - T_{f,out}(t)\right]dt + \frac{1}{\eta_{ut}}\left(\int_{t_{sh}+t_{cy,d}} P_{pump}\,dt\right)$$

$$= \dot{m}_f c_{p,f}\left[\int_{t_{sh}}\left[T_{f,in}(t) - T_{f,out}(t)\right]dt + \int_{t_{cy,d}}\left[T_{f,in}(t) - T_{f,out}(t)\right]dt\right] + \frac{P_{pump}}{\eta_{ut}}\left(t_{sh} + t_{cy,d}\right)$$

Energy efficiency

$$\eta_{st} = \frac{E_{out}}{E_{in} + E_{st} + E_{del}} \times 100\% \tag{4.6}$$

The following assumptions were considered while evaluating the energy efficiency:

1. Quantity of hydrogen absorbed is equal to the quantity of hydrogen desorbed.
2. The density, specific heat capacity and viscosity of the HTF does not change in the working temperature range.
3. Pump power does not vary within the operating temperature.

Hydrogen absorption condition corresponding to each desorption was considered at 15 bar, 20 °C, and 25 LPM. To measure the pump power consumption, an energy meter was used. The measured pump power during absorption at 25 LPM was nearly 0.37 kW, while during desorption at 15 LPM (40-70 °C), it was nearly 0.35 kW.

Influence of HTF temperature alteration on energy efficiency

Energy efficiency at different HTF temperatures is presented in Fig. 4.11. The estimated efficiency at 40 °C was 0.646. When HTF temperature was increased to 40 °C, 50 °C, 60

°C and 70 °C, the efficiency values were reduced to 0.639, 0.616 and 0.586, respectively. Such observation is coherent as the amount of sensible heat required for desorption at higher temperatures increases significantly. The increment in sensible heat increased by roughly 2.2 fold, 3.7 fold and 5.4 fold, respectively, when HTF temperature was raised from 40 °C, 50 °C, 60 °C and 70 °C.

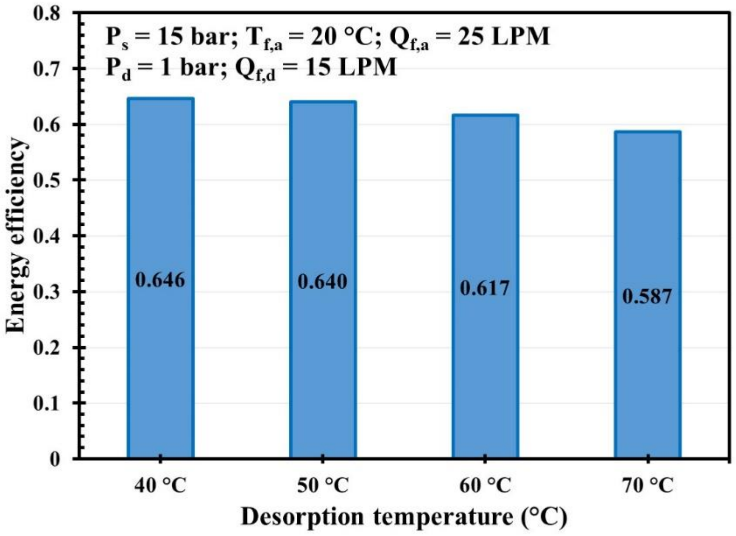

Fig. 4.11: Influence of HTF temperature alteration on energy efficiency.

Influence of partial desorption on energy efficiency

Figure 4.12 portrays the influence of partial desorption on the energy efficiency of hydrogen storage.

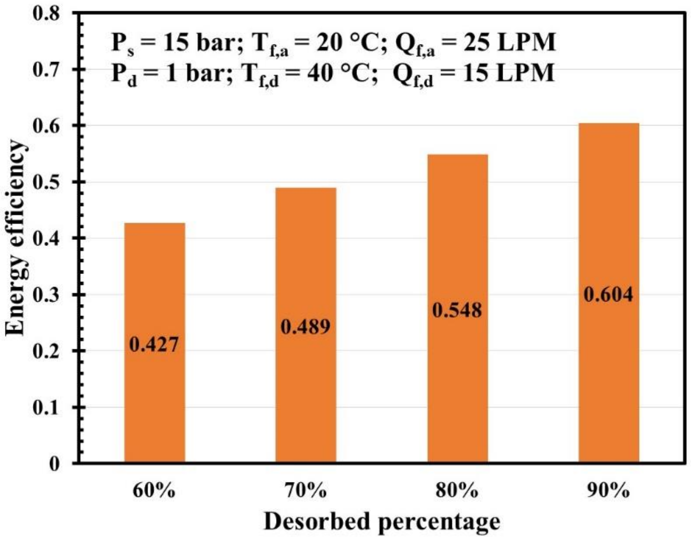

Fig. 4.12: Influence of partial desorption on energy efficiency.

The desorption case considered was 40 °C, 15 LPM corresponding to absorption at 15 bar, 20 °C, 25 LPM. Against the base case desorption of 350.56 g at 40 °C, the corresponding amount of partial hydrogen desorbed was approximately 315 g (90%), 280 g (80%), 245 g (70%) and 210 g (60%). For complete desorption (100%), the estimated efficiency was 0.646. When desorbed partially to 90%, 80%, 70% and 60%, the efficiency was reduced to 0.604, 0.548, 0.489, 0.426 individually. The reduction in energy efficiency can be attributed to reduction in amount of desorbed hydrogen.

4.2.8. Assessment of hydrogen storage performance

To appraise the hydrogen storage performance of different MH based storage devices, a distinctive performance evaluation index is necessary. Hydrogen storage and delivery strongly depend on the alloy's PCT, thermophysical and kinetic properties, reactor construction material's thermophysical properties (specific heat capacity, density, thermal conductivity), MH bed's packing parameters (particle size, distribution, porosity, permeability etc.) and heat exchange parameters of the reactor. Yang et al., 2007 suggested the assessment of hydrogen storage using a pair of parameters accounting for reactor specifications, MH alloy properties, heat transfer parameters and operating variables. However, these formulations were established on an average sense and assumed simplified expressions for temperature and pressure. An inclusive index to reveal the influence of heat transfer capability on the reaction rate of MH reactors was proposed by Meng et al., 2012. Once again, this formulation assumed average values of the parameters. One useful idea to assess MH reactor's heat transfer performance and therefore, its storage performance (assuming there is no mass transfer limitation) is to compare the intrinsic reaction kinetics with the reactor's reaction dynamics **(**Linder et al., 2010**)**. However, most of the time, the intrinsic reaction kinetics data is not available in the literature. A rather simple yet useful approach to gauge an MH reactor's hydrogen storage convenience would be to compare 90% desorption completion time. The 90% desorption completion time of few reported experimental works are charted in Table 4.2 for better comprehension.

Only desorption times were considered, as desorption reactions are slower compared to absorption reactions at any given temperature. For comparison purpose, only recent experimental works were chosen where AB_5-type alloys were used under similar desorption conditions. It was witnessed that under similar desorption conditions, the present reactor could deliver hydrogen at a reasonably faster rate compared to other MH reactors of both large (Afzal et al., 2021; Kumar et al., 2019) as well as small capacities (Karmakar et al., 2021; Chandra et al., 2022). The prime deterrent while scaling up from lab environment to industrial application is the obligation of heat transfer at par with intrinsic reaction kinetics. Although an effort has been made to compare the hydrogen storage performance of the present reactor with existing ones, on a stringent note, such judgment of 90% desorption time is not very rational as MH alloys, their scalability and operating conditions cannot be harmonized.

Table 4.2: Assessment of hydrogen storage performance of the 19 TBR module

Author (Ref.)	**MH reactor configuration**	**MH alloy used and quantity**	**Desorption condition**	**Time taken for 90% desorption completion**
Present work	Tube bundle	26.5 kg $La_{0.8}Ce_{0.2}Ni_5$	70 °C, 1 bar	1214 s
(Kumar et al., 2019)	ECT configuration	40 kg $LaNi_{4.7}Al_{0.3}$	90 °C, 1 bar	~1918 s
(Karmakar et al., 2021)	ECT with outer jacket	10 kg $LaNi_5$	80 °C, 1 bar	~1766 s
(Afzal et al., 2021)	Honeycomb shaped heat exchange networks	47.5 kg $La_{0.9}Ce_{0.1}Ni_5$	50 °C, 1 bar	~7033 s
(Chandra et al., 2022)	Internal conical fin	5 kg $LaNi_5$	60 °C, 1 bar	1206 s

4.3. Experiments on 99 ECTR-OCJ module

4.3.1. Description of MH alloy

The MH alloy was screened as per requirement for near ambient hydrogen storage application.

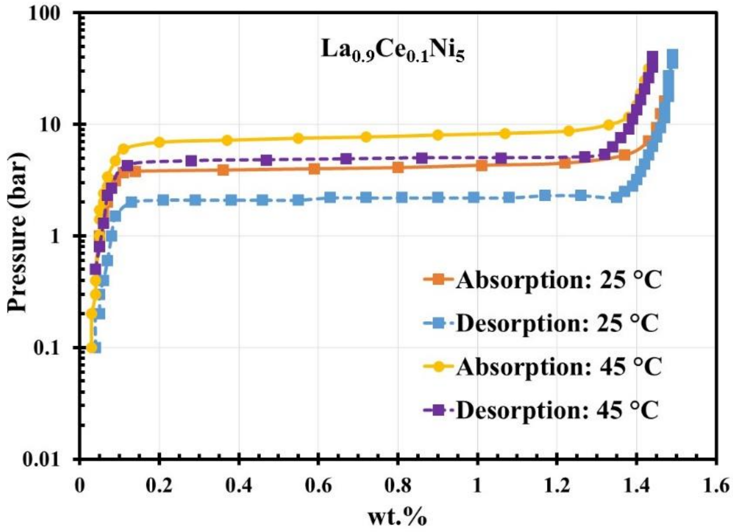

Fig. 4.13: PCT data of $La_{0.9}Ce_{0.1}Ni_5$.

The chosen alloy was procured from M/s Whole Win (Beijing) Materials Sci. & Tech. Co., Ltd., China. The crystallographic composition of the alloy is confirmed as $La_{0.9}Ce_{0.1}Ni_5$. As per PCT data (Fig. 4.13) of the alloy, the midpoint plateau pressure is slightly above 2 bar, with a peak hydrogen storing capacity of 1.48 wt.% besides a hysteresis of 0.62 at 25 °C.

4.3.2. Components of the experimental setup

The description of the components used in experiment is already given in section.4.2.2. The same setup was used for experiments on 99 ECTR-OCJ module. The reactor was filled with 21.5 kg $La_{0.9}Ce_{0.1}Ni_5$ powder. Two 'K-type' thermocouples were fitted at a depth of 30 mm and 55 mm from the reactor inner surface to probe MH bed temperature, whereas another two 'K-type' thermocouples were attached to the inflow and outflow hoses of the MH reactor to probe HTF inflow and outflow temperatures, respectively. A pressure transducer (PT: 0-100 bar, gauge) was attached to the reactor to measure the reactor pressure during absorption and desorption. The photograph of the major components of the test setup and the location of the bed thermocouples and pressure transducer are represented in Fig. 4.14.

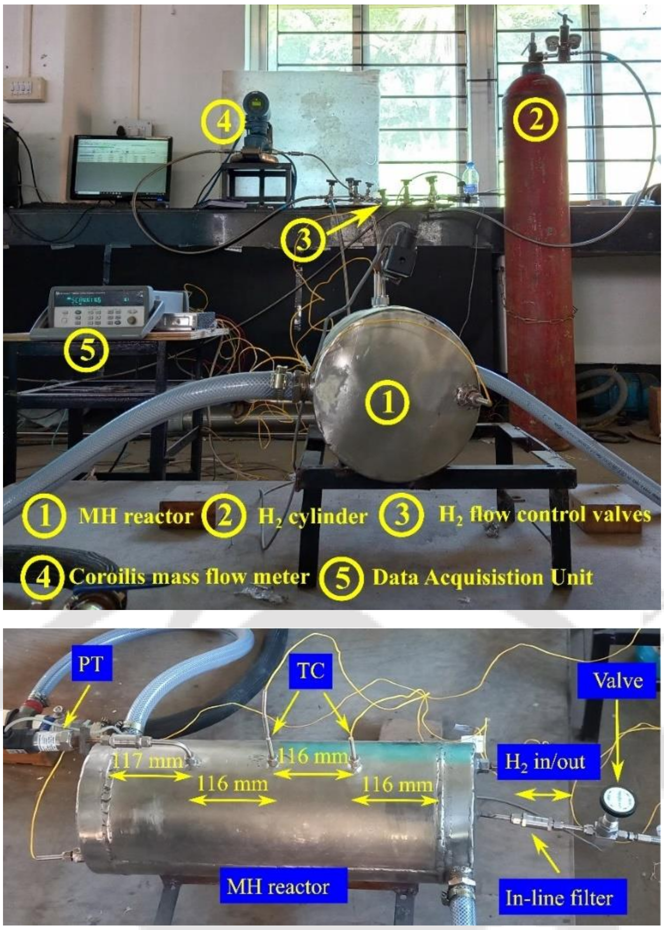

Fig. 4.14: (a) Major components of the test setup and (b) position of thermocouples and pressure transducer.

4.3.3. Description of the experimental protocol

The general experimental procedure has already been described in section 4.2.3.

4.3.4. Activation of the MH alloy

The activation was completed within four consecutive absorption-desorption cycles. Absorption cycles were performed at a supply pressure of 30 bar and 20 °C cold fluid temperature, whereas desorption cycles were carried out at 70 °C hot fluid temperature. In the first absorption, the alloy absorbed 244.78 g hydrogen, which is equivalent to 1.14 wt.%; by the end of the 4th absorption, the storage capacity was increased to 299 g hydrogen (1.39 wt.%).

4.3.5. Parametric study

A series of experiments were conducted to assess the influence of variations in operating parameters on hydrogen absorption and desorption. The designated operating parameters and their operation range are provided in Table 4.3.

Table 4.3: Scheme of the parametric study for 99 ECTR-OCJ module

Process	**Operating parameter**	**Range**	**Remarks**
Absorption	Supply Pressure (P_s):	10-30 bar	HTF temperature ($T_{f,\,a}$) set at: 25 °C; HTF flow rate ($Q_{f,\,a}$) set at: 20 LPM
	HTF temperature ($T_{f,\,a}$):	15-35 °C	Supply Pressure (P_s) set at: 20 bar; HTF flow rate ($Q_{f,\,a}$) set at: 20 LPM
Desorption	HTF temperature ($T_{f,\,d}$):	40-60 °C	Desorption Pressure (P_d) set at: 1 bar; HTF flow rate ($Q_{f,\,d}$) set at:: 20 LPM

Influence of supply pressure alteration on absorbed mass and rate of required cooling

The influence of varying supply pressure on the quantity of hydrogen absorbed, as well as the rate of required cooling, is portrayed in Fig. 4.15. During these experimentations, the HTF temperature and flow rate was kept constant at 25 °C and 20 LPM, correspondingly. At 10 bar supply pressure, the reactor absorbed 268.96 g of hydrogen within 1585 s. When supply pressure was increased from 10 bar to 20 bar and 30 bar, the charged amount was increased by 2.6% and 5.2%, respectively, as shown in Fig. 4.15(a). The reduction in corresponding charging times was 28.7% and 42.5%, respectively. The obtained outcomes are coherent as an increase in supply pressure above equilibrium pressure at a given temperature leads to a rise in the absorption rate. As the absorption reaction is exothermic, a change in the rate of absorption is also translated into the required cooling rate of the MH reactor. Figure 4.15(b) shows the effect of supply pressure variation on the rate of heat removal required during absorption. As absorption is initiated, the rate of heat transfer increases significantly, reaches a peak, and then decreases bit by bit. At 30 bar, the peak rate of heat removal estimated was 9.6 kW at 106 s. Whereas the peak rates registered at 20 bar and 10 bar were 9.3 kW (140 s) and 6.3 kW (166 s), respectively. Although the peak rates were relatively high for all three cases, the average heat removal rates were in the range of 2-3.3 kW only. Based on the quantity of hydrogen absorbed and the degree of heat removal required, the most favourable charging pressure can be considered as 20 bar.

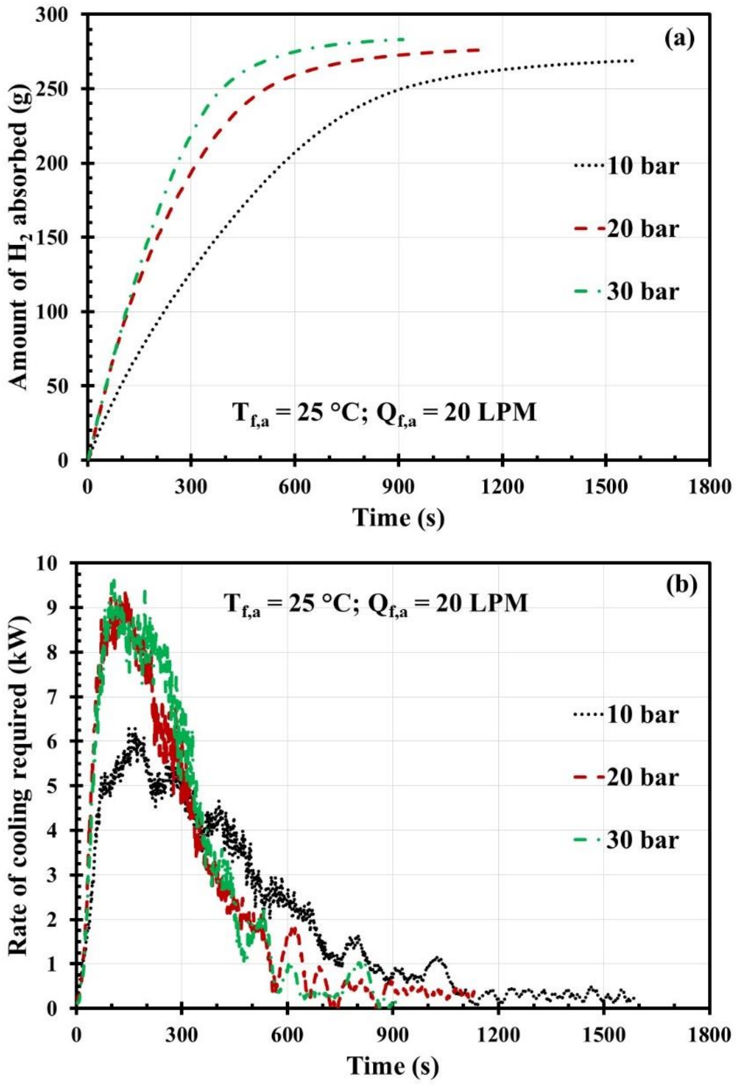

Fig. 4.15: Influence of supply pressure alteration on (a) amount of H_2 absorbed and (b) rate of required cooling.

Influence of HTF temperature alteration on absorbed mass and rate of required cooling

Figure 4.16 illustrates the influence of alteration in HTF temperature on the quantity of hydrogen charged and the rate of heat removal. The hydrogen supply pressure and the HTF flow rate were kept constant at 20 bar and 20 LPM while varying the HTF temperature from 15 to 35 °C. At 25 °C HTF temperature, the MH reactor absorbed 276.08 g hydrogen within 1129 s (Fig. 4.16(a)). When the HTF temperature was reduced to 15 °C, the amount of hydrogen charged remained unchanged; however, the charging time was shortened by 16.7%. On the contrary, when HTF temperature was elevated to 35 °C, the amount of hydrogen charged declined by 1.5%, while charging time was increased by 22.5%.

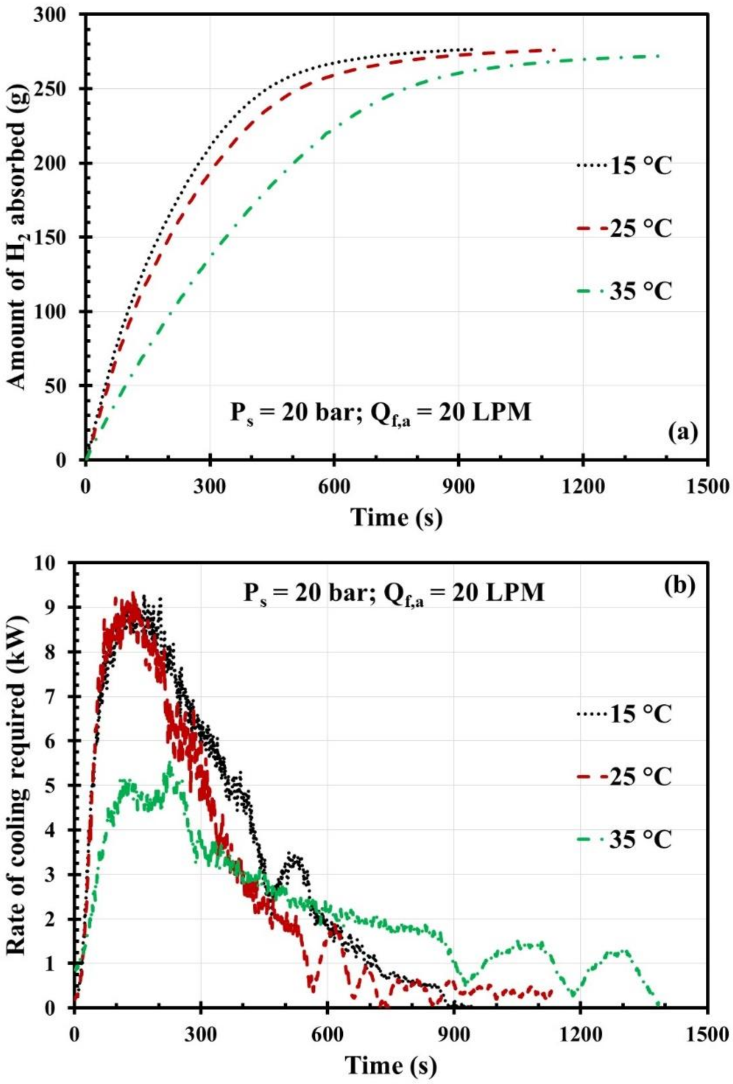

Fig. 4.16: Influence of HTF temperature alteration on (a) amount of H_2 absorbed and (b) rate of required cooling.

As HTF temperature is reduced, the heat transfer potential from MH bed to HTF increases, which accelerates the hydrogen charging process, which is also reflected in the heat removal rate plot as shown in Fig. 4.16(b). The peak rate of heat removal noted at 15 °C, 25 °C, and 35 °C were 9.3 kW, 9.3 kW, and 5.6 kW. Whereas the average rates of heat removal recorded at these HTF temperatures were 3.7 kW, 2.6 kW, and 2.2 kW. Based on the amount of hydrogen charged and the rate of heat removal required at different HTF temperatures, the most favourable HTF temperature for charging can be regarded as 25 °C.

Influence of HTF temperature alteration on desorbed mass and rate of required heating

Hydrogen discharge from MH reactor modules is principally governed by the temperature at which hydrogen release takes place. The influence of HTF temperature alteration on the amount of desorbed hydrogen rate of heating required is plotted in Fig. 4.17. During these set of experiments, the HTF flow rate was sustained at 20 LPM. At 40 °C, the amount of hydrogen discharged was 282.8 g in 4860 s, with an average mass flow rate of 0.058 g.s^{-1}. If discharged through an MFC, the same mass flow rate could run a 3.5 kW LT-PEMFC for the same duration. When HTF temperature was increased to 50 °C and 60 °C, the amount of desorbed hydrogen remained almost constant, while the rates of hydrogen release were faster. The estimated average rate of hydrogen discharge at 50 °C and 60 °C was 0.077 g.s^{-1} and 0.089 g.s^{-1}.

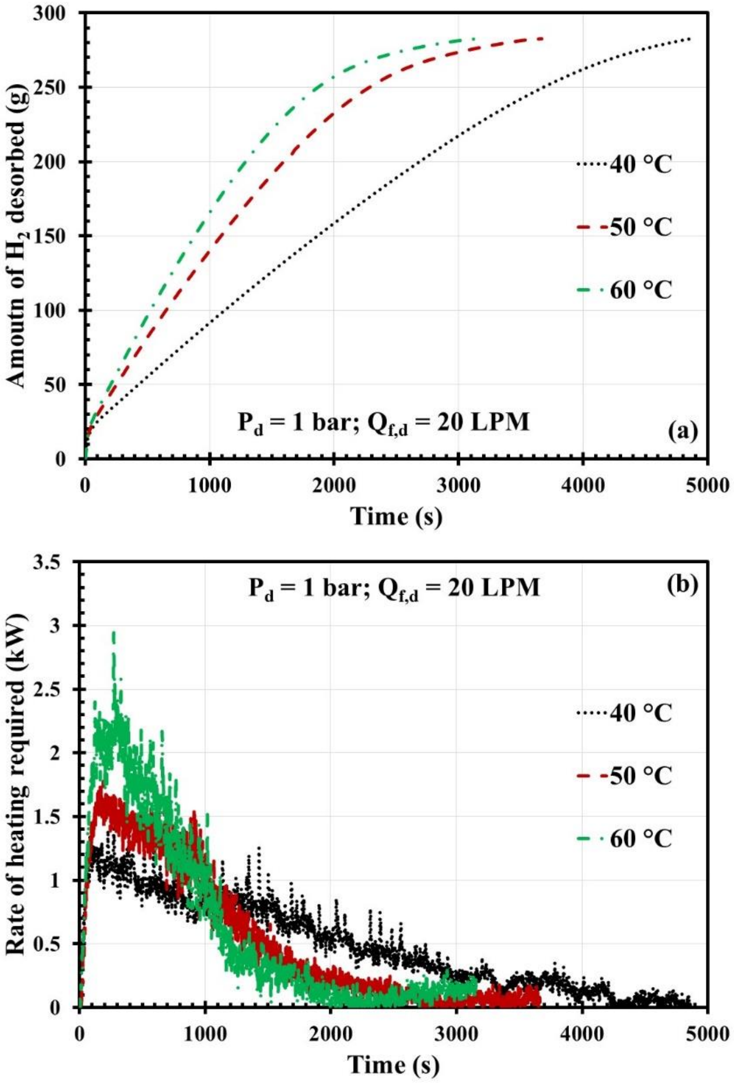

Fig. 4.17: Influence of HTF temperature alteration on (a) amount of H_2 desorbed and (b) rate of heating required.

The influence of HTF temperature alteration on the heat supply rate required during desorption is shown in Fig. 4.17(b). The rate of heat input demanded during hydrogen desorption follows a similar pattern to that of absorption. As desorption is initiated, within a few minutes, the rate of heat transfer increases to a peak and then gradually decreases. The peak rate of heat supply recorded at 60 °C desorption was 2.9 kW at 272 s. Then again, the average rates of heat transfer at 60 °C, 50 °C, and 40 °C were 0.65 kW, 0.54 kW, and 0.49 kW only. The maximum rate of heat input during hydrogen desorption can be lowered by allowing discharge through an MFC.

Influence of HTF temperature alteration on reactor pressure during desorption

Figure 4.18 shows the reactor pressure variation at altered HTF temperatures. Reactor pressure is the highest at the beginning of desorption; as desorption progresses, the pressure goes down till it is completed. The measured values of reactor pressure before the commencement of desorption were 40 bar (gauge), 30.9 bar (gauge), and 28.5 bar (gauge) at 60 °C, 50 °C, and 40 °C. Higher reactor pressure also indicates a higher potential for hydrogen transfer, which escalates the rate of desorption, which in turn reduces the bed pressure. At the end of hydrogen desorption, the reactor pressures recorded were 0.3 bar (gauge), 0.12 bar (gauge), and 0.22 bar (gauge), corresponding to HTF temperatures of 40 °C, 50 °C, and 60 °C.

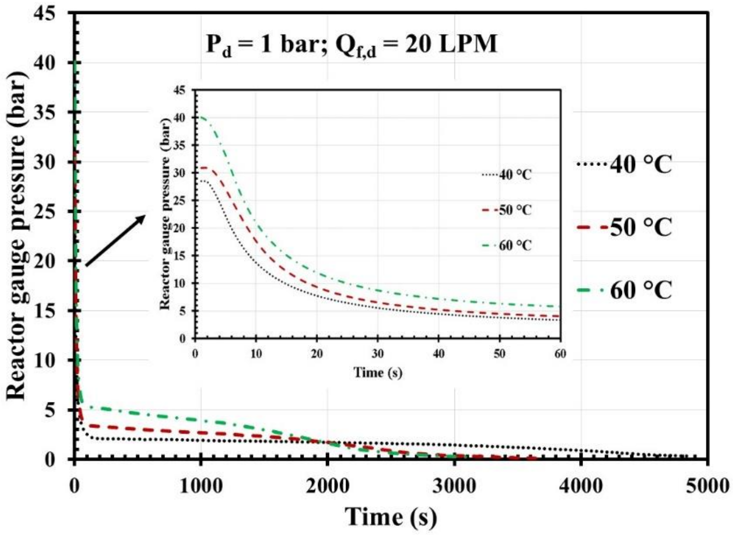

Fig. 4.18: Influence of HTF temperature alteration on reactor pressure during desorption.

Influence of HTF flow rate alteration on reactor pressure during desorption

Figure 4.19 represents the reactor pressure variation during desorption at altered HTF flow rates. At the beginning of desorption, the measured reactor gauge pressures corresponding to 15 LPM, 20 LPM, and 25 LPM flow rates were 31.3 bar, 30.9 bar, and 29 bar, respectively. As desorption progressed, the reactor pressure at higher flow rates was maintained at higher pressures for half of the total desorption duration. By the end of desorption, the measured reactor gauge pressures at 15 LPM, 20 LPM, and 25 LPM flow rates were 0.12 bar, 0.13 bar, and 0.16 bar, respectively.

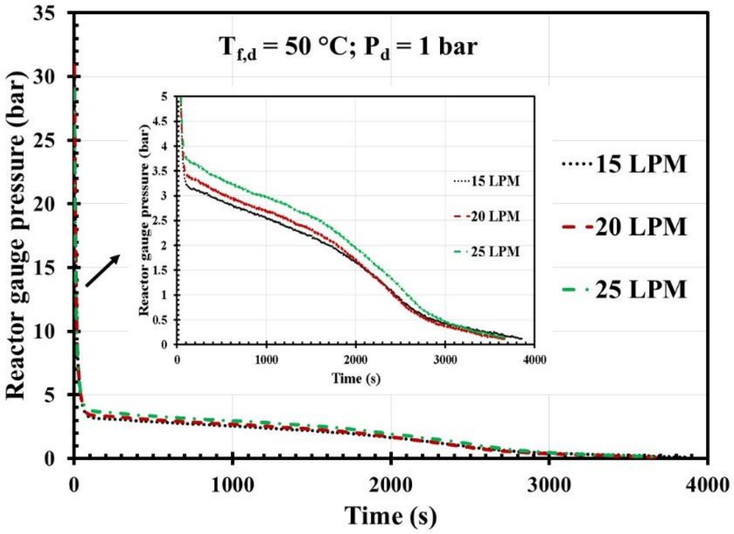

Fig. 4.19: Influence of HTF flow rate alteration on reactor pressure during desorption.

Influence of HTF temperature alteration on energy efficiency

The influence of HTF temperature alteration on energy efficiency is shown in Fig. 4.20.

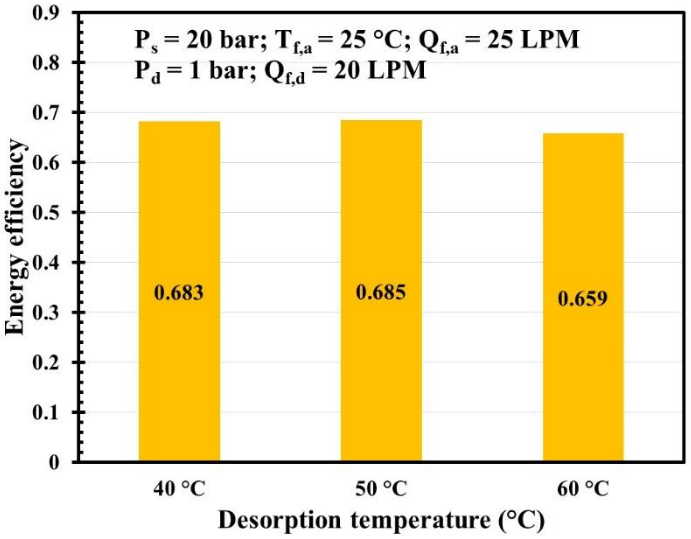

Fig. 4.20: Influence of HTF temperature alteration on energy efficiency.

The reference absorption condition considered was 20 bar, 25 °C, 25 LPM. The energy efficiency at 40 °C, 50 °C desorption conditions were 0.683 and 0.685, respectively. The estimated energy efficiency at 40 °C and 50 °C was similar as the energy transactions pertaining to stored hydrogen, sensible heating, desorption, and corresponding pump power consumptions were identical. The estimated energy efficiency value was reduced by 3.81% when HTF temperature was increased from 50 °C to 60 °C owing to an increase in sensible heat demand.

Influence of partial desorption on energy efficiency

The effect of partial desorption on energy efficiency is shown in Fig. 4.21. Similar to the previous observation on 19 TBR module, the estimated energy efficiency value was reduced as the percentage desorption was reduced. In this case, the reference hydrogen absorption and desorption conditions considered were 20 bar, 25 °C, 25 LPM (absorption), and 50 °C, 20 LPM (desorption). The estimated energy efficiency value at 60%, 70%, 80% and 90% desorption were 0.649, 0.67, 0.687 and 0.697.

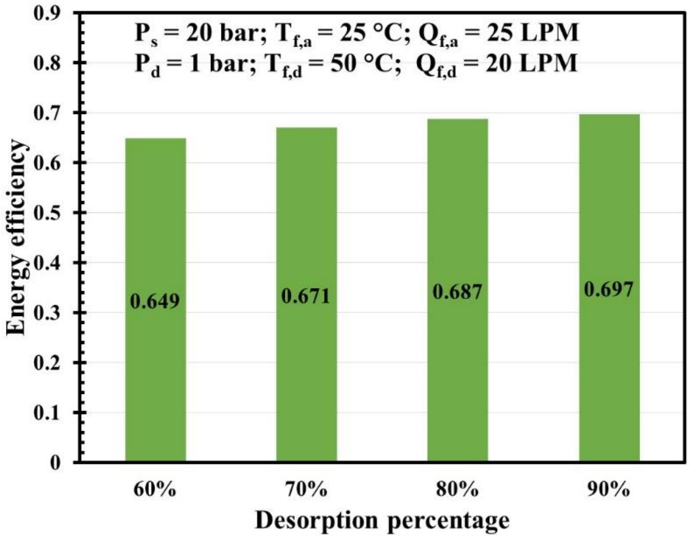

Fig. 4.21: Influence of partial desorption on energy efficiency.

4.3.6. Assessment of hydrogen storage performance

The hydrogen storage performance of the 99 ECTR-OCJ module is assessed in a similar manner to that of 19 TBR module by comparing the 90% desorption completion time of experimental studies reported (Table 4.4) on AB_5 alloy.

Table 4.4: Assessment of hydrogen storage performance of the 99 ECTR-OCJ module

Author (Ref.)	**MH reactor configuration**	**MH alloy used and quantity**	**Desorption condition**	**Time taken for 90% desorption completion**
Present work	ECT with outer jacket	21.5 kg $La_{0.9}Ce_{0.1}Ni_5$	60 °C, 1 bar	1940 s
(Kumar et al., 2019)	ECT configuration	40 kg $LaNi_{4.7}Al_{0.3}$	90 °C, 1bar	~1918 s
(Karmakar et al., 2021)	ECT with outer jacket	10 kg $LaNi_5$	80 °C, 1 bar	~1766 s
(Afzal et al., 2021)	Honeycomb shaped heat exchange networks	47.5 kg $La_{0.9}Ce_{0.1}Ni_5$	50 °C, 1 bar	~7033 s
(Chandra et al., 2022)	Internal conical fin	5 kg $LaNi_5$	60 °C, 1 bar	1206 s
(Sunku Prasad and Muthukumar, 2022)	Annular finned reactor	9 kg $La_{0.7}Ce_{0.1}Ca_{0.3}Ni_5$	50 °C, 1 bar	~1707 s

Desorption results obtained under comparable operating condition shows that the 99 ECTR-OCJ could desorb hydrogen at a decent rate compared to both large and small capacity reactors.

4.4. Experiments on tube-in-tube reactor module

4.4.1. Description of MH alloy

The MH alloy used in this experiment is a combination of two AB_5-type alloys, namely, $La_{0.7}Ce_{0.1}Ca_{0.3}Ni_5$ and $MmNi_{4.5}Fe_{0.5}$. The PCT data of $La_{0.7}Ce_{0.1}Ca_{0.3}Ni_5$ and the desorption isotherm of $MmNi_{4.5}Fe_{0.5}$ at 0 °C is provided below (Fig. 4.22). The alloy $La_{0.7}Ce_{0.1}Ca_{0.3}Ni_5$ is a low-pressure alloy, whereas the $MmNi_{4.5}Fe_{0.5}$ is a high-pressure alloy. Based on the alloy loading capacity of the designed reactor, 1.3 kg of each alloy (total 2.6 kg) in powder form was mixed physically and filled inside the reactor. The motivation of alloy mixing was to verify if physical mixing could alter the absorption and desorption characteristics of the mixture favourably.

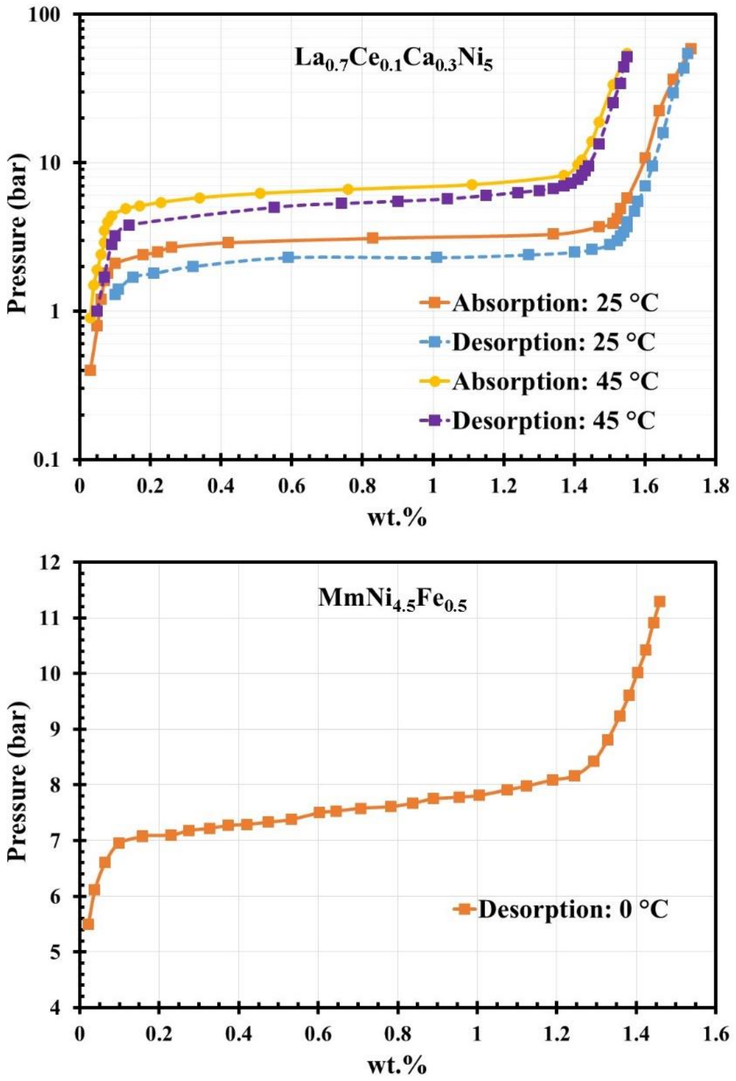

Fig. 4.22: : (a) PCT data of $La_{0.7}Ce_{0.1}Ca_{0.3}Ni_5$ and (b) desorption isotherm of $MmNi_{4.5}Fe_{0.5}$ at 0 °C (Apostolov et al., 1985)

4.4.2. Components of the experimental setup

The description of the major components used in the experiment is already given in section 4.2.2. A mass flow controller and a pressure-reducing valve was additionally included in the gas circuit to facilitate hydrogen desorption at a constant mass flow rate in the range of 0-30 LPM. The photograph of the experimental setup indicating the major components is portrayed in Fig. 4.23. The reactor was equipped with two ‘K type thermocouples’ (TC1: 500 mm, and TC2: 350 mm) for bed temperature measurement, while another pair of ‘K type thermocouples’ were employed to measure HTF temperature at the inlet and outlet. The photograph of the reactor and the position of the bed thermocouples is shown in Fig. 4.24.

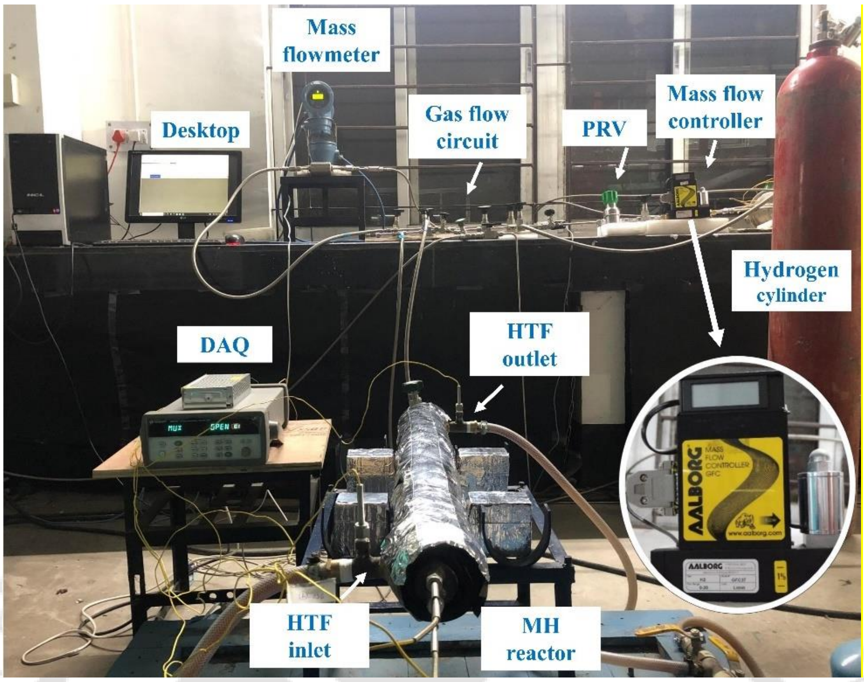

Fig. 4.23: Photograph of the major components of the experimental setup.

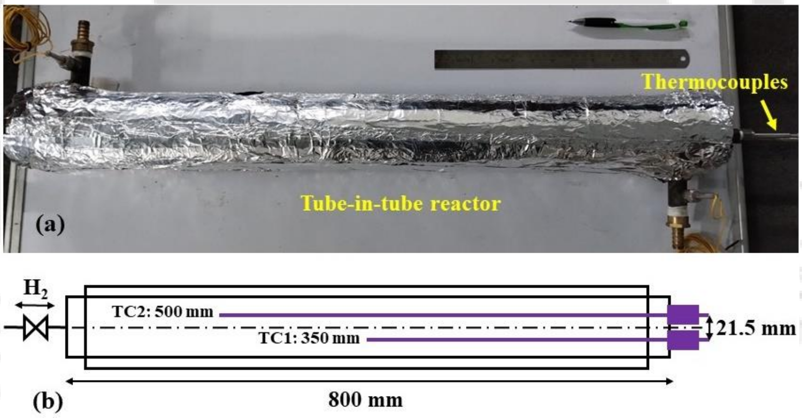

Fig. 4.24: (a) Photograph of the reactor and (b) depiction of thermocouple position.

4.4.3. Description of the experimental protocol

The experimental procedure remains unchanged, as it has already been described in section 4.2.3. A few experiments were also conducted where the desorption of hydrogen was routed through a mass flow controller to the ambient.

4.4.4. Activation of the MH alloy

The activation of the alloy mixture was accomplished within four repeated absorption desorption cycles. In the absorption cycles, hydrogen was supplied at a supply pressure of

60 bar, 15 °C, while desorption cycles were performed at 60 °C. The amount of hydrogen absorbed by the alloy mixture in consecutive 4 absorption cycles was 35.57 g (1.37 wt.%), 38.11 g (1.47 wt.%), 41.11 g (1.58 wt.%), and 42.92 g (1.65 wt.%), correspondingly. The anticipated hydrogen storage capacity of the alloy mixture, as estimated from the PCT data, was 1.57 wt.% or approximately 41 g.

4.4.5. Parametric study

A series of experiments were conducted to assess the influence of operating parameters on hydrogen absorption and desorption characteristics of the alloy mixture. The details of The designated operating parameters and their operation range are provided in Table 4.5.

Table 4.5: Scheme of the parametric study for Tube-in-tube reactor module

Process	**Operating parameter**	**Range**	**Remarks**
Absorption	Supply Pressure (P_s):	10-60 bar	HTF temperature ($T_{f,\,a}$) set at: 25 °C; HTF flow rate ($Q_{f,\,a)}$ set at: 2 LPM
	HTF temperature ($T_{f,\,a}$):	5-25 °C	Supply Pressure (P_s) set at: 50 bar; HTF flow rate ($Q_{f,\,a)}$ set at: 2 LPM
Desorption	HTF temperature ($T_{f,\,d}$):	30-60 °C	Desorption Pressure (P_d) set at: 1 bar; HTF flow rate ($Q_{f,\,d}$) set at:: 2 LPM

Influence of supply pressure and HTF temperature alterations on absorbed mass

Figure 4.25(a) shows the influence of supply pressure and HTF temperature on absorbed mass of the alloy mixture. While assessing the influence of supply pressure variation, the HTF temperature and flow rate was set to 25 °C and 2 LPM. For a supply pressure of 10-30 bar at 25 °C HTF temperature, only 18-20 g hydrogen was absorbed within 455-844 s which corresponds to 0.69-0.76 wt.% storage capacity. Such an outcome is anticipated as the mid-point plateau pressure of $MmNi_{4.5}Fe_{0.5}$ (Apostolov et al., 1985**)** and $La_{0.7}Ce_{0.1}Ca_{0.3}Ni_5$ at 25 °C are approximately 14 bar (desorption) and 2 bar, correspondingly. The high plateau pressure of $MmNi_{4.5}Fe_{0.5}$ contributes to low cumulative hydrogen absorption even at 30 bar supply pressure. When supply pressure was raised from 30 bar (19.55 g at 455 s) to 40 bar, 50 bar, and 60 bar, the amount of absorbed mass increased by 52.7%, 75.3% and 86.2%, respectively. However, the corresponding increment in absorption time was approximately 3 fold, 3.2 fold, and 3.4 fold indicating a significant increase in absorption by $MmNi_{4.5}Fe_{0.5}$ in the pressure range of 40-60 bar.

The supply pressure was not increased beyond 60 bar, considering the alloy pulverization characteristics of $La_{0.7}Ce_{0.1}Ca_{0.3}Ni_5$ from earlier knowledge of handling the alloy.

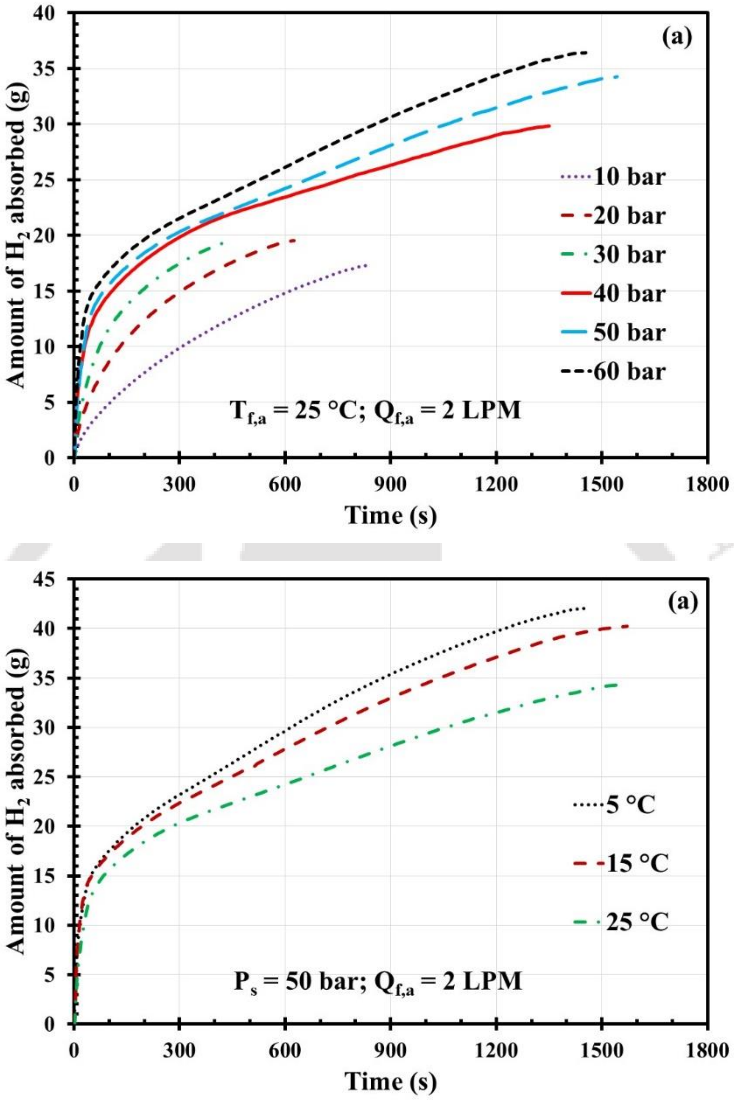

Fig. 4.25: (a) Influence of supply pressure variation on the amount of H_2 absorbed and (b) influence of HTF temperature variation on the amount of H_2 absorbed.

The influence of HTF temperature variation on the amount of absorbed mass of the alloy mixture is depicted in Fig. 4.25(b). While assessing the influence of HTF temperature alteration, the supply pressure was set at 50 bar. At 25 °C, the amount of hydrogen absorbed was 34.29 g within 1544 s. When HTF temperature was reduced to 15 °C, the amount of hydrogen absorbed was increased by 17.38% with a tiny increase in absorption duration (27 s). With further reduction in HTF temperature from 15 °C to 5 °C, the amount of hydrogen absorbed was merely increased by 4.56% with 7.7% reduction in absorption time.

The increase in absorbed mass of hydrogen at 5-15 °C can be attributed lowered equilibrium plateau pressure of $MmNi_{4.5}Fe_{0.5}$.

Influence of HTF temperature alteration on desorbed mass

Figure 4.26 shows the influence of HTF temperature alteration on the amount of desorbed hydrogen mass of the alloy mixture. During this set of experiments, the reactor outlet was open to ambient i.e., desorption pressure was set at 1 bar.

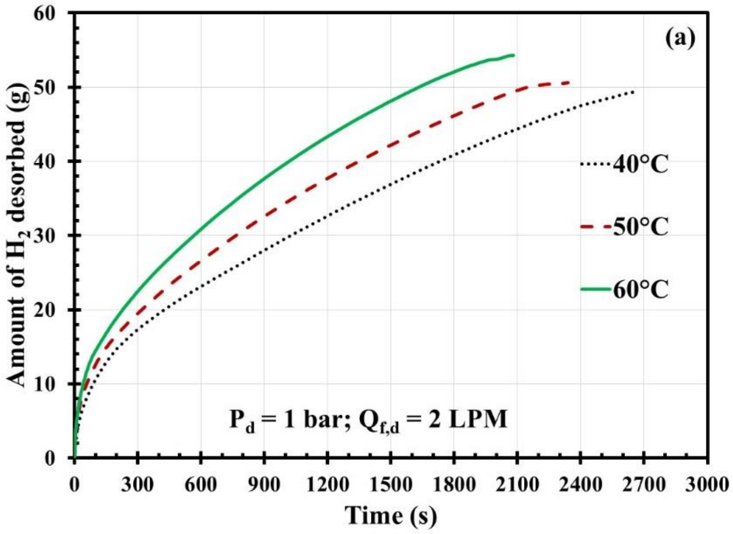

Fig. 4.26: Influence of HTF temperature variation on the amount of hydrogen desorbed.

Before each desorption, hydrogen was charged into the reactor at 50 bar 15 °C. At 40 °C, the amount of hydrogen desorbed was 49.39 g (1.9 wt.%) within 2671 s. When the HTF temperature was raised to 50 °C, the amount desorbed was almost unchanged; however, the desorption time was reduced by 12.1%. When HTF temperature was further raised from 50 °C to 60 °C, the desorbed amount increased by 7.3%, while desorption time was reduced by 11.3%.

4.4.6. Studies on constant flow rate desorption

Hydrogen desorption tests were also conducted at a constant flow rate to assess the viability of feeding hydrogen to PEMFC in the capacity range of 0.5-1 kW. Considering the typical hydrogen consumption rate of a 0.5 kW and 1 kW PEMFC of 6.5 LPM and 13 LPM, individually, hydrogen desorption tests were conducted at 6.5 LPM flow rate at 30-60 °C HTF temperature and at 13 LPM at 40-60 °C.

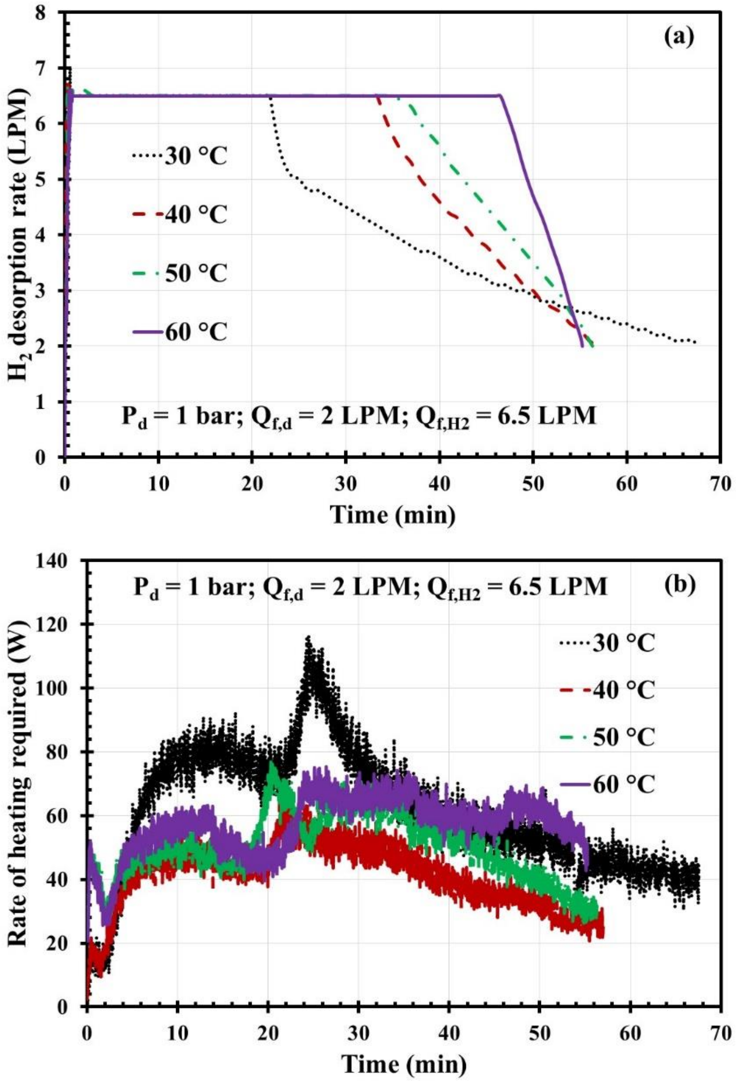

Fig. 4.27: Influence of HTF temperature alteration on hydrogen discharge at 6.5 LPM (a) hydrogen discharge profile and (b) rate of heating required.

Figure 4.27 and 4.28 shows the influence of HTF temperature on steady desorption rate and consequent heating demand for 6.5 LPM and 13 LPM case. As can be observed in Fig. 4.27(a), at 30 °C HTF temperature, the set flow rate (6.5 LPM) was maintained till 21.93 min, beyond which the flow rate gradually dropped to 2 LPM by the end of 67.57 min.

When HTF temperature was raised to 40 °C, 50 °C and 60 °C, the set flow rate was retained till 33.37 min, 35.17 min and 46.52 min. Beyond these marked time durations, the flow rate dipped progressively till 2 LPM. A similar observation was witnessed in the case of 13 LPM experiments, when the set flow rate was retained for a longer duration at 50-60 °C, compared to 40 °C (Fig. 4.28a). For 13 LPM tests, the set flow rate could be sustained for 10.3 min, 17 min and 17.95 min, correspondingly. At a higher set flow rate, the time duration for which the desired flow rate could be maintained was lower as the reactor was charged with almost identical amount of hydrogen in the preceding absorption cycles.

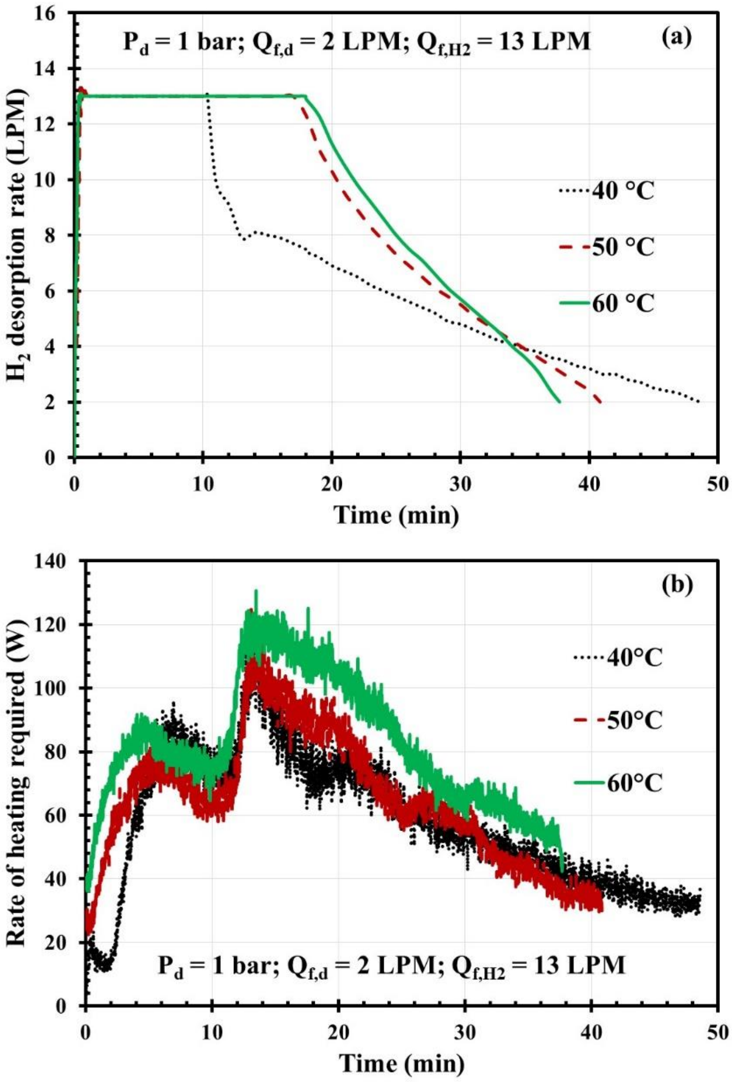

Fig. 4.28: Influence of HTF temperature alteration on hydrogen discharge at 13 LPM (a) hydrogen discharge profile and (b) rate of heating required.

The heat input required to drive hydrogen desorption was estimated and plotted in rate terms in Fig. 4.27(b) and 4.28(b), which correspondingly denotes the case of 6.5 LPM and

13 LPM. As a consequence of steady hydrogen discharge, the heating demand varied between 20-80 W and 20-120 W for 6.5 LPM and 13 LPM experiments, as can be witnessed in heating rate plots. The average rate of heating required for 6.5 LPM and 13 LPM discharge were only 40-60 W and 58-82 W.

4.5. Summary

In this chapter, the outcomes of the hydrogen storage experiments conducted on two large-scale reactors (19 TBR, 99 ECTR_OCJ) and a prototype concentric tube reactor is presented. Total of four different alloys were used for experiments, namely $La_{0.8}Ce_{0.2}Ni_5$, $La_{0.9}Ce_{0.1}Ni_5$, $La_{0.7}Ce_{0.1}Ca_{0.3}Ni_5$, and $MmNi_{4.5}Fe_{0.5}$. These experimental studies are primarily aimed at evaluating the hydrogen charging and discharging performances and resulting heat interactions at near-ambient conditions. The prototype reactor was also discharged through a mass flow controller at 6.5 LPM and 13 LPM rates to assess its suitability to integrate with LT-PEMFC.

5. Experiments on MH based open-cycle cooling systems

5.1. Introduction

In this chapter, the experimental studies carried out on MH-based open-cycle cooling systems are presented. In the first set of studies, results on open-cycle cooling obtained during hydrogen desorption to the ambient are discussed, whereas in the second set of studies, open-cycle cooling obtained while hydrogen discharged to the ambient via a compressor is discussed.

5.2. Experiments on open cycle cooling systems without compressor

5.2.1. Concept of open cycle MH based cooling system

The very concept of an open cycle MH based cooling system is important in context of primarily fuel cell vehicles or any other hydrogen powered automobile applications which houses on board high pressure hydrogen tank (700 bar). The typical amount of hydrogen stored in high pressure on board storage tanks are about 5 kg. The stored hydrogen is fed to the fuel cell for power generation which typically necessities an infeed pressure of 1-10 bar, which implies there is always an unspent potential (pressure energy) in the stored hydrogen which can be utilized. By engaging a suitable MH reactor hydrogen can be stored in a buffer tank and later whenever required can be fed to the fuel cell for power generation. In this process, when hydrogen is desorbed from the MH reactor it would provide cooling effect without hampering the functionality of the fuel cell. The heat generated during hydrogen absorption can be dissipated to ambient. To produce quasi-continuous cooling effect, a pair of MH reactors can be engaged in parallel. The conceptual schematic and van’t Hoff plot of the open cycle MH based cooling system is represented in Fig. 5.1. Nevertheless, this open cycle cooling concept can also be explored in any context with availabity of pressurized hydrogen source and user point e.g., electrolyser and fuel cell. In the work described here, hydrogen is discharged to ambient.

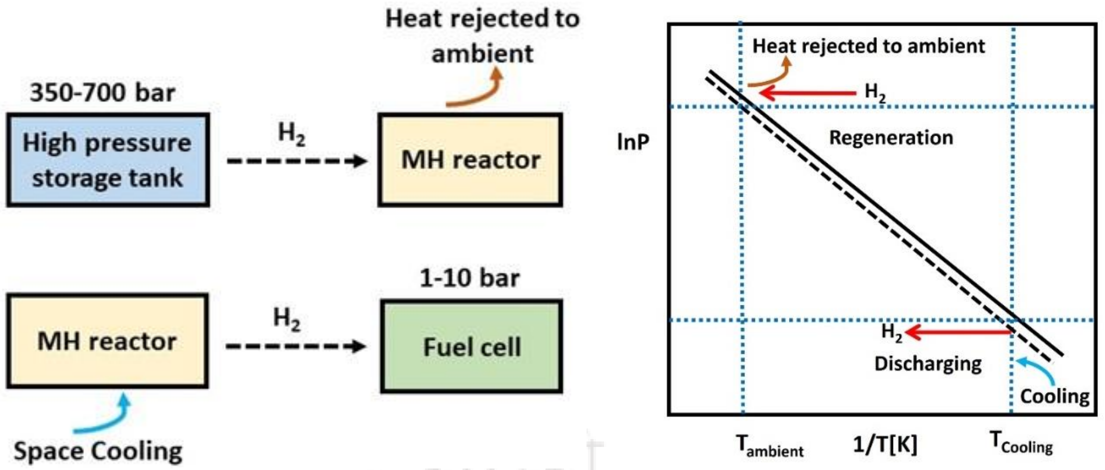

Fig. 5.1: (a) Conceptual illustration of open cycle cooling and (b) ideal van't Hoff representation

5.2.2. Description of MH alloy

The MH alloys used for cooling experiments without compressor are $La_{0.8}Ce_{0.2}Ni_5$ and $La_{0.7}Ce_{0.1}Ca_{0.3}Ni_5$. The PCT characteristics of the alloys are given in sections 4.2.1 and 4.4.1.

5.2.3. Components of the experimental setup

The test setup utilized to perform open-cycle cooling studies without a compressor is exactly the same as described in section 4.2.2 except for the MH reactor. The MH reactor configuration used here is the 48 ECTR_OCJ. An identical pair of 48 ECTR_OCJ configurations were fabricated and filled with 3.4 kg of $La_{0.8}Ce_{0.2}Ni_5$ and $La_{0.7}Ce_{0.1}Ca_{0.3}Ni_5$ individually. Two metal-sheathed 'K' type thermocouples of probe length 75 mm (TC1) and 120 mm (TC2) were fitted (radial location marked in Fig. 5.2(a)) to measure the MH bed temperature, whereas another pair of metal-sheathed 'K' type thermocouples of 32 mm probe length was used for measuring the HTF inlet and outlet temperatures. The photograph of the 48 ECTR_OCJ is shown in Fig. 5.2(b).

5.2.4. Description of the experimental protocol

The detailed experimental protocol is already stated in section 4.2.3. Water was used as HTF in this experiment, which was supplied at a constant flow rate of 5 LPM for both absorption and desorption.

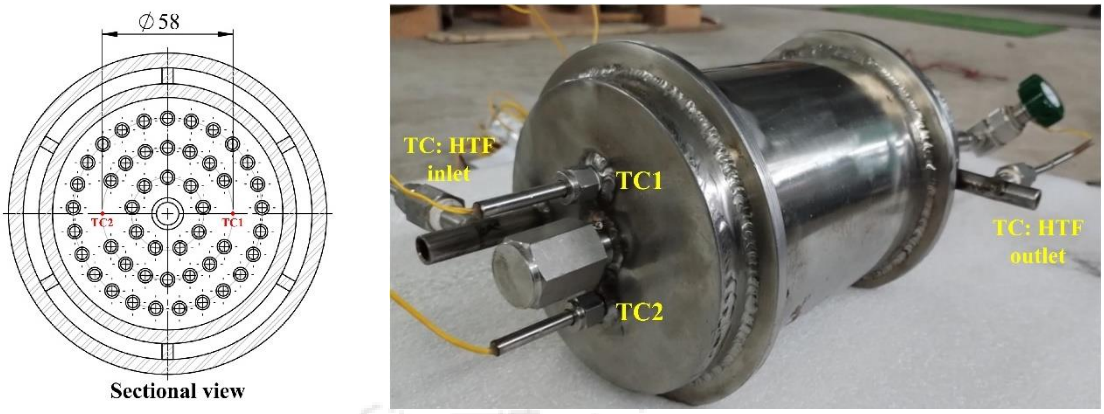

Fig. 5.2: (a) Radial location of the MH bed thermocouples and (b) photograph of the reactor.

5.2.5. Activation of the MH alloys

Activation of the MH alloys was accomplished individually in a couple of consecutive absorption/desorption cycles. Prior to the start of every activation, the reactor and the gas flow circuit were checked for any leakage by supplying argon gas at 80 bar pressure and kept pressurized overnight. It was followed by degassing the reactor down to 0.001 mbar at 90 °C. During activation of $La_{0.8}Ce_{0.2}Ni_5$, the absorption condition was maintained at 60 bar and 20 °C, while activation of $La_{0.7}Ce_{0.1}Ca_{0.3}Ni_5$ was carried out at 30 bar and 25 °C. After every absorption, the reactors were heated and evacuated down to 0.001 mbar. For $La_{0.8}Ce_{0.2}Ni_5$, the reactor was heated up to 80 °C, while for $La_{0.7}Ce_{0.1}Ca_{0.3}Ni_5$, heating was done till 40 °C. In the ninth cycle, $La_{0.8}Ce_{0.2}Ni_5$ absorbed 53.18 g hydrogen, which was equivalent to a storage capacity of 1.56 wt.%. Whereas, in the fourth cycle, $La_{0.7}Ce_{0.1}Ca_{0.3}Ni_5$ absorbed 49.37 g hydrogen, which corresponds to 1.45 wt.%.

5.2.6. Cooling performance of $La_{0.8}Ce_{0.2}Ni_5$ and $La_{0.7}Ce_{0.1}Ca_{0.3}Ni_5$

Parametric study

A couple of experiments were performed to understand the influence of operating parameters on regeneration (hydrogen absorption) and cooling (hydrogen desorption). The designated operating parameters and their operation range are provided in Table 5.1.

Table 5.1: Scheme of the parametric study for open cycle cooling experiments without compressor

Process	Operating parameter	Range	Remarks
Regeneration	Supply Pressure (P_s):	10-30 bar	HTF temperature ($T_{f,\,a}$) set at: 25 °C; HTF flow rate ($Q_{f,\,a}$) set at: 5 LPM
	HTF temperature ($T_{f,\,a}$):	15-35 °C	Supply Pressure (P_s) set at: 20 bar; HTF flow rate ($Q_{f,\,a}$) set at: 5 LPM
Cooling	HTF temperature ($T_{f,\,des}$):	5-25 °C	Desorption Pressure (P_d) set at: 1 bar; HTF flow rate ($Q_{f,\,d}$) set at: 5 LPM

Hydrogen absorption behaviour

Influence of supply pressure on the amount of hydrogen absorbed

The influence of hydrogen supply pressure variation on the amount of hydrogen absorbed for $La_{0.8}Ce_{0.2}Ni_5$ and $La_{0.7}Ce_{0.1}Ca_{0.3}Ni_5$ is represented in Fig. 5.3. The effect of supply pressure variation was more prominent for $La_{0.8}Ce_{0.2}Ni_5$ compared to $La_{0.7}Ce_{0.1}Ca_{0.3}Ni_5$. At a supply pressure of 10 bar, 20.22 g hydrogen was absorbed by $La_{0.8}Ce_{0.2}Ni_5$ in 858 s, whereas $La_{0.7}Ce_{0.1}Ca_{0.3}Ni_5$ absorbed 44.77 g hydrogen in 584 s. An increase in supply pressure from 10 to 20 bar resulted in a 74.6% increase in the absorbed hydrogen for $La_{0.8}Ce_{0.2}Ni_5$, whereas it was merely a 3.7% raise for $La_{0.7}Ce_{0.1}Ca_{0.3}Ni_5$. Further increasing the supply pressure from 20 bar to 30 bar resulted in an increase of 19.8% in the absorption capacity for $La_{0.8}Ce_{0.2}Ni_5$. However, $La_{0.7}Ce_{0.1}Ca_{0.3}Ni_5$ exhibited only a 1.3% increase in absorbed amount when supply pressure was ramped from 20 to 30 bar. It can be observed that $La_{0.8}Ce_{0.2}Ni_5$ necessities higher supply pressure compared to $La_{0.7}Ce_{0.1}Ca_{0.3}Ni_5$ for absorption completion at 25 °C.

Moreover, the absorption reaction in the studied range of supply pressures is faster for $La_{0.7}Ce_{0.1}Ca_{0.3}Ni_5$ (< 600 s) compared to $La_{0.8}Ce_{0.2}Ni_5$ (~900 s). Such absorption behaviour is due to the higher plateau equilibrium pressure of $La_{0.8}Ce_{0.2}Ni_5$ compared to

$La_{0.7}Ce_{0.1}Ca_{0.3}Ni_5$ in the similar temperature range as it can be observed from the PCT diagrams (Fig.4.1 and Fig. 4.22(a)).

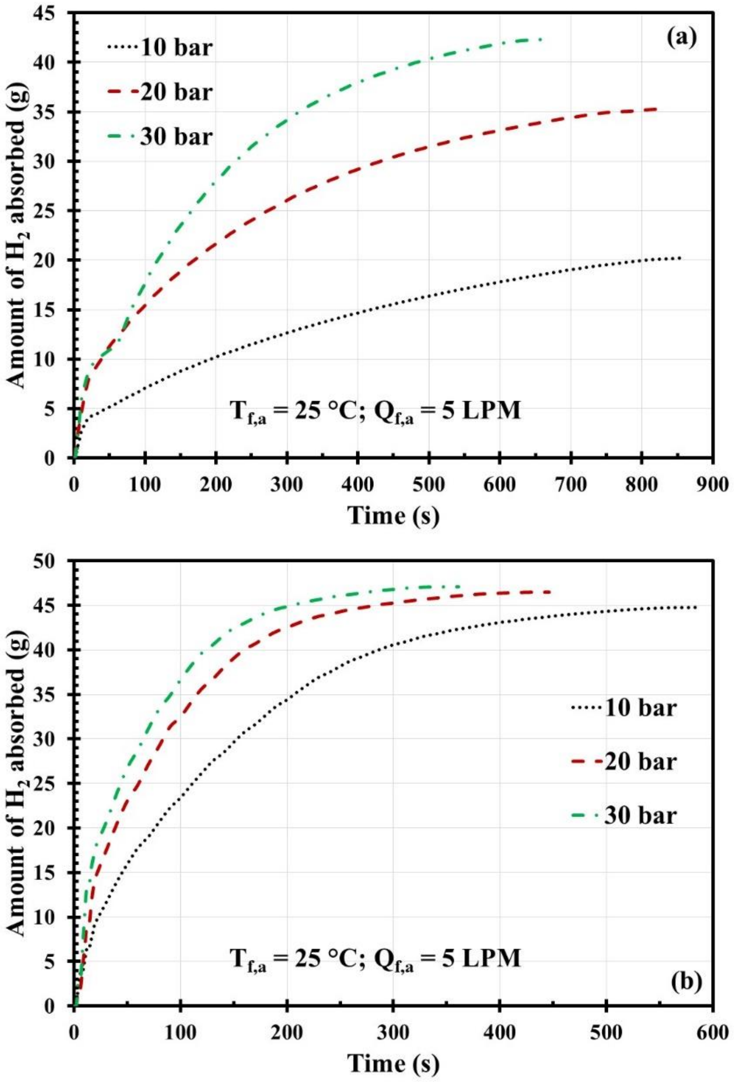

Fig. 5.3: Influence of supply pressure alteration on the amount of hydrogen absorbed for (a) $La_{0.8}Ce_{0.2}Ni_5$ and (b) $La_{0.7}Ce_{0.1}Ca_{0.3}Ni_5$.

Influence of HTF temperature on the amount of hydrogen absorbed

The variation in the amount of hydrogen absorbed at different HTF temperatures for $La_{0.8}Ce_{0.2}Ni_5$ and $La_{0.7}Ce_{0.1}Ca_{0.3}Ni_5$ are depicted in Fig. 5.4. At supply conditions of 20 bar and 25 °C, $La_{0.8}Ce_{0.2}Ni_5$ and $La_{0.7}Ce_{0.1}Ca_{0.3}Ni_5$ absorbed 35.32 g and 46.46 g hydrogen within 828 s and 450 s, correspondingly. An increase in HTF temperature from 25 °C to 35 °C resulted in a 16% reduction in absorbed quantity for $La_{0.8}Ce_{0.2}Ni_5$ while the same was reduced by merely 3% for $La_{0.7}Ce_{0.1}Ca_{0.3}Ni_5$. Conversely, a decrease in HTF temperature from 25 °C to 15 °C resulted in an absorption capacity improvement of 10.4% and 1.7%

for $La_{0.8}Ce_{0.2}Ni_5$ and $La_{0.7}Ce_{0.1}Ca_{0.3}Ni_5$, respectively. At lower HTF temperatures, the heat transfer is improved due to the larger difference in temperature between MH bed and HTF, which influences the bed temperature and, consequently, equilibrium bed pressure, thereby increasing the driving force. Compared to $La_{0.7}Ce_{0.1}Ca_{0.3}Ni_5$, the hydrogen storage performance of $La_{0.8}Ce_{0.2}Ni_5$ was found to be more sensitive toward changes in HTF temperature.

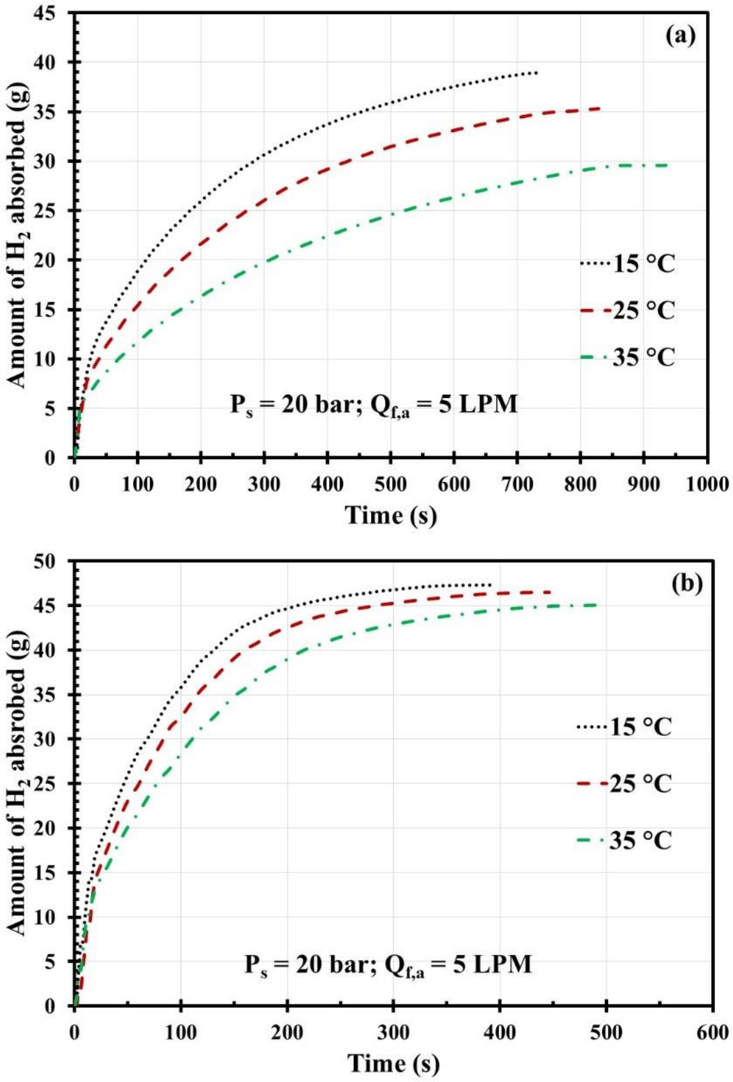

Fig. 5.4: Influence of HTF temperature alteration on the amount of hydrogen absorbed (a) $La_{0.8}Ce_{0.2}Ni_5$ and (b) $La_{0.7}Ce_{0.1}Ca_{0.3}Ni_5$.

Open cycle cooling behaviour

The cooling performance of the system in the temperature range of 5-25 °C was assessed in terms of cooling power and cumulative cooling effect.

Estimation of cooling power

The cooling power is calculated using Eq. 5.1 as given below:

Cooling Power: $$Q_c\left(t\right)=\rho_f Q_f c_{p,f}\left(T_{f,in}-T_{f,out}\right) \tag{5.1}$$

In Eq. (5.1), 'ρ_f' denotes the density of HTF, 'Q_f' denotes the volume flow rate of the HTF, '$c_{p,f}$' stands for the specific heat capacity of the HTF, '$T_{f,in}$' and '$T_{f,out}$' correspondingly signify inlet and outlet temperatures of the HTF. The cumulative cooling effect 'Q_t' obtained over a period of time is estimated using Eq. (5.2).

Cumulative cooling effect: $$Q_t=\int_0^t Q_c\left(t\right)dt \tag{5.2}$$

Influence of HTF temperature alteration on the amount of hydrogen desorbed

During the desorption set of investigation, the desorption temperature was varied from 5 °C to 25 °C while desorption pressure was maintained at 1 bar. Before conducting desorption, for both alloys, each absorption was performed at 20 bar and 25 °C. Figures 5.5(a) and 5.5(b) show the desorption profiles attained by $La_{0.8}Ce_{0.2}Ni_5$ and $La_{0.7}Ce_{0.1}Ca_{0.3}Ni_5$ at different HTF temperatures. At the desorption temperature of 5 °C, the amount of hydrogen desorbed by $La_{0.8}Ce_{0.2}Ni_5$ and $La_{0.7}Ce_{0.1}Ca_{0.3}Ni_5$ were merely 4.26 g and 3.02 g, correspondingly. As the desorption temperature was raised from 5 °C to 15 °C, the amount of desorbed hydrogen was augmented by ~6 times and ~7.8 times for $La_{0.8}Ce_{0.2}Ni_5$ and $La_{0.7}Ce_{0.1}Ca_{0.3}Ni_5$, respectively. Further increase in desorption temperature from 15 °C to 25 °C resulted in a rise in desorbed amount by 1.27 times and ~2 times for $La_{0.8}Ce_{0.2}Ni_5$ and $La_{0.7}Ce_{0.1}Ca_{0.3}Ni_5$, correspondingly. With the rise in desorption temperature, the amount of hydrogen desorbed also increases as the pressure differential between equilibrium pressure and desorption pressure increases.

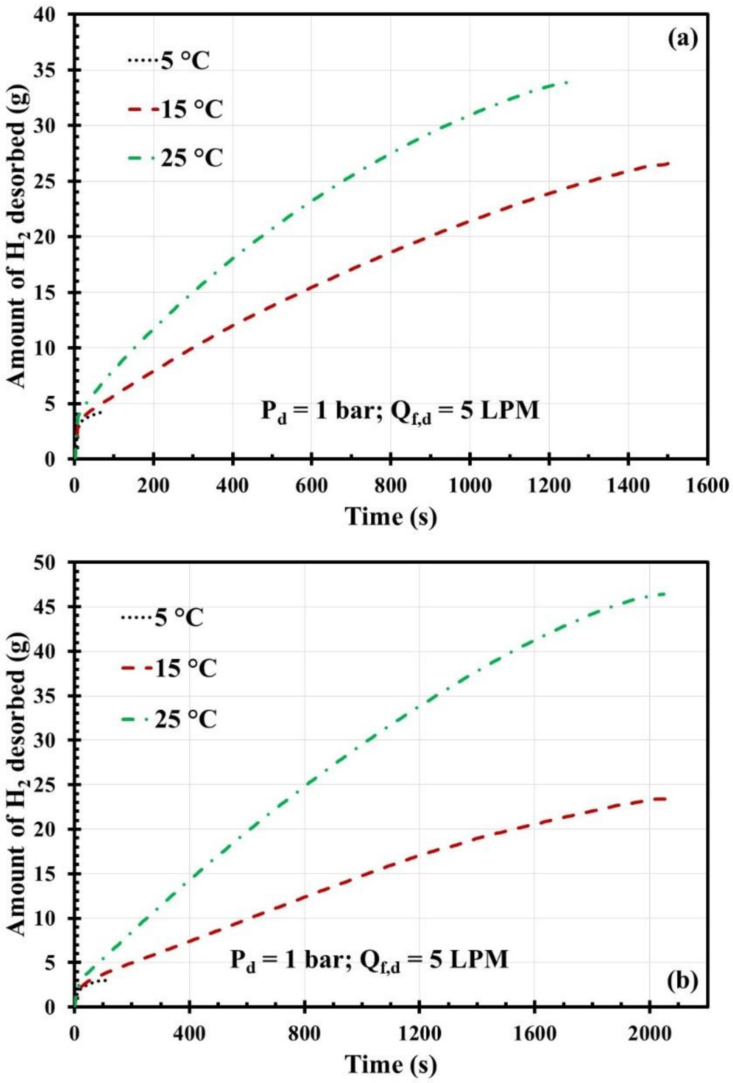

Fig. 5.5: Influence of HTF temperature alteration on desorbed mass (a) $La_{0.8}Ce_{0.2}Ni_5$ and (b) $La_{0.7}Ce_{0.1}Ca_{0.3}Ni_5$.

Influence of HTF temperature on cooling produced

Figure 5.6 depicts the effect of HTF temperature variation on the cumulative cold output and cooling rate for $La_{0.8}Ce_{0.2}Ni_5$ and $La_{0.7}Ce_{0.1}Ca_{0.3}Ni_5$. At 5 °C, the cold output produced by $La_{0.8}Ce_{0.2}Ni_5$ was only 5 kJ in 79 s with a peak and average cooling rate of 0.15 kW and 0.07 kW, correspondingly. Whereas, under the same condition, $La_{0.7}Ce_{0.1}Ca_{0.3}Ni_5$ could harness an average and peak cooling rate of 0.13 kW and 0.22 kW, generating ~16 kJ cold output in 125 s. At 5 °C, achieving a sustained cooling effect was not feasible as the equilibrium pressure at this temperature would be very close to 1 bar, leading to discontinuation of desorption within a short time (~120 s). As the desorption temperature was raised from 5 °C to 15 °C, the quantity of cold output harnessed by $La_{0.8}Ce_{0.2}Ni_5$ and

$La_{0.7}Ce_{0.1}Ca_{0.3}Ni_5$ increased by ~41 times and ~17 times, amounting to 224.4 kJ and 274.3 kJ, respectively. The peak and average cooling rate achieved at 15 °C desorption condition by $La_{0.8}Ce_{0.2}Ni_5$ and $La_{0.7}Ce_{0.1}Ca_{0.3}Ni_5$ were 0.31 kW, 0.15 kW, and 0.34 kW, 0.13 kW, respectively. With a further rise in desorption temperature from 15 °C to 25 °C, the cold output generated by $La_{0.8}Ce_{0.2}Ni_5$ was raised by 1.08 times, while $La_{0.7}Ce_{0.1}Ca_{0.3}Ni_5$ cold output was raised by ~1.6 times. The peak and average cooling rates attained by $La_{0.8}Ce_{0.2}Ni_5$ and $La_{0.7}Ce_{0.1}Ca_{0.3}Ni_5$ at 25 °C desorption were 0.48 kW, 0.19 kW, and 0.43 kW, 0.21 kW, respectively. The cooling performance of the alloys at different HTF temperatures indicates that $La_{0.7}Ce_{0.1}Ca_{0.3}Ni_5$ is a better candidate for cooling applications compared to $La_{0.8}Ce_{0.2}Ni_5$ in the temperature range of 15-25 °C.

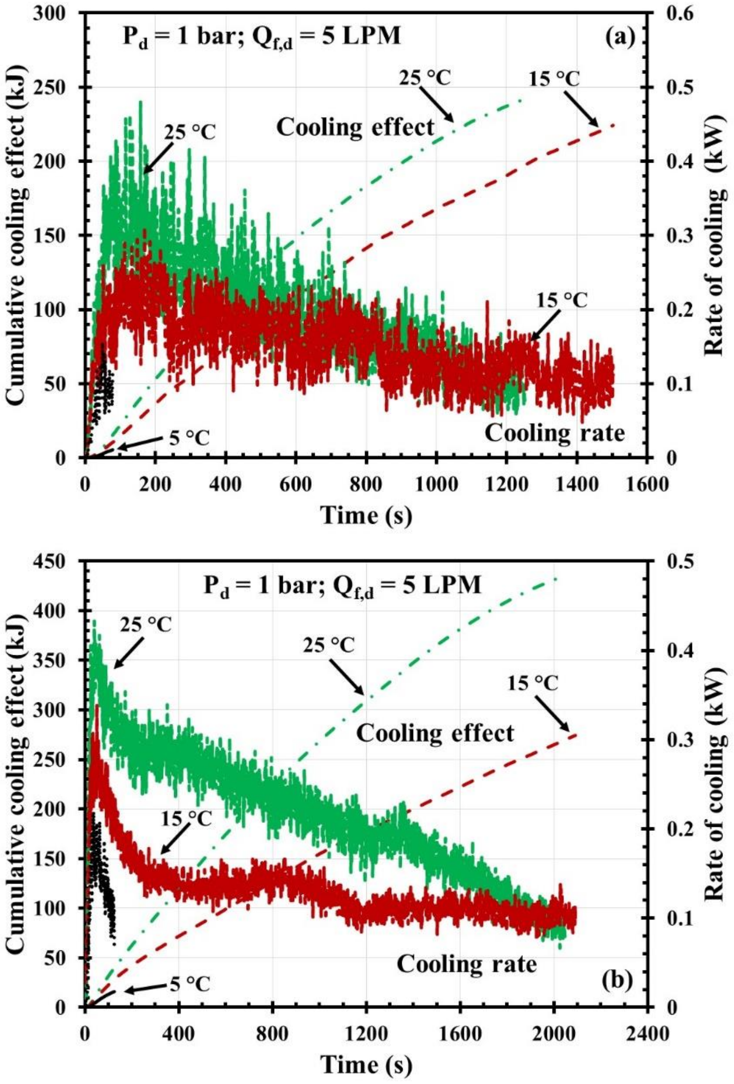

Fig. 5.6: Influence of HTF temperature alteration on cooling performance (a) $La_{0.8}Ce_{0.2}Ni_5$ and (b) $La_{0.7}Ce_{0.1}Ca_{0.3}Ni_5$.

5.3. Experiments on open cycle cooling systems driven by compressor

5.3.1. Concept of operation of an open cycle compressor driven cooling system

The underlying operating principle of an open cycle compressor-driven cooling system (OC-CDMHCS) has been schematically represented in Fig. 5.7. The primary components of an OC-CDMHCS are a hydrogen storage tank, MH reactor and a hydrogen compressor. The MH reactor would be operating between two modes, i.e., cooling mode and regeneration mode. During cooling operation, it would desorb hydrogen (by taking away the heat from the cooling space), which would be delivered to the PEMFC through a compressor. Meanwhile, the hydrogen compressor can be run from the part of the electricity generated by PEMFC. Once the MH reactor is fully desorbed, it can be regenerated from electrolyser. During regeneration, the heat of regeneration can be dissipated to the ambient. To obtain a quasi-continuous cooling effect, a pair of MH reactors can be arranged in parallel so that when one reactor operates in cooling mode, the other reactor can be regenerated. The key advantage of such a system is that for regeneration of the reactor, merely 30-40 bar hydrogen supply pressure would be sufficient, thus eliminating the need of high-pressure hydrogen tank (150-700 bar). Such systems can be easily integrated with a renewable energy-driven electrolyser to regenerate the MH reactors. As the purity of the desorbed hydrogen would be fuel-cell grade (> 99.9995%), it can be directly fed to a fuel cell for power generation. The system would simultaneously act a green hydrogen storage module as well as a cooling and purification system.

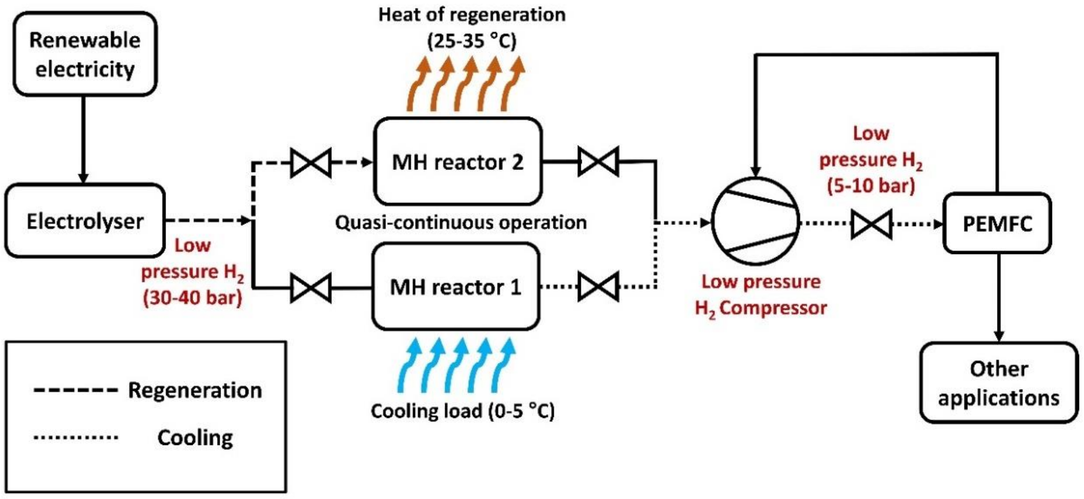

Fig. 5.7: Principle of operation of an OC-CDMHCS.

5.3.2. Description of MH alloy

The MH alloys used for cooling experiments with a compressor are the same as those used in cooling experiments without a compressor, i.e., $La_{0.8}Ce_{0.2}Ni_5$ and $La_{0.7}Ce_{0.1}Ca_{0.3}Ni_5$.

5.3.3. Components of the experimental setup

The components of the experimental setup, including reactors, are unchanged as described in section 5.2.2, except the inclusion of a hydrogen compressor. The compressor used is a hermetically sealed oil-lubricated refrigerant compressor (R-134a) customized to serve the purpose of hydrogen compression. The compressor surface was coiled with a water flow liner (copper tube) to take away the heat of hydrogen compression. The compressor could operate expediently between 1-16 bar up to 0.5 $g.s^{-1}$ hydrogen flow rate. An oil separator was engaged in the discharge circuit to refrain any oil contamination in the gas circuit or reactors. The compressor has a designed cooling capacity of 1 TR. The photograph of the compressor is shown in Fig. 5.8.

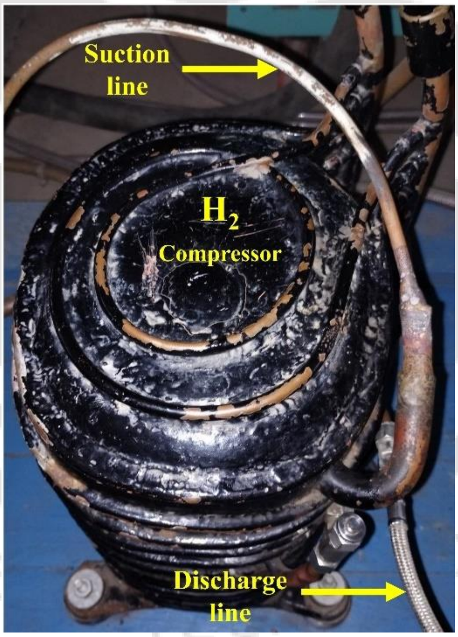

Fig. 5.8: Photograph of the hydrogen compressor.

5.3.4. Description of the experimental protocol

Figure 5.9 displays the schematic of operation of an OC-CDMHCS and the major components of the test setup. There are two half cycles in the experiment: regeneration and cooling. During regeneration, hydrogen is supplied from the hydrogen cylinder at a constant set pressure. The hydrogen flow path is set by opening the valves V1, V2, V11, V3 and V6. While regeneration is in process, all other valves are closed. Once the desired amount of hydrogen is transferred to the reactor, the regeneration process is stopped by closing valve V6. To facilitate heat removal during regeneration, water at a medium temperature (30-35 °C) is circulated through the reactor. Before the desorption/cooling cycle can be processed, HTF at desired cooling temperature is pumped through the reactor and taken to the cooling temperature. During the cooling cycle, hydrogen gas travels through the compressor and is eventually discharged to the ambient. In the course of the cooling cycle, the valves V6, V4, V9, V10, V5 and V7 are set to open, and all other valves are closed. The sole purpose of the compressor in this experiment is to facilitate a sustained cooling effect at a sub-ambient temperature range (5-20 °C). Once the desired cooling cycle time is completed, desorption is stopped by closing the valves V6, V9, V10 and V7 simultaneously, and compressor power is turned off. In the next regeneration cycle, the amount of hydrogen desorbed in replenished. For subsequent test cycles, the same procedure is followed.

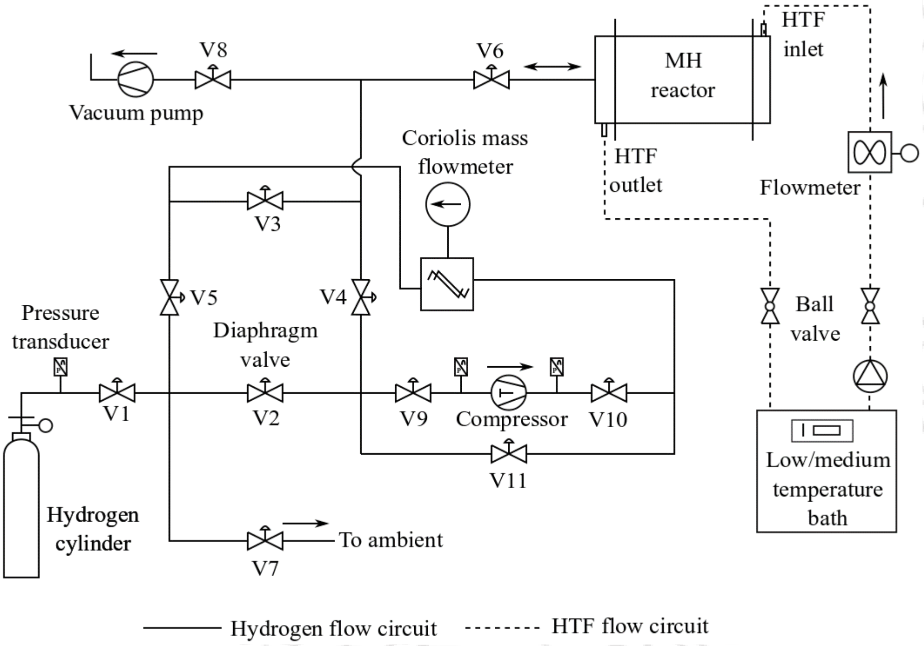

Fig. 5.9: Schematic of operation of OC-CDMHCS.

5.3.5. Activation of the MH alloys

The activation procedure of $La_{0.8}Ce_{0.2}Ni_5$ in 19 TBR module is already stated in section 4.2.4. The second reactor filled with an identical amount of $La_{0.8}Ce_{0.2}Ni_5$ was activated within 4 cycles.

5.3.6. Compressor driven cooling performance of $La_{0.8}Ce_{0.2}Ni_5$ and $La_{0.7}Ce_{0.1}Ca_{0.3}Ni_5$

Parametric study

A set of experiments were conducted to assess the influence of operating parameters on cooling performance. The designated operating parameters and their operation range are provided in Table 5.2.

Table 5.2: Scheme of the parametric study for open cycle cooling with compressor

Process	Operating parameter	Range	Remarks
Cooling	Refrigeration temperature (T_{ref}):	5-20 °C	Desorption Pressure (P_d) set at: 1 bar; HTF flow rate ($Q_{f,\ ref}$) set at:: 5 LPM
	Half-cycle time (t_{hc}):	120-480 s	Desorption Pressure (P_d) set at: 1 bar; HTF flow rate ($Q_{f,\ ref}$) set at:: 5 LPM

Open cycle cooling behaviour with compressor

Performance parameters

The key performance indices evaluated for the cooling system are COP and SCP. In continuation with the estimation of cooling power and cumulative cooling effect represented in (Eq. (5.1) -(5.2)), instantaneous COP can be estimated using Eq. (5.3).

Instantaneous COP: $$COP_i = \frac{Q_c(t)}{P_c(t)} \tag{5.3}$$

where *'P(t)'* denotes instantaneous compressor input power.

In a similar manner, the mean COP can be estimated using Eq. (5.4).

Mean COP: $$COP_m = \frac{\int_0^t Q_c(t)\,dt}{\int_0^t P_c(t)\,dt} \tag{5.4}$$

Also, the specific cooling power (SCP) can be obtained by Eq. (5.5).

Specific Cooling Power: $$SCP = \frac{Q_t}{m_a t_{hc}} \tag{5.5}$$

where *'m_a'* stands for the mass of alloy and 't_{hc}' denotes cooling half-cycle time.

Characterization of compressor and cooling power profile

The temporal variation in compressor power input, cooling power output and instantaneous COP for the alloys $La_{0.8}Ce_{0.2}Ni_5$ and $La_{0.7}Ce_{0.1}Ca_{0.3}Ni_5$ are shown in Fig. 5.10. In the beginning of desorption, the compressor power input is the highest for both the alloys as the mass flow rate of the hydrogen is the highest. As desorption proceeds forward, the power input reduces significantly within the first 15-20 s and then steadily goes down till the end of the cycle. In contrast, the cooling power output is the lowest in the beginning, which gradually goes up and then becomes almost steady till the end of desorption.

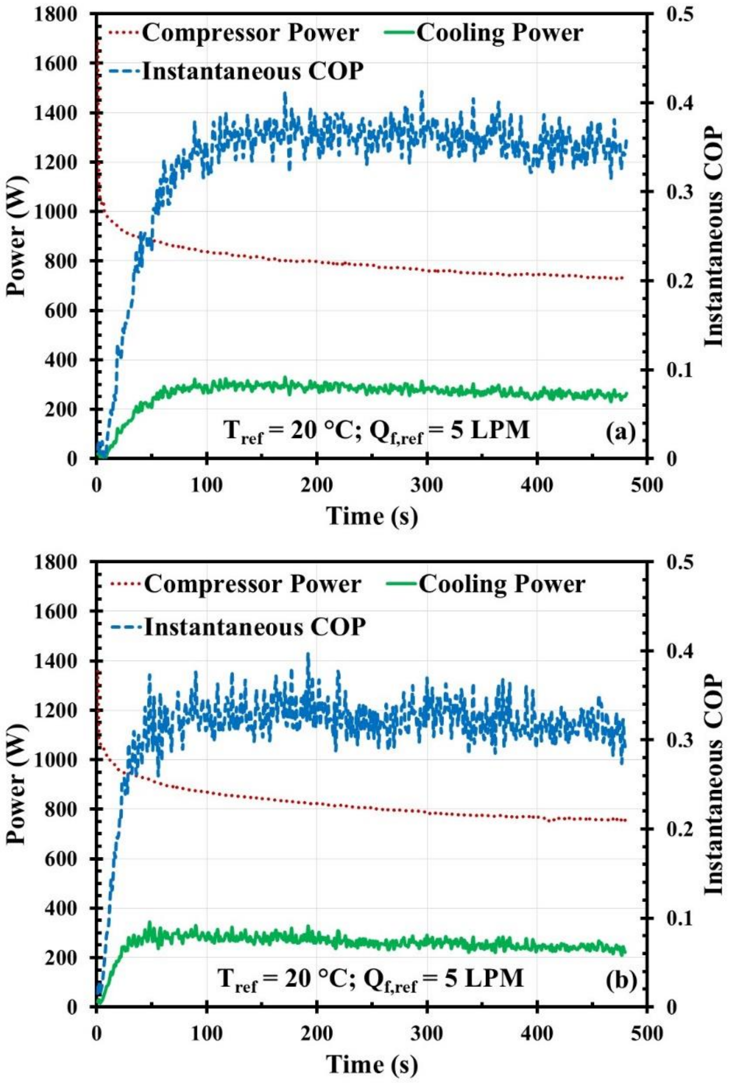

Fig. 5.10: Temporal variation of compressor power, cooling power and instantaneous COP for (a) $La_{0.8}Ce_{0.2}Ni_5$ and (b) $La_{0.7}Ce_{0.1}Ca_{0.3}Ni_5$.

The COP being dependent on both cooling power output and compressor power input, increased drastically from a minimum value to a maximum and then became steady till the end of the cycle. The maximum value of compressor power input and cooling power was 1680 W and 330 W, respectively, for $La_{0.8}Ce_{0.2}Ni_5$ (Fig. 5.10(a)). Whereas, for $La_{0.7}Ce_{0.1}Ca_{0.3}Ni_5$ (Fig. 5.10(b)), the maximum compressor and cooling powers were 1360 W and 343 W, correspondingly. The maximum value of instantaneous COP estimated for $La_{0.8}Ce_{0.2}Ni_5$ and $La_{0.7}Ce_{0.1}Ca_{0.3}Ni_5$ was 0.41 and 0.4, respectively.

Influence of half-cycle time and refrigeration temperature on the amount of hydrogen transferred

Figure 5.11 shows the influence of HC time variation on the amount of hydrogen transferred at different refrigeration temperatures for $La_{0.8}Ce_{0.2}Ni_5$ and $La_{0.7}Ce_{0.1}Ca_{0.3}Ni_5$.

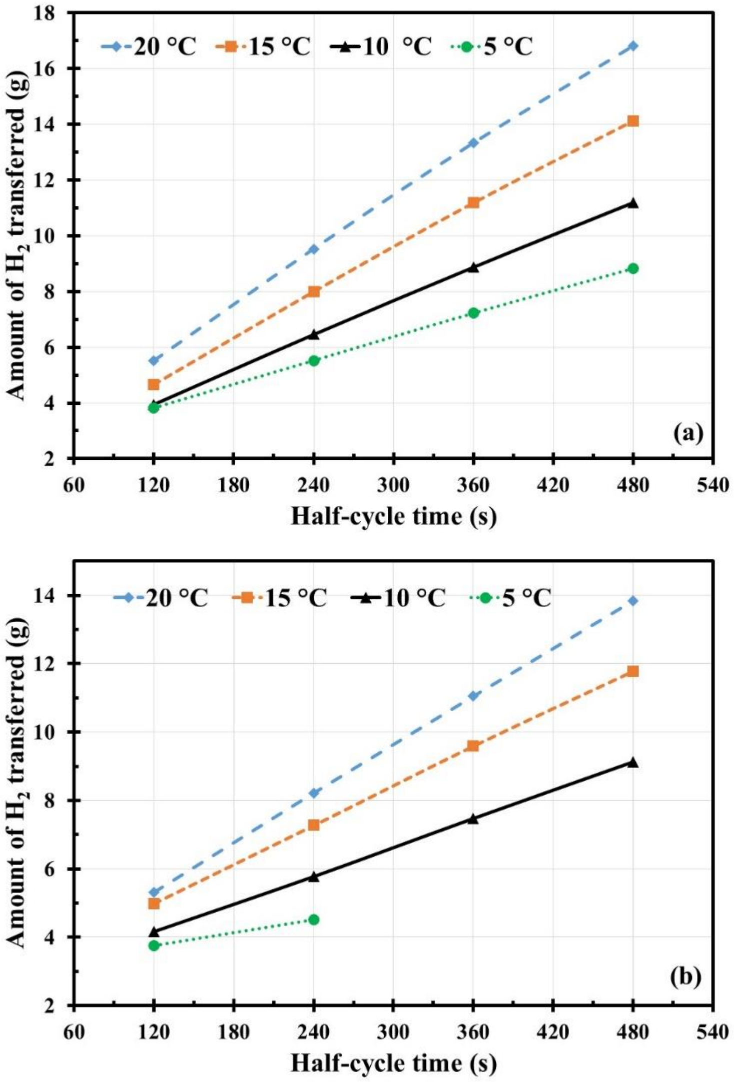

Fig. 5.11: Influence of half-cycle time and refrigeration temperature alteration on H_2 transfer for (a) $La_{0.8}Ce_{0.2}Ni_5$ and (b) $La_{0.7}Ce_{0.1}Ca_{0.3}Ni_5$.

For both alloys, at any given refrigeration temperature, as the HC time was increased, the amount of hydrogen transferred was also increased, which is apparent as the amount of hydrogen transferred would rise until the MH reactor is completely desorbed. For $La_{0.8}Ce_{0.2}Ni_5$ at 20 °C refrigeration temperature, the amount of hydrogen transferred was 5.5 g for 120 s HC time, which increased by 73% and 205% when cycle time was increased to 240 s and 480 s, respectively. Analogously, the amount of hydrogen transferred for $La_{0.7}Ce_{0.1}Ca_{0.3}Ni_5$ was increased by 54.8% and 160.8% from a base value of 5.3 g (at 20 °C, 120 s), extended to 240 s and 480 s, individually. However, for both alloys, the rate of hydrogen transfer was slowed down as the cycle time was extended.

Also, it can be observed from Fig. 5.11 that at any given cycle time duration, as refrigeration temperature was increased, the amount of hydrogen transferred was also increased. An increase in refrigeration temperature results in an increase in the desorption pressure, which eventually leads to an increase in the initial hydrogen desorption rate. Since complete hydrogen desorption would not be accomplished within the stipulated time period of 480 s, with an increase in refrigeration temperature, the quantity of desorbed hydrogen would also be higher. For $La_{0.8}Ce_{0.2}Ni_5$ and $La_{0.7}Ce_{0.1}Ca_{0.3}Ni_5$, the amount of hydrogen transfer was increased from 11.18 g to 16.82 g and 9.13 g to 13.84 g when refrigeration temperature was increased from 10 °C to 20 °C (HC time:480 s).

Influences of half-cycle time and refrigeration temperature on mean COP

The influences of HC time and refrigeration temperature on mean COP for $La_{0.8}Ce_{0.2}Ni_5$ and $La_{0.7}Ce_{0.1}Ca_{0.3}Ni_5$ are depicted in Fig. 5.12. At 20 °C refrigeration temperature, for 120 s HC time, the estimated mean COP was 0.26 and 0.27 for $La_{0.8}Ce_{0.2}Ni_5$ and $La_{0.7}Ce_{0.1}Ca_{0.3}Ni_5$. When HC time was extended from 120 s to 240 s, the mean COP was increased by 22.8% ($La_{0.8}Ce_{0.2}Ni_5$) and 10.2% ($La_{0.7}Ce_{0.1}Ca_{0.3}Ni_5$), correspondingly. However, further extension of HC time resulted in only 6.4% (240 s to 360 s) and 3% (360 s to 480 s) rise in mean COP for $La_{0.8}Ce_{0.2}Ni_5$. Then again, under identical operating conditions, for $La_{0.7}Ce_{0.1}Ca_{0.3}Ni_5$, the corresponding increment was only 2.5% (240 s to 360 s) and 0.7% (360 s to 480 s). At lower refrigeration temperatures (10-15 °C), similar mean COP variations were observed for $La_{0.8}Ce_{0.2}Ni_5$; although at 5 °C, the mean COP decreased beyond 360 s owing to an extremely low desorption rate. On the other hand, for $La_{0.7}Ce_{0.1}Ca_{0.3}Ni_5$, the mean COP reduced marginally beyond 360 s (0.04%) and 240 s (0.75%) at 15 °C and 10 °C, respectively.

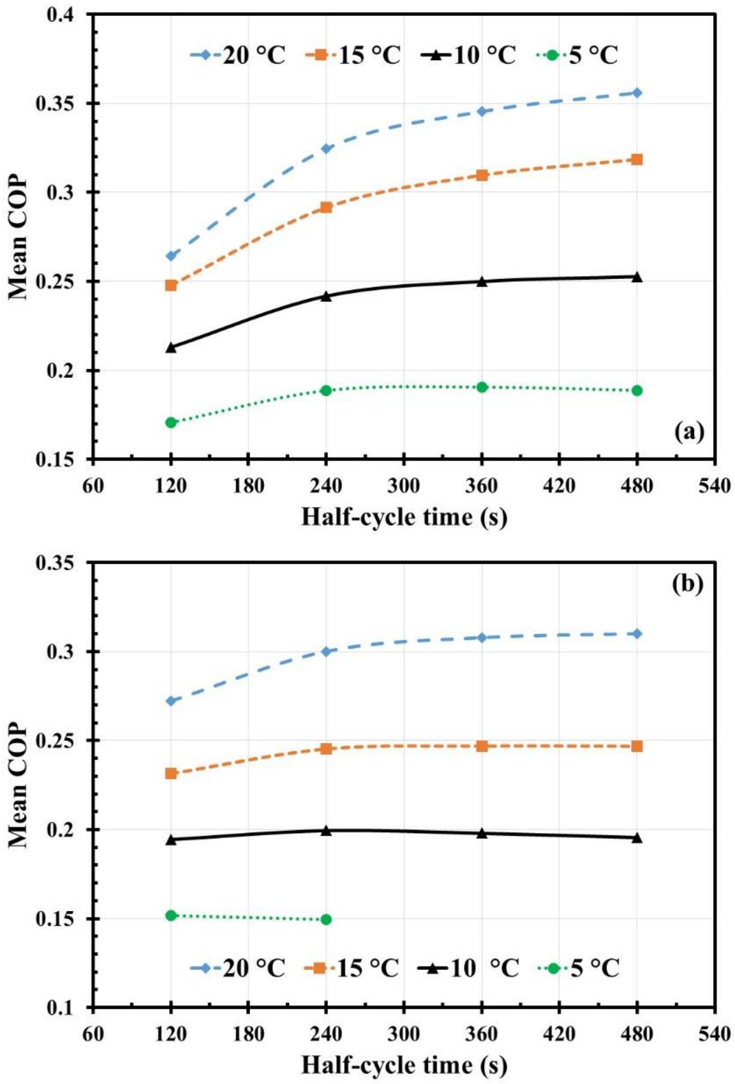

Fig. 5.12: Influence of half-cycle time and refrigeration temperature alteration on mean COP for (a) $La_{0.8}Ce_{0.2}Ni_5$ and (b) $La_{0.7}Ce_{0.1}Ca_{0.3}Ni_5$.

Hydrogen could not be desorbed beyond 4.69 g (280 s) even with the aid of compressor at 5 °C for $La_{0.7}Ce_{0.1}Ca_{0.3}Ni_5$. For both the alloys, the mean COP first increased up to a cycle time duration of 240 s, and then depending upon the relative sinking rate of compressor power and cooling power, it was either increased or decreased therefore. With an increase in cooling temperature, the mean COP increases as the compressor power input remains almost unaffected by variation in cooling temperature. For $La_{0.8}Ce_{0.2}Ni_5$ and $La_{0.7}Ce_{0.1}Ca_{0.3}Ni_5$, the increase in mean COP (HC time: 480 s) was 40.8% and 58.4% when refrigeration temperature was changed from 10 °C to 20 °C.

Influence of half-cycle time and refrigeration temperature on mean SCP

Figure 5.13 shows the variation of SCP with cycle time at different refrigeration temperatures for $La_{0.8}Ce_{0.2}Ni_5$ and $La_{0.7}Ce_{0.1}Ca_{0.3}Ni_5$. At 20 °C refrigeration temperature, the mean SCP achieved for $La_{0.8}Ce_{0.2}Ni_5$ at 120 s, 240 s, 360s, and 480 s were s 72.8 $W.kg^{-1}$, 84.5 $W.kg^{-1}$, 86.6 $W.kg^{-1}$, and 86.8 $W.kg^{-1}$, respectively reflecting increment of 15.9%, 18.8% and 19.2% over every 120 s from 120-480 s HC duration. At 15 °C, a similar trend of SCP variation with cycle time was observed, although at 10 °C and 5 °C cases, beyond 240 s HC time, the SCP remained almost the same or decreased a bit. For $La_{0.7}Ce_{0.1}Ca_{0.3}Ni_5$, at 20 °C refrigeration temperature, the mean SCP achieved at 120 s, 240 s, 360s, and 480 s were s 73.1 $W.kg^{-1}$, 76.95 $W.kg^{-1}$, 76.4 $W.kg^{-1}$, and 75.11 $W.kg^{-1}$, respectively reflecting a change of 5.26% rise, 0.7% drop and 1.7% drop over every 120 s from 120-480 s HC duration.

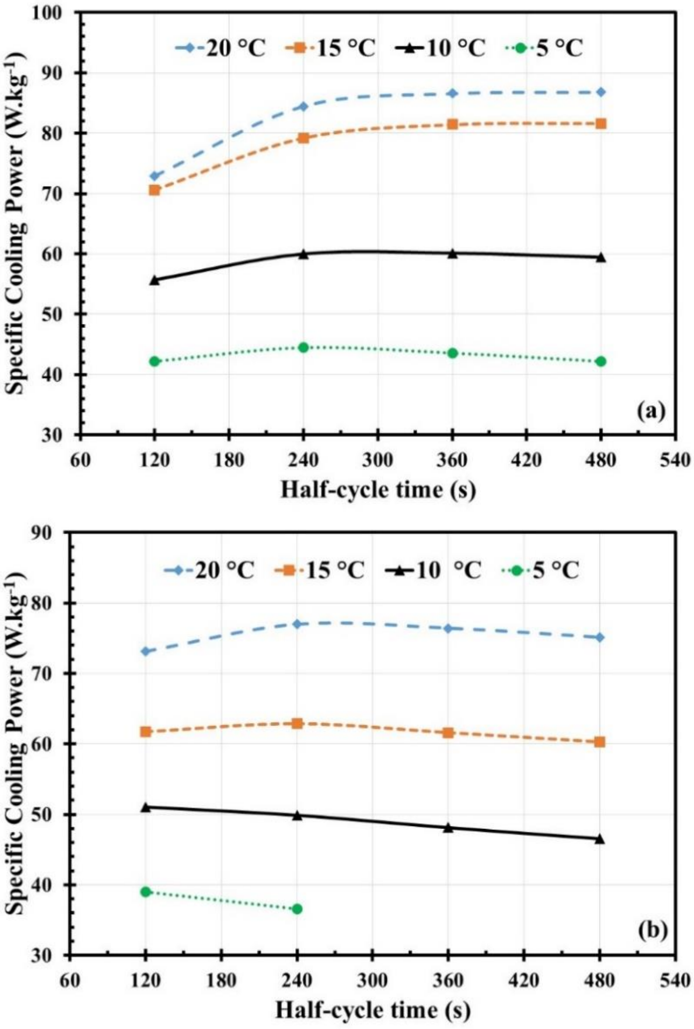

Fig. 5.13: Influence of half-cycle time and refrigeration temperature alteration on SCP for (a) $La_{0.8}Ce_{0.2}Ni_5$ and (b) $La_{0.7}Ce_{0.1}Ca_{0.3}Ni_5$.

A similar variation in SCP was witnessed at 15 °C refrigeration temperature. However, for 5-10 °C refrigeration temperature, the SCP value steadily dropped from 120 to 480 s HC time, as the hydrogen desorption rate was substantially low. With progress in cycle time, the rate of cooling increases first and then steadily decreases. At any given HC time duration, as the refrigeration temperature was increased, SCP was increased as the desorption rate would go up at higher temperatures. Increments in SCP value (HC time: 480 s) as high as 106% and 61.2% were registered for $La_{0.8}Ce_{0.2}Ni_5$ and $La_{0.7}Ce_{0.1}Ca_{0.3}Ni_5$ when refrigeration temperature was changed from 10 °C to 20 °C.

5.4. Summary

In this chapter, experimental outcomes of the open-cycle cooling systems are discussed. The cooling experiments have been performed with and without the aid of a mechanical compressor. The technical concept of an open-cycle compressor-driven cooling system has been presented. Two different MH alloys, namely $La_{0.8}Ce_{0.2}Ni_5$ and $La_{0.7}Ce_{0.1}Ca_{0.3}Ni_5$ have been experimented by varying the operational parameters. In open-cycle cooling tests without compressor, the optimum regeneration and cooling conditions have been determined by varying the supply pressure, and HTF temperature for regeneration and cooling. Whereas, in cooling tests with a compressor, a series of parametric tests have been conducted to assess the influence of half-cycle time and refrigeration temperature on the amount of hydrogen transferred, COP and SCP.

6. Experiments on MH based closed-cycle cooling system

6.1. Introduction

In this chapter, the experimental outcomes of a closed-cycle compressor driven cooling system are presented. A number of closed-cycle cooling tests aided by a mechanical compressor was performed on a pair of 19 TBR reactor module packed with $La_{0.8}Ce_{0.2}Ni_5$. In this work, in a first, an attempt has been made to understand the behaviour of a large-scale (~300 g hydrogen) compressor-operated cooling system. To ensure the compressor is able to handle the flow rate and pressure ramp during cyclic operation, open cycle desorption tests via compressor was performed beforehand.

6.2. Experiments on closed cycle compressor driven cooling system

6.2.1. Description of MH alloy

The MH alloy used for closed-loop cooling experiments operated by a compressor is $La_{0.8}Ce_{0.2}Ni_5$. The PCT characteristic of the alloy is given in section 4.2.1.

6.2.2. Components of the experimental setup

The test setup comprised of two identical MH reactors, a hydrogen compressor, hydrogen flow control circuit, a hydrogen mass flow meter, a constant low-temperature bath, a constant medium-temperature bath, mass flow meters for water flow measurement, and a water flow control circuit. The MH reactors used in this experiment are an identical pair 19 TBR modules, one of which is already used for hydrogen storage experiments mentioned in section 4.2. Another 19 TBR module was filled with 26.5 kg of $La_{0.8}Ce_{0.2}Ni_5$ and used for experiments. These two 19 TBR modules will be identified as TBR1 and TBR2 from now onwards. The photograph of the test setup is shown in Fig. 6.1. The details of the thermocouples and pressure transducers attached to the TBR1 used are already stated in section 4.2.2. The other module (TBR2) was also equipped with 4 ‘K’ type thermocouples and a pressure transducer.

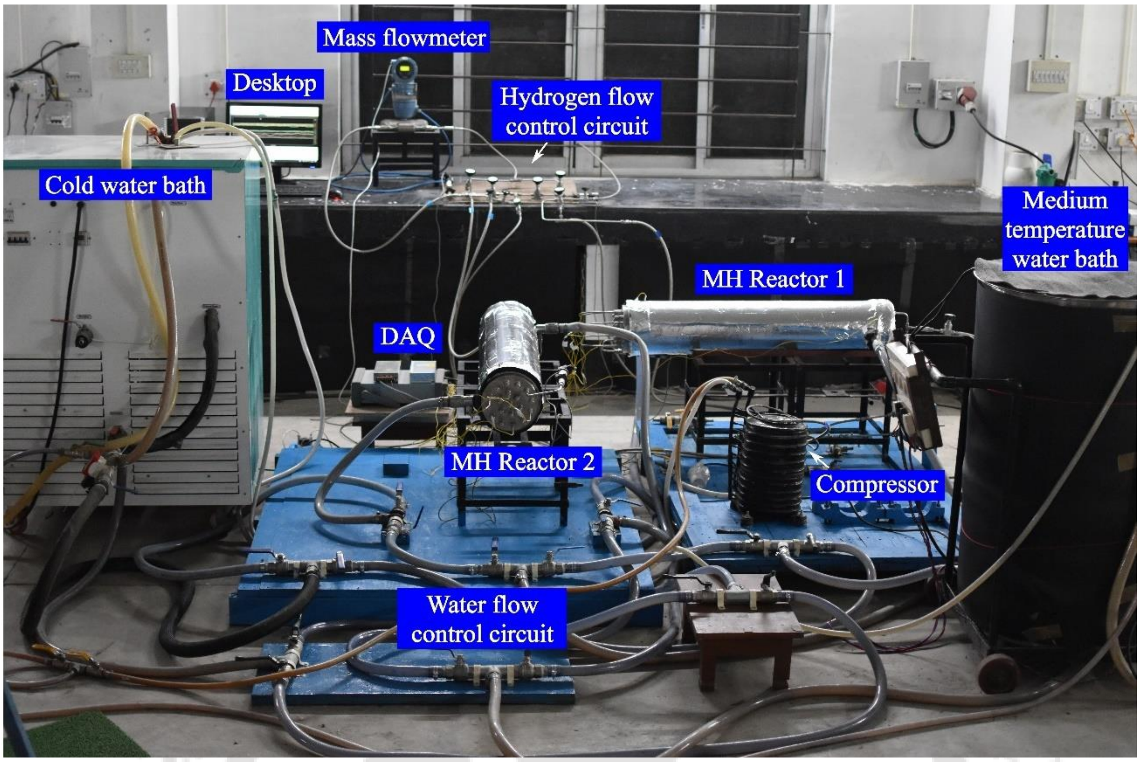

Fig. 6.1: Photograph of coupled bed compressor driven cooling test bench.

6.2.3. Description of the experimental protocol

The diagrammatic representation of test procedure is shown in Fig.6.2. The general absorption and desorption experiment protocols have been mentioned in section 4.2.3. After the successful activation of the MH reactors, another couple of absorption-desorption cycles on each reactor were done to ensure the repeatability of the results. Before starting compressor-driven cooling tests, reactor TBR1 was charged with approximately 90% of the reversible hydrogen content (~336 g), while TBR2 was charged with approximately 70% of the reversible hydrogen content (~252 g). The hydrogen flow circuit was detached from both the hydrogen cylinder as well as vacuum pump before starting the cooling tests. In the first HC, TBR1 desorbed and TBR2 absorbed. Before the first HC commences, the valves V6, V2, V7, V8 and V3 were opened and all other valves were closed. Also, cold water was supplied through TBR1, whereas medium temperature water was circulated through the TBR2 and it was made sure the TBR1 and TBR2 are at the desired refrigeration and sink temperatures. To commence the first HC, the reactor valves V11 and V10 are opened and then the compressor is switched on almost simultaneously. As soon as the first half cycle starts, the desorbed hydrogen from TBR1 is pumped to TBR1. Once the predefined half-cycle time is over, valves V11 and V10 are shut off and the compressor is switched off simultaneously. Once the 1st HC is concluded, the valves V11 and V10 are shut off and the compressor is switched off simultaneously. Alongside, the valves V6, V2, V7, V8 and V3 are also closed. The temperature inside the reactor beds and water inlet and outlet temperature are measured using ‘K’ type thermocouples, while the gauge pressure inside the reactor beds and in the suction and discharge line of the compressor is measured by using piezo resistive pressure transducers (0-100 bar). A data acquisition system is employed to record the temperature, pressure and mass flow rate data at every second. After the end of the first HC, the water flow valves are switched such that cold water is supplied through TBR2 and medium temperature is supplied through TBR1. Before the second HC commences, the valves V4, V7, V8, V5, and V6 are opened and all other valves are closed. To commence the second HC, the reactor valves V10 and V11 are opened and the compressor is switched on simultaneously. With the second HC beginning, hydrogen is transferred from TBR2 to TBR1 through the compressor. Similarly, to 1st HC, 2nd HC is continued till a predefined time duration. Once the 2nd HC ended, the valves V10 and V11 were shut off and the compressor is switched off simultaneously. Alongside, valves V4, V7, V8, V5, and V6 are also closed. The next cycles are operated in a similar method by setting the desired refrigeration and sink temperatures.

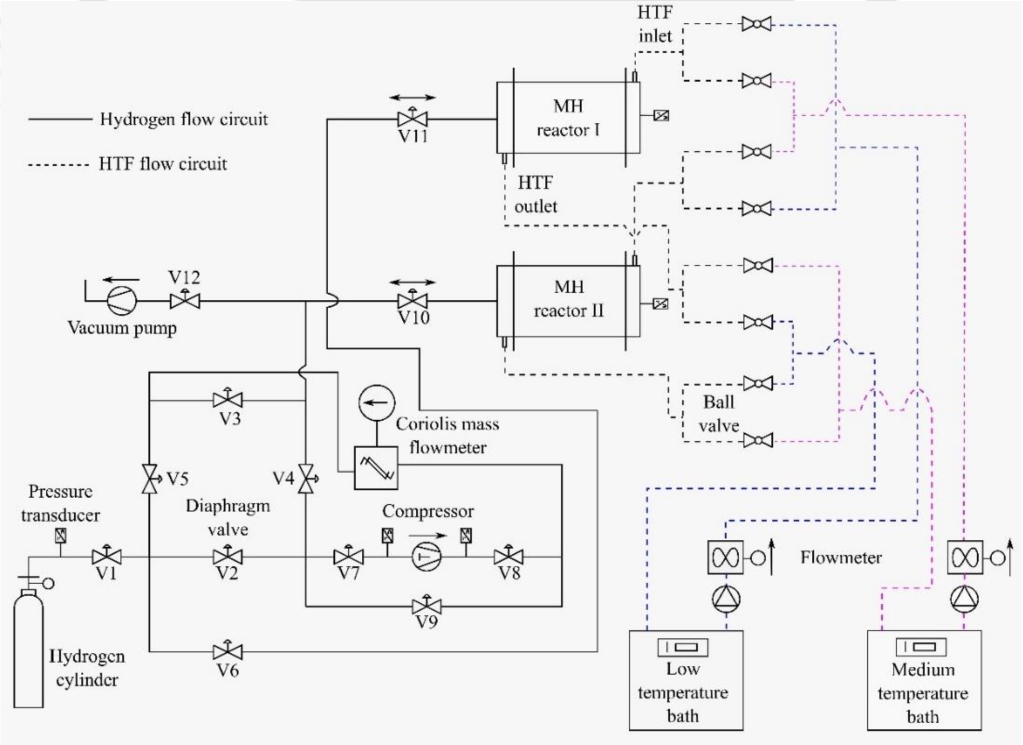

Fig. 6.2: Schematic of operation of the coupled bed compressor driven cooling system.

6.2.4. Activation of the MH alloys

The activation procedure of $La_{0.8}Ce_{0.2}Ni_5$ in the TBR1 module is already stated in section 4.2.4. The second reactor (TBR2) filled with an identical amount of $La_{0.8}Ce_{0.2}Ni_5$ (26.5 kg) was activated following a similar protocol within 7 cycles subjected to absorptions at 25 bar, 15 °C and desorption at 80 °C.

6.2.5. Cooling performance analysis of the coupled system

In this section, the outcomes of the experiments conducted on the compressor-driven coupled bed metal hydride-based cooling system are presented. The experiments were conducted by varying three parameters viz. refrigeration temperature (desorbing bed), sink temperature (absorbing bed), and HC time. The range of refrigeration and sink temperatures were decided based on the desorption and absorption characteristics of the chosen MH alloy from the author's previous parametric studies. While the extent of HC time was limited by the compressor's capability to transfer hydrogen for the specified time duration without being heated. Water has been used as heat transfer fluid for all the experiments performed in this experiment.

Analysis of cyclic behaviour of the coupled system

Cyclic variation of coupled reactor bed temperatures

The cyclic variation in bed temperatures of the coupled reactors for 15 °C refrigeration temperature and 30 °C sink temperature for 480 s HC time are shown in Fig. 6.3. The average bed temperature refers to the arithmetic average of the readings obtained from four thermocouples attached to each of the reactors TBR1 and TBR2. During the first HC, the TBR1 desorbs while TBR2 absorbs. The bed temperatures exhibit identical drop and rise during all the 4 HCs shown here. The maximum drop in average bed temperature during HC 1 and HC 3 for TBR1 were in the range of 2.5-3.1 °C, while the corresponding drop for TBR2 during HC 2 and HC 4 were in the range of 2.3 °C. Similarly, the maximum rise in bed temperature for TBR1 during HC 2 and HC 4 was in the range of 2.45-3.25 °C, while the corresponding rise for TBR2 during HC 1 and HC 3 was in the range of 2.2-2.3 °C. Such a small drop and rise in bed temperature can be attributed to the fact that during the coupled cooling cycle, merely 1/10th of the reversible hydrogen stored (around 36 g) is transferred between the reactors, which is again contributed by 19 MH tubes i.e. the individual MH tubes might just desorb and absorb roughly 1.8-2 g hydrogen during the complete half cycle.

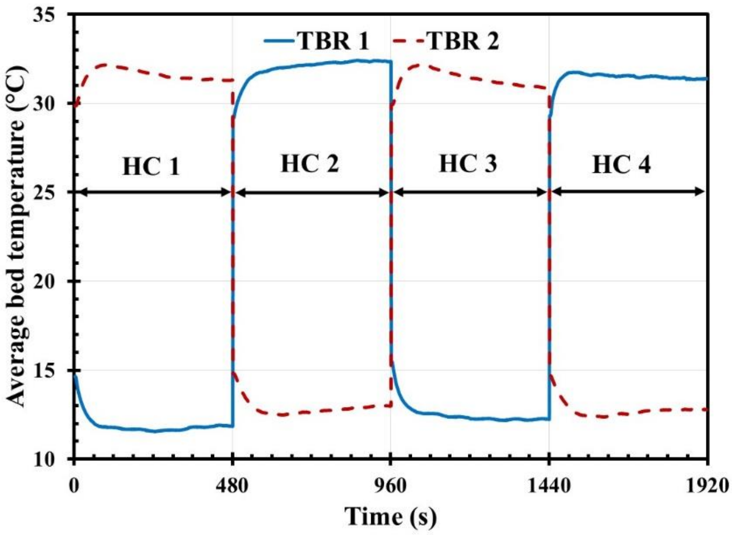

Fig. 6.3: Cyclic variation in bed temperature.

Cyclic variation of bed pressure, compressor pressure and mass flow rate

Figure 6.4(a) illustrates the variation in the reactor pressures (TBR1 and TBR2) as well as the variation in suction line and discharge line pressures of the compressor. Before starting the cyclic study, TBR1 was filled with ~336 g hydrogen, while TBR2 was filled with ~252 g hydrogen. In each half cycle of 480 s duration, approximately 36 g hydrogen was transferred between the coupled reactors. The bed pressure recorded for TBR1 varied approximately between 4 bar to 7 bar, whereas, for TBR2, it varied between approximately 1 bar to 9 bar. The compressor suction and discharge line pressure variations were in the range of 0.8 bar and 9 bar. During HC 1 and HC 3, the bed pressure for TBR1 did not descend as low as TBR2 (Case HC2 and HC4), as the starting hydrogen inventory for TBR1 was higher compared to TBR2. As the difference between TBR1 pressure and compressor suction side pressure was higher during HC1 and HC3, the rate of hydrogen transferred was marginally higher at the beginning of half cycles compared to HC 2 and HC 4, as can be observed in Fig 6.4(b). Similarly, during HC 2 and HC 4, as TBR2 desorbed, owing to low starting hydrogen inventory, the reactor pressure descended from approximately 4 bar to 0.8 bar yielding a lower mass transfer rate compared to TBR1 (Case HC 1 and HC 3). As the rate of hydrogen transfer from TBR2 to TBR1 was low, the reactor pressure for TBR1 did not climb as much as TBR2 (Case HC 1 and HC 3). The rate of hydrogen transfer for successive 4 HCs is shown in Fig 6.4(b). The rate of hydrogen transfer is the highest at the beginning of HC, as the mass transfer potential is the highest; with progression in time, the rate of transfer gradually reduces and remains quasi-steady till the end.

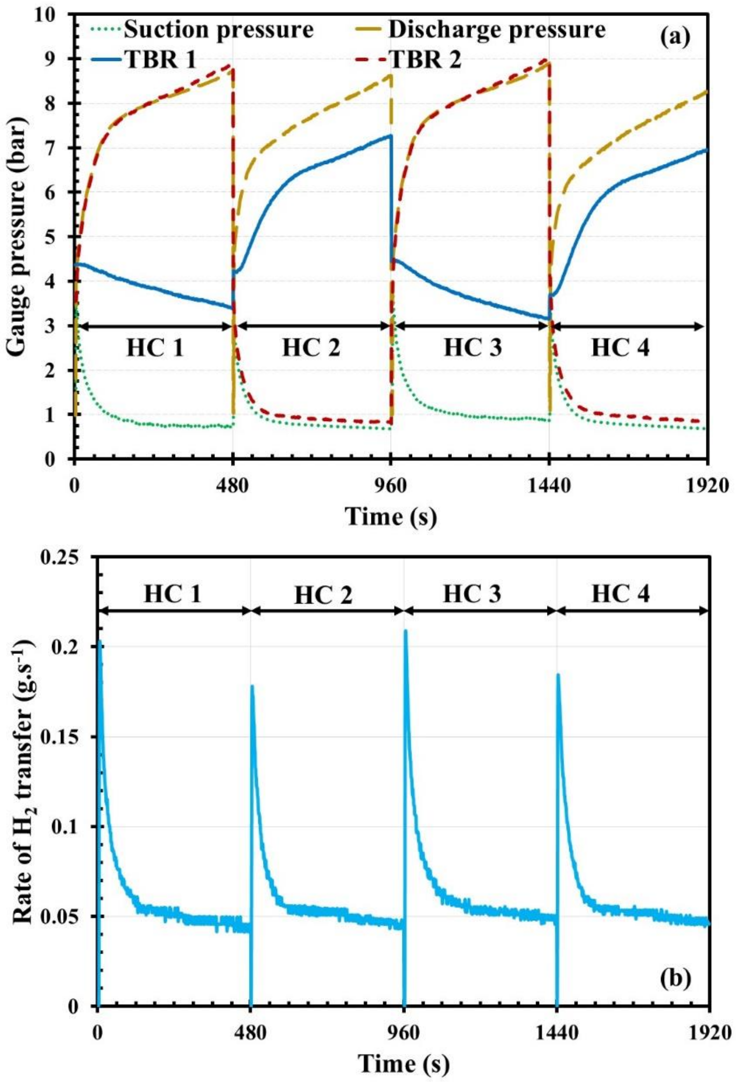

Fig. 6.4: Cyclic variation in (a) reactor and compressor pressure and (b) rate of hydrogen transfer.

Analysis of temporal variation of compressor power and cooling power

Figure 6.5 depicts the variation of compressor input power and cooling output power over time for 20 °C refrigeration temperature and 30 °C sink temperature. In the considered case, the reactor TBR2 desorbed while TBR1 absorbed. As soon as the hydrogen transfer starts, the compressor power input goes to a peak and then comes down instantly and then steadily reduces over time. Such a power consumption pattern is in accordance with the rate of hydrogen flow between the coupled reactors. However, the cooling power output steadily surges and reaches a peak only after a while and then again goes down steadily till the end. Although the rate of hydrogen transfer is highest in the beginning, the corresponding thermal response doesn't follow the same pattern owing to the low effective thermal conductivity of the MH bed. The peak and average compressor power input for the considered case were 1.81 kW (1 s) and 1.01 kW, correspondingly.

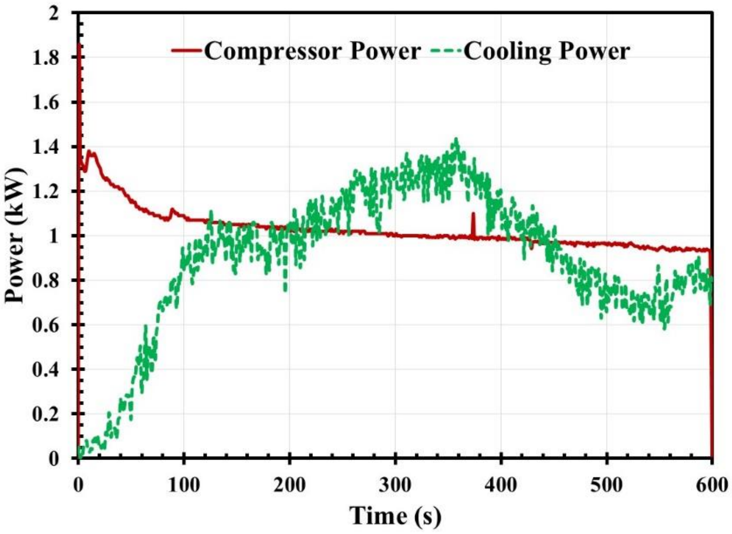

Fig. 6.5: Temporal variation of compressor power and cooling power.

Likewise, the cooling power peak and average were 1.44 kW (358 s) and 0.89 kW, respectively. The temporal variation of compressor power and cooling power jointly influence the COP of the system. The cooling power pattern directly influences both mean COP as well as SCP. The influence of some operating conditions on mean COP and SCP is discussed in the subsequent section.

6.2.6. Parametric study

The designated operating parameters and their operation range are provided in Table 6.1.

Table 6.1: Scheme of the parametric study for open cycle cooling experiments with compressor

Process	Operating parameter	Range	Remarks
Coupled bed cooling	Half-cycle time (t_{hc}):	120-600 s	HTF temperature of the refrigerating bed (T_{ref}) set at: 20 °C; HTF temperature of the sink (T_{sink}) set at: 30 °C HTF flow rate of the sink ($Q_{f, sink}$) set at: 15 LPM HTF flow rate of the refrigerating bed ($Q_{f, ref}$) set at: 10 LPM
	Sink temperature (T_{sink}):	30-35 °C	T_{ref} set at: 20 °C; $Q_{f, sink}$ set at: 15 LPM $Q_{f, ref}$ set at: 10 LPM
	Refrigeration temperature (T_{ref}):	10-20 °C	T_{sink} set at: 30 °C, $Q_{f,sink,}$ set at: 15 LPM $Q_{f, ref}$ set at: 10 LPM

Influence of refrigeration temperature variation on hydrogen transfer

Figure 6.6 illustrates the influence of refrigeration temperature variation on the rate and amount of hydrogen transferred. During this assessment, the sink temperature was fixed at 30 °C while the refrigeration temperature was varied from 10-20 °C. As portrayed in Fig. 6.6(a), at any given refrigeration temperature, the hydrogen transfer rate goes up as soon as the half-cycle starts, reaches a peak and then gradually goes down and becomes stable till the completion. The peak rate of hydrogen transferred at 10 °C, 15 °C and 20 °C were 0.12 $g.s^{-1}$, 0.21 $g.s^{-1}$, and 0.45 $g.s^{-1,}$ respectively, whereas the average rates of hydrogen transfer were 0.046 $g.s^{-1}$, 0.063 $g.s^{-1}$ and 0.081 $g.s^{-1}$. For a specified sink temperature, at a higher refrigeration temperature, the rate of hydrogen transfer is higher as the equilibrium pressure difference between the coupled reactor is higher. For an HC duration of 480 s, the cumulative amount of hydrogen transferred at 10 °C, 15 °C and 20 °C were 22.12 g, 30.41 g, and 39.12 g, respectively (Fig. 6.6(b)).

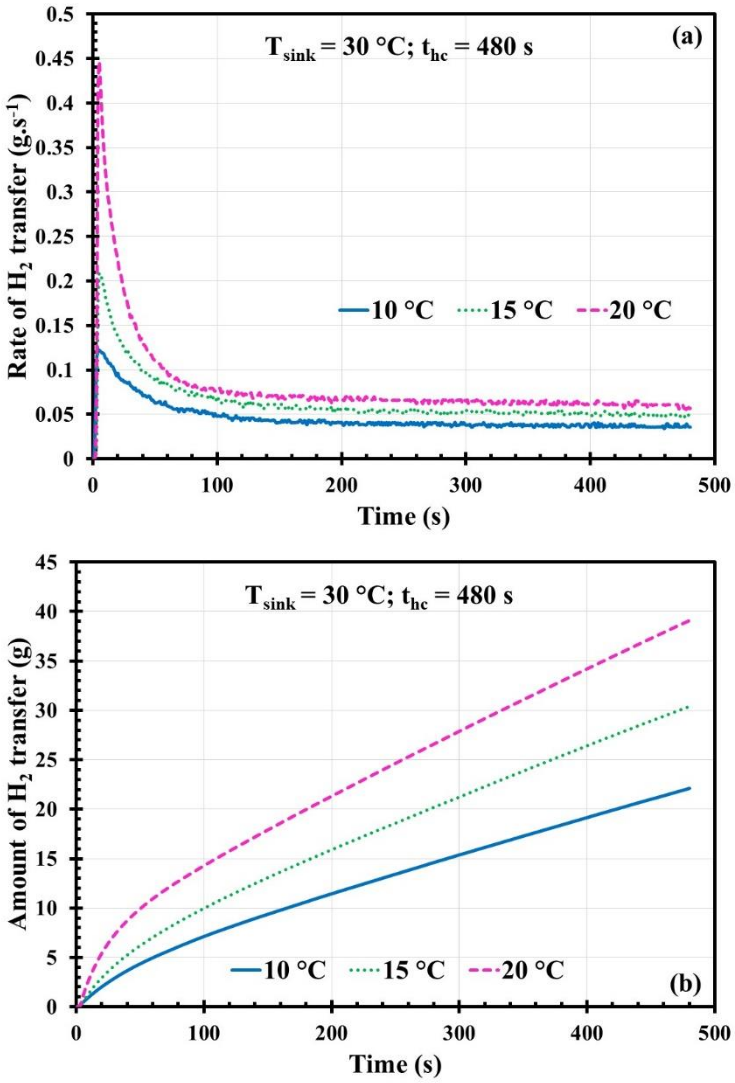

Fig. 6.6: Influence of refrigeration temperature on (a) rate of hydrogen transferred and (b) amount of hydrogen transferred.

Influence of refrigeration temperature and half cycle time variation on mean COP

Figure 6.7 illustrates the influence of refrigeration temperature and HC time variation on mean COP. The mean COP was estimated using Eq. (5.3) is provided in section 5.3.6. During this study, the HC time was varied from 120 s to 600 s at an interval of 120 s. At any given refrigeration temperature, as HC time is extended, COP value increases significantly till a certain period and then it decreases or increases marginally as exhibited in Fig. 6.7. Such observation is rational as the cooling effect produced first increases and then decreases with the HC time while compressor energy consumption first decreases and then remains almost unchanged with HC time. The mean COP obtained at 20 °C refrigeration temperature for 120 s HC duration was 0.49; as HC time was extended to 240 s, 360 s, 480 s and 600 s, the mean

COP was found to be 0.68, 0.88, 0.95 and 0.87. Similar trends in COP variation with the increase in HC time were observed for 15 °C and 10 °C.

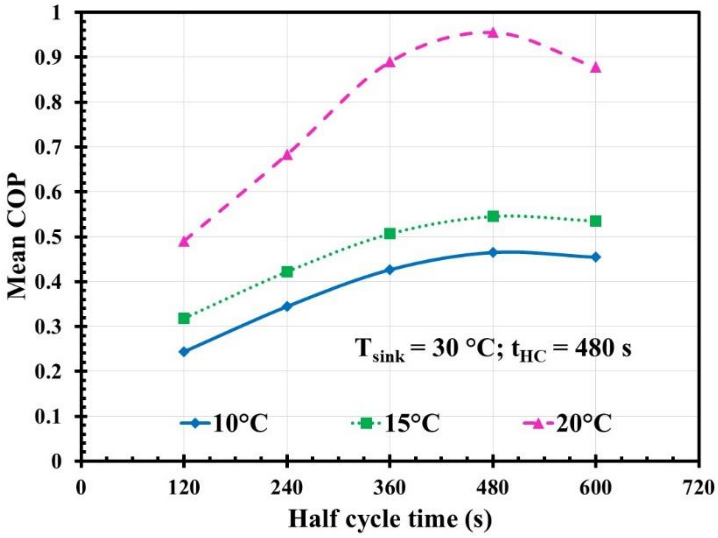

Fig. 6.7: Influences of refrigeration temperature and half cycle time on mean COP.

Influences of refrigeration temperature and half-cycle time on SCP

Figure 6.8 illustrates the effect of refrigeration temperature and HC time variation on SCP**.**

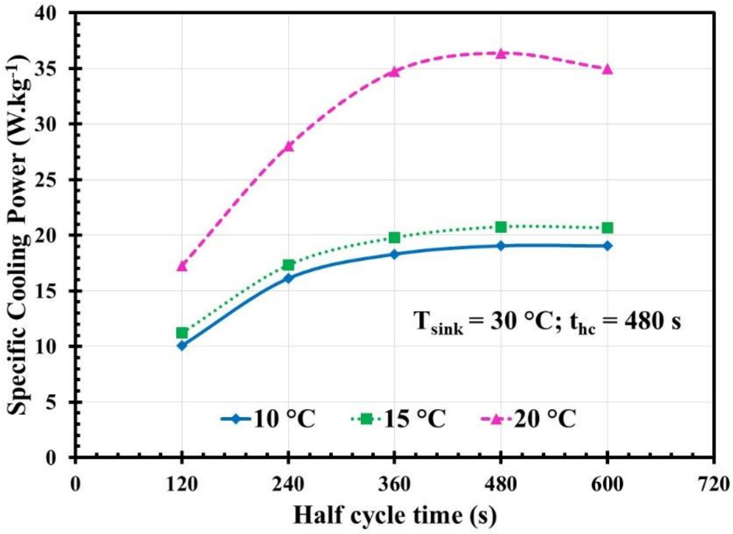

Fig. 6.8: Influences of refrigeration temperature and half-cycle time on SCP.

The SCP was estimated using Eq. (5.5), as discussed in section 5.3.6. At any given refrigeration temperature, as the HC time is stretched, the amount of cooling produced increases until the rate of cooling decreases and hence the SCP first increases and then decreases. At 20 °C, for 120 s HC time, the SCP achieved was 17.25 W.kg^{-1}. When HC time was stretched to 240 s, 360 s, 480 s, and 600 s, the corresponding SCP values achieved were 28 W.kg^{-1}, 34.75 W.kg^{-1}, 36.39 W.kg^{-1}, and 34.98 W.kg^{-1}. The SCP achieved is quite low as the hydrogen utilized to harness cooling is only a small fraction (roughly 10%) of the available hydrogen inventory (350 g hydrogen, 26.5 kg alloy). For any given HC time, at 15 °C and 10 °C, the achieved SCP values were lower compared to SCP achieved at 20 °C. The low SCP attained at lower refrigeration temperatures is due to a reduction in equilibrium pressure at lower temperatures which impedes hydrogen transfer from desorbing reactor to the absorbing reactor.

Influence of sink temperature on hydrogen transfer

The influence of sink temperature on the rate and amount of hydrogen transfer between the coupled reactors is shown in Fig. 6.9. During the assessment of sink temperature variation, the refrigeration temperature was set to 20 °C, and the HC time was set to 480 s. At 30 °C sink temperature, the maximum and average rate of hydrogen transfers was 0.35 g.s^{-1} and 0.08 g.s^{-1}, whereas for 35 °C sink temperature, the maximum and average hydrogen transfer rates were 0.27 g.s^{-1} and 0.075 g.s^{-1} (Fig. 6.9(a)). The peak and average rates of hydrogen transfer at elevated sink temperature were reduced as the equilibrium pressure difference between the coupled reactors is reduced due to the increase in equilibrium pressure of the absorbing reactor. The cumulative amount of hydrogen transferred for 480 s duration at 30 °C and 35 °C were 39.4 g and 35.9 g, respectively.

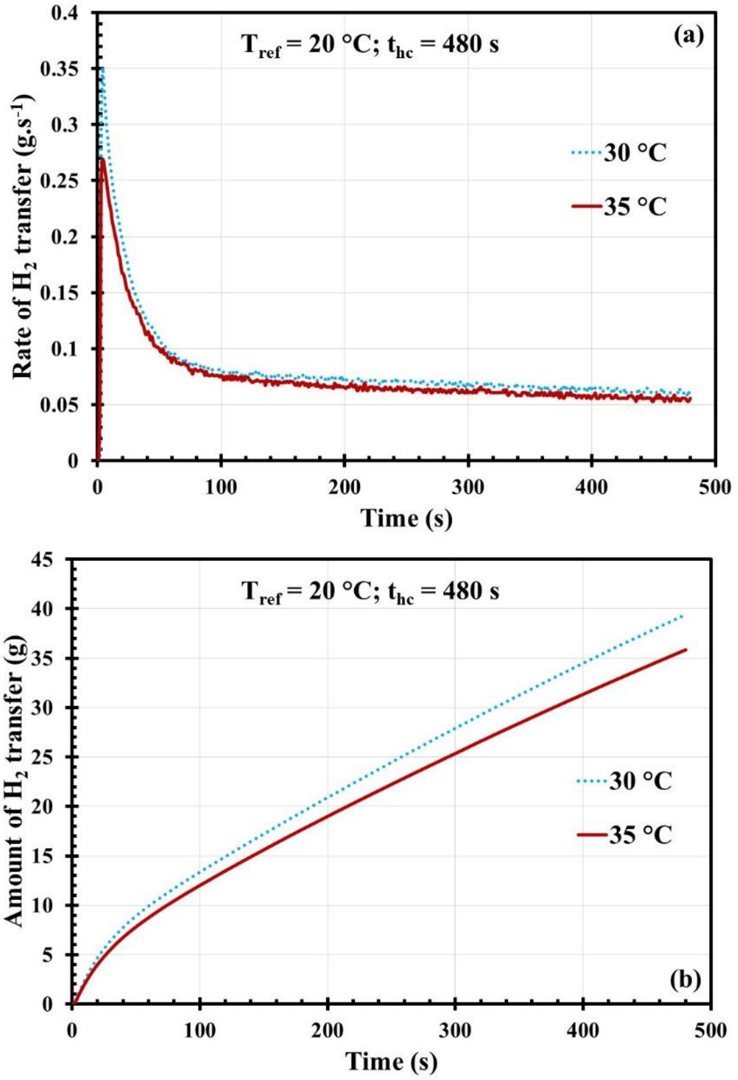

Fig. 6.9: Influence of sink temperature variation on (a) rate of hydrogen transferred and (b) amount of hydrogen transferred.

Influences of sink temperature and half-cycle time on mean COP

The influences of sink temperature and HC time on mean COP are shown in Fig. 6.10. While assessing the effect, the refrigeration temperature was fixed at 20 °C, and sink temperature was varied from 30-35 °C. Experiments were carried out for five different HC times, i.e., 120 s, 240 s, 360 s, 480 s, and 600 s. For any given HC time duration, as sink temperature is increased, the mean COP is found to decrease as a rise in sink temperature leads to a rise in the equilibrium pressure of the absorbing reactor resulting in lowered hydrogen transfer and hence lowered cooling effect produced. The mean COP obtained at 35 °C sink temperature for HC time of 120 s was 0.22, whereas, the corresponding mean

COP at 30 °C sink temperature was 0.49. When HC time was stretched beyond 120 s to 240 s, 360 s, 480 s, and 600 s, the mean COP value for 35 °C sink temperature were 0.44, 0.68, 0.73, and 0.7, respectively. For any given refrigeration and sink temperature, as HC time duration is increased, the mean COP increases till the rate of cooling increases. During this set of experiments, the mean COP increased to 480 s for both 30 °C and 35 °C cases. The mean COP attained at 30 °C sink temperature for HC times of 120 s, 240 s, 360 s, 480 s and 600 s were 0.68, 0.89, 0.95, and 0.88.

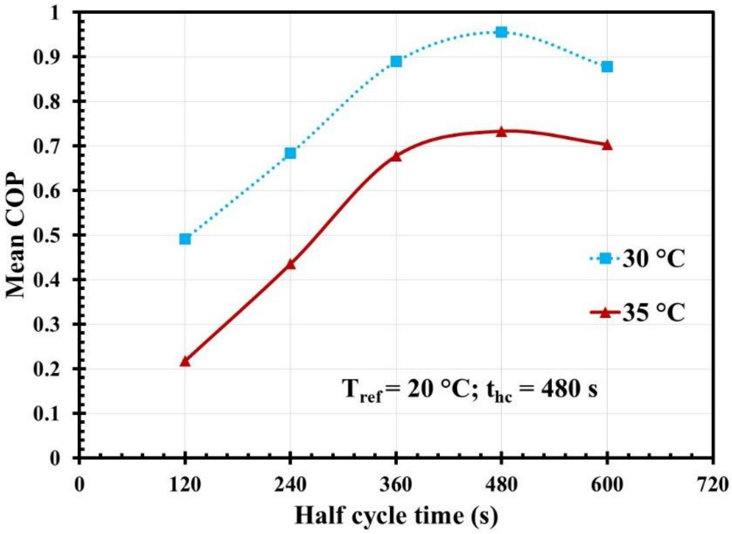

Fig. 6.10: Influence of sink temperature variation on mean COP.

Influences of sink temperature and half-cycle time on SCP

Figure 6.11 illustrates the influences of sink temperature and HC time on SCP. At any given HC time duration, as sink temperature was increased, the SCP decreased, which is quite obvious, as stated in the preceding sections. The SCP value obtained at 30 °C sink temperature for 120 s HC time was 17.24 $W.kg^{-1}$. When the sink temperature was increased to 35 °C, for the same HC time duration, the SCP attained was only 9.9 $W.kg^{-1}$. For 30 °C case, an extension of HC time beyond 120 s to 240 s, 360 s, till 480 s resulted in 1.6 fold, 2 fold and 2.1 fold increments in SCP. However, stretching HC time from 480 s to 600 s resulted in 3.8% reduction in SCP. Analogously, the SCP obtained for 35 °C case exhibited an increase of 2 fold, 2.8 fold and 2.95 fold, respectively when HC time was extended from 120 s to 240 s, 360 s, and 480 s. A further extension in HC time from 480 s to 600 s resulted in 5.2% reduction in SCP. The reduction in SCP value beyond 480 s duration may be attributed to a reduction in the rate of cooling.

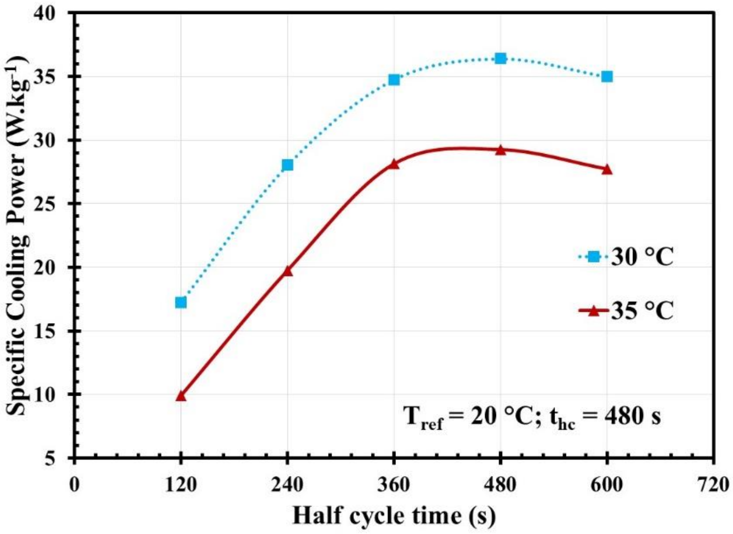

Fig. 6.11: Influence of sink temperature on SCP.

6.2.7. Remarks on the large-scale compressor driven cooling system

Two large-scale MH reactors with a large hydrogen inventory (~290 g) were coupled via a compressor to produce quasi-continuous cooling effect. The compressor was tested beforehand to check if it was able to handle the desorption rates at specified refrigeration temperatures and was found to operate aptly. However, the compressor, when operated beyond approximately 700 s duration at a stretch, resulted in heating of the compressor body, which inhibited the scope of HC time duration to a maximum of 600 s. Within the specified HC time, the quantity of hydrogen transported between the reactors was only around 10% of the available hydrogen inventory, which led to harnessing only part of the potential cooling production. The exact amount of hydrogen transported between the reactors at 20 °C refrigeration temperature and 30 °C sink temperature was 39.11 g within 480 s. A simple arithmetic calculation shows that 39.11 g hydrogen desorption should provide approximately 520 kJ cooling effect considering the desorption enthalpy of $La_{0.8}Ce_{0.2}Ni_5$ to be 26.73 kJ.mol^{-1} as obtained from Sharma and Kumar, (2015). In our study, the accomplished cooling effect under the same condition is 448 kJ which is at par with the expected cold output (86% output harnessed) considering minor heat losses. Also, under the same operating condition, the average rate of cold production (0.89 kW) is at par with the theoretically estimated cold production rate (1.08 kW). However, the difference between the theoretically possible highest cooling rate (5.94 kW) based on the maximum hydrogen desorption rate (0.446 g.s^{-1}) and actually achieved highest cooling rate (1.44 kW) was considerably large. Such an outcome is realistic as the MH bed is not thermally enhanced (i.e., not furnished with any thermal conductivity enhancing agent or technique), and thereby there is a time lag between actual hydrogen desorption from the MH bed and the resulting endothermic effect being translated to the HTF. The MH reactors used in this study were originally designed and developed considering large-scale hydrogen storage without the addition of any thermal performance enhancer.

To utilize maximum hydrogen inventory (80-90%) in a large-scale compressor-operated cooling system, the hydrogen compressor should be able to handle the flow rate and pressure ramp effectively; however, such hydrogen compressors are not yet commercially available as they neither belong to positive displacement (i.e., reciprocating) or rotodynamic category (i.e., centrifugal). In this work, a reciprocating refrigerant compressor was subjected to tailor-made modifications to perform the experiments.

6.3. Summary

In this chapter, the experimental results of a closed-cycle compressor-driven cooling system are presented. The mechanical compressor used in this work, being a customized refrigerant compressor, was not able to effectively compress hydrogen beyond 700 s without being heated, thereby compromising the half-cycle duration for which actual cooling could be harnessed. Nevertheless, within the safe compressor operation duration, a series of parametric tests were conducted by altering the refrigeration temperature, sink temperature and half-cycle duration. The influences of above mentioned operating parameters on the amount of hydrogen transferred, system COP and SCP are also discussed.

7. Numerical studies on hydrogen storage and cooling systems

7.1. Introduction

In this chapter, two different numerical models are developed. The first numerical study deals with the development of an extended numerical model to simulate the hydrogen storage performance of the 19 TBR configuration. In this model, the HTF flow and heat transfer simulation has been included by specifying the mass, momentum and energy equations and appropriate initial and boundary conditions. Whereas, in the second study, a lumped model has been developed for a compressor operated MH based closed loop cooling system. This model mimics the compressor effect by invoking suitable pressure and flow correlation.

7.2. Extended numerical model

The numerical model described in section 3.6 is extended to incorporate the HTF flow and heat transfer effects by solving the mass, momentum and energy equations for the HTF. The physical system considered is the 19 TBR configuration described in section 4.2.2. This model accounts for the influence of the actual experimental condition on the hydrogen storage performance by specifying the HTF flow rate and temperature boundary conditions.

7.2.1. Extended model assumptions

- The HTF is considered to be incompressible.
- The thermo-physical properties of the HTF are assumed to remain constant in the studied temperature range.
- The HTF enters the reactor flow channel with a constant mass flow rate and a constant temperature.
- Heat exchange occurs only between HTF and MH bed.

7.2.2. Governing Equations for HTF

Continuity Equation

$$\nabla \cdot \vec{u}_f = 0 \qquad (7.1)$$

Momentum Equation

$$\rho_f\left(\frac{\partial u_f}{\partial t}+\vec{u}_f\cdot\nabla u_f\right)=-\nabla P_f+\nabla\cdot\left[\mu_f\left(\nabla u_f+\left(\nabla u_f\right)^T\right)\right] \tag{7.2}$$

In Eq. (7.2), 'ρ_f', 'P_f' and 'μ_f' correspondingly designate the density, pressure, and dynamic viscosity of the HTF.

Energy Equation

$$\rho_f c_{p,f}\left(\frac{\partial T_f}{\partial t}+\vec{u}_f.\nabla T_f\right)=k_f\nabla^2 T_f \tag{7.3}$$

In Eq. (7.3), '$c_{p,f}$', 'T_f' and 'k_f' individually denote the specific heat capacity, temperate, and thermal conductivity of the HTF.

Initial and boundary conditions

Initial conditions

Initially (at t = 0), the HTF temperature is set to desired absorption/desorption temperature.

$$T_f=T_0 \tag{7.4}$$

Boundary conditions

The mass flow rate and temperature of the HTF is specified at the inlet.

$$\int_{A_{in}}\rho_f\left(\vec{u}_f\cdot\vec{dA}\right)=\dot{m}_{in} \tag{7.5}$$

$$T_f=T_0 \tag{7.6}$$

The HTF outlet is open to the atmosphere and there is no heat loss at the outlet.

$$P_f=P_0 \tag{7.7}$$

$$\frac{\partial T_f}{\partial z}=0 \tag{7.8}$$

The heat exchange between MH bed to HTF and vice versa is by design, taken care of by maintaining the continuity of heat flux at the interface. Therefore, no heat transfer boundary condition was explicitly invoked.

7.2.3. Solution methodology

The solution methodology is already described in section 3.6.3. The continuity, momentum and energy equations for the HTF (Eq. (7.1) - (7.3)) along with the (Eq. (3.1) - (3.22)), excluding Eq. (3.19), subjected to initial and boundary conditions (Eq. (7.4) - (7.8)) for the HTF are solved in COMSOL Multiphysics 5.5.

Table 7.1: Simulation parameters for $La_{0.8}Ce_{0.2}Ni_5$ and hydrogen

Parameters	**Value**
Properties of $La_{0.8}Ce_{0.2}Ni_5$	
Density of metal alloy	8400 $kg.m^{-3}$
Specific heat capacity of metal (c_{ps})	400 $J.kg^{-1}.K^{-1}$
Thermal conductivity of metal (k_s)	1 $W.m^{-1}.K^{-1}$
Porosity (ε)	0.5
Effective density of metal alloy (ρ_{emp})	4200 $kg.m^{-3}$
Effective density of saturated MH (ρ_{ss})	4261 $kg.m^{-3}$
Activation energy (E_a)	31040 $J.(mol\ H_2)^{-1}$
(E_d)	29010 $J.(mol\ H_2)^{-1}$
Reaction entropy (ΔS_a)	105 $J.(mol\ H_2)^{-1}.K$
(ΔS_d)	105 $J.(mol\ H_2)^{-1}.K$
Reaction enthalpy (ΔH_a)	24920 $J.(mol\ H_2)^{-1}$
(ΔH_d)	26730 $J.(mol\ H_2)^{-1}$
Properties of hydrogen	
Thermal conductivity (k_g)	0.1272 $W.m^{-1}.K^{-1}$
Specific heat capacity (c_{pg})	14283 $J.kg^{-1}.K^{-1}$
Molecular weight (M_g)	2.016 $g.mol^{-1}$
Constants used	
Universal gas constant (R_u)	8.314 $J.mol^{-1}.K^{-1}$
Reaction constant (C_a)	300 s^{-1}
(C_d)	15 s^{-1}
Slope factor ($\varphi_{s,a}/\ \varphi_{s,d}$)	0.032/0.286
Slope constant ($\varphi_{o,a}/\ \varphi_{o,d}$)	0.06/0.155
Hysteresis factor ($\varphi_a,\ \varphi_d$)	-1.9/0.86

Eq. (3.19), which specifies the convective heat flux boundary condition at the MH bed and HTF interface, is now unnecessary as the heat exchange between the MH bed and HTF is accounted for by specifying the HTF flow and temperature boundary conditions. During simulation, relative and absolute tolerances are set to 10^{-4} and 10^{-3}, respectively. For the simulation of the hydrogen storage, the PCT properties and kinetic parameters of the alloy $La_{0.8}Ce_{0.2}Ni_5$ are used. The model input parameters are given below in Table 7.1.

7.2.4. Mesh independence test

The mesh independence test is performed at four different mesh configurations, as shown in Fig. 7.1. The corresponding absorption condition is chosen as 20 bar, 20 °C, and 20 LPM.

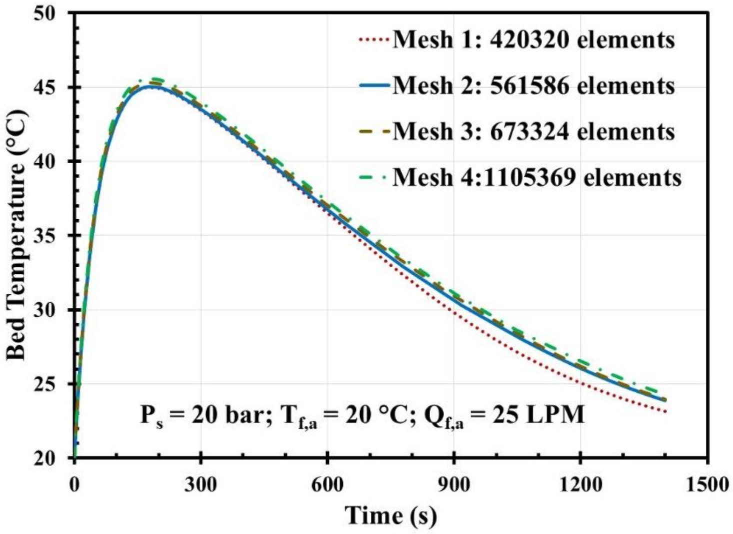

Fig. 7.1: Mesh independence test for the extended numerical model.

Based on the mesh independence test results, Mesh 1 with 420320 elements is chosen for further analysis.

7.2.5. Model Validation

The extended numerical model results are compared with the hydrogen storage experimental results of the 19 TBR module. Both absorption and desorption model predictions are compared in terms of hydrogen storage capacity profiles. Figure 7.2(a) and 7.2(b) correspondingly shows the validation plots for absorption and desorption. The numerically predicted hydrogen capacity profiles are found to have a comprehensive match with the experimentally observed hydrogen capacity profiles. A minor discrepancy in the validation plots may be attributed to a lack of accuracy in estimating the PCT parameters, viz. slope constants, hysteresis factor, etc.

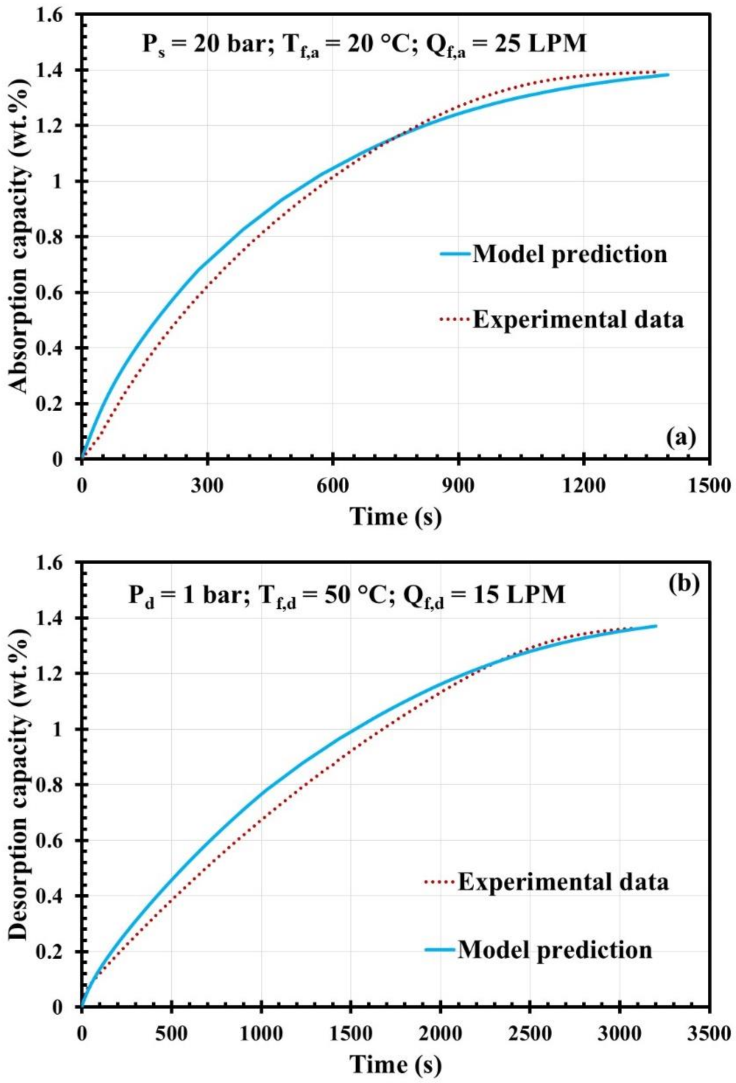

Fig. 7.2: Validation of the extended model: (a) absorption capacity and (b) desorption capacity.

7.2.6. Prediction of hydrogen desorption with constant mass flow rates

In this section, the simulation outcomes of the extended numerical model are presented for the 19 TBR module in terms of hydrogen desorption at constant mass flow rates. Constant mass flow rate desorption is important for feeding hydrogen to fuel cells. A set of simulations is performed on the 19 TBR module for hydrogen desorption to assess its suitability to feed 1-2 kW LT-PEMFC in the temperature range of 40-70 °C. The mass flow rate requirement for a rated LT-PEMFC is estimated using Eq. (4.1) (Larminie and Dicks, 2013).

Influence of HTF temperature on bed temperature during constant flow desorption

Figure 7.3 depicts the influence of HTF temperature variation on bed temperature during constant flow rate desorption. Two different mass flow rate cases are considered viz. 0.97 g.min^{-1} and 1.94 g.min^{-1}; which correspondingly denotes the estimated mass flow rates to run a 1 kW and 2 kW PEMFC. For both the set mass flow rates, the bed temperature first drops steadily and remains constant for a certain duration and then climbs up to the specified inlet HTF temperature.

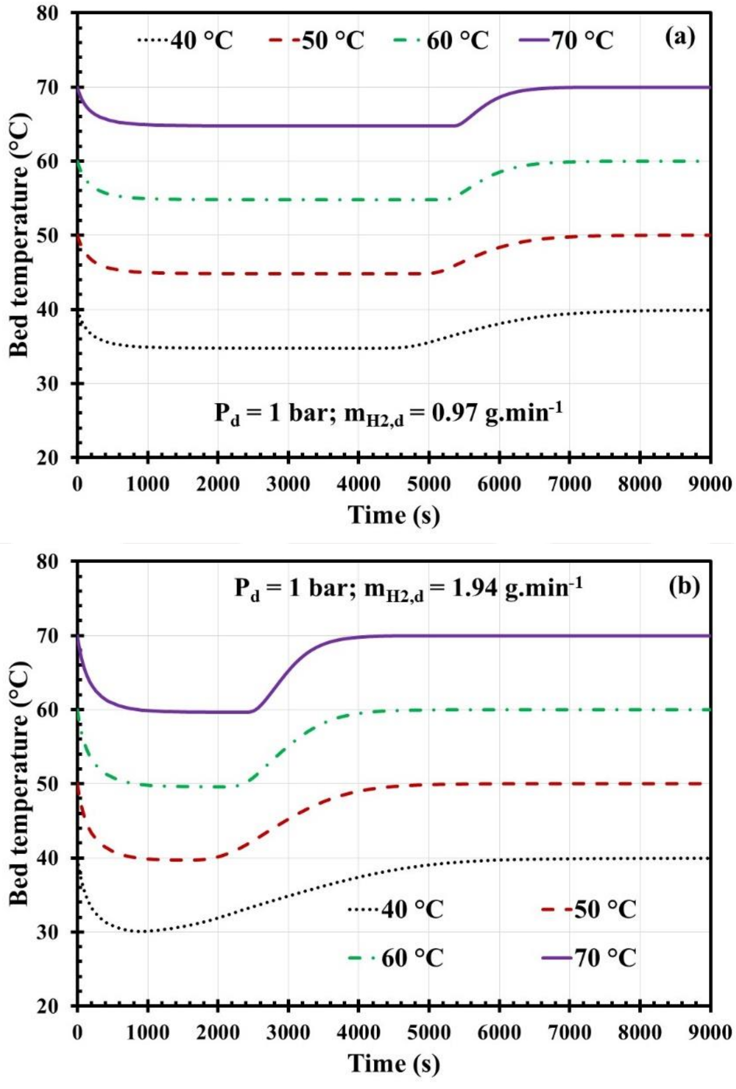

Fig. 7.3: Influence of HTF temperature alteration on bed temperature during constant flow desorption: (a) 0.97 g.min^{-1} and (b) 1.94 g.min^{-1}.

The initial drop in bed temperature is due to the surge in desorption flow rate to attain the set value. The duration for which the reactor is able to desorb at a constant mass flow rate at any HTF temperature is reflected in the near isothermal regime of the bed temperature profile before it climbs to the HTF inlet temperature. For a set flow rate of 0.97 g.min^{-1}, (shown in Fig. 7.3(a)), the maximum drop in bed temperature is 5.2 °C for HTF temperature 40-70 °C. Whereas, for 1.94 g.min^{-1} set flow rate, the maximum drop in bed temperature is approximately 10 °C for HTF temperature 40-70 °C (Fig. 7.3(b)). The maximum drop in bed temperature is higher for a higher mass flow rate, which is quite obvious. Once the reactor is not able to sustain the set constant flow rate, the flow rate drops, which results in an increase in bed temperature as the rate of heat supply to the bed exceeds the required rate. With an increase in HTF temperature, for any set mass flow rate, the duration of the constant discharge is elongated as the equilibrium pressure would be higher at elevated temperatures, enabling the reactor to discharge hydrogen for a longer duration. The influence of HTF temperature alteration on bed pressure is elucidated in the subsequent section.

Influence of HTF temperature on mass flow rate during constant flow desorption

Figure 7.4 depicts the influence of HTF temperature on hydrogen mass flow rate profiles during constant flow desorption. For a set flow rate of 0.97 g.min^{-1}, at 40 °C HTF temperature, the flow rate could be sustained till 4410 s. As HTF temperature is increased to 50 °C, 60 °C and 70 °C, the constant flow discharge durations are augmented by approximately 1.12 fold, 1.18 fold and 1.21 fold compared to 40 °C case. However, for a set flow rate of 1.94 g.min^{-1}, the constant flow discharge duration at 40 °C is merely 635 s, which is increased tremendously by 2.4 fold, 3.3 fold and 3.8 fold when HTF temperature is raised to 50 °C, 60 °C and 70 °C correspondingly. Evidently, for a specified lower discharge rate, the reactor is better able to sustain the flow demand even at 40 °C. Nevertheless, the cumulative amount of hydrogen transferred at all four HTF temperatures (40-70 °C) is identical (approximately 1.41 wt.%) by the end of 9000 s.

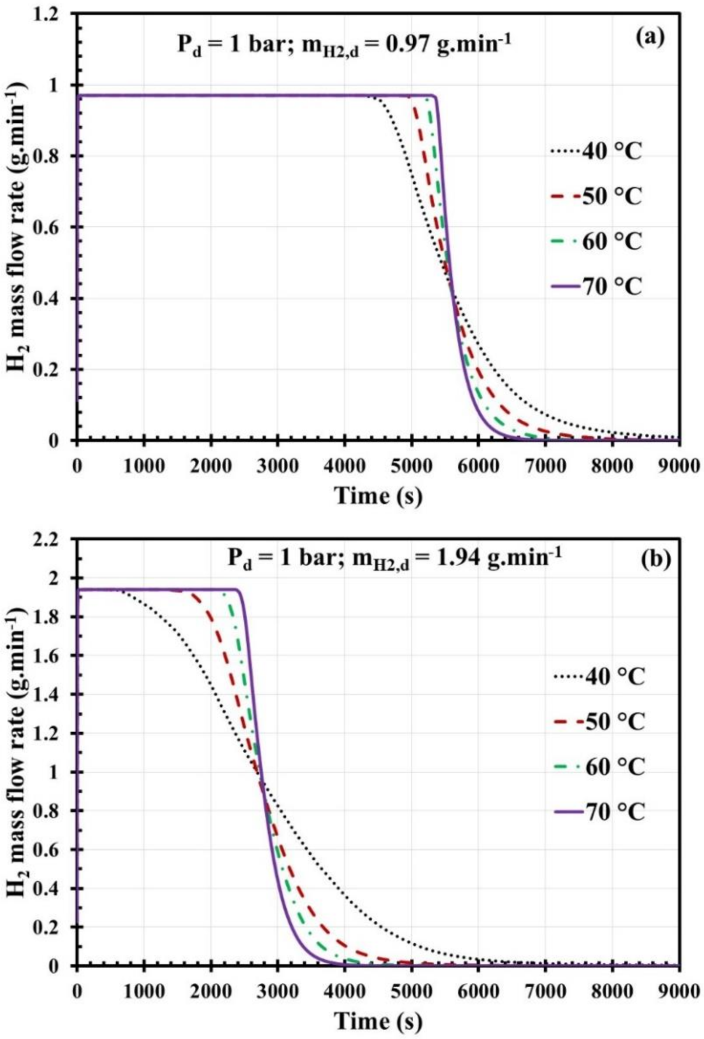

Fig. 7.4: Influence of HTF temperature alteration on mass flow rate during constant flow desorption (a) 0.97 g.min^{-1} and (b) 1.94 g.min^{-1}.

Influence of HTF temperature on bed pressure during constant flow desorption

Figure 7.5 shows the influence of HTF temperature variation on bed pressure during constant flow desorption. The bed pressure is the highest at the beginning of desorption, which gradually drops as desorption progresses and beyond a threshold when the pressure differential is not able to sustain the set flow rate; it drops swiftly close to the set desorption pressure. The drop in bed pressure is more in the case of a higher set desorption rate. Comparing the pressure drop for the 70 °C HTF temperature case, as can be observed from Fig. 7.5(a) and Fig. 7.5(b), the bed pressure drops from 75.5 bar to 18.5 bar within 300 s, for 1.94 g.min^{-1} flow rate scenario, while, the corresponding drop for 0.97 g.min^{-1} scenario is from 75.6 bar to 25.6 bar within 300 s.

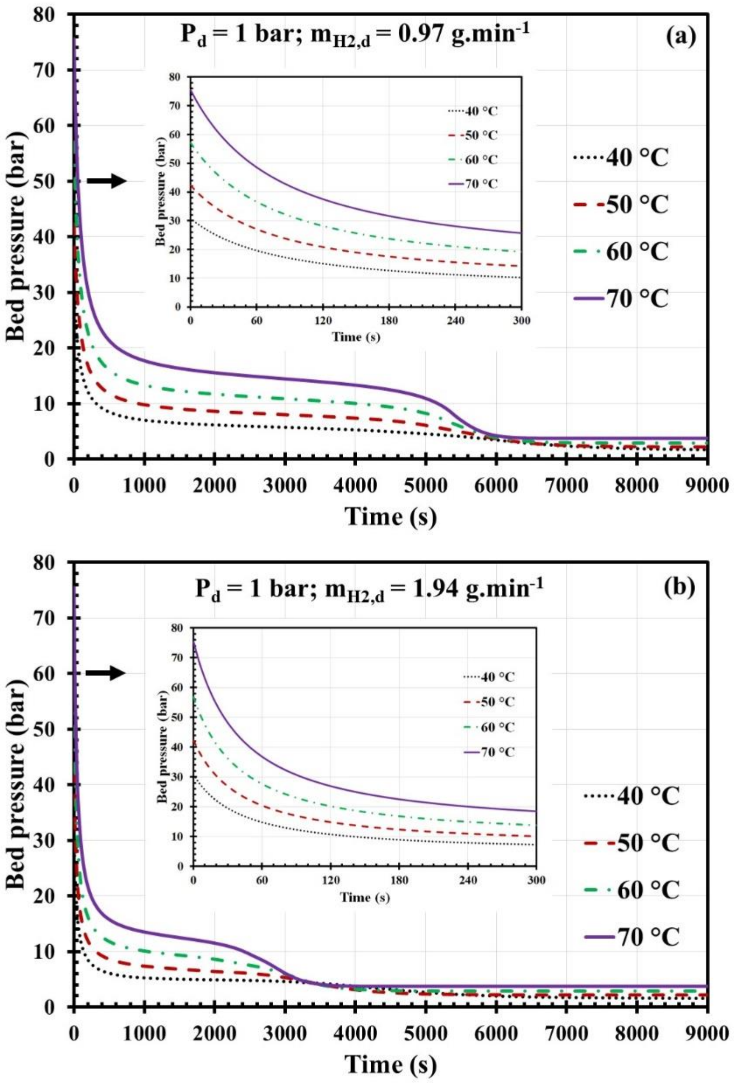

Fig. 7.5: Influence of HTF temperature alteration on bed pressure during constant flow desorption (a) 0.97 g.min^{-1} and (b) 1.94 g.min^{-1}.

7.3. Numerical model for compressor driven closed cycle cooling system

To simulate the behaviour of the coupled bed compressor-operated cooling system, a lumped model is developed and solved in COMSOL Multiphysics 5.5. The model takes care of the compressor effect by invoking suitable flow and pressure conditions. The complete model description is given in subsequent sections.

7.3.1. Description of the physical system

The physical model considered for simulation is a concentric tube reactor. In this study, multiple concentric reactors of identical dimensions, where MH alloy would be filled inside in the inner tube, and HTF flow would occur though the annulus section are analysed.

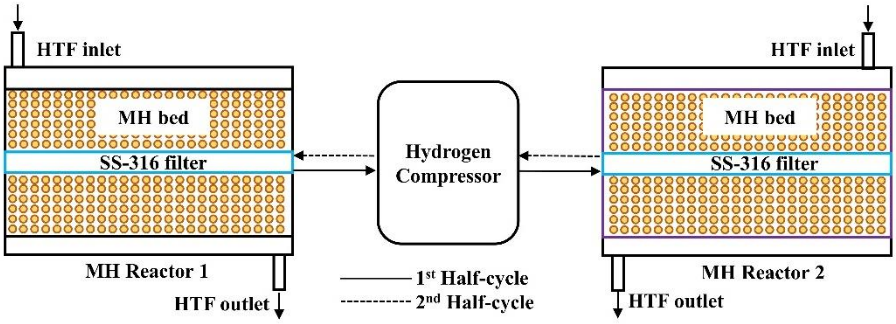

Fig. 7.6: Schematic of operation of the compressor-operated cooling system.

Standard SS-316 tubes are chosen as inner tubes ranging from dimensions of φ 10×1 mm to φ 25×1.2 mm. An SS-316 sintered porous filter of dimension φ 6×0.8 mm is chosen to be placed at the centre to inhibit MH particles from coming out of the reactor. The schematic of the operation of the coupled bed cooling system is illustrated in Fig.7.6.

Table 7.2: Technical specification of the considered concentric tube reactors

Tube OD (mm)	**Tube thickness (mm)**	**Desired length (m)**	**Yielded surface area (m^2)**	**Weight of the tube (W_T) (kg)**	**Weight of the reactor ($1.4*W_T$) (kg)**
10	1	5.41	0.17	1.19	1.67
12	1	2.37	0.0893	0.64	0.89
14	1	1.4	0.0617	0.45	0.63
15	1	1.14	0.0537	0.39	0.55
16	1.2	1.02	0.0511	0.44	0.62
18	1.2	0.73	0.0413	0.36	0.51
20	1.2	0.55	0.0348	0.31	0.43
22	1.2	0.44	0.0301	0.27	0.37
25	1.2	0.32	0.0251	0.22	0.31

The complete specification of the reactors considered for the present study is shown in Table 7.2. For the fixed tube diameter, the length is calculated to accommodate 0.5 kg of $MmNi_{4.6}Al_{0.4}$ alloy considering a packing density of 4200 kg.m^{-3}.

7.3.2. Description of the mathematical model

The mathematical model essentially considers the reaction rate and energy equations of the absorbing and desorbing beds supplemented by the equilibrium pressure expressions given by van’t Hoff law. For lumped modelling, the set of coupled ordinary differential equations subjected to suitable initial conditions are solved for concentration and bed temperature. The equations and model assumptions are given below:

Assumptions

- Hydrogen is treated as an ideal gas within the operating temperature and pressure.
- Local thermal equilibrium exists between gas and solid phases.
- The solid phase is continuous, isotropic and homogeneous.
- The reaction enthalpy and entropy don't change with temperature, pressure, or hydrogen concentration.
- Reaction concentration and bed temperature vary only with time.
- The compression work is isentropic.
- The thermo-physical properties of the HTF are constant.
- The reactors are well insulated.

Governing Equations

Desorbing bed:

$$\frac{dX_d}{dt} = C_d \ln\left(\frac{P_{eq,d}}{P_{c,s}}\right) \exp\left(\frac{E_d}{R_u T_d}\right) X_d \tag{7.9}$$

In Eq. (7.9), 'X_d', 'C_d', '$P_{eq,d}$', '$P_{c,s}$', 'E_d', and 'T_d' correspondingly denote the concentration of the desorbing bed (H/M), the desorption reaction rate constant, equilibrium pressure of the desorbing bed, suction pressure of the compressor, and desorbing bed temperature. Also, 'R_u' stands for universal gas constant.

$$\frac{P_{eq,d}}{P_0} = \exp\left[\frac{\Delta S_d}{R_u} - \frac{\Delta H_d}{R_u T_d} + (\varphi_{s,d} - \varphi_{o,d}) \tan\left(\pi\left(\frac{X_d}{X_{\max}} - \frac{1}{2}\right)\right) - \frac{\varphi_d}{2}\right] \tag{7.10}$$

In Eq. (7.10), 'ΔS_d' and 'ΔH_d' are desorption entropy and desorption enthalpy, respectively. Whereas '$\varphi_{s,d}$', '$\varphi_{0,d}$', 'φ_d' and 'X_{max}' stand for slope factor, hysteresis factor, slope constant and maximum hydrogen concentration, individually.

$$\left(m_{hyd} c_{p,hyd} + m_r c_{p,r}\right)_d \frac{dT_d}{dt} = U_o A\left(T_{f,d,in} - T_d\right) - Q_{g,d} \tag{7.11}$$

In Eq. (7.11), 'm_{hyd}', '$c_{p,hyd}$', 'm_r' and '$c_{p,r}$' denote the mass of the hydride, the specific heat capacity of the hydride, the mass of the reactor and the specific heat capacity of the reactor, respectively. Also, 'U_o', 'A', '$T_{f,d,in}$', and '$Q_{g,d}$' denotes the overall heat transfer coefficient, heat exchange surface area, HTF temperature of the desorbing bed, and reaction heat of the desorbing bed. The expression for calculation of '$Q_{g,d}$' is given in Eq. (7.12).

$$Q_{g,d} = \Delta H_d \left(\frac{dX_d}{dt}\right)\left[\frac{N_a m_{hyd}}{2M_{hyd}}\right] \tag{7.12}$$

In Eq. (7.12), 'N_a' and 'M_{hyd}' correspondingly stand for the number of atoms of hydrogen per mole of the hydride alloy and the molecular weight of the hydride alloy. The heat transfers between hydride bed and HTF stream is also equal to the heat loss of the HTF. Therefore, the energy balance can be expressed as:

$$m_{f,d}\, c_{p,f,d}\left(T_{f,d,in} - T_{f,d,\mathrm{out}}\right) = U_o A\left(T_{f,d,in} - T_d\right) \tag{7.13}$$

In Eq. (7.13), '$m_{f,d}$', '$c_{p,f,d}$', '$T_{f,d,in}$' and '$T_{f,d,out}$' stand for mass flow rate, specific heat capacity, inlet and outlet temperature of the HTF for desorbing reactor.

Absorbing bed:

$$\frac{dX_a}{dt} = \frac{dX_d}{dt} \tag{7.14}$$

$$\frac{P_{eq,\mathrm{a}}}{P_0} = \exp\left[\frac{\Delta S_a}{R_u} - \frac{\Delta \mathrm{H}_a}{R_u T_a} + (\varphi_{s,\mathrm{a}} + \varphi_{o,\mathrm{a}})\tan\left(\pi\left(\frac{X_a}{X_{\max}} - \frac{1}{2}\right)\right) + \frac{\varphi_a}{2}\right] \tag{7.15}$$

$$\left(m_{hyd} c_{p,hyd} + m_r c_{p,r}\right)_a \frac{dT_a}{dt} = Q_{g,a} + Q_{gas} - U_o A\left(T_a - T_{f,\mathrm{a},in}\right) \tag{7.16}$$

In Eq. (7.16), the symbols '$Q_{g,a}$' and 'Q_{gas}' denotes the reaction heat of absorption and heat carried to the absorbing reactor from the compressor discharge. The terms '$Q_{g,a}$' and 'Q_{gas}' are quantified in Eq. (7.17) and Eq. (7.18).

$$Q_{g,a} = \Delta H_a \left(\frac{dX_a}{dt}\right)\left[\frac{N_a m_{hyd}}{2M_{hyd}}\right] \tag{7.17}$$

$$Q_{gas} = \left(\frac{dX_d}{dt}\right)\left[\frac{N_a m_{hyd}}{2M_{hyd}}\right] M_{H_2} c_{p,H_2} \left\{T_d\left(r_p^{\frac{\gamma-1}{\gamma}}\right) - T_a\right\} \tag{7.18}$$

The energy balance between the HTF of the absorbing reactor and hydride bed can be expressed in a similar manner (Eq. (7.19)) to that of desorbing bed as stated in Eq. (7.13).

$$m_{f,\mathrm{a}}\, c_{p,f,\mathrm{a}}\left(T_{f,a,out} - T_{f,a,in}\right) = U_o A\left(T_a - T_{f,a,in}\right) \tag{7.19}$$

Hydrogen compressor:

The compression ratio achieved during hydrogen transfer from desorbing bed to the absorbing bed can be expressed as:

$$r_p = \frac{P_{eq,a}}{P_{eq,d}} \tag{7.20}$$

The compressor work input is calculated using Eq. (7.21):

$$W_{comp} = \left(\frac{\gamma}{\gamma-1}\right)\left(\frac{1}{\eta_{comp}}\right)\left(\frac{dX_d}{dt}\right)\left[\frac{N_a m_{hyd}}{2M_{hyd}}\right]\left\{M_{H_2} c_{p,H_2} T_d \left(r_p^{\frac{\gamma-1}{\gamma}} - 1\right)\right\} \tag{7.21}$$

In Eq. (7.21), the compression efficiency (η_{comp}) is considered 0.7.

Initial conditions:

Desorbing reactor:

$$T_d = T_{0,d} \tag{7.22}$$

$$X_d = X_{0,d} \tag{7.23}$$

Absorbing reactor:

$$T_a = T_{0,a} \tag{7.24}$$

$$X_a = X_{0,a} \tag{7.25}$$

7.3.3. Numerical procedure:

The modelling parameters of the $MmNi_{4.6}Al_{0.4}$-H_2 system needed for the simulation is already given in Table 3.4. The set of coupled differential equations is solved using the Backward Euler method in COMSOL Multiphysics 5.5. The time step and relative tolerance are set to 0.05 s and 10^{-5}, respectively.

7.3.4. Model Validation

The developed lumped model has been validated against the experimental results reported by Muthukumar et al., 2005. The description of the reactor geometry is already mentioned in section 3.6.5. Figure 7.7 shows a reasonable match of the predicted results with the experimentally obtained results.

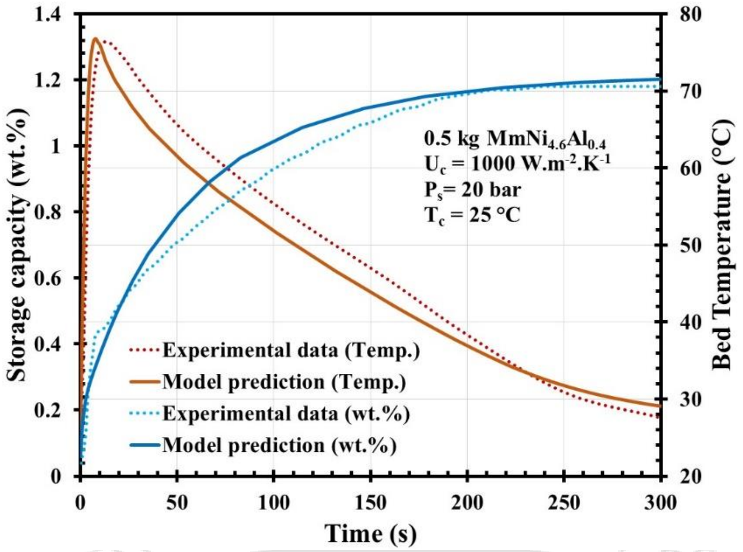

Fig. 7.7: Validation of the lumped model.

7.3.5. Characterization of the coupled bed cooling system

In this section, the cyclic variation of the coupled system in terms of bed temperature, bed concentration, compressor power and cooling power is presented. During this study, the refrigeration and sink temperatures are set to 20 °C and 35 °C, respectively. A total of 6 consecutive operations of the system is presented, where the 1st half-cycle (HC) starts with hydrogen transfer from reactor 2 to reactor 1. It is observed that beyond the 4th HC, the cyclic operation became steady. A study is also conducted to understand the effects of considering variable and constant flow between the reactors.

Cyclic variation in bed concentration and temperature

Figure 7.8 shows the variation in bed concentration and temperature over six consecutive HCs. In the 1st HC, the initial concentrations are set at 0.4 and 0.8, respectively, for reactor 1 and reactor 2. By the end of 1st HC, the concentrations reach from 0.8 to 0.52 and 0.4 to 0.68, correspondingly. With the starting concentration of 0.52 and 0.68, by the end of 2nd HC, the concentrations reach from 0.52 to 0.72 and 0.68 to 0.48. Till the end of 3rd HC, the cyclic operation of the system does not reach a steady state; however, with further progression in cycles, beyond 4th HC, the cyclic operation becomes steady, as it can be witnessed from the concentration profiles of the reactor 1 and 2 in Fig. 7.8(a). The cyclic operation till 6th HC has been portrayed for better comprehension. The resultant influence of concentration change i.e., absorption and desorption on bed temperature over consecutive HCs are shown in Fig. 7.8(b). The effect of high initial concentration in reactor 2 (0.8) and low initial concentration in reactor 1 (0.4) in the 1st HC is reflected in the bed temperature fall and rise of the reactors that are distinctly different from the rest HCs. Analogous to the concentration profiles, the bed temperature profiles beyond 4th HC are uniform as the cyclic operation becomes steady.

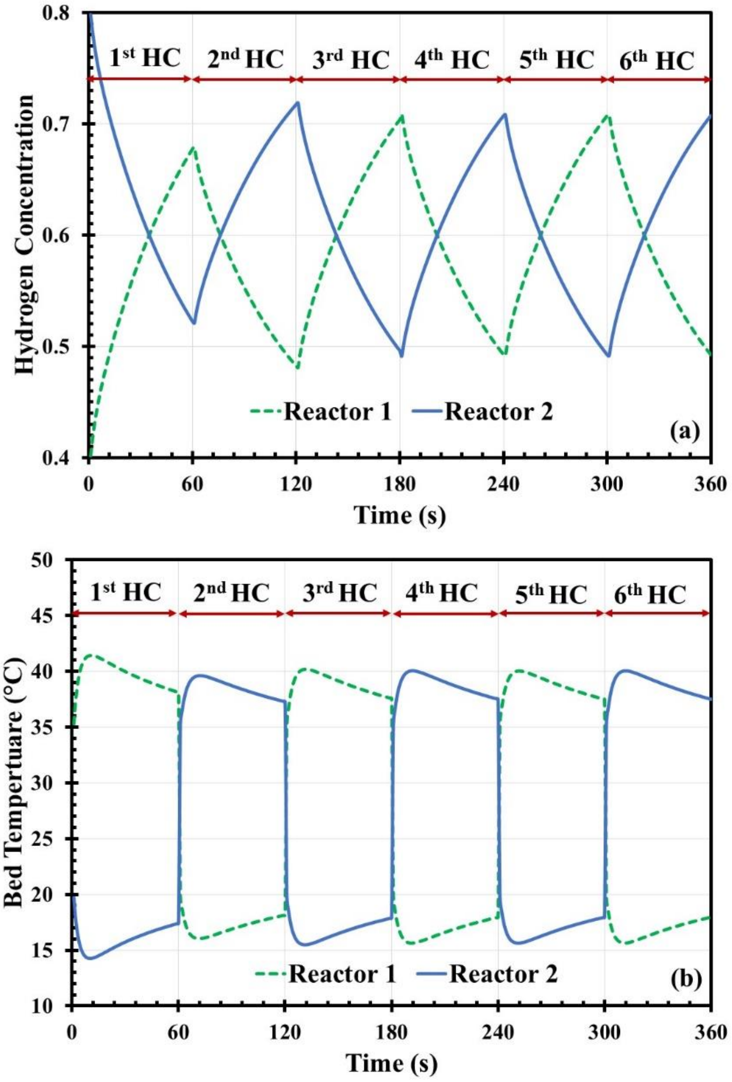

Fig. 7.8: Cyclic variation of (a) bed concentration and (b) bed temperature.

Cyclic variation in compressor power and cooling power

Figure 7.9 shows the variation in compressor power and cooling power over six consecutive half-cycles. As soon as the hydrogen transfer takes place between the reactors, the compressor power consumption goes to a peak and then gradually decreases as time progresses. The initial power consumption is high as the mass flow rate is high; as the cycle progresses, the equilibrium pressure in the desorbing reactor goes down while the same goes up in the absorbing reactor, which in turn reduces the mass flow rate between the reactors. The initial power consumption is high as the mass flow rate is high; as cycle progresses, the equilibrium pressure in the desorbing reactor goes down while the same goes up in the absorbing reactor, which in turn reduces the mass flow rate between the reactors. The average compressor power consumptions over six HCs are 106 W, 88 W, 95 W, 93 W, 93 W, and 93 W, respectively. The compressor power consumption pattern during the 4th, 5th and 6th HC are identical which are overlapped, as witnessed in Fig. 7.9(a). The cyclic variation of cooling power produced by the coupled system is shown in Fig. 7.9(b). The cooling produced is minimum in the beginning as hydrogen desorption starts and then goes to maximum within a very short period (~10 s) and then progressively goes down till end of HC

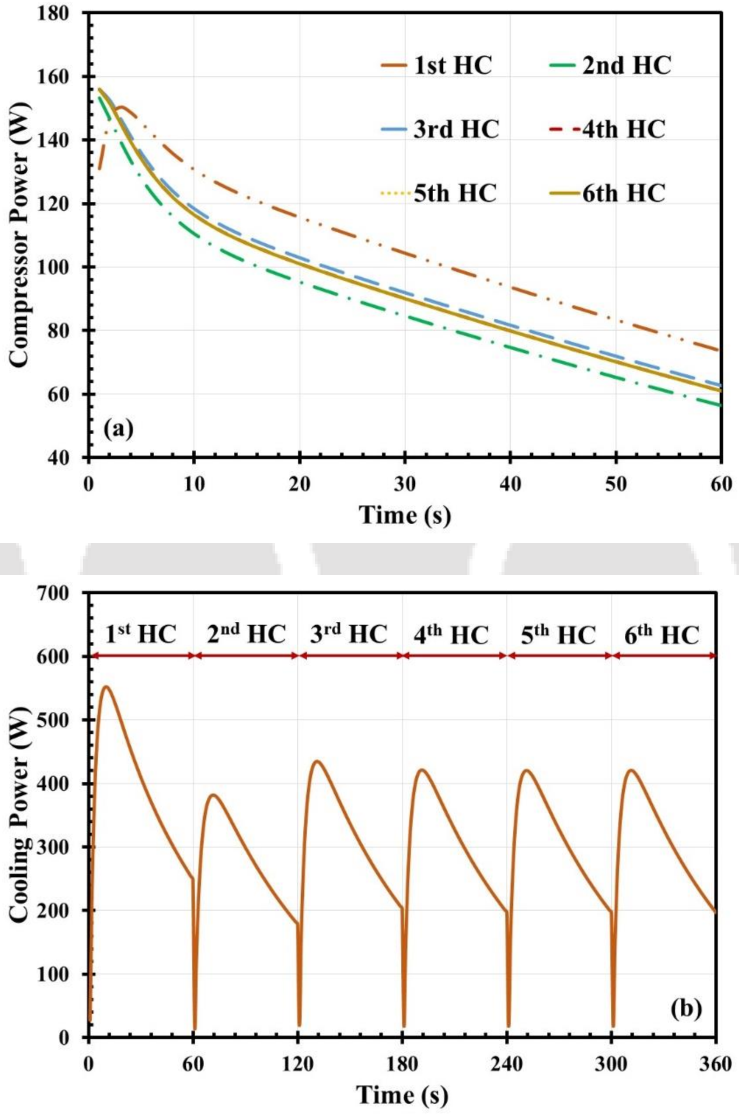

Fig. 7.9: Cyclic variation of (a) compressor power and (b) cooling power.

The delay between hydrogen desorption and the resulting endothermic effect translated to HTF is due to the thermal inertia of the system, which is dominated by the poor effective thermal conductivity of the MH bed. Similar to the concentration and bed temperature pattern observed, the cooling power produced becomes steady beyond 4th HC. The average steady cooling power obtained is approximately 302 W.

Influence of variable flow and constant flow

Figure 7.10 shows the effect of considering variable hydrogen flow over constant flow in between the reactors of the coupled system. To study the effect, the average value of the variable flow rate case over 60 s was given as input for the constant flow rate case. As can be witnessed from Fig. 7.10(a), the cumulative hydrogen transferred between the reactors was the same in both cases. A distinct difference in compressor power input can be appreciated from the predicted profiles, as shown in Fig. 7.10(b).

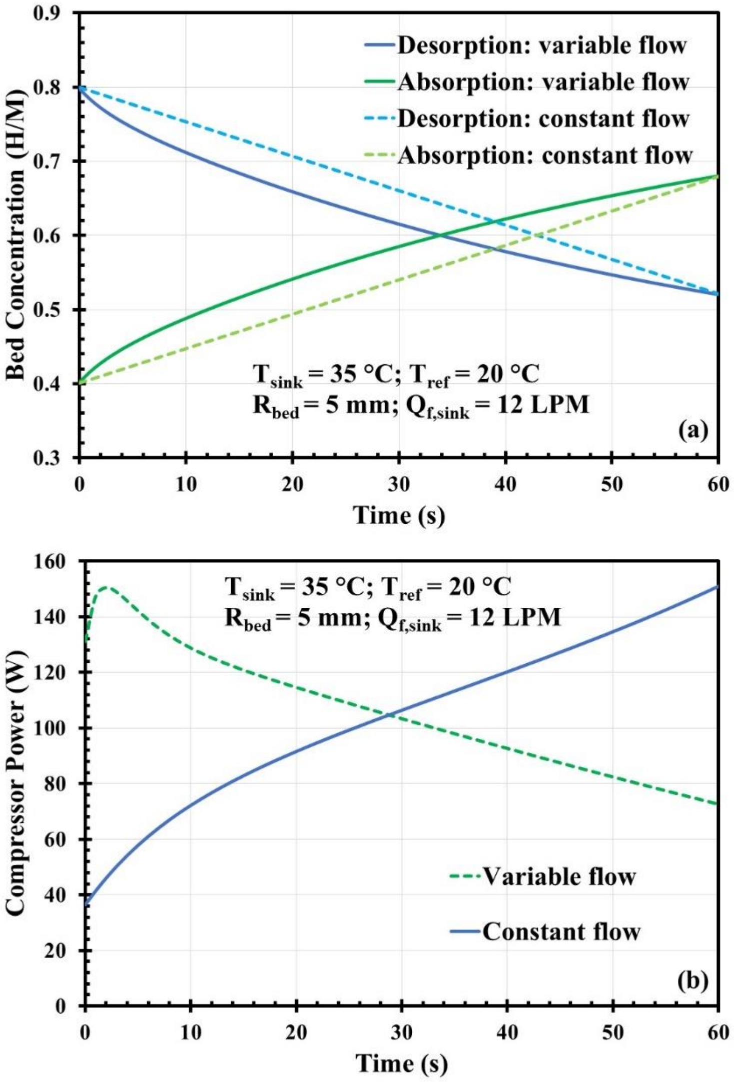

Fig. 7.10: Effect of compressor flow condition on (a) bed concentration and (b) compressor power.

In the case of variable flow, the rate of flow is the highest during the initial period, which dictates the compressor input power profile, which is also explained in previous sections. However, in the case of constant flow rate compression, the power consumption is minimum during the initial period as the set flow rate is lower than the flow rate achieved during variable flow compression. With progression in cycle time, as the pressure ratio goes up, the power consumption goes up, which is clearly understood from the power consumption profile shown in Fig. 7.10(b).

7.3.6. Parametric study

In this section, the sensitivity of the performance parameters viz. SCP and COP against change in a few design and operating parameters are evaluated and presented. Bed thickness is as identified as a vital design parameter whereas HTF flow rate, HC time, initial hydrogen concentration, refrigeration and sink temperatures are identified as operating parameters for this study.

Table 7.3: Scheme of the simulation study for closed cycle cooling system

Process	**Operating parameter**	**Range**	**Remarks**
Coupled bed cooling	Bed thickness (R_{bed}):	4-11.3 mm	HTF temperature of the refrigerating bed T_{ref}) set at: 20 °C; HTF temperature of the sink (T_{sink}) set at: 35 °C Half-cycle time (t_{HC}) set at: 60 s HTF flow rate of the refrigerating bed ($Q_{f,sink}$) set at: 2 LPM
	HTF flow rate ($Q_{f, sink}$):	2-16 LPM	T_{ref} = 20 °C; T_{sink} = 35 °C t_{HC} = 60 s; R_{bed} = 5 mm
	Half-cycle time (t_{HC}):	15-150 s	T_{ref} = 20 °C; T_{sink} = 35 °C R_{bed} = 5 mm; $Q_{f,sink}$ = 12 LPM
	Initial concentration (H/M):	0.5-0.8	T_{ref} = 20 °C; T_{sink} = 35 °C t_{HC} = 60 s; R_{bed} = 5 mm $Q_{f,sink}$ = 12 LPM
	Sink temperature (T_{sink}):	10-20 °C	T_{ref} = 20 °C; t_{HC} = 60 s; R_{bed} = 5 mm; $Q_{f,sink}$ = 12 LPM
	Refrigeration temperature (T_{ref}):	25-35 °C	T_{sink} = 35 °C; t_{HC} = 60 s R_{bed} = 5 mm; $Q_{f,sink}$ = 12 LPM

The designated operating parameters and their operation range are provided in Table 7.3.

Influence of bed thickness

The influence of MH bed thickness variation on SCP and COP of the system is depicted in Fig.7.11. The bed thickness chosen for the study corresponds to standard tube dimensions ranging from φ 10×1 mm to φ 25×1.2 mm yielding bed thickness from 4-11.3 mm. While evaluating the effect of bed thickness variation, the amount of MH alloy that can be filled is set to 0.5 kg for each case. Thereby, depending on the internal volume available for MH filling, the length is adjusted accordingly to accommodate 0.5 kg alloy. The SCP and COP estimated at different bed thicknesses displayed a similar pattern, i.e., beyond 5 and 6 mm bed thickness, the COP and SCP are estimated to reduce with an increase in bed thickness. The key factor influencing the system's cooling performance is the thermal resistance offered by the MH bed, as it dominates the overall heat transfer rate.

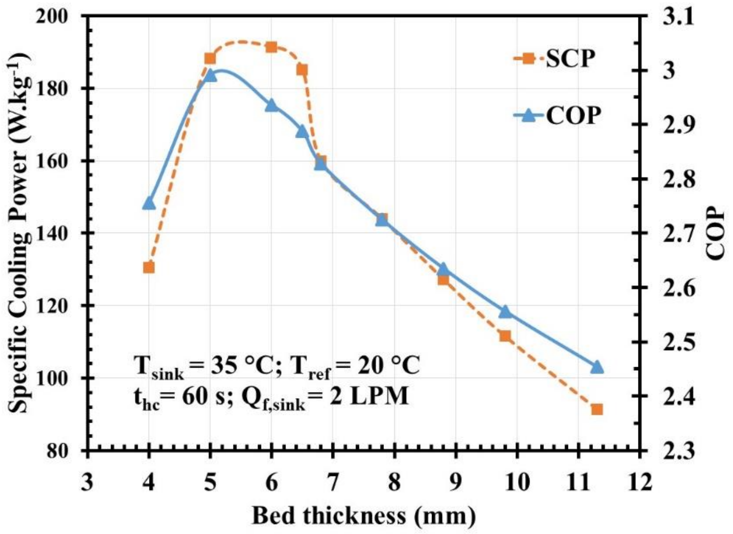

Fig. 7.11: Influence of bed thickness variation on SCP and COP.

For a given effective thermal conductivity, the thermal resistance is influenced by the bed thickness; therefore with a redcution in bed thickness, performance improvement is expected. However, with a reduction in bed thickness, the mass of the containment material increases, which again contributes to the sensible cooling load. For 5 mm bed thickness, the optimum values of SCP and COP are estimated to be 188.2 W.kg^{-1}and 2.99, respectively.

Influence of HTF flow rate

Figure 7.12 illustrates the influence of HTF flow rate variation of the desorbing reactor on system SCP and COP. The HTF flow rate is varied from 2-16 LPM at a step of 2 LPM. With an increase in HTF flow rate, the overall heat transfer coefficient increases, which contributes to the increase in SCP and COP at a higher flow rate. However, the effect of increasing flow rate on system performance becomes marginal beyond 12 LPM flow rate as the dominating factor constituting the overall heat transfer coefficient is the bed thermal resistance.

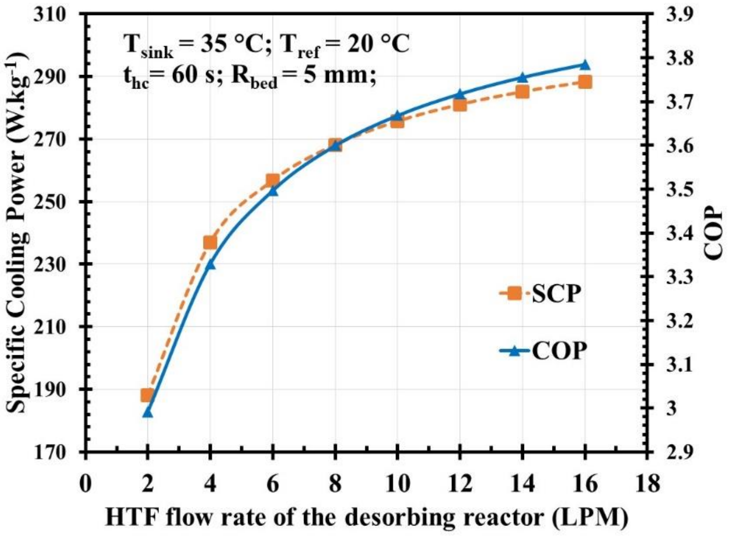

Fig. 7.12: Influence of HTF flow rate variation on SCP and COP.

Moreover, considering pressure drop across the flow channel at elevated flow rate, the optimum flow rate is decided to be 12 LPM.

Influence of half-cycle time

Figure 7.13 shows the effect of increasing HC time on system SCP and COP. For 15 s HC time, the estimated COP and SCP are 3.52 and 337.5 W.kg^{-1}, respectively. As HC time is increased to 30 s, the COP value increases to 3.82, while SCP is reduced slightly. Such an outcome is in accordance with the pattern followed by compressor power and cooling power, i.e., the cooling power achieved during the first 10-15 s is quite low compared to the compressor power consumption during the first 10-15 s. Beyond 30 s, till 150 s HC time, the COP and SCP reduce monotonously. Based on the cooling performance of the system, the optimum HC time is determined to be 30 s. However, in practical systems, 30 s is too short of achieving any meaningful cooling effect; hence the HC time considered for simulation is taken as 60 s.

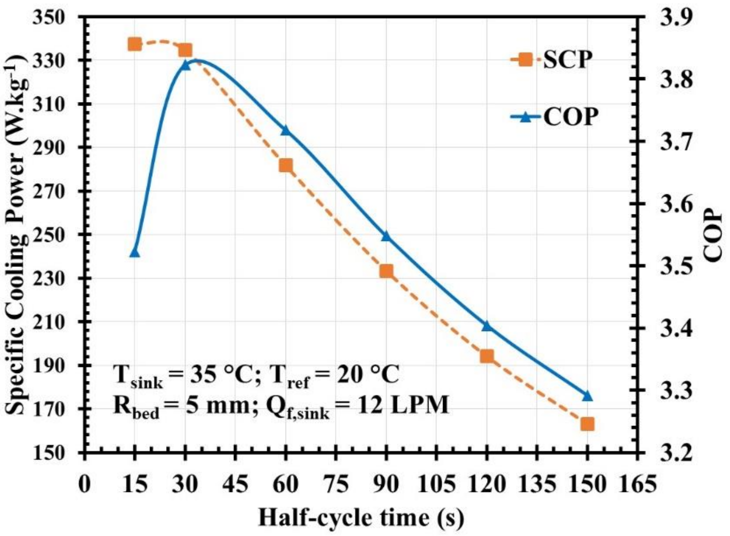

Fig. 7.13: Influence of half-cycle time variation on SCP and COP.

Influence of initial concentration

Figure 7.14 shows the influence of the initial concentration variation of the desorbing reactor on system performance. During this assessment, the initial concentration of the desorbing reactor is varied from 0.5-0.8, while the initial concentration of the absorbing reactor is set to 0.4.

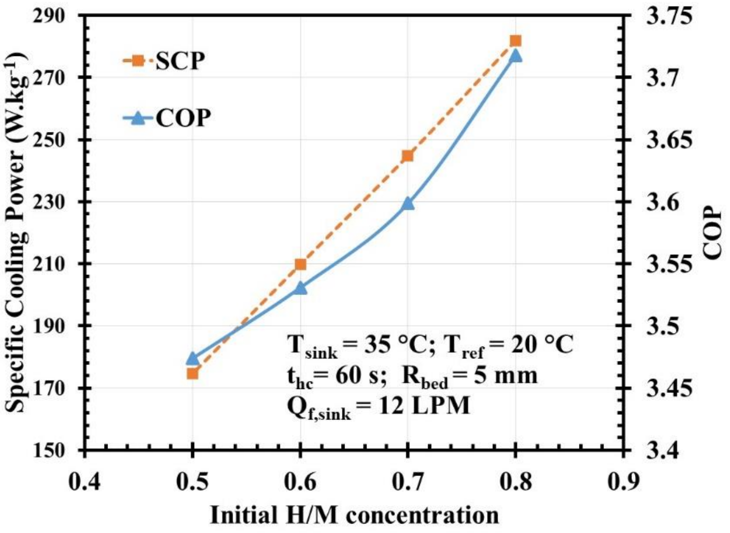

Fig. 7.14: Effect of initial desorption concentration variation on SCP and COP.

For a fixed initial concentration in the absorbing reactor, as the initial concentration in the desorbing reactor is increased, the potential for hydrogen transfer increases within a stipulated HC time. The amount of hydrogen transferred between the reactors at different initial concentrations are 0.39 wt.%, 0.34 wt.%, 0.29 wt.% and 0.25 wt.%, respectively.

The maximum value of SCP and COP estimated at 0.8 desorbing concentration are 281.8 W.kg-1 and 3.72, respectively.

Influence of refrigeration and sink temperature

Figure 7.15 elucidates the influence of refrigeration and sink temperature variations on system COP and SCP. For a set sink temperature of 35 °C, refrigeration temperature is varied from 10-20 °C at a step of 5 °C.

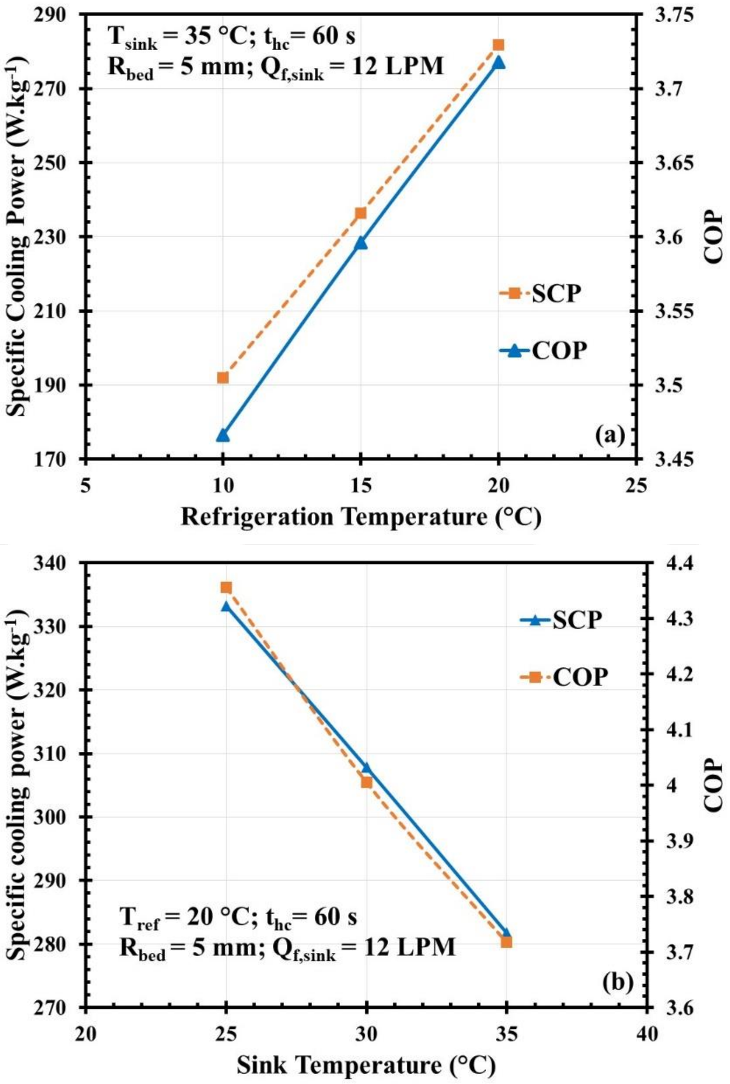

Fig. 7.15: Influence of operating temperature variation on SCP and COP (a) refrigeration temperature and (b) sink temperature.

With an increase in refrigeration temperature, the estimated COP and SCP values are increased as an increase in refrigeration temperature results in increased hydrogen transfer potential between the reactors due to an increase in the equilibrium pressure of the desorbing bed. The maximum COP and SCP obtained at 20 °C refrigeration temperature are 3.72 and 281.79 W.kg^{-1}, correspondingly (Fig. 7.15(a)). The effect of sink temperature variation on system COP and SCP (Fig. 7.15(b)) is similar to the effect observed in the case of refrigeration temperature variation. With an increase in sink temperature, the potential for hydrogen transfer between the reactors is reduced owing to an increase in the equilibrium pressure of the absorbing bed. For the set refrigeration temperature of 20 °C, the sink temperature is increased from 25 °C to 35 °C at a step of 5 °C. The maximum COP and SCP obtained at 25 °C sink temperature are 4.36 and 333.2 W.kg$^{-1,}$ correspondingly.

7.4. Summary

This chapter deals with the development of two different numerical models which individually predict the hydrogen storage and closed-loop cooling system performance. This first model is a 3-D model which considers the flow simulation of the HTF and its implication on heat transfer of the MH reactor. These model predictions are validated with the obtained experimental results. Upon validation, this model is further used to project the constant flow rate desorption characteristics of the 19 TBR module. The second numerical model is a simplified 0-D model which attempts to capture the dynamics of hydrogen transfer for a closed-loop compressor-driven cooling system. The effect of hydrogen compression is incorporated within the model by specifying the flow and pressure correlations. This model is further utilized to predict the influence of bed thickness, HTF flow rate, initial concentration, half-cycle time and operating temperatures on system COP and SCP.

8. Thesis Summary, Conclusions and Recommendations

8.1. Thesis summary

The research work presented in this thesis has been carried out with a key motive to support a smooth energy transition from fossil fuels to renewables. Nations across the globe are continuing to roll out policy documents to bring forth hydrogen, more specifically green hydrogen-based energy economy, in place to alleviate the climate crisis. In this regard, metal hydrides are one of the outstanding classes of materials that can mitigate the hydrogen storage and transportation challenges over long distances and even longer periods. They are predominantly attractive as hydrogen storage materials as they can store significant amounts of hydrogen within a compact space in near ambient temperature and pressure. Moreover, hydrogen released from the MH is highly pure that can be directly fed to fuel cells. Another remarkable feature of MH material is that the absorption and desorption of hydrogen within MH is assisted by large thermal effects (20-75 kJ.mol $^{-1}$), which can be channelled to provide considerable heating and cooling output. Cooling systems based on MH are environment-friendly and are also promising in terms of system COP and SCP when operated by a compressor.

In this thesis work, a number of lab-scale (3-5 kg) as well as large-scale (25-30 kg) MH reactors have been conceptualized, designed, fabricated and tested for hydrogen storage as well cooling applications. Experiments are mainly targeted at testing scalable off-grid systems for power generation and cooling. The design and optimization of the MH reactors are supported by numerical projections. COMSOL Multiphysics platform has been utilized to implement and solve 0-D, 2-D, and 3-D numerical models for hydrogen storage and cooling systems. The order in which research work has been conducted is 'Thermodynamic screening of suitable MH alloys', 'Design and simulation on MH reactors for heat transfer enhancement, and 'Testing and thermal performance assessment of the reactors'.

8.2. Key conclusions

Chapter 3 of the thesis discusses the design and fabrication of the MH reactors considering two key configurations, viz., the embedded cooling tube reactor and the tube bundle reactor. The design of the reactors accounted for minimum MH bed thickness, reduced thermal mass, and ease of fabrication, transportation and handling. Numerical predictions of the hydrogen storage performance indicated that both ECTR and TBR configurations are fast dynamics reactors with identical absorption profiles. Further, it was concluded that for the same alloy capacity (6.3 kg) the TBR configuration could offer 17% less system weight.

Chapter 4 of the thesis discusses the hydrogen storage performance of two large-scale MH reactors, namely the 19 TBR module and the 99 ECTR_OCJ module and a lab-scale concentric tube reactor. The key conclusions of this chapter are as follows:

- 19 TBR module:
    - The reactor was able to reversibly store approximately 350 g hydrogen (1.37 wt.%), necessitating an average heating rate of 0.64–1.72 kW in the temperature range of 40-70 °C.
    - Experimentally derived optimal absorption and desorption conditions were 15 bar, 20 °C (absorption) and 50 °C (desorption).
    - The estimated average cooling rate required for hydrogen absorption was 1.7–5.6 kW at 10–20 bar, 20 °C.
    - The maximum energy efficiency of the hydrogen storage system was estimated to be 64.6% (40 °C, 15 LPM desorption; 15 bar, 20 °C, 25 absorption).
    - The influence of partial desorption indicated hydrogen should be recovered as much as possible to improve energy efficiency.
    - At 40 °C desorption, energy efficiency plunged from 60% to 42% when the amount of desorbed hydrogen was reduced from 90% to 60%.
    - It was concluded that under similar desorption conditions, the reactor could deliver hydrogen at a reasonably faster rate compared to other MH reactors of both large as well as small capacities.
- 99 ECTR_OCJ module:
    - At 20 bar, 25 °C, the MH reactor absorbed 276.08 g hydrogen in 1129 s, accounting for 1.28 wt.% charged capacity.
    - The peak rates of heat removal required during charging at 10-30 bar were 6-10 kW, whereas the corresponding average heat removal rates were 2-3 kW only.
    - At 40 °C, 282.8 g (1.31 wt.%) hydrogen was discharged in 4860 s, with an average mass flow rate of 0.058 g.s^{-1}. By the end of discharging at 40 °C, the

  recorded reactor pressure was 1.3 bar. If discharged through an MFC, the reactor could feed a 3.5 kW LT-PEMFC for the same duration.
  - The peak rates of heat supply required during 40-60 °C discharging were estimated in the range of 1.5-3 kW. For the same temperature range, the estimated average rates of heat supply required were in the range of 0.5-0.65 kW.
  - The recorded rector gauge pressure at the end of discharging in the temperature range of 40-60 °C was 1.1-1.3 bar.
  - The energy efficiency of the reactor was 65-68% in the temperature range of 40-60 °C.
  - At 50 °C, the estimated energy efficiency at 60%, 70%, 80% and 90% desorption were 0.649, 0.67, 0.687 and 0.697, respectively, indicating loss in efficiency with fractional desorption.
  - Desorption results obtained under comparable operating condition shows that the reactor could desorb hydrogen at a decent rate compared to both large and small-capacity reactors.
- Tube and tube reactor module:
  - For the mechanically mixed sample, parametric tests indicated the optimum hydrogen absorption condition to be 30-50 bar, 15 °C. At the same time, hydrogen desorption was favourable in the temperature range of 40-60 °C.
  - Desorption tests at 6.5 LPM hydrogen flow rate indicated that the alloy mixture could sustain the set flow rate for 21-46 min at 30-60 °C
  - When desired flow rate was increased to 13 LPM, the set flow could be sustained for 10-18 min at 40-60 °C.
  - The peak and average heat input required to drive desorption at a steady rate of 6.5-13 LPM was only 80-120 W, and 60-80 W, correspondingly.

Chapter 5 discusses about the performance testing of open-cycle cooling systems with and without the aid of a mechanical compressor. Experiments were conducted on two identical 48 ECTR_OCJ modules. The key conclusions of this chapter are as follows:

- Open cycle cooling without compressor
    - The optimum hydrogen absorption condition for $La_{0.8}Ce_{0.2}Ni_5$ was identified as 30 bar, 25 °C. At this regeneration condition, the reactor absorbed 42.3 g (1.24 wt.%) within 617 s.
    - The optimum hydrogen absorption condition for $La_{0.7}Ce_{0.1}Ca_{0.3}Ni_5$ was identified as 20 bar, 25 °C. At this regeneration condition, the reactor absorbed 46.4 g (1.37 wt.%) within 446 s.
    - The cooling study showed that the optimum temperature ranges for achieving a sustained cooling effect was 15–25 °C. At 25 °C, $La_{0.7}Ce_{0.1}Ca_{0.3}Ni_5$ was able to produce 435.5 kJ cold output within 2048 s, yielding a peak and average cooling rate of 0.43 kW and 0.21 kW, respectively.
- Open cycle cooling with compressor
    - The concept of an open-cycle compressor-driven cooling system was explored for the first time in this study. The key advantage of such a system is that for regeneration of the reactor, merely 30-40 bar hydrogen supply pressure would be sufficient, thus eliminating the need of a high-pressure hydrogen tank (150-700 bar). The system would simultaneously act as a green hydrogen storage module as well as a cooling and purification system.
    - It was witnessed that at the beginning of desorption, the compressor power input was the highest for both alloys. As desorption proceeded forward, the power input reduced significantly within the first 15-20 s, and then steadily went down till the end of the cycle.
    - The maximum values of instantaneous COP estimated for $La_{0.8}Ce_{0.2}Ni_5$ and $La_{0.7}Ce_{0.1}Ca_{0.3}Ni_5$ were 0.41 and 0.4, respectively.
    - The maximum value of mean COPs estimated for $La_{0.8}Ce_{0.2}Ni_5$ and $La_{0.7}Ce_{0.1}Ca_{0.3}Ni_5$ were 0.36 (20 °C, HC: 480 s) and 0.31 (20 °C, HC: 480 s), respectively.
    - The maximum value of SCPs predicted for $La_{0.8}Ce_{0.2}Ni_5$ and $La_{0.7}Ce_{0.1}Ca_{0.3}Ni_5$ were 86.8 $W.kg^{-1}$ (20 °C, HC: 480 s) and 76.9 $W.kg^{-1}$ (20 °C, HC: 240 s), respectively.

Chapter 6 discusses about the experiments on closed cycle compressor-driven cooling system employing a pair 19 TBR modules. The key conclusions of this chapter are as follows:

- The TBR modules were coupled with a custom-built compressor to provide cooling effect in a quasi-continuous mode of operation. The compressor was tested to operate smoothly up to a hydrogen flow rate of 0.5 g. s^{-1} in the temperature range of 10-35 °C, yielding pressure ratio up-to 12.8.
- The maximum cooling power attained at 20 °C refrigeration temperature and 30 °C sink temperature was 1.44 kW, generating 537.3 kJ cooling within 600 s.
- The corresponding mean COP and SCP were 0.95 and 36.4 W.kg^{-1} for 480 s half-cycle time.
- Within the specified half-cycle time, the quantity of hydrogen transported between the reactors was only around 10% of the available hydrogen inventory, which led to harnessing only part of the potential cooling production.

Chapter 7 discusses two different numerical models applied to predict the hydrogen storage performance and coupled bed cooling performance individually. The first model is an extended version of the numerical model described in Chapter 3, which incorporates the flow and heat transfer effects of the HTF by solving the continuity, momentum, and energy equations for the HTF. The second work deals with the development of a lumped model to predict the dynamic performance of a compressor-operated closed-cycle cooling system. The key conclusions of this chapter are as follows:

- Extended numerical model
    - With an increase in HTF temperature, for any given set mass flow rate, the duration of constant discharge was found to be elongated as the equilibrium pressure would be higher at elevated temperatures, enabling the reactor to discharge hydrogen for a longer duration.
    - During constant flow discharge, the drop in bed pressure was greater in the case of a set higher desorption rate.
    - The reactor was projected to provide constant mass flow to 1 kW and 2 kW PEMFCs for a maximum duration of 5350 s and 2400 s, respectively at 70 °C.
- Lumped model for compressor-driven cooling system
    - The effect of considering variable hydrogen flow over constant flow in between the reactors of the coupled system showed that the cumulative hydrogen transferred between the reactors was the same in both cases. However, in the case of variable flow, the rate of flow is the highest during the initial period,

wherein, in the case of constant flow rate compression, the power consumption is minimum during the initial period as the set flow rate is lower than the initial flow rate achieved during variable flow compression.

- Parametric studies dictated optimum bed thickness and optimum half-cycle time to be 5 mm and 30 s, respectively.
- For a fixed initial concentration in the absorbing reactor, as the initial concentration in the desorbing reactor is increased, the potential for hydrogen transfer increases within a stipulated half-cycle time.
- The maximum COP and SCP obtained at 20 °C refrigeration temperature and 25 °C sink temperature were 4.36 and 333.2 $W.kg^{-1}$, correspondingly.

8.3. Recommendations for future work

The research work embodied in this thesis can be extended to accomplish design, development and testing of poly-generation engineering devices based on MH. A few research directions are highlighted below:

- The large-scale MH reactors studied in this work can be simultaneously integrated with an electrolysers and an LT-PEMFC to check their performance under actual condition.
- To promote the development of compressor-driven MH-based cooling systems, focus should be given to the selection of the MH alloy from a reaction kinetic standpoint and the careful selection of a dedicated hydrogen compressor.
- An inclusive numerical model can be developed to test the feasibility of open-cycle compressor-driven heating and cooling systems.
- Higher-order numerical models (2-D, 3-D) can be developed to predict the dynamic performance of compressor-driven closed-cycle cooling systems.

References

Afzal, M., Gupta, N., Mallik, A., Vishnulal, K.S., Sharma, P., 2021. Experimental analysis of a metal hydride hydrogen storage system with hexagonal honeycomb-based heat transfer enhancements-part B. Int. J. Hydrogen Energy 46, 13131–13141. https://doi.org/10.1016/j.ijhydene.2020.11.275

Afzal, M., Mane, R., Sharma, P., 2017. Heat transfer techniques in metal hydride hydrogen storage: A review. Int. J. Hydrogen Energy 42, 30661–30682. https://doi.org/10.1016/j.ijhydene.2017.10.166

Afzal, M., Sharma, P., 2018a. Design of a large-scale metal hydride based hydrogen storage reactor: Simulation and heat transfer optimization. Int. J. Hydrogen Energy 43, 13356–13372. https://doi.org/10.1016/j.ijhydene.2018.05.084

Afzal, M., Sharma, P., 2018b. Design of a large-scale metal hydride based hydrogen storage reactor: Simulation and heat transfer optimization. Int. J. Hydrogen Energy 43, 13356–13372. https://doi.org/10.1016/j.ijhydene.2018.05.084

Alqahtani, T., Bamasag, A., Mellouli, S., Askri, F., Phelan, P.E., 2020. Cyclic behaviors of a novel design of a metal hydride reactor encircled by cascaded phase change materials. Int. J. Hydrogen Energy 45, 32285–32297. https://doi.org/10.1016/j.ijhydene.2020.08.280

Anbarasu, S., Muthukumar, P., Mishra, S.C., 2014. Thermal modeling of $LmNi_{4.91}Sn_{0.15}$ based solid state hydrogen storage device with embedded cooling tubes. Int. J. Hydrogen Energy 39, 15549–15562. https://doi.org/10.1016/j.ijhydene.2014.07.088

Andersson, J., Grönkvist, S., 2019. Large-scale storage of hydrogen. Int. J. Hydrogen Energy 44, 11901–11919. https://doi.org/10.1016/j.ijhydene.2019.03.063

Andreasen, G., Melnichuk, M., Ramos, S., Corso, H.L., Visintin, A., Triaca, W.E., Peretti, H.A., 2013. Hydrogen desorption from a hydride container under different heat exchange conditions. Int. J. Hydrogen Energy 38, 13352–13359. https://doi.org/10.1016/j.ijhydene.2013.07.115

Apostolov, A., Stanev, N., Tcholakov, P., 1985. Hydrogen desorption characteristics of $MmNi_{5-x}Fe_x$ compounds. J. Less Common Met. 110, 127–129. https://doi.org/10.1016/0022-5088(85)90313-3

Armato, M., 2013. Energy Consumption By Source [WWW Document]. My Energy Blog. URL https://ourworldindata.org/grapher/energy-consumption-by-source-and-country?stackMode=absolute (accessed 4.27.23).

Bao, Z., Mou, X., 2021. Experimental study on temperature variation of metal hydride reactor incorporating helically coiled heat exchanger during absorption. J. Energy Storage 44, 103438. https://doi.org/10.1016/j.est.2021.103438

Bao, Z., Wu, Z., Nyamsi, S.N., Yang, F., Zhang, Z., 2013. Three-dimensional modeling and sensitivity analysis of multi-tubular metal hydride reactors. Appl. Therm. Eng. 52, 97–108. https://doi.org/10.1016/j.applthermaleng.2012.11.023

Bedbak, S., Ramgopal, M., 2005. Performance analysis of a compressor driven metal hydride cooling system. Int. J. Hydrogen Energy 30, 1127–1137. https://doi.org/10.1016/j.ijhydene.2004.10.014

Bhouri, M., Goyette, J., Hardy, B.J., Anton, D.L., 2012. Numerical modeling and performance evaluation of multi-tubular sodium alanate hydride finned reactor. Int. J. Hydrogen Energy 37, 1551–1567. https://doi.org/10.1016/j.ijhydene.2011.10.044

Bhuiya, M.M.H., Kumar, A., Kim, K.J., 2015. Metal hydrides in engineering systems, processes, and devices: A review of non-storage applications. Int. J. Hydrogen Energy 40, 2231–2247. https://doi.org/10.1016/j.ijhydene.2014.12.009

Bjurström, H., Suda, S., 1989. The metal hydride heat pump: Dynamics of hydrogen transfer. Int. J. Hydrogen Energy 14, 19–28. https://doi.org/10.1016/0360-3199(89)90152-3

Blinov, D. V., Borzenko, V.I., Dunikov, D.O., Romanov, I.A., 2014. Experimental investigations and a simple balance model of a metal hydride reactor. Int. J. Hydrogen Energy 39, 19361–19368. https://doi.org/10.1016/j.ijhydene.2014.07.048

Botzung, M., Chaudourne, S., Gillia, O., Perret, C., Latroche, M., Percheronguegan, A., Marty, P., 2008. Simulation and experimental validation of a hydrogen storage tank with metal hydrides. Int. J. Hydrogen Energy 33, 98–104. https://doi.org/10.1016/j.ijhydene.2007.08.030

Briki, C., Belkhiria, S., Dhaou, M.H., Askri, F., Jemni, A., 2018. Dynamic study of a new design of a tanks based on metallic hydrides. Int. J. Hydrogen Energy 43, 1566–1576. https://doi.org/10.1016/j.ijhydene.2017.11.085

Chandra, S., Sharma, P., Muthukumar, P., Sarma V Tatiparti, S., 2022. Experimental hydrogen sorption study on a $LaNi_5$-based 5 kg reactor with novel conical fins and water tubes and its numerical scale-up through a modular approach. Int. J. Hydrogen Energy. https://doi.org/10.1016/j.ijhydene.2022.08.098

Chen, Z., Kirlikovali, K.O., Idrees, K.B., Wasson, M.C., Farha, O.K., 2022. Porous materials for hydrogen storage. Chem 8, 693–716. https://doi.org/10.1016/j.chempr.2022.01.012

Chen, Z., Ma, Z., Zheng, J., Li, X., Akiba, E., Li, H.W., 2021. Perspectives and challenges of hydrogen storage in solid-state hydrides. Chinese J. Chem. Eng. 29, 1–12. https://doi.org/10.1016/j.cjche.2020.08.024

Chernikov, A.., Izhvanov, L.., Solovey, A.., Frolov, V.., Shanin, Y.., 2002. An installation for water cooling based on a metal hydride heat pump. J. Alloys Compd. 330–332, 907–910. https://doi.org/10.1016/S0925-8388(01)01479-7

Choi, H., Mills, A.F., 1990. Heat and mass transfer in metal hydride beds for heat pump applications. Int. J. Heat Mass Transf. 33, 1281–1288. https://doi.org/10.1016/0017-9310(90)90257-U

Chung, C.A., Yang, S.W., Yang, C.Y., Hsu, C.W., Chiu, P.Y., 2013. Experimental study on the hydrogen charge and discharge rates of metal hydride tanks using heat pipes to enhance heat transfer. Appl. Energy 103, 581–587. https://doi.org/10.1016/j.apenergy.2012.10.024

Column: China on track to hit new clean & dirty power records in 2022 | Reuters [WWW Document], n.d. URL https://www.reuters.com/business/energy/china-track-hit-new-clean-dirty-power-records-2022-maguire-2022-11-23/ (accessed 2.13.23).

Da-Wen, S., Song-Jiu, D., 1989. Study of the heat and mass transfer characteristics of metal hydride beds: A two-dimensional model. J. Less Common Met. 155, 271–279. https://doi.org/10.1016/0022-5088(89)90236-1

Dehouche, Z., de Jong, W., Willers, E., Isselhorst, A., Groll, M., 1998. Modelling and simulation of heating/air-conditioning systems using the multi-hydride-thermal-wave concept. Appl. Therm. Eng. 18, 457–480. https://doi.org/10.1016/S1359-4311(97)00043-4

Delhomme, B., de Rango, P., Marty, P., Bacia, M., Zawilski, B., Raufast, C., Miraglia, S., Fruchart, D., 2012. Large scale magnesium hydride tank coupled with an external heat source. Int. J. Hydrogen Energy 37, 9103–9111. https://doi.org/10.1016/j.ijhydene.2012.03.018

Dong, J., Wang, X., Xu, H., Zhao, Q., Li, J., 2007. Hydrogen storage in several microporous zeolites. Int. J. Hydrogen Energy 32, 4998–5004. https://doi.org/10.1016/j.ijhydene.2007.08.009

El Mghari, H., Huot, J., Tong, L., Xiao, J., 2020. Selection of phase change materials, metal foams and geometries for improving metal hydride performance. Int. J. Hydrogen Energy 45, 14922–14939. https://doi.org/10.1016/j.ijhydene.2020.03.226

Fedorov, E., Shanin, Y.., Izhvanov, L.., 1999. Simulation of hydride heat pump operation. Int. J. Hydrogen Energy 24, 1027–1032. https://doi.org/10.1016/S0360-3199(98)00138-4

Førde, T., Næss, E., Yartys, V.A., 2009. Modelling and experimental results of heat transfer in a metal hydride store during hydrogen charge and discharge. Int. J. Hydrogen Energy 34, 5121–5130. https://doi.org/10.1016/j.ijhydene.2009.03.019

Freni, A., Cipitì, F., Cacciola, G., 2009. Finite element-based simulation of a metal hydride-based hydrogen storage tank. Int. J. Hydrogen Energy 34, 8574–8582. https://doi.org/10.1016/j.ijhydene.2009.07.118

Furukawa, H., Yaghi, O.M., 2009. Storage of hydrogen, methane, and carbon dioxide in highly porous covalent organic frameworks for clean energy applications. J. Am. Chem. Soc. 131, 8875–8883. https://doi.org/10.1021/ja9015765

Garrison, S.L., Hardy, B.J., Gorbounov, M.B., Tamburello, D.A., Corgnale, C., VanHassel, B.A., Mosher, D.A., Anton, D.L., 2012. Optimization of internal heat exchangers for hydrogen storage tanks utilizing metal hydrides. Int. J. Hydrogen Energy 37, 2850–2861. https://doi.org/10.1016/j.ijhydene.2011.07.044

Global Hydrogen Review 2022, 2022., Global Hydrogen Review 2022. OECD. https://doi.org/10.1787/a15b8442-en

Goodell, P.D., Sandrock, G.D., Huston, E.L., 1980. Kinetic and dynamic aspects of rechargeable metal hydrides. J. Less Common Met. 73, 135–142. https://doi.org/10.1016/0022-5088(80)90352-5

Goudy, A.J., Stokes, D.G., Gazzillo, J.A., 1983. The effect of heat transfer on the desorption kinetics of LaNi,H. J. Less-Common Met. 91, 149–158.

Government of India, 2023. National Green Hydrogen Mission Ministry of New and Renewable Energy.

Groll, M., Supper, W., Mayer, U., Brost, O., 1987. Heat and mass transfer limitations in metal hydride reaction beds. Int. J. Hydrogen Energy 12, 89–97. https://doi.org/10.1016/0360-3199(87)90085-1

Gruen, D.M., Mendelsohn, M.H., Sheft, I., 1978. Metal hydrides as chemical heat pumps. Sol. Energy 21, 153–156. https://doi.org/10.1016/0038-092X(78)90043-9

GX Implementation Council (The Prime Minister in Action) | Prime Minister's Office of Japan [WWW Document], n.d. URL https://japan.kantei.go.jp/101_kishida/actions/202212/_00050.html (accessed 4.27.23).

Ha, M.Y., Kim, I.K., Song, H.D., Sung, S., Lee, D.H., 2004. A numerical study of thermo-fluid phenomena in metal hydride beds in the hydriding process. Int. J. Heat Mass Transf. 47, 2901–2912. https://doi.org/10.1016/j.ijheatmasstransfer.2004.03.014

Han, J., Lee, J., 1987. A study of the hydriding kinetics of Mg_2Ni at the near isothermal condition. Int. J. Hydrogen Energy 12, 417–424. https://doi.org/10.1016/0360-3199(87)90161-3

Han, J.I., Lee, J.-Y., 1989. Hydriding kinetics of $LaNi_5$ and $LaNi_{4.7}Al_{0.3}$. Int. J. Hydrogen Energy 14, 181–186. https://doi.org/10.1016/0360-3199(89)90052-9

Hwang, H.T., Varma, A., 2014. Hydrogen storage for fuel cell vehicles. Curr. Opin. Chem. Eng. 5, 42–48. https://doi.org/10.1016/j.coche.2014.04.004

IEA, 2022. Global CO_2 emissions rebounded to their highest level in history in 2021 [WWW Document]. IEA. URL https://www.iea.org/news/global-co2-emissions-rebounded-to-their-highest-level-in-history-in-2021 (accessed 12.27.22).

Imoto, T., Yonesaki, T., Fujitani, S., Yonezu, I., Hiro, N., Saito, T., Materials, N., 1996. Development of an F-class refrigeration system using hydrogen-absorbing alloys. Int. J. Hydrogen Energy 21, 451–455. https://doi.org/10.1016/0360-3199(95)00106-9

International Energy Agency (IEA), 2022. International Energy Agency (IEA) World Energy Outlook 2022, https://iea.blob.core.windows.net/assets/830fe099-5530-48f2-a7c1-11f35d510983/WorldEnergyOutlook2022.pdf.

Izhvanov, L., Solovey, A.., Frolov, V.., Shanin, Y.., 1996. Metal hydride heat pump? New type of heat converter. Int. J. Hydrogen Energy 21, 1033–1038. https://doi.org/10.1016/S0360-3199(96)00046-8

Jang, K., Fateev, G.., Park, J.., Han, S.., Lee, P., Lee, J.., 2001. Simulation of the metal hydride heat pump system with the single and double reactors. Int. J. Hydrogen Energy 26, 237–241. https://doi.org/10.1016/S0360-3199(00)00066-5

Jensen, J.O., Vestbø, A.P., Li, Q., Bjerrum, N.J., 2007. The energy efficiency of onboard hydrogen storage. J. Alloys Compd. 446–447, 723–728. https://doi.org/10.1016/j.jallcom.2007.04.051

Kang, B., Park, C.., Lee, C.., 1996. Dynamic behavior of heat and hydrogen transfer in a metal hydride cooling system. Int. J. Hydrogen Energy 21, 769–774. https://doi.org/10.1016/0360-3199(96)00017-1

Karmakar, A., Mallik, A., Gupta, N., Sharma, P., 2021. Studies on 10kg alloy mass metal hydride based reactor for hydrogen storage. Int. J. Hydrogen Energy 46, 5495–5506. https://doi.org/10.1016/j.ijhydene.2020.11.091

Keshari, V., Maiya, M.P., 2018. Design and investigation of hydriding alloy based hydrogen storage reactor integrated with a pin fin tube heat exchanger. Int. J. Hydrogen Energy 43, 7081–7095. https://doi.org/10.1016/j.ijhydene.2018.02.100

Kikkinides, E.., Georgiadis, M.., Stubos, A.., 2006. On the optimization of hydrogen storage in metal hydride beds. Int. J. Hydrogen Energy 31, 737–751. https://doi.org/10.1016/j.ijhydene.2005.06.021

Kim, K.J., Feldman Jr, K.T., Lloyd, G., Razani, A., 1997. Compressor-driven metal-hydride heat pumps. Appl. Therm. Eng. 17, 551–560. https://doi.org/10.1016/S1359-4311(96)00067-1

Kim, K.J., Montoya, B., Razani, A., Lee, K.-H., 2001. Metal hydride compacts of improved thermal conductivity. Int. J. Hydrogen Energy 26, 609–613. https://doi.org/10.1016/S0360-3199(00)00115-4

Kirchheim, R., Pundt, A., 2014. Hydrogen in Metals, in: Physical Metallurgy. Elsevier, pp. 2597–2705. https://doi.org/10.1016/B978-0-444-53770-6.00025-3

Kline, S. J., McClintock, F. A., 1953. Describing Uncertainties in Single-Sample Experiments. Mech. Eng. 75,3-8.

Klein, H.-P., Groll, M., 2002. Development of a two-stage metal hydride system as topping cycle in cascading sorption systems for cold generation. Appl. Therm. Eng. 22, 631–639. https://doi.org/10.1016/S1359-4311(01)00115-6

Koh, J.T., Goudy, A.J., Huang, P., Zhou, G., 1989. A comparison of the hydriding and dehydriding kinetics of $LaNi_5$ hydride. J. Less-Common Met. 153, 89–100. https://doi.org/10.1016/0022-5088(89)90536-5

Krokos, C.A., Nikolic, D., Kikkinides, E.S., Georgiadis, M.C., Stubos, A.K., 2009. Modeling and optimization of multi-tubular metal hydride beds for efficient hydrogen storage. Int. J. Hydrogen Energy 34, 9128–9140. https://doi.org/10.1016/j.ijhydene.2009.09.021

Kumar, A., Raju, N.N., Muthukumar, P., Selvan, P.V., 2019. Experimental studies on industrial scale metal hydride based hydrogen storage system with embedded cooling tubes. Int. J. Hydrogen Energy 44, 13549–13560. https://doi.org/10.1016/j.ijhydene.2019.03.180

Kumar, A., Muthukumar, P., 2022a. Experimental studies on poisoning of $La_{0.9}Ce_{0.1}Ni_5$ based hydrogen purification system with CO_2 as impurity. Int. J. Hydrogen Energy 1–10. https://doi.org/10.1016/j.ijhydene.2022.10.137

Kumar, A., Muthukumar, P., 2022b. Experimental investigation on the poisoning characteristics of methane as impurity in $La_{0.9}Ce_{0.1}Ni_5$ based hydrogen storage and purification system. Energy 259, 124888. https://doi.org/10.1016/j.energy.2022.124888

Kumar Phate, A., Prakash Maiya, M., Murthy, S.S., 2007. Simulation of transient heat and mass transfer during hydrogen sorption in cylindrical metal hydride beds. Int. J. Hydrogen Energy 32, 1969–1981. https://doi.org/10.1016/j.ijhydene.2006.09.020

Langmi, H.W., Ren, J., North, B., Mathe, M., Bessarabov, D., 2014. Hydrogen storage in metal-organic frameworks: A review. Electrochim. Acta 128, 368–392. https://doi.org/10.1016/j.electacta.2013.10.190

Larminie, J., Dicks, A., 2013. Appendix 2: Useful Fuel Cell Equations, in: Fuel Cell Systems Explained. John Wiley & Sons, Ltd,., West Sussex, England, pp. 395–400. https://doi.org/10.1002/9781118878330.app2

Laurencelle, F., Goyette, J., 2007. Simulation of heat transfer in a metal hydride reactor with aluminium foam. Int. J. Hydrogen Energy 32, 2957–2964. https://doi.org/10.1016/j.ijhydene.2006.12.007

Lee, S.., Kim, Y.., Lee, J.., 1995. Operating characteristics of metal hydride heat pump using Zr-based laves phases. Int. J. Hydrogen Energy 20, 77–85. https://doi.org/10.1016/0360-3199(93)E0005-6

Linder, M., Mertz, R., Laurien, E., 2010a. Experimental analysis of fast metal hydride reaction bed dynamics. Int. J. Hydrogen Energy 35, 8755–8761. https://doi.org/10.1016/j.ijhydene.2010.05.023

Linder, M., Mertz, R., Laurien, E., 2010b. Experimental results of a compact thermally driven cooling system based on metal hydrides. Int. J. Hydrogen Energy 35, 7623–7632. https://doi.org/10.1016/j.ijhydene.2010.04.184

Liu, Y., Wang, H., Prasad, A.K., Advani, S.G., 2014. Role of heat pipes in improving the hydrogen charging rate in a metal hydride storage tank. Int. J. Hydrogen Energy 39, 10552–10563. https://doi.org/10.1016/j.ijhydene.2014.04.197

Lototskyy, M. V., Davids, M.W., Tolj, I., Klochko, Y. V., Sekhar, B.S., Chidziva, S., Smith, F., Swanepoel, D., Pollet, B.G., 2015. Metal hydride systems for hydrogen storage and supply for stationary and automotive low temperature PEM fuel cell power modules. Int. J. Hydrogen Energy 40, 11491–11497. https://doi.org/10.1016/j.ijhydene.2015.01.095

Lozano, G.A., Ranong, C.N., Bellosta von Colbe, J.M., Bormann, R., Hapke, J., Fieg, G., Klassen, T., Dornheim, M., 2012. Optimization of hydrogen storage tubular tanks based on light weight hydrides. Int. J. Hydrogen Energy 37, 2825–2834. https://doi.org/10.1016/j.ijhydene.2011.03.043

Lucas, G., Richards, W., 1984. Mathematical modelling of hydrogen storage systems. Int. J. Hydrogen Energy 9, 225–231. https://doi.org/10.1016/0360-3199(84)90123-X

Ma, J., Wang, Y., Shi, S., Yang, F., Bao, Z., Zhang, Z., 2014. Optimization of heat transfer device and analysis of heat & mass transfer on the finned multi-tubular metal hydride tank. Int. J. Hydrogen Energy 39, 13583–13595. https://doi.org/10.1016/j.ijhydene.2014.03.016

Magnetto, D., Mola, S., DaCosta, D.H., Golben, M., Rosso, M., 2006. A Metal Hydride Mobile Air Conditioning System, in: SAE Technical Papers. pp. 1150–1159. https://doi.org/10.4271/2006-01-1235

Makridis, S.S., 2016. Hydrogen storage and compression, in: Methane and Hydrogen for Energy Storage. Institution of Engineering and Technology, pp. 1–28. https://doi.org/10.1049/PBPO101E_ch1

Martin, M., Gommel, C., Borkhart, C., Fromm, E., 1996. Absorption and desorption kinetics of hydrogen storage alloys. J. Alloys Compd. 238, 193–201. https://doi.org/10.1016/0925-8388(96)02217-7

Mayer, U., Groll, M., Supper, W., 1987. Heat and mass transfer in metal hydride reaction beds: Experimental and theoretical results. J. Less Common Met. 131, 235–244. https://doi.org/10.1016/0022-5088(87)90523-6

Mazumdar, S., Bhattacharyya, S., Ramgopal, M., 2005. Compressor driven metal hydride cooling systems—mathematical model and operating characteristics. Int. J. Refrig. 28, 798–809. https://doi.org/10.1016/j.ijrefrig.2005.02.002

Mellouli, S., Abhilash, E., Askri, F., Ben Nasrallah, S., 2016. Integration of thermal energy storage unit in a metal hydride hydrogen storage tank. Appl. Therm. Eng. 102, 1185–1196. https://doi.org/10.1016/j.applthermaleng.2016.03.116

Mellouli, S., Askri, F., Dhaou, H., Jemni, A., Ben Nasrallah, S., 2010. Numerical simulation of heat and mass transfer in metal hydride hydrogen storage tanks for fuel cell vehicles. Int. J. Hydrogen Energy 35, 1693–1705. https://doi.org/10.1016/j.ijhydene.2009.12.052

Mellouli, S., Askri, F., Dhaou, H., Jemni, A., Ben Nasrallah, S., 2009. Parametric studies on a metal-hydride cooling system. Int. J. Hydrogen Energy 34, 3945–3952. https://doi.org/10.1016/j.ijhydene.2009.03.010

Mellouli, S., Askri, F., Dhaou, H., Jemni, A., Ben Nasrallah, S., 2007. A novel design of a heat exchanger for a metal-hydrogen reactor. Int. J. Hydrogen Energy 32, 3501–3507. https://doi.org/10.1016/j.ijhydene.2007.02.039

Melnichuk, M., Andreasen, G., Corso, H., Visintin, A., Peretti, H., 2008. Study and characterization of a metal hydride container. Int. J. Hydrogen Energy 33, 3571–3575. https://doi.org/10.1016/j.ijhydene.2007.12.029

Meng, X., Bao, Z., Wu, Z., Yang, F., Zhang, Z., 2012. A Comprehensive Performance Evaluation Index for Metal Hydrides Reactor. Energy Procedia 29, 421–430. https://doi.org/10.1016/j.egypro.2012.09.049

Meng, X., Wu, Z., Bao, Z., Yang, F., Zhang, Z., 2013. Performance simulation and experimental confirmation of a mini-channel metal hydrides reactor. Int. J. Hydrogen Energy 38, 15242–15253. https://doi.org/10.1016/j.ijhydene.2013.09.056

Miyamoto, M., Yamaji, K., Nakata, Y., 1983. Reaction kinetics of $LaNi_5$. J. Less-Common Met. 89, 111–116. https://doi.org/10.1016/0022-5088(83)90254-0

Moffat, R.J., 1988. Describing the uncertainties in experimental results. Exp. Therm. Fluid Sci. 1, 3–17. https://doi.org/10.1016/0894-1777(88)90043-X

Mohammadshahi, S.S., Gould, T., Gray, E.M.A., Webb, C.J., 2016. An improved model for metal-hydrogen storage tanks - Part 1: Model development. Int. J. Hydrogen Energy 41, 3537–3550. https://doi.org/10.1016/j.ijhydene.2015.12.050

Mohammadshahi, S. S., Gray, E.M.A., Webb, C.J., 2016. A review of mathematical modelling of metal-hydride systems for hydrogen storage applications. Int. J. Hydrogen Energy 41, 3470–3484. https://doi.org/10.1016/j.ijhydene.2015.12.079

Mohan, G., Prakash Maiya, M., Srinivasa Murthy, S., 2007. Performance simulation of metal hydride hydrogen storage device with embedded filters and heat exchanger tubes. Int. J. Hydrogen Energy 32, 4978–4987. https://doi.org/10.1016/j.ijhydene.2007.08.007

Muthukumar, P., Linder, M., Mertz, R., Laurien, E., 2009. Measurement of thermodynamic properties of some hydrogen absorbing alloys. Int. J. Hydrogen Energy 34, 1873–1879. https://doi.org/10.1016/j.ijhydene.2008.12.052

Muthukumar, P., Madhavakrishna, U., Dewan, A., 2007. Parametric studies on a metal hydride based hydrogen storage device. Int. J. Hydrogen Energy 32, 4988–4997. https://doi.org/10.1016/j.ijhydene.2007.08.010

Muthukumar, P., Patil, M.S., Raju, N.N., Imran, M., 2016. Parametric investigations on compressor-driven metal hydride based cooling system. Appl. Therm. Eng. 97, 87–99. https://doi.org/10.1016/j.applthermaleng.2015.10.155

Muthukumar, P., Prakash Maiya, M., Murthy, S., 2005. Experiments on a metal hydride-based hydrogen storage device. Int. J. Hydrogen Energy 30, 1569–1581. https://doi.org/10.1016/j.ijhydene.2004.12.007

Muthukumar, P., Ramana, S.V., 2009. Numerical simulation of coupled heat and mass transfer in metal hydride-based hydrogen storage reactor. J. Alloys Compd. 472, 466–472. https://doi.org/10.1016/j.jallcom.2008.04.088

Muthukumar, P., Singhal, A., Bansal, G.K., 2012. Thermal modeling and performance analysis of industrial-scale metal hydride based hydrogen storage container. Int. J. Hydrogen Energy 37, 14351–14364. https://doi.org/10.1016/j.ijhydene.2012.07.010

Muthukumar, P., Venkata Ramana, S., 2010. Study of heat and mass transfer in $MmNi_{4.6}Al_{0.4}$ during desorption of hydrogen. Int. J. Hydrogen Energy 35, 10811–10818. https://doi.org/10.1016/j.ijhydene.2010.02.069

Na Ranong, C., Höhne, M., Franzen, J., Hapke, J., Fieg, G., Dornheim, M., Eigen, N., Bellosta von Colbe, J.M., Metz, O., 2009. Concept, Design and Manufacture of a Prototype Hydrogen Storage Tank Based on Sodium Alanate. Chem. Eng. Technol. 32, 1154–1163. https://doi.org/10.1002/ceat.200900095

Nagar, R., Srivastava, S., Hudson, S.L., Amaya, S.L., Tanna, A., Sharma, M., Achayalingam, R., Sonkaria, S., Khare, V., Srinivasan, S.S., 2023. Recent developments in state-of-the-art hydrogen energy technologies – Review of hydrogen storage materials. Sol. Compass 5, 100033. https://doi.org/10.1016/j.solcom.2023.100033

Nagel, M., Komazaki, Y., Suda, S., 1986. Effective thermal conductivity of a metal hydride bed augmented with a copper wire matrix. J. Less Common Met. 120, 35–43. https://doi.org/10.1016/0022-5088(86)90625-9

Nagel, M., Komazaki, Y., Uchida, M., Suda, S., Matsubara, Y., 1984. Operating characteristics of a metal hydride heat pump for generating cooled air. J. Less Common Met. 104, 307–318. https://doi.org/10.1016/0022-5088(84)90415-6

Nakagawa, T., 2000. Numerical analysis of heat and mass transfer characteristics in the metal hydride bed. Int. J. Hydrogen Energy 25, 339–350. https://doi.org/10.1016/S0360-3199(99)00036-1

Nakano, A., Ito, H., Maeda, T., Munakata, T., Motyka, T., Corgnale, C., Greenway, S., Perez-Berrios, J.M., 2013. Study on a metal hydride tank to support energy storage for renewable energy. J. Alloys Compd. 580, S418–S422. https://doi.org/10.1016/j.jallcom.2013.03.152

Nasrallah, S., Jemni, A., 1997. Heat and mass transfer models in metal-hydrogen reactor. Int. J. Hydrogen Energy 22, 67–76. https://doi.org/10.1016/S0360-3199(96)00039-0

Ni, J., Liu, H., 2007. Experimental research on refrigeration characteristics of a metal hydride heat pump in auto air-conditioning. Int. J. Hydrogen Energy 32, 2567–2572. https://doi.org/10.1016/j.ijhydene.2006.09.038

Nishizaki, T., Miyamoto, K., Yoshida, K., 1983. Coefficients of performance of hydride heat pumps. J. Less Common Met. 89, 559–566. https://doi.org/10.1016/0022-5088(83)90372-7

Nyamsi, S.N., Yang, F., Zhang, Z., 2012. An optimization study on the finned tube heat exchanger used in hydride hydrogen storage system – analytical method and numerical simulation. Int. J. Hydrogen Energy 37, 16078–16092. https://doi.org/10.1016/j.ijhydene.2012.08.074

Oi, T., Maki, K., Sakaki, Y., 2004. Heat transfer characteristics of the metal hydride vessel based on the plate-fin type heat exchanger. J. Power Sources 125, 52–61. https://doi.org/10.1016/S0378-7753(03)00822-X

Parida, A., Muthukumar, P., 2023. Reactor design and numerical study on metal hydride based finned reactor configurations for hydrogen compression application. Int. J. Hydrogen Energy. https://doi.org/10.1016/j.ijhydene.2022.10.183

Parida, A., Muthukumar, P., 2022. Thermal Performance Comparisons of ECT and Helical-Coiled based Metal-Hydride Reactor, in: Proceedings of the 26thNational and 4th International ISHMT-ASTFE Heat and Mass Transfer Conference December 17-20, 2021, IIT Madras, Chennai-600036, Tamil Nadu, India. Begellhouse, Connecticut, pp. 2157–2162. https://doi.org/10.1615/IHMTC-2021.3260

Park, J.., Han, S.., Jang, H.., Lee, S.., Lee, P.., Lee, J.., 2002. The development of compressor-driven metal hydride heat pump (CDMHHP) system as an air conditioner. Int. J. Hydrogen Energy 27, 941–944. https://doi.org/10.1016/S0360-3199(01)00187-2

Park, J., Jang, K.-J., Lee, P.., Lee, J.-Y., 2001. The operating characteristics of the compressor-driven metal hydride heat pump system. Int. J. Hydrogen Energy 26, 701–706. https://doi.org/10.1016/S0360-3199(01)00006-4

Payá, J., Linder, M., Laurien, E., Corberán, J.M., 2009. Dynamic model and experimental results of a thermally driven metal hydride cooling system. Int. J. Hydrogen Energy 34, 3173–3184. https://doi.org/10.1016/j.ijhydene.2009.01.085

Payá, J., Linder, M., Mertz, R., Corberán, J.M., 2011. Analysis and optimization of a metal hydride cooling system. Int. J. Hydrogen Energy 36, 920–930. https://doi.org/10.1016/j.ijhydene.2010.08.112

Prachi R., P., Mahesh M., W., Aneesh C., G., 2016. A Review on Solid State Hydrogen Storage Material. Adv. Energy Power 4, 11–22. https://doi.org/10.13189/aep.2016.040202

Qin, F., Chen, J., Lu, M., Chen, Z., Zhou, Y., Yang, K., 2007. Development of a metal hydride refrigeration system as an exhaust gas-driven automobile air conditioner. Renew. Energy 32, 2034–2052. https://doi.org/10.1016/j.renene.2006.10.014

Raju, M., Kumar, S., 2012. Optimization of heat exchanger designs in metal hydride based hydrogen storage systems. Int. J. Hydrogen Energy 37, 2767–2778. https://doi.org/10.1016/j.ijhydene.2011.06.120

Raju, N.N., Muthukumar, P., Selvan, P.V., Malleswararao, K., 2019. Design methodology and thermal modelling of industrial scale reactor for solid state hydrogen storage. Int. J. Hydrogen Energy 44, 20278–20292. https://doi.org/10.1016/j.ijhydene.2019.05.193

Ramgopal, M., Srinivasa Murthy, S., 1992. Prediction of heat and mass transfer in annular cylindrical metal hydride beds. Int. J. Hydrogen Energy 17, 795–805. https://doi.org/10.1016/0360-3199(92)90024-Q

Ramimoghadam, D., Gray, E.M.A., Webb, C.J., 2016. Review of polymers of intrinsic microporosity for hydrogen storage applications. Int. J. Hydrogen Energy 41, 16944–16965. https://doi.org/10.1016/j.ijhydene.2016.07.134

Ren, J., Musyoka, N.M., Langmi, H.W., Mathe, M., Liao, S., 2017. Current research trends and perspectives on materials-based hydrogen storage solutions: A critical review. Int. J. Hydrogen Energy 42, 289–311. https://doi.org/10.1016/j.ijhydene.2016.11.195

Ron, M., 1984. A hydrogen heat pump as a bus air conditioner. J. Less Common Met. 104, 259–278. https://doi.org/10.1016/0022-5088(84)90411-9

Rusman, N.A.A., Dahari, M., 2016. A review on the current progress of metal hydrides material for solid-state hydrogen storage applications. Int. J. Hydrogen Energy 41, 12108–12126. https://doi.org/10.1016/j.ijhydene.2016.05.244

Sakintuna, B., Lamari-Darkrim, F., Hirscher, M., 2007. Metal hydride materials for solid hydrogen storage: A review. Int. J. Hydrogen Energy. https://doi.org/10.1016/j.ijhydene.2006.11.022

Sandrock, G., 1999. A panoramic overview of hydrogen storage alloys from a gas reaction point of view. J. Alloys Compd. 293–295, 877–888. https://doi.org/10.1016/S0925-8388(99)00384-9

Sandrock, G., Suda, S., Schlapbach, L., 1992. Applications, in: Hydrogen in Intermetallic Compunds II. pp. 197–258. https://doi.org/10.1007/3-540-54668-5_12

Satheesh, A., Muthukumar, P., 2010. Performance investigations of a single-stage metal hydride heat pump. Int. J. Hydrogen Energy 35, 6950–6958. https://doi.org/10.1016/j.ijhydene.2010.04.043

Satheesh, A., Muthukumar, P., Dewan, A., 2009. Computational study of metal hydride cooling system. Int. J. Hydrogen Energy 34, 3164–3172. https://doi.org/10.1016/j.ijhydene.2009.01.083

Sharma, V.K., Anil Kumar, E., 2014. Measurement and analysis of reaction kinetics of La – based hydride pairs suitable for metal hydride – based cooling systems. Int. J. Hydrogen Energy 39, 19156–19168. https://doi.org/10.1016/j.ijhydene.2014.09.083

Sharma, V.K., Kumar, E.A., 2015. Studies on la based intermetallic hydrides to determine their suitability in metal hydride based cooling systems. Intermetallics 57, 60–67. https://doi.org/10.1016/j.intermet.2014.10.004

Singh, A., Maiya, M.P., Srinivasa Murthy, S., 2017. Experiments on solid state hydrogen storage device with a finned tube heat exchanger. Int. J. Hydrogen Energy 42, 15226–15235. https://doi.org/10.1016/j.ijhydene.2017.05.002

Skripnyuk, V., Ron, M., 2003. Hydrogen desorption kinetics in intermetallic compounds C2, C5 and C5 with Laves phase structure. Int. J. Hydrogen Energy 28, 303–309. https://doi.org/10.1016/S0360-3199(02)00081-2

Skripnyuk, V.M., Ron, M., 1999. Evaluation of kinetics by utilizing the normalized pressure dependence method for the alloy $Ti_{0.95}Zr_{0.05}Mn_{1.48}V_{0.43}Fe_{0.08}Al_{0.01}$. J. Alloys Compd. 293, 385–390. https://doi.org/10.1016/S0925-8388(99)00375-8

Souahlia, A., Dhaou, H., Mellouli, S., Askri, F., Jemni, A., Ben Nasrallah, S., 2014. Experimental study of metal hydride-based hydrogen storage tank at constant supply pressure. Int. J. Hydrogen Energy 39, 7365–7372. https://doi.org/10.1016/j.ijhydene.2014.02.121

Sreeraj, R., Aadhithiyan, A.K., Anbarasu, S., 2022. Integration of thermal augmentation methods in hydride beds for metal hydride based hydrogen storage systems: Review and recommendation. J. Energy Storage 52, 105039. https://doi.org/10.1016/j.est.2022.105039

Srinivasan, S.S., Sharma, P.C., Stefanakos, E.K., Goswami, D.Y., 2020a. Metal Hydrides, in: Handbook of Hydrogen Energy. Routledge Handbooks Online, pp. 726–781. https://doi.org/10.1201/b17226-28

Srinivasan, S.S., Sharma, P.C., Stefanakos, E.K., Goswami, D.Y., 2020b. Complex Hydrides. Handb. Hydrog. Energy 782–827. https://doi.org/10.1201/b17226-29

Statement, W.E.C., 2003. RENEWABLE ENERGY TARGETS.

Sterner, M., Specht, M., 2021. Power-to-Gas and Power-to-X—The History and Results of Developing a New Storage Concept. Energies 14, 6594. https://doi.org/10.3390/en14206594

Stetson, N.T., Jr., R.C.B., Olson, G.L., 2014. Overview of Hydrogen Storage, Transportation, Handling, and Distribution. Handb. Hydrog. Energy 670–685. https://doi.org/10.1201/B17226-23

Suda, S., Kobayashi, N., Yoshida, K., 1980. Reaction kinetics of metal hydrides and their mixtures. J. Less Common Met. 73, 119–126. https://doi.org/10.1016/0022-5088(80)90350-1

Sunku prasad, J., Muthukumar, P., 2021. Experimental investigation on annular metal hydride reactor for medium to large-scale hydrogen storage applications. J. Energy Storage 44, 103473. https://doi.org/10.1016/j.est.2021.103473

Supper, W., Groll, M., Mayer, U., 1984. Reaction kinetics in metal hydride reaction beds with improved heat and mass transfer. J. Less Common Met. 104, 279–286. https://doi.org/10.1016/0022-5088(84)90412-0

The US Press Office, 2022. FACT SHEET: The Inflation Reduction Act Supports Workers and Families.

Tong, L., Xiao, J., Yang, T., Bénard, P., Chahine, R., 2019. Complete and reduced models for metal hydride reactor with coiled-tube heat exchanger. Int. J. Hydrogen Energy 44, 15907–15916. https://doi.org/10.1016/j.ijhydene.2018.07.102

US DoE, 2017. Target Explanation Document: Onboard Hydrogen Storage for Light-Duty Fuel Cell Vehicles, U.S Drive.

Visaria, M., Mudawar, I., 2012. Experimental investigation and theoretical modeling of dehydriding process in high-pressure metal hydride hydrogen storage systems. Int. J. Hydrogen Energy 37, 5735–5749. https://doi.org/10.1016/j.ijhydene.2011.12.140

Wang, D., Wang, Y., Huang, Z., Yang, F., Wu, Z., Zheng, L., Wu, L., Zhang, Z., 2019. Design optimization and sensitivity analysis of the radiation mini-channel metal hydride reactor. Energy 173, 443–456. https://doi.org/10.1016/j.energy.2019.02.033

Wang, X.-L., Suda, S., 1990. A dehydriding kinetic study of $LaNi_{4.7}Al_{0.3}$ hydride by a step-wise method. J. Less Common Met. 159, 83–90. https://doi.org/10.1016/0022-5088(90)90135-7

Wang, X., Suda, S., 1990. Reaction kinetics of hydrogen-metal hydride systems. Int. J. Hydrogen Energy 15, 569–577. https://doi.org/10.1016/0360-3199(80)90005-1

Wang, X.L., Suda, S., 1990. Study of the hydriding kinetics of $LaNi_{4.7}Al_{0.3}H$ system by a step-wise method. J. Less-Common Met. 159, 109–119. https://doi.org/10.1016/0022-5088(90)90138-A

Weckerle, C., Bürger, I., Linder, M., 2017. Novel reactor design for metal hydride cooling systems. Int. J. Hydrogen Energy 42, 8063–8074. https://doi.org/10.1016/j.ijhydene.2017.01.066

Wulf, C., Linssen, J., Zapp, P., 2018. Power-to-Gas—Concepts, Demonstration, and Prospects, in: Hydrogen Supply Chains. Elsevier, pp. 309–345. https://doi.org/10.1016/B978-0-12-811197-0.00009-9

Yang, F., Cao, X., Zhang, Z., Bao, Z., Wu, Z., Serge, N.N., 2012. Assessment on the Long Term Performance of a $LaNi_5$ based Hydrogen Storage System. Energy Procedia 29, 720–730. https://doi.org/10.1016/j.egypro.2012.09.084

Yang, F., Meng, X., Deng, J., Wang, Y., Zhang, Z., 2007. Identifying heat and mass transfer characteristics of metal hydride reactor during adsorption—Parameter analysis and numerical study. Int. J. Hydrogen Energy 33, 1014–1022. https://doi.org/10.1016/j.ijhydene.2007.11.007

Yang, J., Sudik, A., Wolverton, C., Siegel, D.J., 2010. High capacity hydrogenstorage materials: attributes for automotive applications and techniques for materials discovery. Chem. Soc. Rev. 39, 656–675. https://doi.org/10.1039/B802882F

Yasuda, N., Tsuchiya, T., Okinaka, N., Akiyama, T., 2013. Application of metal hydride sheet to thermally driven cooling system. Int. J. Hydrogen Energy 38, 7469–7476. https://doi.org/10.1016/j.ijhydene.2013.04.011

Zhou, L., 2005. Progress and problems in hydrogen storage methods. Renew. Sustain. Energy Rev. 9, 395–408. https://doi.org/10.1016/j.rser.2004.05.005

Züttel, A., 2004. Hydrogen storage methods. Naturwissenschaften 91, 157–172. https://doi.org/10.1007/s00114-004-0516-x

Appendix A: Uncertainty Analysis

Directly measured data

The accuracy limits for directly measured variables such as temperature, pressure, flow rate of hydrogen as well HTF are presented in Table A.1.

Table A.1: Specification of the measuring apparatus used in experiments

Measuring apparatus	Measurement range	Accuracy
Thermocouple: K type	-200-1300 °C	± 0.5 °C
Gauge pressure transducer: HTA Instruments	0-100 bar	± 0.5% FS
Gauge pressure transducer: HTA Instruments	0-25 bar	± 0.5% FS
Flow meter: ATN Instruments	0-60 LPM	±1% FS
Coriolis mass flow meter (hydrogen): Emerson	0-10 $g.s^{-1}$	± 0.35% RD
Mass flow controller (hydrogen): Aalborg	0-30 LPM	±1% FS
Energy meter: AmiciSense	0-2000 W	± 1%
Weighing balance: Radwag	0-2000 g	± 0.01 g

Estimated data

The uncertainty associated with indirectly measured data like hydrogen storage capacity, heat flux etc. can be estimated by knowing individual uncertainties linked to directly measured variables. In this context, the scheme proposed by Moffat, (1988) has been used to estimate the uncertainty of indirectly measured variables. The proposed scheme is illustrated below:

If an indirectly measured variable 'Z' depends on a number of directly measured variable X_1, X_2, $X_3 \ldots X_n$, and the individual uncertainties of the directly measured variables are expressed as ΔX_1, ΔX_2, $\Delta X_3 \ldots$ ΔX_n; the uncertainty in measurement of 'Z' can be expressed as:

$$\Delta Z = \pm\sqrt{\left\{\left(\frac{\partial Z}{\partial X_1}\right)\Delta X_1\right\}^2 + \left\{\left(\frac{\partial Z}{\partial X_2}\right)\Delta X_2\right\}^2 + \left\{\left(\frac{\partial Z}{\partial X_3}\right)\Delta X_3\right\}^2 + \ldots + \left\{\left(\frac{\partial Z}{\partial X_n}\right)\Delta X_n\right\}^2} \qquad (A.1)$$

Hydrogen storage capacity (wt.%):

The hydrogen storage capacity is estimated by calculating the amount of hydrogen absorbed or desorbed from the MH bed containing known quantity of MH powder. The amount of MH powder loaded in MH reactor was estimated using the mass balance with accuracy of 0.01 g. Therefore, the maximum uncertainty associated with measurement of hydrogen storage capacity is calculated to be ± 0.25%.

Rate of heat transferred to/from HTF:

The uncertainty associated with rate of heat transferred with HTF can be estimated by knowing the individual uncertainties associated with measurement of HTF properties (density, specific heat capacity) within operated temperature-pressure range, flow rate measurement and temperature measurement of the thermocouples attached to the HTF inlet and the outlet sections. The maximum possible uncertainty is estimated as ± 6.22%.

Specific Cooling Power:

The uncertainty associated with estimation of SCP can be calculated from the individual uncertainties linked to mass of MH estimation and rate of heat transferred from the HTF. The maximum uncertainty is calculated as ± 6.23%.

COP:

The uncertainty linked to estimation of COP is due to uncertainty in measuring compressor power input and rate of heat transferred from the HTF. The maximum uncertainty is estimated as ± 6.35%.

Appendix B: Specification of the major experimental apparatus

1. Thermocouple

Type:	K-type (metal-sheathed)
Make:	Industrial Heators
Range:	-200 to 1300 °C
Accuracy:	± 0.5 °C

2. Pressure transducer

Make:	Equinox
Model:	EQ-PT-1000
Range:	0 to 100 bar
Accuracy:	± 0.5% FS
Output:	4 to 20 mA

3. Data Acquisition System

Make:	Keysight
Model:	34972A
Scan rate:	22 to 66 channels per second
Scan intervals:	0 to 99 hours; 1 ms time step
Accuracy:	± 0.004%

4. Mass flow meter

Type:	Coriolis mass flow meter
Make:	Emerson Process Management Pvt. Ltd.
Model:	CMF010P323NQBZEZZZ
Fluid:	Hydrogen
Flow rate range:	0-50 $g.s^{-1}$
Accuracy:	± 0.35 % RD
Sensitivity	0.001 g
Operating temperature:	50 °C (max)
Operating pressure:	0-80 bar
Output:	4 to 20 mA

5. Mass flow controller

Make:	Aalborg Inc.
Type:	Thermal mass flow controller
Model:	GFC37
Flow rate range:	0-30 LPM
Accuracy:	1% FS
Pressure range:	69 bar (max)
Temperature range:	0-50 °C
Output:	4 to 20 mA
End fittings:	1/4 inch NPT

6. Hydrogen flow control valves

Make:	Swagelok Inc.
Type:	High pressure diaphragm sealed valve
Model:	SS-DSS4
Pressure range	241 bar at 20 °C
Temperature range	(-73)-121 °C
End fittings	1/4 inch NPT

7. Recirculating Constant Temperature Bath (cold)

Make:	Siskin Instruments Pvt. Ltd.
Model:	RCC 7000 ST40
Temperature range:	-30 °C to 50 °C
Pumping rate:	60 LPM (max)
Cooling capacity:	7 kW at 0 °C
Heating capacity:	3.5 kW

8. Recirculating Constant Temperature Bath (hot)

Make:	Siskin Instruments Pvt. Ltd.
Model:	HCB 200S
Temperature range:	40 °C to 110 °C
Pumping rate:	50 LPM
Heating capacity:	9 kW

9. Vacuum pump

Make:	Ranvac Technologies Pvt. Ltd.
Model:	RV 2035
Pump type:	Rotary vacuum pump
Pumping rate:	585 LPM
Vacuum range:	999 to 10^{-3} mbar

10. Weighing balance

Make:	Radwag Inc.
Model:	WTC 2000
Capacity:	0-2000 g
Accuracy:	0.01 g

List of Publications

In Peer-reviewed Journals

Publication from thesis

1. **Sayantan Jana**, P. Muthukumar, Experimental Studies on a Closed Cycle Compressor Operated Metal Hydride Based Cooling System with Large Hydrogen Inventory, Int. J. Hydrogen Energy. (2023) 1–14. https://doi.org/10.1016/j.ijhydene.2023.07.007.
2. **Sayantan Jana**, P. Muthukumar, Design, development and hydrogen storage performance testing of a tube bundle metal hydride reactor, Journal of Energy Storage. 63 (2023) 106936. https://doi.org/10.1016/j.est.2023.106936.
3. **Sayantan Jana**, P. Muthukumar, Raju NN. Hydrogen charging and discharging studies on embedded cooling tube metal hydride reactor designed for fuel cell applications. Int J. Hydrogen Energy 2022. doi:10.1016/j.ijhydene.2022.07.118.
4. **Sayantan Jana**, NN Raju, P. Muthukumar, Performance tests on Embedded Cooling Tube type Metal Hydride reactor for heating and cooling applications, Thermal Science and Engineering Progress, 33 (2022) 101349
5. **Sayantan Jana**, P. Muthukumar, Design and Performance Prediction of a Compact $MmNi_{4.6}Al_{0.4}$ based Hydrogen Storage System, Journal of Energy Storage, 39 (2021) 102612
6. Sayantan Jana, P. Muthukumar, Performance tests on open-cycle compressor driven metal hydride based cooling system (***Manuscript ready to submit***)
7. Sayantan Jana, P. Muthukumar, Absorption and desorption studies on mechanically mixed $La_{0.7}Ce_{0.1}Ca_{0.3}Ni_5$ and $MmNi_{4.5}Fe_{0.5}$ for hydrogen storage application (***Manuscript under preparation***)
8. Sayantan Jana, P. Muthukumar, Dynamic model development and performance prediction of a compressor operated metal hydride based closed cycle cooling system (***Manuscript under preparation***)
9. Sayantan Jana, P. Muthukumar, Numerical modelling of constant flow discharge and tank refuelling from a Tube bundle Metal Hydride reactor (***Manuscript under preparation***)

Review paper

1. P Muthukumar, A Kumar, M Afzal, S Bhogilla, P Sharma, A Parida, **Sayantan Jana**, E Anil Kumar, R K Pai, I P Jain. Review on large-scale hydrogen storage systems for better sustainability. Int J Hydrogen Energy 2023. doi:10.1016/j.ijhydene.2023.04.304.

Book Chapters

1. A. Kumar, **Sayantan Jana**, P. Muthukumar, Thermodynamic Analysis on Hydrogen Storage System, in: Encycl. Energy Storage, Elsevier Inc., 2021: pp. 1–11. https://doi.org/10.1016/B978-0-12-819723-3.00134-7.

Conference presentations

1. **Sayantan Jana**, P. Muthukumar (2022). Hydrogen Desorption Studies on Embedded Cooling Tube type Metal Hydride Reactor Designed for Fuel Cell Application. Presented at ICRE 2022 - International Conference on Renewable Energy, Feb 25-27, 2022, University of Rajasthan, Jaipur, India
2. **Sayantan Jana**, Ila Abhay Kulkarni, P. Muthukumar (2022). Performance tests on an open-cycle compressor driven metal hydride based cooling system. Presented at NCRAC 2022 – 7th National and 1st International Conference on Refrigeration and Air Conditioning, Feb 24-26, 2022, IIT Guwahati, India
3. **Sayantan Jana**, Nithin Narmda Raju, P. Muthukumar (2021), Experimental studies on Embedded Cooling Tube type Metal Hydride Reactor for Heating and Cooling application, Presented at International Conference on Polygeneration (ICP-2021), University of Zaragoza, Spain, October 4-6, 2021
4. **Sayantan Jana**, J. Sunku Prasad, P. Muthukumar (2020), Design and numerical modelling of a compact metal hydride-hydrogen storage reactor, Presented at Hydrogen Power Theoretical & Engineering Solutions International Symposium (HYPOTHESIS-2020), University of Cape Town, South Africa, June 3-5, 2020.